Mechanistic insight into homogeneous catalytic reactions by ESI-MS

by

Zohrab Ahmadi
M.Sc., Iran University of Science and Technology, 2006
B.Sc., Kashan University, 2003

A Dissertation Submitted in Partial Fulfillment
of the Requirements for the Degree of

DOCTOR OF PHILOSOPHY

in the Department of Chemistry

© Zohrab Ahmadi, 2013
University of Victoria

All rights reserved. This dissertation may not be reproduced in whole or in part, by
photocopy or other means, without the permission of the author.

Supervisory Committee

Mechanistic insight into homogeneous catalytic reactions by ESI-MS

by

Zohrab Ahmadi
M.Sc., Iran University of Science and Technology, 2006
B.Sc., Kashan University, 2003

Supervisory Committee

Dr. J. Scott McIndoe, Department of Chemistry
Supervisor

Dr. Alexander Brolo, Department of Chemistry
Departmental Member

Dr. Robin Hicks, Department of Chemistry
Department Member

Roberta C. Hamme, Department of Earth and Ocean Science
Outside Member

Abstract

Supervisory Committee
Dr. J. Scott McIndoe, Department of Chemistry
Supervisor

Dr. Alexander Brolo, Department of Chemistry
Departmental Member

Dr. Robin Hicks, Department of Chemistry
Departmental Member

Roberta C. Hamme, Department of Earth and Ocean Science
Outside Member

For the study of homogeneous catalytic reaction mechanisms, the ideal technique would be capable of identifying and measuring in real time the abundances of all components of the reaction mixture, including reactants, products, byproducts, intermediates, and catalyst resting states. This thesis details the development of methodologies designed to transform electrospray ionization mass spectrometry into just such a tool.

Species of interests must be charged otherwise invisible in ESI-MS. Therefore, charge-tagged aryl iodide ($[4\text{-I-}C_6H_4CH_2PPh_3]^+[Br]^-$) and a terminal alkyne ($[\textit{para}\text{-}(HCC)C_6H_4CH_2PPh_3]^+[Br]^-$) were synthesized as the ESI-active substrates for the homogeneous catalysis study. A method named PSI (pressurized sample infusion) was developed to introduce the air and moisture sensitive reaction mixtures to the ESI-MS. The analytical aspects of the method were investigated and optimized. Applicability of the technique was demonstrated through several organic and organometallic mechanism investigations.

The above developments were employed to the detailed study of the copper-free Sonogashira (Heck alkynylation) reaction and the hydrodehalogenation of the charged-tag aryl iodide. Simultaneous monitoring of the charged substrate, products and intermediates in the copper-free Sonogashira reaction by PSI-ESI-MS provided rich information about the kinetic and mechanism of this reaction. Kinetic isotope effect study

shows a remarkable inverse kinetic isotope effect which is completely unexpected. Numerical models were constructed to simulate the mechanistic observation and to extract the rate constant of each step in the proposed mechanism cycle.

The same methodology (PSI technique) was used to the study of the hydrodehalogenation reaction. Key intermediates were detected under the typical reaction conditions. Kinetic isotope effect study was performed in CH_3OD and CD_3OD. A primary KIE was observed in both deuterated solvents. A revised mechanism cycle was suggested for this reaction based on KIE results, numerical modelling and other experiments. In the proposed cycle deprotonation of methanol occurs on the palladium metal centre instead of the conventional in solution deprotonation (off metal deprotonation).

The mechanism of the ligand substitution of charged-tag of a palladium aryl iodide $[Pd(TMEDA)(Ar)(I)]^+$ (Ar = $[C_6H_4CH_2PPh_3]^+[PF_6]^-$) complex against PPh_3 was studied in methanol by PSI-ESI-MS. Results revealed that the pathway proceeds quite differently to what had been assumed by others; there was a very fast displacement of $[I]^-$ by PPh_3 to form $[Pd(TMEDA)(Ar)(PPh_3)]^{2+}$, followed by a much slower displacement of TMEDA and recoordination of $[I]^-$ to form the product $[Pd(PPh_3)_2ArI]^+$.

We successfully integrated UV/Vis spectroscopy, as a complementary method with ESI-MS to shed light into the systems where ESI-MS only is unable to provide a full assignment to homogenous catalysis. The combination of the two fast and sensitive techniques provides a unique opportunity to study the composition of the organometallic reaction mixtures over time.

Table of Contents

Supervisory Committee ii
Abstract iii
Table of Contents v
List of Schemes vii
List of Figures xii
List of Abbreviations xxi
Acknowledgments xxiv
Dedication xxv
Chapter 1 Literature review 1
1.1 Applying ESI-MS to organometallic catalysis 1
1.1.1. Inherently-charged systems 2
1.1.2 Adventitiously-charged systems 15
1.1.3 Charged or chargeable tags 22
1.2 Continuous reaction monitoring 30
1.3 Conclusion 35
Chapter 2 Techniques and methodologies 36
2.1 Introduction 36
2.2 A brief history of mass spectrometry 37
2.3 ESI-QToF-MS 39
2.3.1 The electrospray ionization process 39
2.3.2 Q-Tof Micro 40
2.3.3 Experiment types by mass spectrometry 43
2.4 Numerical modeling 45
2.5 UV/Vis spectroscopy as a tool in kinetic and mechanistic study 49
2.5.1 Introduction 49
2.5.2 From Reaction *in situ* to *Operando* methodology in catalysis study 50
Chapter 3 Method Development 54
3.1 Introduction 54
3.2 Pressurized Sample Infusion 55
3.3 Employing PSI-ESI-MS to study metal catalyzed systems 63
3.4 ESI-MS-UV/Vis integration 65
Chapter 4 Mechanistic investigation of the Copper-free Sonogashira reaction 69
4.1 Introduction 69
4.2 Sonogashira mechanism investigation by PSI-ESI-MS 75
4.2.1 Proof of principle 75
4.2.2 Mechanism investigation by base alteration 83
4.2.3 Reaction with a charged terminal alkyne 95
4.2.4 Multisubstrates screening by PSI-ESI-MS 97
4.2.5 Kinetic isotope effect 102
4.2.6 Effect of phenylacetylene and product inhibition on reaction rate 108
4.2.7 Reaction on ESI(-)-MS with negative tagged substrate 113
4.3 Experimental 115
Chapter 5 A mechanism investigation of dehalogenation using palladium catalyst 119

5.1 Introduction 119
5.2 Reaction review 120
5.3 Kinetic isotope effect 124
5.4 Numerical modelling of the proposed mechanism 128
5.5 Enthalpy and entropy of activation 134
5.6 Experimental 134
Chapter 6 An unexpected pathway for ligand substitution in an aryl halide complex of palladium 136
6.1 Introduction 136
6.2 Mechanism investigation of the ligand substitution 137
6.3 Enthalpy and Entropy of activation 148
6.4 Conclusion 150
6.5 Experimental 151
Chapter 7 Conclusion 154
Bibliography 155
Appendix A Crystallographic details for [*p*-Ph(C_2)$C_6H_4CH_2PPh_3$]$^+$[PF_6]$^-$ 167
Appendix B Crystallographic details for [Pd(TMEDA)($C_6H_4CH_2PPh_3$)(I)]$^+$[PF_6]$^-$ (1) . 177

List of Schemes

Scheme 1.1: Proposed mechanism of the palladium-catalyzed 2-phenyl pyridine oxidative coupling reactions. Dependence of intermediates and products to the type of solvents were clearly observed. Redrawn from reference 38. 7

Scheme 1.2: Observed fragmentation pathways. Redrawn from reference 38. 7

Scheme 1.3: Proposed mechanistic cycle for palladium-catalyzed decarboxylative addition of benzoic acid based on observation of cationic palladium complexes by ESI-MS. Reprinted with permission from "Synthesis of Aryl Ketones by Palladium(II)-Catalyzed Decarboxylative Addition of Benzoic Acids to Nitriles" J. Lindh, P. J. R. Sjöberg and M. Larhed, *Angew. Chem. Int. Ed.*, **2010**, 49, 7733-7737.Copyright © 2010 WILEY-VCH Verlag GmbH & Co. KGaA, Weinheim. 8

Scheme 1.4: Rhodim-catalyzed [2+2+2] cycloaddition mechanism for of diynes and monoynes based on detected species by ESI-MS and CID characterization. Reprinted with permission from "Direct Detection of Key Intermediates in Rhodium(I)-Catalyzed [2+ 2+ 2] Cycloadditions of Alkynes by ESI-MS" M. Parera, A. Dachs, M. Solà, A. Pla-Quintana and A. Roglans, *Chem.--Eur. J.*, **2012**, 18, 13097-13107. Copyright © 2012 WILEY-VCH Verlag GmbH & Co. KGaA, Weinheim. 10

Scheme 1.5: Proposed pathway for the reaction of $[(\mathbf{1}-H)Cu(CH_3CN)]^+$ to the product. **1** and **2** refer to enaminone and pyrazole respectively. Reprinted with permission from "Electrospray Ionization Mass Spectrometry Reveals an Unexpected Coupling Product in the Copper-Promoted Synthesis of Pyrazoles" K. Jiang, G. Bian, Y. Chai, H. Yang, Q. Lai and Y. Pan, *Int. J. Mass Spectrom.*, **2012**, 321–322, 40-48. Copyright © 2012, Elsevier. 11

Scheme 1.6: Suggested catalytic cycle for copper-catalyzed cross coupling reaction of thiophenol and aryl halide based on detected species by ESI-MS. Redrawn from reference 42. 12

Scheme 1.7: Four mechanistic pathways of the ligand exchange reaction between cationic nickel complex (**CI-a**) and acetonitrile. Reprinted with permission from "Electrospray mass spectrometric studies of nickel(II)-thiosemicarbazones complexes: Intra-complex proton transfer in the gas phase ligand exchange reactions" K. Jiang, G. Bian, Y. Chai, H. Yang, Q. Lai and Y. Pan, *Int. J. Mass Spectrom.*, **2012**, 321–322, 40-48. Copyright © 2012, Elsevier. 13

Scheme 1.8: Generation of the of Pt-Cu complexes with analogues of PR_3 in solution and direct observation by ESI-MS. Redrawn from reference 56. 14

Scheme 1.9: Different dissociation pathways in bimetallic Pt-Cu complexes with analogues of phosphine ligands. Redrawn from reference 56. 15

Scheme 1.10: Proposed mechanistic cycle for Suzuki–Miyaura cross-coupling based on the observation of binuclear palladium complexes. Reprinted with permission from "Observation of Binuclear Palladium Clusters upon ESI-MS Monitoring of the Suzuki–Miyaura Cross-Coupling Catalyzed by a Dichloro-bis(aminophosphine) Complex of Palladium" D. Agrawal, D. Schröder and C. M. Frech, *Organometallics*, **2011**, 30, 3579-3587. Copyright © 2011 American Chemical Society. 17

Scheme 1.11: Formation and gas-phase reactivity of Pd-NHC complexes. Reductive elimination of phenyl group and NHC ligand (**3**) occurred through CID experiment. Reprinted with permission from "Gas-Phase Energetics of Reductive Elimination from a Palladium(II) N-Heterocyclic Carbene Complex" E. P. A. Couzijn, E. Zocher, A. Bach and P. Chen, *Chem--Eur. J.*, **2010**, 16, 5408-5415. Copyright © 2010 WILEY-VCH Verlag GmbH & Co. KGaA, Weinheim. 18

Scheme 1.12: Oxidation of $[RuL_3]^-$, ReL_3 and NiL_2 during electrospray ionization process. The observed cation in each case was regarded as metal-stabilized thiyl radical. Reprinted with permission from "Probing the Reactivity and Radical Nature of Oxidized Transition Metal-Thiolate Complexes by Mass Spectrometry" M. Lu, J. L. Campbell, R. Chauhan, C. A. Grapperhaus and H. Chen, *J. Am. Soc. Mass Spectrom.*, **2013**, 24, 502-512. Copyright © 2013, American Society for Mass Spectrometry. 20

Scheme 1.13: Reactivity of $[RuL_3]^+$ with alkenes, methyl ketones and dimethyl disulfide. Ions and reactivity shown here were observed in the gas phase. Reprinted with permission from "Probing the Reactivity and Radical Nature of Oxidized Transition Metal-Thiolate Complexes by Mass Spectrometry" M. Lu, J. L. Campbell, R. Chauhan, C. A. Grapperhaus and H. Chen, *J. Am. Soc. Mass Spectrom.*, **2013**, 24, 502-512. Copyright © 2013, American Society for Mass Spectrometry. 21

Scheme 1.14: Cationic Ru carbene complexes observed in solution of catalysts **2** in the presence of alkali metal chlorides. L :H_2IMes, Me: $[Li]^+$, $[Na]^+$, $[K]^+$, $[Cs]^+$. Modified from reference 74. 22

Scheme 1.15: A proposed mechanism of rhodium-catalyzed hydroformylation by ESI(+)-MS analysis. Modified from reference 86. 25

Scheme 1.16: Observation of charge-tagged complexes generated in reaction of charged-tagged acetylene imidazolium salt with neutral $M(OAc)_2$ complexes (M = Cu, Ni, Pd). Modified from reference 1. 26

Scheme 1.17: Formation of **3a** $[RP{=}W(CO)_5]$ in CID experiment on 3H-benzophosphepines which was proceed through loss of naphthalene. Redrawn from reference 52. 26

Scheme 1.18: Synthesis of **1** from a proton sponge (1,8-bis(dimethylamino)naphthalene. a) *N*-bromosuccinimide, THF and −78 ^{o}C. b) $Pd(OAc)_2$, PPh_3, $NaCO_3H$ and mixture of *n*-propanol with water. Reflux 12 h. Redrawn from reference 97. 28

Scheme 1.19: Direct observation of numbered species by ESI(+)-MS and NMR results led to proposal a reaction mechanism for dehydrocoupling of silane catalyzed by Wilkinson's catalyst. Modified from reference 95. 33

Scheme 1.20: Pathway of charged substrate for intramolecular Pauson-Khand reaction and observed intermediate by ESI(+)-MS. Reprinted with permission from "The Pauson-Khand Reaction: A Gas-Phase and Solution-Phase Examination Using Electrospray Ionization Mass Spectrometry" M. A. Henderson, J. Luo, A. Oliver and J. S. McIndoe, *Organometallics*, **2011**, 30, 5471-5479. Copyright © 2011 American Chemical Society. 34

Scheme 2.1: Mechanism of carbonium ion formation and its collision to another methane molecule leading to proton transfer in chemical ionization process. 38

Scheme 2.2: A Sonogashira reaction and hydrodehalogenation (as the side-reaction) mechanism. A step was included as the "loss" which represents the decomposition of PdP_2ArI. 47

Scheme 2.3: Timescales of the oxidative addition and subsequent isomerisation. Redrawn from reference 140. 52

Scheme 3.1: Proposed TFA-deprotection mechanism of Fmoc-Arg(Pbf)-OH adapted from reference 144. 59

Scheme 3.2: Copper-free Sonogashira reaction between $[4\text{-I-}C_6H_4CH_2PPh_3]^+$ $[PF_6]^-$ and phenylacetylene using tetrakistriphenylphosphine as the catalyst and triethylamine as the base. 64

Scheme 4.1: Two proposed mechanisms for the palladium-catalyzed copper-free Sonogashira between a terminal alkyne and an aryl halide. Reprinted with permission from "Two Competing Mechanisms for the Copper-Free Sonogashira Cross-Coupling Reaction" T. Ljungdahl, T. Bennur, A. Dallas, H. Emtenäs and J. Mårtensson, *Organometallics*, **2008**, 27, 2490-2498. Copyright © 2008, American Chemical Society. 71

Scheme 4.2: Carbopalladation of terminal alkyne with PdL_2ArX. 71

Scheme 4.3: Proposed (a) anionic pathway and (b) cationic pathway for deprotonation of para-substituent terminal alkyne. Pathway (a) is operative for EWG substituents while pathway (b) is operative for EDG substituents. Reprinted with permission from "Two Competing Mechanisms for the Copper-Free Sonogashira Cross-Coupling Reaction" T. Ljungdahl, T. Bennur, A. Dallas, H. Emtenäs and J. Mårtensson, *Organometallics*, **2008**, 27, 2490-2498. Copyright © 2008, American Chemical Society. 73

Scheme 4.4: A proposed catalytic cycle based on direct observation of intermediates on ESI(-)-MS for the copper-free Sonogashira using piperidine as the base. (**1**) is the charge tagged ligand triphenylphosphinemonosulfonate. Modified from reference 164. 74

Scheme 4.5: Synthesis pattern of $[4\text{-I-}C_6H_4CH_2PPh_3]^+$ $[PF_6]^-$ 75

Scheme 4.6: Copper-free Sonogashira reaction with a charged aryl iodide as an ESI(+)-handle. 76

Scheme 4.7: Mechanism of palladium-catalyzed cross-coupling reactions by Jutand et al. Reprinted with permission from "Anionic Pd(0) and Pd(II) Intermediates in Palladium-Catalyzed Heck and Cross-Coupling Reactions" C. Amatore and A. Jutand, *Acc. Chem. Res.*, **2000**, 33, 314-321. Copyright © 2008, American Chemical Society. 85

Scheme 4.8: Proposed mechanism for Sonogashira reaction based on direct observation of key intermediates as well as reaction modifications. Gray intermediate was not observed, but its existence was inferred. 86

Scheme 4.9: Catalytic cycle and rate constants (red) used to simulate the reaction progress. Concentrations used were the same as employed experimentally. In this model product inhibition was hypothesized in the cycle, however further study on this part will be explained in section (4.2.6). 91

Scheme 4.10: Reaction of charged tag alkyne $[p\text{-}HCCC_6H_4CH_2PPh_3]^+$ with 1-iodo-4-methylbenzene. 96

Scheme 4.11: Multisubstrates screening of the charged alkyne with six *para*- substituted aryl iodides. 99

Scheme 4.12: Multisubstrate screening of six *para*-substituted phenylacetylenes with charge-tagged aryl iodide monitored by ESI(+)-MS. 106

Scheme 4.13: Reaction of neutral substrates: 1-iodo-4-methylbenzene with phenylacetylene at different conditions. 114

Scheme 4.14: Reaction scheme of negatively charged aryl iodide with phenylacetylene in "standard condition" on ESI(-)-MS. 114

Scheme 5.1: A possible mechanism of dehalogenation of aryl halides. Redrawn from reference 178. 119

Scheme 5.2: H/D exchange and formation of a mixture of products. 125

Scheme 5.3: Catalytic cycle and rate constants used to simulate the reaction progress. Concentrations used were the same as employed experimentally. 127

Scheme 5.4: Numerical model of hydrodehalogenation (applied for the reactions in MeOH, CH_3OD, CD_3OD and iodide addition). 129

Scheme 5.5: Numerical model of hydrodehalogenation including $[Ag]^+$ reaction with $[I]^-$. 132

Scheme 6.1: Possible reaction pathways for the substitution of TMEDA for 2 × PPh_3. PSI-ESI-MS reveals the reaction to proceed via **1** → **2** → **3a** → **4**. Of these four complexes, only **3a** is not directly observed, but its involvement can be inferred by the effect of $[I]^-$ vs. PPh_3 on the reaction **2** → **4**..... 145

List of Figures

Figure 1.1: Manganese-containing complexes observed by ESI(+)-MS. 3

Figure 1.2: Vanadium-containing complexes detected by ESI-MS..... 4

Figure 1.3: Mono and Bi-nuclear palladium complexes detected by ESI(+)-MS and suggested as catalytic intermediates in the enantioselective Manich-type.Redrawn from reference 34..... 5

Figure 1.4: Two binuclear palladium-bridged allylic complexes observed by ESI(+)-MS. They are proposed to act as sources for the active catalyst in a palladium-catalyzed allylic substitution reaction. Redrawn from reference 9. 5

Figure 1.5: Initial rate dependence to concentration of palladium precatalyst in the Wacker oxidation of alkene. Modified from reference 36..... 6

Figure 1.6: ESI-MS spectrum for the reaction mixture of 2,6 dimethoxybenzoic acid as the substrate and acetonitrile as the reactant/solvent with using $Pd(O_2CCF_3)_2$. Reprinted with permission from "Synthesis of Aryl Ketones by Palladium(II)-Catalyzed Decarboxylative Addition of Benzoic Acids to Nitriles1" J. Lindh, P. J. R. Sjöberg and M. Larhed, *Angew. Chem. Int. Ed.*, **2010**, 49, 7733-7737.Copyright © 2010 WILEY-VCH Verlag GmbH & Co. KGaA, Weinheim. 8

Figure 1.7: Relative intensities of the main components as monitored via ESI-MS in the positive ion mode. The sum of ions containing the reactant, the product, and the potential intermediate (imidazolid-3-one) are shown. Reprinted with permission from "Electrospray Ionization Mass Spectrometry Reveals an Unexpected Coupling Product in the Copper-Promoted Synthesis of Pyrazoles" K. Jiang, G. Bian, Y. Chai, H. Yang, Q. Lai and Y. Pan, *Int. J. Mass Spectrom.* **2012**, 321–322, 40-48. Copyright © 2012, Elsevier. 11

Figure 1.8: Ionization pathways: a) protonation of a basic site b) association of a alkali metal to a basic site c) halide dissociation d) oxidation e) deprotonation of an acidic site. 16

Figure 1.9: (A and B) Oxidative addition intermediates $[(pyrH)Pd(PPh_3)_2Br]^+$ and $[(pyr)Pd(PPh_3)_2]^+$, Transmetallation intermediates with (C) and without (D) pyr group in $[(pyrH)(R^1R^2C_6H_3)Pd(PPh_3)_2]^+$. Redrawn from reference 75. 23

Figure 1.10: (A and B) Two charge-tagged analogues of first generation ruthenium catalysts, and (C) the related 14-electron active species detected by ESI(+)-MS. Redrawn from reference 83. 24

Figure 1.11: Top: (A and B) Reactivity of **3a** $[RP=W(CO)_5]$ with propane and 1,4-dioxene respectively . Insets show the overly of the experimental isotope patterns of adducts **6a** and **7a** and calculated (red bars) isotope patterns. Bottom: (C and D) show

CID experiments of **6a** and **7a** respectively. The marked signals (*) show fragmentation product formed by loss of CO. Reprinted with permission from "Reactive Intermediates: A Transient Electrophilic Phosphinidene Caught in the Act" H. Jansen, M. C. Samuels, E. P. A. Couzijn, J. C. Slootweg, A. W. Ehlers, P. Chen and K. Lammertsma, *Chem. -- Eur. J*, **2010**, 16, 1454-1458. Copyright © 2010 WILEY-VCH Verlag GmbH & Co. KGaA, Weinheim. 27

Figure 1.12: ESI(+)-MS of **2** chromium(**1**) tricarbonyl complex in methanol ($[M + H]^+$ = *m/z* 457). A small amount of free ligand **1** is also observed ($[M + H]^+$ = *m/z* 321). Reprinted with permission from "1,8-Bis(dimethylamino)-2-(4-methoxyphenyl)naphthalene: An electrospray-active analogue for η^6-coordinating ligands" K. L. Vikse, S. Kwok, R. McDonald, A. G. Oliver and J. S. McIndoe, *J. Organomet. Chem.*, **2012**, 716, 252-257. Copyright © 2012, Elsevier. 29

Figure 1.13: ESI(+)-MS (top) and MS/MS (bottom) of [Ru(η^6-p-cymene)Cl(**3a**)]+. Loss of *p*-cymene instead of loss of **3a** is strong evidence that **3a** is strongly bound and thus not monodentate. Modified from reference 98. 30

Figure 1.14: Time dependence of the normalized signal intensities of $[ArI]^+$ and $[ArBn]^+$, (red) formed in the Pd-catalyzed reaction with BnZnBr in CH_3CN at room temperature. Results of two experiments with different catalyst loadings are shown ([cat] =100 mol %, 4.5 mol%).The solid lines represent simulated time profiles based on a second-order rate constant. Reprinted with permission from "Charged Tags as Probes for Analyzing Organometallic Intermediates and Monitoring Cross-Coupling Reactions by Electrospray-Ionization Mass Spectrometry" M. A. Schade, J. E. Fleckenstein, P. Knochel and K. Koszinowski, *J. Org. Chem.*, **2010**, 75, 6848-6857. Copyright © 2010 American Chemical Society. 31

Figure 1.15: Reaction profile of the six Rh-containing species observed over time by ESI-MS. Each trace is generated by normalizing of each species to the total ion current. Inset: $\ln[RhHP_3]$ vs. time for the consumption of this species, representing first-order kinetic. Modified from reference 95. 32

Figure 1.16: Relative intensity starting material, intermediate, and product. System was pressurized with CO gas and sample infused with online dilution with acetone to the source of ESI-MS. Reprinted with permission from "The Pauson-Khand Reaction: A Gas-Phase and Solution-Phase Examination Using Electrospray Ionization Mass Spectrometry" M. A. Henderson, J. Luo, A. Oliver and J. S. McIndoe, *Organometallics*, **2011**, 30, 5471-5479. Copyright © 2011 American Chemical Society. 35

Figure 2.1: The process of electrospray ionization. Modified with permission of the author from Henderson, W., McIndoe J. S., *Mass Spectrometry of Inorganic and Organometallic Compounds*. John Wiley & Sons, Ltd. West Sussex: 2005, p. 92. 40

Figure 2.2: Schematic of the source of ESI-MS. **A**. ESI capillary, **B**. inlet for cone gas, **C**. sampling cone; **D**. extraction cone, **E.** baffle.; **F.** power supply. Modified from reference 123. 41

Figure 2.3: Block diagram of the Q-Tof mass spectrometer. **A**. ESI source; **B**. cone; **C**. hexapole ion guide; **D**. quadrupole mass analyser; **E**. hexapole collision cell; **F**. pusher; **G**. reflectron; **H**. MCP detector. Bottom left shows the quadrupole mass analyzer showing the trajectory of two ions with different mass-to-charge ratios. Bottom right shows a cartoon of MCP. 42

Figure 2.4: The left-hand contour plot of $[H_3Ru_4(CO)_{12}]^-$ clearly shows the loss of all CO ligands as the cone voltage is increased. Right snapshots show the ligand dissociation at three different voltages. Reprinted with permission from "Gas-phase reactivity of ruthenium carbonyl cluster anions" M. Henderson, S. Kwok and J. McIndoe, *J. Am. Soc. Mass Spectrom.*, **2009**, 20, 658-666. Copyright © 2009, American Society for Mass Spectrometry. 45

Figure 2.5: Equilibrium rate constant determination for two initiated styrene polymerization by graphical overlay of the simulated plot over the experimental one. Reprinted with permission from "A New Sterically Highly Hindered 7-Membered Cyclic Nitroxide for the Controlled Living Radical Polymerization" C.-C. Chang, K. O. Siegenthaler and A. Studer, *Helv.Chim. Acta*, **2006**, 89, 2200-2210.Copyright © 2006 Verlag Helvetica Chimica Acta AG, Zürich, Switzerland. 46

Figure 2.6: Simulated models for Sonogashira reaction constructed by: (left): Maple (right) Powersim.The same responses in both ensure the data validity obtained by Powersim software. 47

Figure 2.7: Constructed model for a generic reaction of A + B $\rightleftharpoons$ C + D by Powersim program. 49

Figure 2.8: Real time monitoring of UV-Vis spectral bands (432 and 491 nm) and the related XANES data. 10 equivalents of PhI reacted with 40 mM $[(PPh_3)_2Pd(dba)]$ in toluene. Modified from reference 140. 53

Figure 3.1: (left) MS spectrum of a fluorobenzene solution of MAO and terabutylammonium chloride under normal source conditions. (right) MS spectrum of a fluorobenzene solution of MAO and terabutylammonium chloride after purging the source with N_2 for 20 minutes. 55

Figure 3.2: The relationship between the pressure applied to the system and the measured flow rate for a various common solvents when a 60 cm length of PEEK tubing is used. Vertical error bars shows the small range of errors. 57

Figure 3.3: Experimental flow rates plotted against theoretical flow rates. Data points include all the data including five different solvents, four different tube lengths and five different pressures. The solid line indicates a 1:1 correspondence while the dashed lines show the expected variation if the inner diameter was 25% less (1:0.32) or 25% more (1:2.44) than the reported value. 58

Figure 3.4: ESI(+)-MS spectra of reaction mixture (a) at t = 0, starting material at m/z 649 (b) t = 10minutes, appearance of both products at *m/z* 191 and 397 are evident..... 60

Figure 3.5: Raw intensity of the protected amino acid (*m/z* 649) and the hydrolyzed products (*m/z* 397 and 191) against time. ESI-MS spectra were collected for 3 s to generate each set of data. 62

Figure 3.6: Normalized intensity for the protected amino acid (*m/z* 649) and the hydrolyzed products (*m/z* 397 and 191) against time. The inset shows the abundance of the $[C_{13}H_{17}O_3S]^+$ intermediate on different scale since its abundance is very low..... 62

Figure 3.7: (left) Conventional Schlenk flask (right) Modified PSI-flask for running the reaction at elevated temperatures. 64

Figure 3.8: Pressurized sample infusion (PSI) with dilution system. A T-mixer is used to dilute the reaction mixture with desired solvent. 65

Figure 3.9: A sample of flow through cell and a transmission dip probe. 66

Figure 3.10: Set-up of the integrated UV/Vis with ESI-MS. Sample is introduced to the UV/Vis detector first and to the ESI-MS source via another piece of tubing..... 67

Figure 3.11: Injection of 0.2 mM of caffeine (first) without formic acid (second) with addition of 2% formic acid to protonate caffeine and hence increasing ion current in ESI-MS. Blue line corresponds to protonated caffeine and red line corresponds to PDA (photodiode array: a snapshot of the entire spectrum in less than one second). Delay time is less than 30 s when flow rate is 50 µL min^{-1}..... 68

Figure 4.1:X-ray crystal structure of $Ph(C_2)C_6H_4CH_2PPh_3]^+$, including the $[PF_6]^-$ counterion. 76

Figure 4.2: Relative intensity of starting material $[4\text{-}I\text{-}C_6H_4CH_2PPh_3]^+$ (green) and product $[Ph(C_2)C_6H_4CH_2PPh_3]^+$ (blue) as a function of mixture composition showing the linear relationship between intensity and concentration. 77

Figure 4.3: Appearance of $[PPh_3CH_2ArC_2Ar]^+$ $[PF_6]^-$ as tracked by UV/Vis, ESI-MS and ^1H NMR. 78

Figure 4.4: ^1H NMR spectrum collected during the parallel UV-Vis/NMR/MS experiment, with substrate and product peaks of interest labeled. 78

Figure 4.5: UV/Vis spectra collected during the parallel UV-Vis/NMR/MS experiment with product peaks of interest increasing at 307 nm..... 79

Figure 4.6: A single spectrum of the reaction. Pd-containing intermediates are lost in the baseline and require 100x magnifications to become appreciably intense with respect to reactant and product. 80

Figure 4.7: ESI(+)-MS/MS of $PdP_2(Ar)(I)$ (*m/z* 1109.4). Fragmentation occurs via loss of triphenylphosphine not loss of ArI indicating that elimination of ArI is not facile..... 81

Figure 4.8: ESI(+)-MS/MS of $PdP_2(Ar)(C_2Ph)$ (*m/z* 1083.4). ArC_2Ph is the most abundant fragment which denotes that reductive elimination of the product is favourable. Loss of one and two triphenylphoshpine is observed. No attempt was made to assign all the peaks..... 82

Figure 4.9: Sonogashira reaction with the same condition and same stock catalyst solution. Reactions were performed on two different days. 83

Figure 4.10: ESI(+)-MS intensities over time of all key species bearing the charged tag $[C_6H_4CH_2PPh_3]^+$ (Ar = $[C_6H_4CH_2PPh_3]^+$; P = PPh_3). The intensities of the palladium-containing intermediates have been multiplied by 100..... 84

Figure 4.11: ESI(+)-MS over time for the intensity of all key species bearing the charged tag aryl iodide for the reaction with one equivalent $[Et_3NH]^+[I]^-$ as the source of protons. 87

Figure 4.12: ESI(+)-MS over time for the intensity of all key species bearing the charged tag aryl iodide where DBU was used in place of NEt_3. 88

Figure 4.13: ESI(+)-MS over time for the intensity of charged tag product when using different bases and added acid (all other experimental conditions kept constant). 89

Figure 4.14: Reaction progress: experimental (left) and numerically modelled using Maple (right), under standard conditions. 90

Figure 4.15: Reaction progress: experimental (left) and numerically modelled using Maple (right), under the same conditions in Figure 4.14 except for the addition of one equivalent of $[NEt_3H]^+[I]^-$ at the start of the reaction. 90

Figure 4.16: Reaction progress: experimental (left) and numerically modelled using Maple (right), under the same conditions in Figure 4.14 except NEt_3 has been substituted by DBU, and this effect was approximated by decreasing the rate constant of the reverse reaction of **3** from 100 to 10. 91

Figure 4.17: ESI(+)-MS/MS of $PdP_2(Ar)(DBU)$ (doubly charged, *m/z* 567.1). The most abundant fragment is obtained by the loss of one triphenylphoshpine (doubly charged, *m/z* 436.2). Also the loss of DBU is observed (doubly charged, *m/z* 491.5). 93

Figure 4.18: ESI(+)-MS/MS of $PdP(Ar)(DBU)_2$ (doubly charged, *m/z* 512.3). The most abundant fragment is obtained by the loss of one DBU (doubly charged, *m/z* 436.2). Also the loss of the second DBU (doubly charged, *m/z* 360.1)..... 93

Figure 4.19: Addition of ten equivalents of DBU to the mixture of charged ArI and catalyst in standard condition at reflux. 94

Figure 4.20: ESI(+)-MS over time for the intensity of all key species bearing the charged tag. The intensities of the product and $PdP_2(Ar)(I)$ have been multiplied by 50..... 95

Figure 4.21: ESI(+)-MS over time for the intensity of all key species bearing the charged tag [p- $HCCC_6H_4CH_2PPh_3]^+$ (Ar' = $[C_6H_4CH_2PPh_3]^+$; P = PPh_3) (Ar = 1-iodo-4-methylbenzene). The intensities of the palladium-containing intermediates have been multiplied by 10. 97

Figure 4.22: Conversion versus time curves and determination of the initial rates of the product-forming reaction. "R" symbols indicate the *para*-substituent on the aryl bromide. R^2 is the correlation coefficient of the linear fit. Reprinted with permission from "Insights into Sonogashira Cross-Coupling by High-Throughput Kinetics and Descriptor Modeling" M. R. an der Heiden, H. Plenio, S. Immel, E. Burello, G. Rothenberg and H. C. J. Hoefsloot, *Chem. --Eu. J.*, **2008**, 14, 2857-2866. Copyright © 2008 WILEY-VCH Verlag GmbH & Co. KGaA, Weinheim. 98

Figure 4.23: Relative intensity versus time for determination of the initial rates of the product-forming reaction. Colored (-) symbols denote the *para*-substituent on the aryl iodide and HC_2Ar' refers to charged tag alkyne as the reactant. 100

Figure 4.24: Clear formation of products with different rates. Colored (-) symbols denote the *para*-substituent on the aryl iodide and HC_2Ar' refers to charged acetylene as the reactant. Inset: Zoom on first few minutes of product formation. The best linear fit is selected for the reaction rate calculation of each product. Concentration of HC_2Ar' is 0.6 mM versus equal amount of 0.1 mM for each *para*-substituted aryl iodide..... 100

Figure 4.25: Plot of $\log_{10}(P/R)$ vs. Hammett σ_p parameter for a various of para-substituted aryl iodides. R = reaction rate for variable substituent, R_0 = reaction rate for reference substituent H. 101

Figure 4.26: Hammett plot for Sonogashira reaction of several para-substituted aryl bromides. Conditions: HN^iPr_2, 80 ^oC, Na_2PdCl_4, $^tBu_3P$, CuI. Reprinted with permission from "Insights into Sonogashira Cross-Coupling by High-Throughput Kinetics and Descriptor Modeling" M. R. an der Heiden, H. Plenio, S. Immel, E. Burello, G. Rothenberg and H. C. J. Hoefsloot, *Chem. --Eu. J.*, **2008**, 14, 2857-2866. Copyright © 2008 WILEY-VCH Verlag GmbH & Co. KGaA, Weinheim. 101

Figure 4.27: ESI(+)-MS over time for the intensity of all key species bearing the charged tag for the normal reaction in MeOH in the presence of DBU. The intensities of the PdP_nArX (X = $[I]^-$ or DBU) and $PdP_2(Ar)(C_2Ph)$ have been multiplied by 50. 104

Figure 4.28: ESI(+)-MS over time for the intensity of all key species bearing the charged tag for the normal reaction in CH_3OD in the presence of DBU. The intensities of the PdP_nArX (X = $[I]^-$ or DBU) and $PdP_2(Ar)(C_2Ph)$ have been multiplied by 50. 105

Figure 4.29: ESI(+)-MS over time for the intensity of all key species bearing the charged tag for the normal reaction in CD_3OD in the presence of DBU. The intensities of the PdP_nArX (X = $[I]^-$ or DBU) and $PdP_2(Ar)(C_2Ph)$ have been multiplied by 50. 105

Figure 4.30: Overlay of product built-up in CH_3OH (blue), CH_3OD (green) and CD_3OD (red). Error bars are generated from triplicates (green) and quadruplicates (blue) quintuplicates (red). 106

Figure 4.31 One by one comparison of conversion rate of each *para*-substituted acetylene with charged aryl iodide in MeOH (red) and CD_3OD (blue). Left figures show the EWG-substituted products whereas right figures show EDG-substituted products..... 108

Figure 4.32: ESI(+)-MS of reaction with "standard conditions" and three equivalents of phenylacetylene..... 109

Figure 4.33: ESI(+)-MS of reaction with "standard conditions" and six equivalents of phenylacetylene..... 110

Figure 4.34: ESI(+)-MS of reaction with "standard conditions" and three equivalents of biphenylacetylene. 111

Figure 4.35: ESI-MS intensity data over time for the appearance of products when using excess of phenylacetylene (pink): three equivalents, (green): six equivalents, (red) three equivalents biphenylacetylene and (blue): standard condition (average of five runs).... 112

Figure 4.36: Rate of formation of product (left) and byproduct (right) using three different amounts of catalyst..... 113

Figure 4.37: Release of the iodide and $[I_2(Et_3NH)]^-$ clearly indicates the reaction progress on ESI-(-)MS. 114

Figure 4.38: Three key intermediates observed on negative mode: (left) the first two are OA species and (right) is the TM intermediate..... 115

Figure 5.1: Normalized relative abundance of all charged tag containing species in MeOH. 121

Figure 5.2: *Pseudo* first-order kinetics of dehalogenation of aryl iodide in methanol. .. 121

Figure 5.3: MS/MS on $PdP_2(Ar)(H)$ (*m/z* at 983). Average of 17 spectra at voltages lower than 10V..... 122

Figure 5.4: MS/MS on $PdP_2(Ar)(H)$ (*m/z* at 983). Average of 30 spectra at voltages between 15 - 20..... 123

Figure 5.5: MS/MS on $PdP_2(Ar)_2$ (*m/z* at 668). Average of 16 spectra at voltages lower than 10 V..... 123

Figure 5.6: MS/MS on $PdP_2(Ar)_2$ (*m/z* at 668). Average of 12 spectra at voltages between 15 - 20V. 124

Figure 5.7: Overlay of product built-up in CH_3OH (blue), CH_3OD (red) and CD_3OD (green). Error bars are generated from triplicates (red and blue). Green is generated from duplicates. 125

Figure 5.8: Isotope patterns of $[PdP_2PhI+K]^+$ and $[PdP_2Ph]^+$. Average of about 500 spectra over the course of reaction..... 126

Figure 5.9: A comparison of the "normal" reaction (green) and after addition of one equivalent of $AgNO_3$ (blue) or $[I]^-$ (red). Blue and red are generated from duplicates.. 128

Figure 5.10: Experimental (left) and numerically modelled dehalogenation (right). Intermediate intensity has been multiplied by 20 to get them on the same scale. 130

Figure 5.11: Reaction progress in CH_3OD: experimental (left) and numerically modeled using Powersim (right), under standard conditions. 131

Figure 5.12: Reaction progress in CD_3OD: experimental (left) and numerically modeled using Powersim (right), under standard conditions. 131

Figure 5.13: Reaction progress in CH_3OH with addition of 1 equivalent $[I]^-$: experimental (left) and numerically modeled using Powersim (right), under standard conditions..... 132

Figure 5.14: Reaction progress in CH_3OH with addition of 1 equivalent $[Ag]^+$: experimental (left) and numerically modeled using Powersim (right), under standard conditions..... 133

Figure 5.15: Eyring plot of hydrodehalogenation in MeOH..... 134

Figure 6.1***:*** Reaction progress in methanol at 55 °C, as measured by positive-ion (traces for blue **1**, red **2** and green **4**) and negative-ion mode (orange $[I]^-$, from a duplicate experiment) PSI-ESI-MS. 138

Figure 6.2: *Pseudo*-first order kinetics for the first couple of minutes after addition of PPh_3 gives $k = 0.9 \pm 0.1\ s^{-1}$. These data are duplicated in Figure 6.1. 139

Figure 6.3: *Pseudo*-first order kinetics for the first couple of minutes after addition of PPh_3 gives $k = 0.8 \pm 0.1\ s^{-1}$. These data are duplicated in Figure 6.1. 139

Figure 6.4**:** Appearance and disappearance of charged $[Pd(TMEDA)(Ph)(PPh_3)]^+$ in conversion of neutral Pd(TMEDA)PhI to $Pd(PPh_3)_2(Ph)I$ observed by positive ion PSI-ESI-MS at 327 (black) and 338 K (red). 140

Figure 6.5: ^1H NMR monitoring experiment. The bottom spectrum shows two siglets of Me groups of TMEDA in Pd(TMEDA)PhI before addition of PP_3. Second spectrum from the bottom shows the formation of $Pd(TMEDA)PhPPh_3$ at 25 minute. Downfield shift in chemical shift of methyl groups is observed due to replacement of PPh_3 with TMEDA in Pd complex. Appearance of free TMEDA is evident at δ 2.26. Spectra were collected every five minutes but only a few of them are show in this figure. 141

Figure 6.6: Reaction progress in CD_3OD at 22°C, as measured by ^1H NMR using the methyl groups of the TMEDA ligand. 142

Figure 6.7: X-ray crystal structure of **1**, including the $[PF_6]^-$ counterion and $CDCl_3$ of crystallization. Selected bond lengths (Å): Pd1-I1 2.5807(2); Pd1-N1 2.2009(15); Pd1-N2 2.1411(17); Pd1-C7 1.9842(17). Selected bond angles (°): C7-Pd1-N2 92.62(7); C7-Pd1-11 87.54(5); N2-Pd1-N1 83.72(6); N1-Pd1-I1 96.12(5)..... 143

Figure 6.8: Reaction progress in methanol at 55°C, as measured by positive-ion PSI-ESI-MS. The reaction has been greatly lowered in rate by reducing the concentration of both reactants. Inset: fit of 1/[**1**] vs time confirming a good match to second-order kinetics. 144

Figure 6.9: Rate of formation of **4** from **1** under different experimental conditions. Additional PPh_3 does not affect the rate, but additional $[I]^-$ does. 146

Figure 6.10: A single spectrum of the reaction after 16 minutes of addition NaCl into reaction..... 147

Figure 6.11: A single spectrum of the reaction after 18 minutes of addition KBr into reaction..... 147

Figure 6.12: A single spectrum of the reaction at 30 minutes after addition of $AgNO_3$ followed by addition of 10eq KBr. The amount of $Pd(PPh_3)_2(Ar)(I)$ is less than 3% (based on the intensity) compared to the bromide analogue. 148

Figure 6.13: Eyring plot for the reaction of **1** to **2** at same conditions but different temperatures..... 149

Figure 6.14: Eyring plot for the reaction of **1** to **4** at the same conditions but different temperatures..... 150

Figure 6.15: Positive ion ESI-MS of **1** along with its experimental and calculated isotope pattern. 152

List of Abbreviations

acac	acetylacetone
$[M]^-$	negative molecular ion peak
$[M]^+$	positive molecular ion peak
Ar	aryl
b.p	boiling point
Bn	benzyl
bpy	2,2'-bipyridyl
cat	catalyst
CI	chemical ionization
CID	collision induced dissociation
COD	cyclooctadiene
Col V	collision voltage
cP	centipoise
Cp	cyclopentadienyl ligand
Cp*	pentamethylcyclopentadienyl ligand
CV	cone voltage
Cy	cyclohexyl
Da	Dalton
dba	dibenzylideneacetone
DBSQ	3,5-di-tert-butylsemiquinone
DBU	1,8-diazabicyclo[5.4.0]undec-7-ene
DC	direct current
DFT	density functional theory
dmpe	1,2-bis(dimethylphosphino)ethane
ED	energy dispersive
EDESI	energy-dependent electrospray ionization
EDG	electron donating group
EI	electron impact
EPR	electron paramagnetic resonance
ESI	electrospray ionization
ESI(-)-MS	negative-ion electrospray ionization mass spectrometry
ESI(+)-MS	positive-ion electrospray ionization mass spectrometry
EWG	electron withdrawing group
EXAFS	extended X-Ray Absorption Fine Structure
FT-ICR	Fourier transform ion cyclotron resonance
GC	gas chromatography
GPC	gel permeation chromatography
HPLC	high performance liquid chromatography
ID	inner diameter
*i*Pr	isopropyl
IR	infrared
IS	internal standard

KE	kinetic energy
KIE	kinetic isotope effect
L	ligand
m	*meta*
m.p.	melting point
m/z	mass-to-charge ratio
MALDI	matrix-assisted laser desorption ionization
MAO	methylaluminoxane
MCP	microchannel plate
Me	methyl
MeTACN	1,4,7-trimethyl-1,4,7-triazacyclononane
MS	mass spectrometry/ mass spectrometer/ mass spectrum
MS/MS	tandem mass spectrometry
NEt_3	triethylamine
NHC	*N*-heterocyclic carbene
NMR	nuclear magnetic resonance
OA	oxidative addition
OAc	acetate
OTf	trifluoromethanesulfonate
p	*para*
Pbf	2,2,4,6,7-pentamethyldihydrobenzofuran-5-sulfonyl
PDA	photodiode array
PEEK	polyetheretherketone
$[PF_6]^-$	hexafluorophosphate
Ph	phenyl
Pmf	2,2,5,7,8-pentamethylchroman-6-sulfonyl
ppm	parts per million
PPN	bis(triphenylphosphoranylidene)ammonium
PSI	pressurized sample infusion
psi	pound per square inch
Pyr	pyridine
Q-TOF	quadrupole-time-of-flight
RE	reductive elimination
RF	radio frequency
Rp	rate of polymerization
RSD	relative standard deviation
*t*Bu	tertiary butyl
TFA	trifluoroacetic acid
THF	tetrahydrofuran
TIC	total ion current
TM	transmetallation
TMEDA	tetramethyl ethylene diamine
TOF	time-of-flight
TPPMS	triphenylphosphine monosulfonate
UV	ultraviolet

UV/Vis	ultraviolet/visible
XAFS	X-ray absorption fine structure
XANES	X-ray absorption near edge structure
XAS	X-ray absorption spectroscopy
XRD	X-ray diffraction

Acknowledgments

Completion of this thesis would not have been possible without continuous support of my advisor- Professor Scott McIndoe, our research group, friends and family to only some of whom it is possible to express particular appreciation here.

First, my sincere thanks go to Dr. Scott McIndoe for his encouragement and enthusiasm and providing insightful technical directions over the course of the past four years. He taught me how to convert a challenge to an opportunity when all doors seem to be closed and hopes gone. Professor McIndoe's advice, support and friendship have been invaluable on both an academic and a personal level for which, I am extremely grateful.

I would like to acknowledge the UVIC chemistry faculty and staff for their scientific and technical support. I thank Jane Browning for being such a wonderful TA supervisor. I never doubted to knock on her door to get assistance and she always treated me patiently with a smile on her face. I am also most grateful to Dr. Ori Granot, who helped me enormously in dealing with the MS instrument issues, Dr. Allen Oliver for providing the X-ray crystallography and Christopher Barr for NMR services.

I was fortunate to work with incredible colleagues in our research team. Especial thanks to Krista Vikse, who mentored me in early stages of my work and Jingwei Luo, who nicely shared his lab work experience with me. Also Danielle, Ali, Jenny, Cara, Lars, Rhonda, Eric, Peter and Jessamyn deserve huge credit for making the lab a desirable working place for me.

I am blessed to have two great families, whose prayers and support have always been with me. My father used to call me a "Doctor" from early days encouraging me to pursue my doctoral degree and my mother encouraged me to work hard to achieve my goals.

Last and foremost, I am so thankful to my lovely wife, Fatemeh, who is responsible for all my achievements, since we got married. What she told me when I was experiencing so much stress at early days of my Ph.D. program is always echoing in my soul: "Don't worry, I am with you!" She did indeed. She was with me in all rainy days and I never forget the sacrifices she made for our life.

Dedication

To Fatemeh, Mom and Dad

Chapter 1 Literature review

1.1 Applying ESI-MS to organometallic catalysis

Electrospray ionization mass spectrometry (ESI-MS) is becoming a popular tool in the study of organometallic catalytic reactions. Since only charged species (ions) are detectable in ESI-MS, most common solvents are invisible, which significantly simplifies the spectra. The softness of ionization (ESI-MS transfers ions from the solution phase to the gas phase via evaporation of solvent) means no fragmentation. High sensitivity and fast response (spectrum per second) enables this technique to detect active species especially catalytic intermediates at very low concentration in "real" catalytic condition. "Ion fishing" [1] of catalytic reactions by ESI-MS is becoming a mature technique in the field of organometallic chemistry which refers to detection of the intermediates in the reaction mixture.

An increasing number of reports exist in which investigators have taken advantage of these aspects of ESI-MS to study organometallic reactions. In 1991 Berman used ESI-MS to detect a number of environmentally important organoarsenic ions for the first time.[2] In another noteworthy early example Canty in 1993 used positive ESI-MS and MS/MS techniques for analyzing many palladium and platinum complexes.[3] Identification of short lived intermediates and other low concentration species has been the focal point in application of ESI-MS in this field in past two decades. Among all catalytic systems, palladium-catalyzed carbon-carbon bond formation have been studied most extensively by this method.[4-10] Catalytic oxidation,[11-14] hydrogenation,[15-17] and hydrosilylation[18] reactions are some other examples of this application. ESI-MS analyses of organometallic reaction intermediates have led to a number of book chapters on this topic.[19-21] This chapter reviews a number of the recent applications of ESI-MS in organometallic catalysis, especially those relevant to our study.

Species of interest in catalytic systems or organometallic reactions must be charged to be visible by ESI-MS. There are several categories for the means by which organometallic species acquire a charge; inherently charged species (i.e. cationic or

anionic complexes), adventitiously charged (e.g. by protonation or loss of a halide) or charged by design via appending a charged or chargeable tag.

1.1.1. Inherently-charged systems

Study of reactions with inherently charged species are straightforward and cause little fear of any complications arising from the electrospray ionization process or tag interference with the reaction site. The reaction mixture is sampled and introduced to the source of the ESI-MS and the ions of interest are investigated. This type of system is particularly suitable for oxidation reactions, since intermediates are often naturally charged. Bortolini[22-25] and Smith[26-28] had considerable contributions in the early 2000s to this research field, specifically upon study of a range of manganese-containing intermediates for a variety of reactions. Study of an iron-catalyzed oxidation reaction in 1997 is one of the earliest reports, wherein $[Fe^{III}\text{-TPA(OOH)}]^{2+}$ was characterized as the intermediate in the hydroxylation of alkanes by H_2O_2 (TPA= tris(2-pyridyl-methyl)amine) by ESI-MS.[29]

Manganese-catalyzed reactions

In 1998 the speculative intermediate $[O{=}Mn^{V}]$ in many oxygen transfer reactions was intercepted in the form of $[O{=}Mn^{V}(salen)(OIPh)]^{+}$ complex (Figure 1.1 A), and a binuclear $[\mu\text{-}O(Mn^{IV}(salen)(OIPh))_2]^{2+}$ complex (Figure 1.1 B) [30]. Afterwards, detection of an analogous manganese salen intermediate $Mn^{V}(salen)(PhIO)(OCH(CH_3)Ph)]^{+}$ [12] as well as observation of $[Mn^{III}(salen)(PhI(OAc)_2)]^{+}$ in Mn-catalyzed oxidative kinetic resolution of secondary alcohols by $PhI(OAc)_2$ led to the suggestion of a potential catalytic cycle for the kinetic resolution of secondary alcohols by this system.

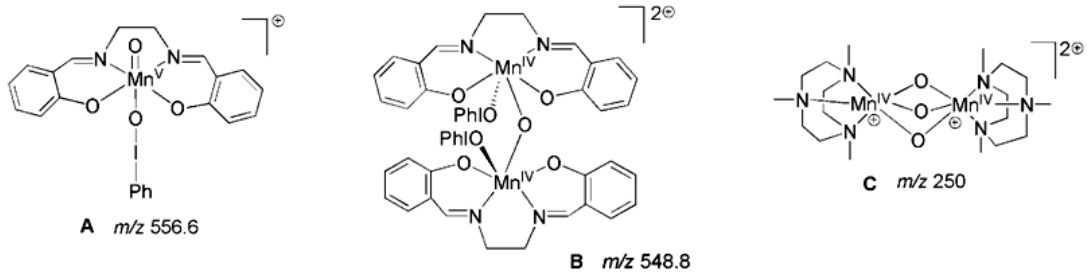

Figure 1.1: Manganese-containing complexes observed by ESI(+)-MS.

ESI-MS also has been employed to study Mn-MeTACN complexes in the oxidation of many organic substrates using hydrogen peroxide (MeTACN = 1,4,7-trimethyl-1,4,7-triazacyclononane). A variety of mononuclear and binuclear complexes were detected. [26,13,28] One noteworthy application of these complexes is for the oxidative drying of alkyd paints. The binuclear complex, $[Mn_2^{IV}(\mu\text{-}O)_3MeTACN)_2]^{2+}$ (Figure 1.1 C), was proved to be an efficient catalyst for oxidation of ethyl linoleate.[31] In 2010 the self-assembly of a hybrid polyoxometalate (POM) was studied by "real-time" monitoring of ESI-MS. A pathway was proposed based on observed intermediates followed by rearrangement of $[\alpha\text{-}Mo_8O_{26}]^{4-}$, coordination of Mn^{III} and coordination of two tris(hydroxymethyl)aminomethane ligands (TRIS) to form a symmetrical Mn cluster. [32]

Vanadium-catalyzed reactions

There are only a few vanadium systems studied by ESI-MS, and as was the case for Mn, most of the attention has been focused on identification of key intermediates in oxidations. It was found that monoperoxovanadium intermediates play the key roles in oxidation of isopropyl alcohol to acetone.[22] MS/MS analysis clearly shows loss of acetone from $[OV(O_2)(O^iPr)_2]^-$ (Figure 1.2 A, *m/z* 217), verifying that the reaction proceeds through the inner coordination sphere of the metal.

ESI-MS revealed the species $[VO(OH_2)(OH)(OBr)]^+$, as a potential intermediate in the vanadium-catalyzed oxidation of bromide by hydrogen peroxide (Figure 1.2 B, *m/z* 197/199).[25]

Oxygenation of 3,5-ditert-butylcatechol catalyzed by a series of vanadium catalysts was studied by ESI-MS. Inspection of reaction solutions after completion revealed two common negative ions: $[V(DTBC)_3]^-$ (DTBC = 3,5-di-tert-butylcatecholate dianion) [33] and $[VO(DTBC)_2]^-$ (Figure 1.2 C). The second species was ruled out as the active species through kinetic studies and $(VO(DBSQ)(DTBC))_2$ (DBSQ = 3,5-di-tert-butylsemiquinone anion). The species that was shown to correspond to $[VO(DTBC)_2]^-$, was recognized as a common catalyst for this reaction.

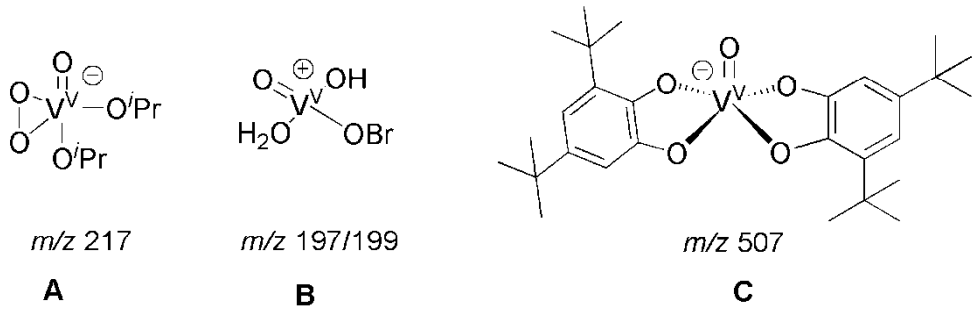

Figure 1.2: Vanadium-containing complexes detected by ESI-MS.

Palladium-catalyzed reactions

Unlike most oxidation reactions, palladium-catalyzed cross-coupling reactions generally proceed via neutral intermediates, nevertheless there are a few exceptions listed in here.

Observation of the exceptional binuclear sandwich Pd complex by ESI-MS is an early example reported in 1999 (Figure 1.3 A). It was proposed to participate in the enantioselective Manich-type reaction of enol silyl ethers with N-aryl-iminoacetic acid esters. Also observation of mononuclear palladium species with an empty coordination site (Figure 1.3 B) led to a proposed reaction mechanism based on these two species.[34]

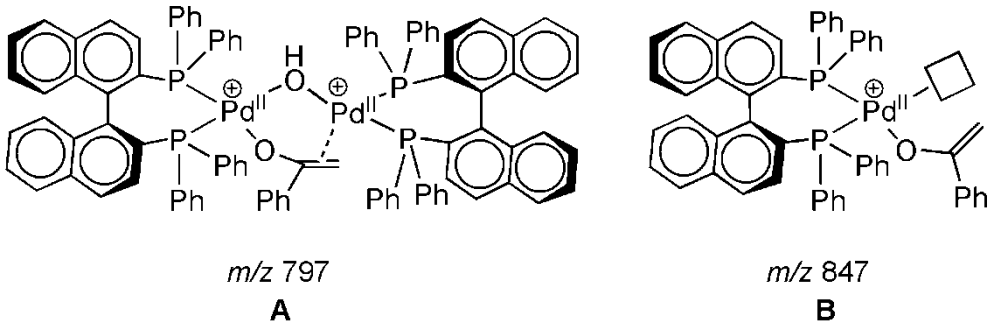

Figure 1.3: Mono and Bi-nuclear palladium complexes detected by ESI(+)-MS and suggested as catalytic intermediates in the enantioselective Manich-type.Redrawn from reference 34.

In another example, two reversibly formed binuclear bridged Pd species were observed in a palladium-catalyzed allylic substitution reaction (Figure 1.4)). It is suggested that Pd-Pd bond cleavage is the source of the active mononuclear catalyst.[9] The binuclear structure was confirmed by ^{31}P and ^{1}H NMR and *in situ* XAFS studies to make sure of the reliability of the ESI-MS observations.[35]

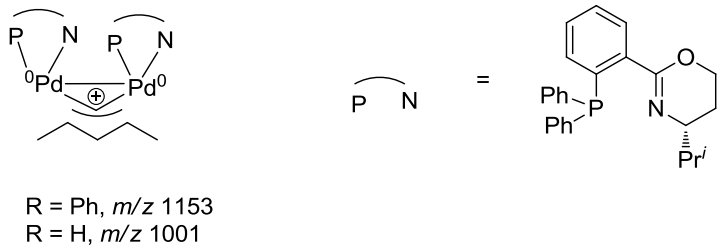

Figure 1.4: Two binuclear palladium-bridged allylic complexes observed by ESI(+)-MS. They are proposed to act as sources for the active catalyst in a palladium-catalyzed allylic substitution reaction. Redrawn from reference 9.

Another binuclear active Pd intermediate was reported in 2012 in the Wacker oxidation of alkenes.[36] ESI-MS revealed several binuclear Pd species carried alkene or ketone (as the product) suggesting that binuclear Pd species play active role in this transformation. Kinetic experiments performed by GC showed greater than one dependency of the rate on the concentration of the palladium precursor, which suggested that binuclear species played a role in the reaction (Figure 1. 5).

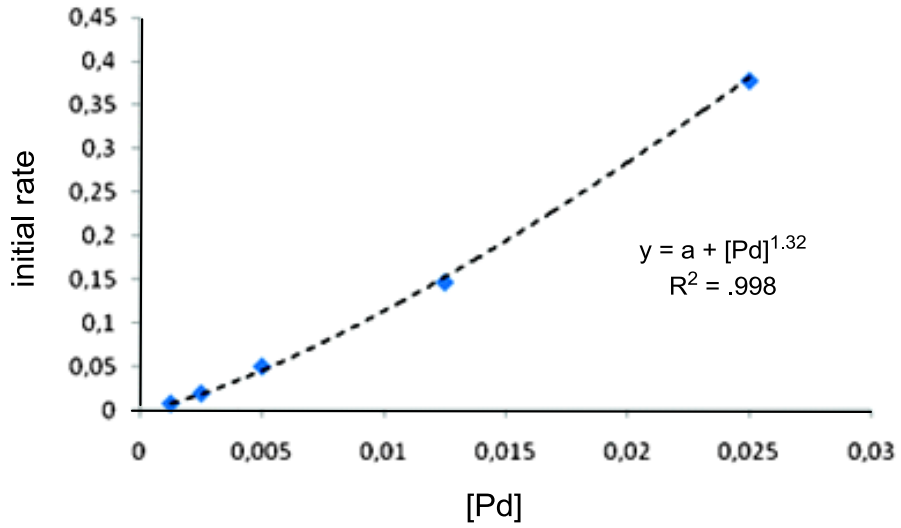

Figure 1.5: Initial rate dependence to concentration of palladium precatalyst in the Wacker oxidation of alkene. Modified from reference 36.

A mechanism was proposed for this reaction based on these observations. Although there is evidence of the existence of dimeric palladium in many catalytic cycles, it is still unclear as to whether these species contribute directly to the catalytic cycle. Therefore further synthetic and computational attempts are required to address this question.[37]

In 2013, Pd^{IV} was detected for the first time in oxidative coupling reactions catalyzed by $Pd(OAc)_2$. The intermediacy of Pd^{IV} was proved by MS/MS study of analogues of this Pd complex, which is produced Pd^{II} through reductive elimination of the product. The effect of different solvents and different anionic acetate ligands were also studied and different fragmentation pathways were obtained (Scheme 1.1). An MS/MS study performed on an authentic Pd^{IV} complex provided the same fragments as those of the assigned Pd^{IV} intermediates (Scheme 1.2).[38]

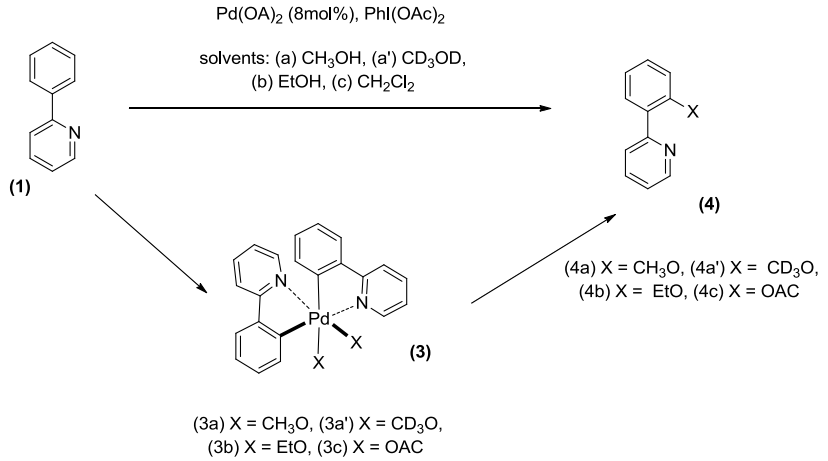

Scheme 1.1: Proposed mechanism of the palladium-catalyzed 2-phenyl pyridine oxidative coupling reactions. Dependence of intermediates and products to the type of solvents were clearly observed. Redrawn from reference 38.

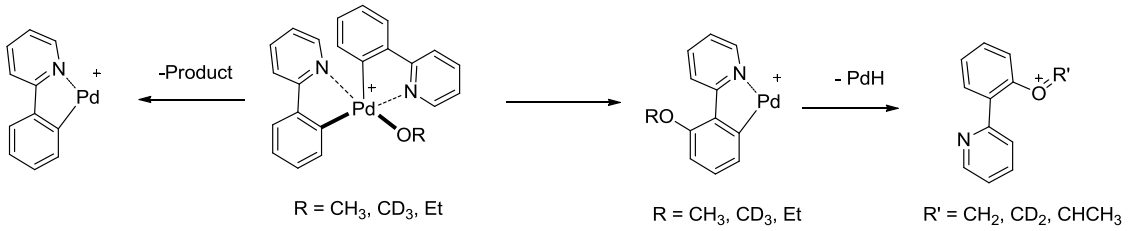

Scheme 1.2: Observed fragmentation pathways. Redrawn from reference 38.

A new method of fast and facile synthesis of aryl ketones from ortho-functionalized benzoic acid and nitriles were proposed in 2010. A Pd^{II} complex is used as the catalyst and as opposed to many other Pd catalysts, the oxidation state of Pd does not change over the course of reaction, which gives the opportunity to observe more intermediates by ESI-MS. A spectrum of the reaction mixture is shown in (Figure 1.6), in which various Pd containing complexes were observed. A mechanistic pathway was proposed subsequently based on assigned putative intermediates (Scheme 1.3). [39]

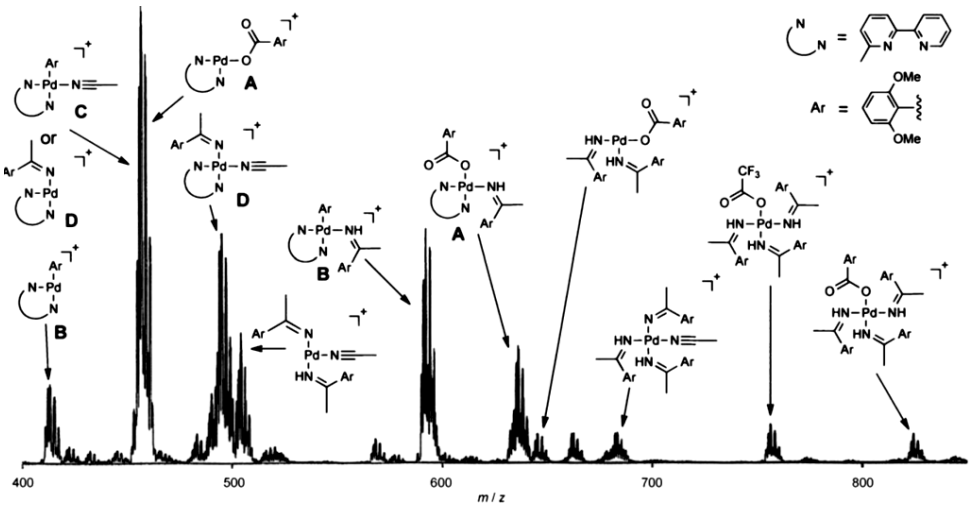

Figure 1.6: ESI-MS spectrum for the reaction mixture of 2,6 dimethoxybenzoic acid as the substrate and acetonitrile as the reactant/solvent with using $Pd(O_2CCF_3)_2$. Reprinted with permission from "Synthesis of Aryl Ketones by Palladium(II)-Catalyzed Decarboxylative Addition of Benzoic Acids to Nitriles1" J. Lindh, P. J. R. Sjöberg and M. Larhed, *Angew. Chem. Int. Ed.*, **2010**, 49, 7733-7737.Copyright © 2010 WILEY-VCH Verlag GmbH & Co. KGaA, Weinheim.

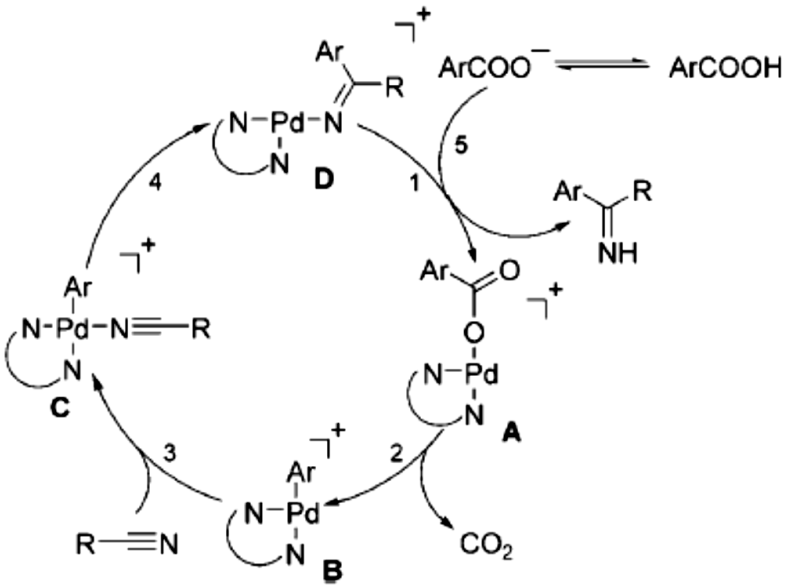

Scheme 1.3: Proposed mechanistic cycle for palladium-catalyzed decarboxylative addition of benzoic acid based on observation of cationic palladium complexes by ESI-MS. Reprinted with permission from "Synthesis of Aryl Ketones by Palladium(II)-Catalyzed Decarboxylative Addition of Benzoic Acids to Nitriles" J. Lindh, P. J. R. Sjöberg and M. Larhed, *Angew. Chem. Int. Ed.*, **2010**, 49, 7733-7737.Copyright © 2010 WILEY-VCH Verlag GmbH & Co. KGaA, Weinheim.

Other metal-catalyzed reactions

ESI studies of other metal-catalyzed reactions are rare; a ruthenium-catalyzed reaction with inherently charged cluster intermediates is one of the few examples. The cubane structure $[Ru_4(\eta^6\text{-}C_6H_6)_4(OH)_4]^{4+}$ was detected in solution by direct observation of $[Ru_4(\eta^6\text{-}C_6H_6)_4(O)_3(OH)]^+$.[15] Also the related dimer $[Ru_2(\eta^6\text{-}C_6H_6)_2(O)(OH)]^+$ was observed in solution which drew the attention. 16 electron structure of the Ru in the dimer may suggest that it is potentially an active catalyst. This hypothesis was examined in hydrogenation of benzene and ESI-MS showed that Ru dimer indeed is an active catalyst.

In 2012 the first ESI-MS investigation of Rh catalyzed [2+2+2] cycloaddition reaction was reported.[40] In this study which is supported by DFT calculation, several key intermediates were observed and characterized by MS/MS tandem spectrometry. Although reactant and product are neutral, the charged catalyst provided a good opportunity to intercept visible intermediates. A species with *m/z* 974.1 was assigned based on its accurate mass and CID experiments, however, mass spectrometry is unable to distinguish between isomeric structures (Scheme 1.4).

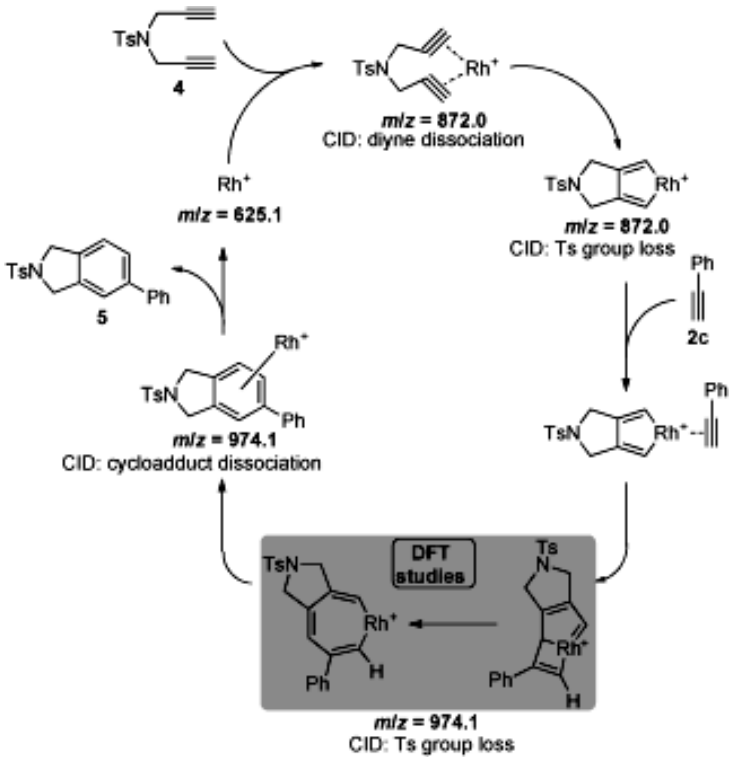

Scheme 1.4: Rhodim-catalyzed [2+2+2] cycloaddition mechanism for of diynes and monoynes based on detected species by ESI-MS and CID characterization. Reprinted with permission from "Direct Detection of Key Intermediates in Rhodium(I)-Catalyzed [2+ 2+ 2] Cycloadditions of Alkynes by ESI-MS" M. Parera, A. Dachs, M. Solà, A. Pla-Quintana and A. Roglans, *Chem. Eur. J.*, **2012**, 18, 13097-13107. Copyright © 2012 WILEY-VCH Verlag GmbH & Co. KGaA, Weinheim.

Copper-catalyzed synthesis of pyrozoles in the presence of CH_3CN is an interesting transformation, which involves C-C and N-N bond formation of enaminone. An ESI-MS study of this reaction gave no direct observation of intermediates. However, an unknown copper adduct was observed, which was isolated and characterized as an imidazolid-3-one. This observation suggests the participation of oxidative dimerization of enaminone in the presence of dioxygen. Figure 1.7 shows the trend of this hypothetical intermediate over the course of reaction. "Reagent" in here indicates all the enaminone containing copper species, while "product" indicates all pyrozoles containing copper species. As the authors pointed out, relative abundance is far different from concentration due to different intensity response factor of each species. However, it illustrates an insightful

(dis)appearance of the relevant intermediate. Finally, based on these observations, a mechanism was proposed for copper-catalyzed synthesis of pyrozoles (Scheme 1.5). [41]

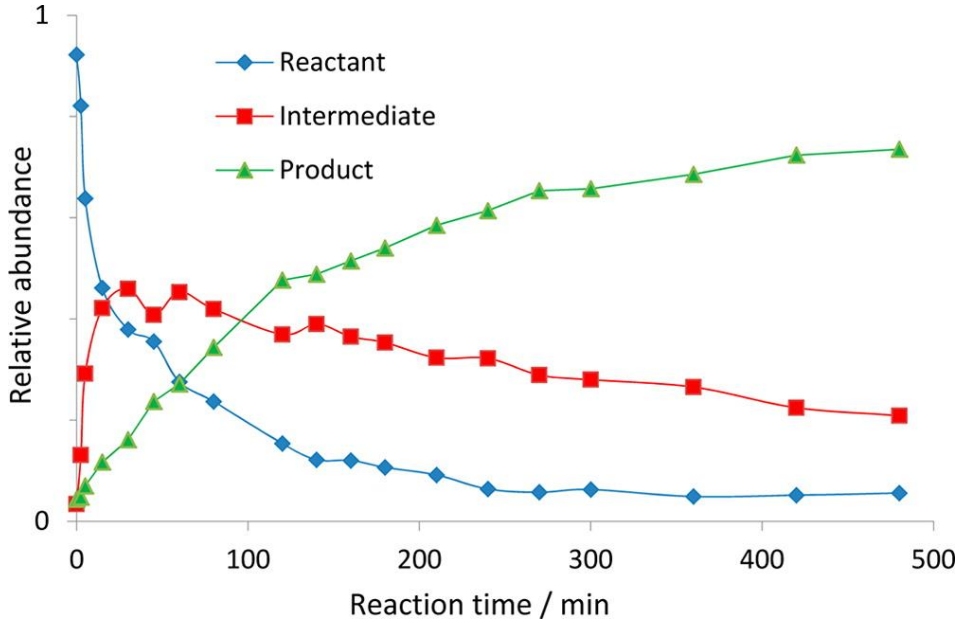

Figure 1.7: Relative intensities of the main components as monitored via ESI-MS in the positive ion mode. The sum of ions containing the reactant, the product, and the potential intermediate (imidazolid-3-one) are shown. Reprinted with permission from "Electrospray Ionization Mass Spectrometry Reveals an Unexpected Coupling Product in the Copper-Promoted Synthesis of Pyrazoles" K. Jiang, G. Bian, Y. Chai, H. Yang, Q. Lai and Y. Pan, *Int. J. Mass Spectrom.* **2012**, 321–322, 40-48. Copyright © 2012, Elsevier.

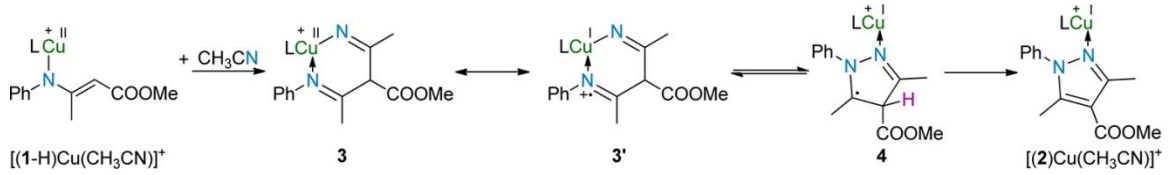

Scheme 1.5: Proposed pathway for the reaction of [(**1**−H)Cu(CH_3CN)]$^+$ to the product. **1** and **2** refer to enaminone and pyrazole respectively. Reprinted with permission from "Electrospray Ionization Mass Spectrometry Reveals an Unexpected Coupling Product in the Copper-Promoted Synthesis of Pyrazoles" K. Jiang, G. Bian, Y. Chai, H. Yang, Q. Lai and Y. Pan, *Int. J. Mass Spectrom.,* **2012**, 321–322, 40-48. Copyright © 2012, Elsevier.

Copper catalyzed cross coupling reaction of thiophenol and aryl halide is another example reported in 2011. In this study several anionic complexes were assigned as the active intermediates. Ion investigation was also performed in the positive ion mode, which only indicated the potassium adducts of thiophenol. A reaction mechanism was proposed based on these observations (Scheme 1.6).[42]

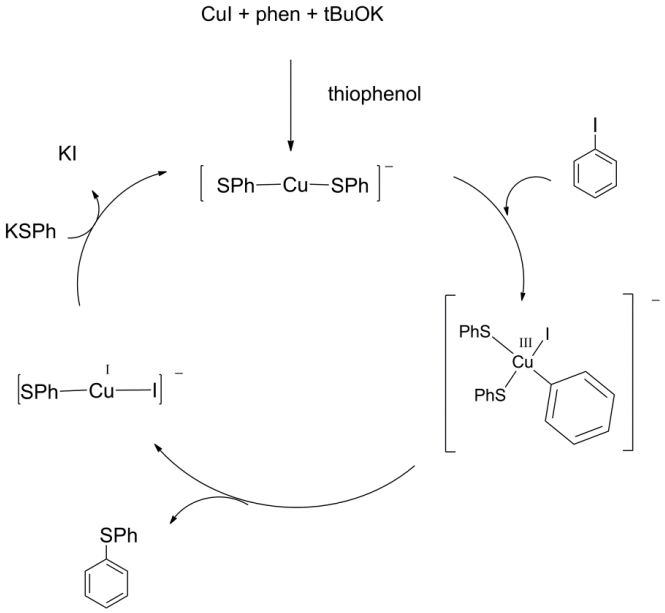

Scheme 1.6: Suggested catalytic cycle for copper-catalyzed cross coupling reaction of thiophenol and aryl halide based on detected species by ESI-MS. Redrawn from reference 42.

A ligand substitution mechanism of Ni^{II} complex with acetonitrile as the solvent was reported in 2012. Mechanistic investigation of this substitution included MS^n, isotope labelling and computational studies. Both associative and dissociative mechanisms were determined to be operating in this reaction and key intermediates of both pathways were detected. Four effective pathways eventually were proposed (Scheme 1.7).[43]

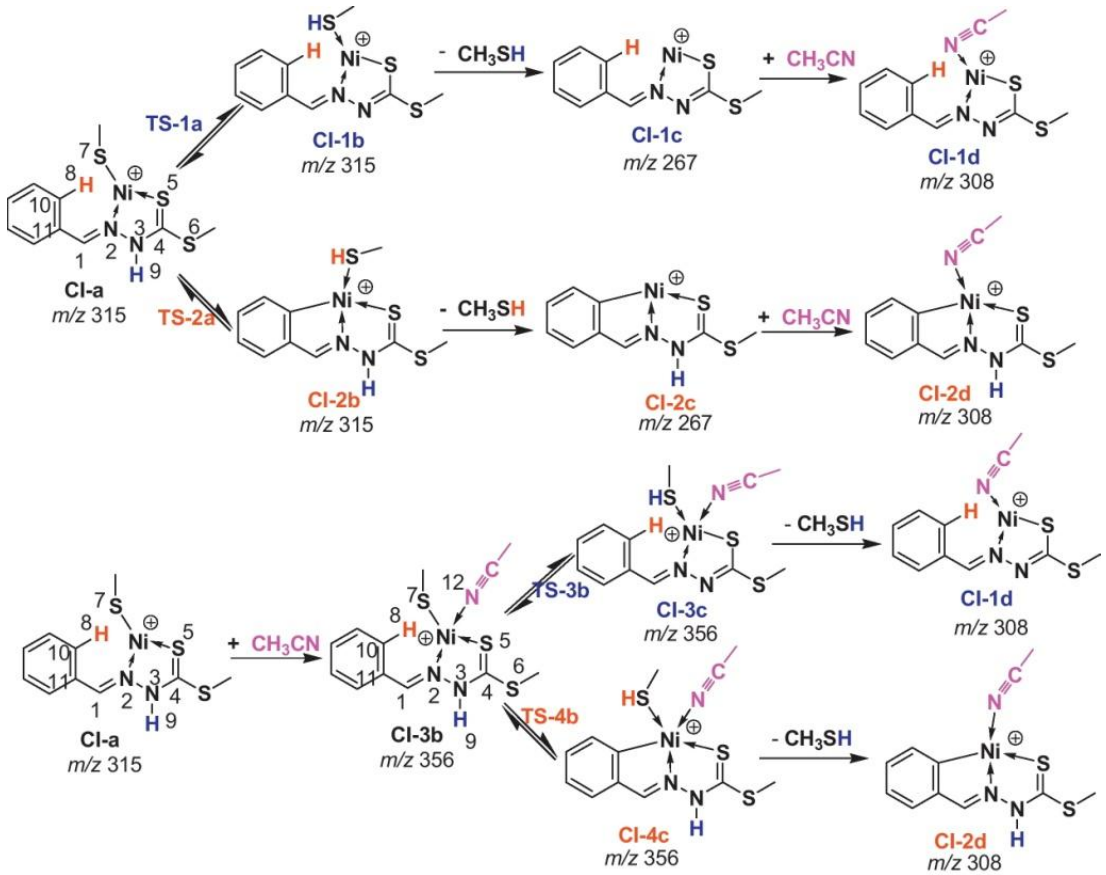

Scheme 1.7: Four mechanistic pathways of the ligand exchange reaction between cationic nickel complex (**CI-a**) and acetonitrile. Reprinted with permission from "Electrospray mass spectrometric studies of nickel(II)-thiosemicarbazones complexes: Intra-complex proton transfer in the gas phase ligand exchange reactions" K. Jiang, G. Bian, Y. Chai, H. Yang, Q. Lai and Y. Pan, *Int. J. Mass Spectrom.*, **2012**, 321–322, 40-48. Copyright © 2012, Elsevier.

Ultimately, mechanisms of both the hydro- and dehydrogenative silylation were elucidated by direct observation of several intermediates involved in the hydrosilylation and dehydrogenative silylation of phenylacetylene by an Ir^{II}-NHC type catalyst. [18]

Peter Chen initiated the mechanistic study of gas-phase organometallic reactions by ESI-MS. [44-59] The gas-phase reagent along with neutral gas were introduced to the first octopole of a modified mass spectrometer and reacted with the analyte. The gas phase product was subsequently analyzed in the first quadrupole. Further structural and

reactivity details were obtained by collision- induced dissociation of the product in the second octopole and mass analysis of the fragments in the second quadrupole.

Transmetallation is one the key steps in cross coupling reactions and in many cases is believed to be turnover limiting step. For example silver (I) has shown catalytic activity in methyl scrambling on Pt complex [(bpy)$PtMe_2$], (bpy = 2,2'-bipyridyl).[60] The pathway which is believed to have a Pt-Ag dative interaction is speculative in the sandwich complex, {[(bpy)$PtMe_2$]$_2Ag^+$}. However, the detailed role of these cocatalysts and their thermochemical data are not well known. In recent years, gas phase investigation by mass spectrometry has lent itself to study the metal-metal interaction in organometallic field and rich information has been obtained from bimetallic systems.[55, 56] Equivalent amount of reactants (Scheme 1.8) in solution were electrosprayed and the analogue of Pt-Cu bimetallic cations were identified. XRD analysis confirms that metal-metal bond exists in {[(dmpe)$PtMe_2$]Cu(P^{t}Bu)$_3$}OTf, (dmpe = 1,2-Bis(dimethylphosphino)ethane).

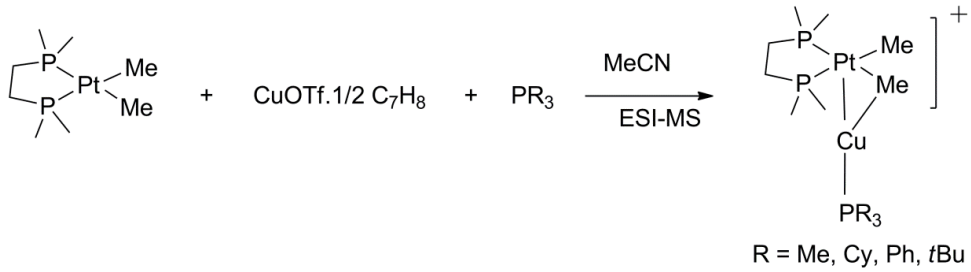

Scheme 1.8: Generation of the of Pt-Cu complexes with analogues of PR_3 in solution and direct observation by ESI-MS. Redrawn from reference 56.

The gas phase reactivities of the complex, {[(dmpe)$PtMe_2$]Cu(P^{t}Bu)$_3$}OTf toward CID experiments were investigated and methyl transfer from platinum to copper demonstrated. The CID experiment showed transmetallation reaction of Cu by abstracting of Me group and formation of Cu-C bond. Also it turned out that the analogues of R in PR_3 show different fragmentations depends of the bulkiness of P. For example while PMe_3-complex afford only (a and b) in the Scheme 1.9, the P^{t}Bu$_3$-complex doesn't afford Cu-Me presumably due to destabilization of cationic Pt complex but extra fragments were appeared (c and d). Ph and Cy complexes show the mixture of fragments with different rations (Scheme 1.9). DFT calculation fully supported the

experimental approaches.[56] Scheme 1.9 shows the fragmentation pathways in different phosphine ligands.

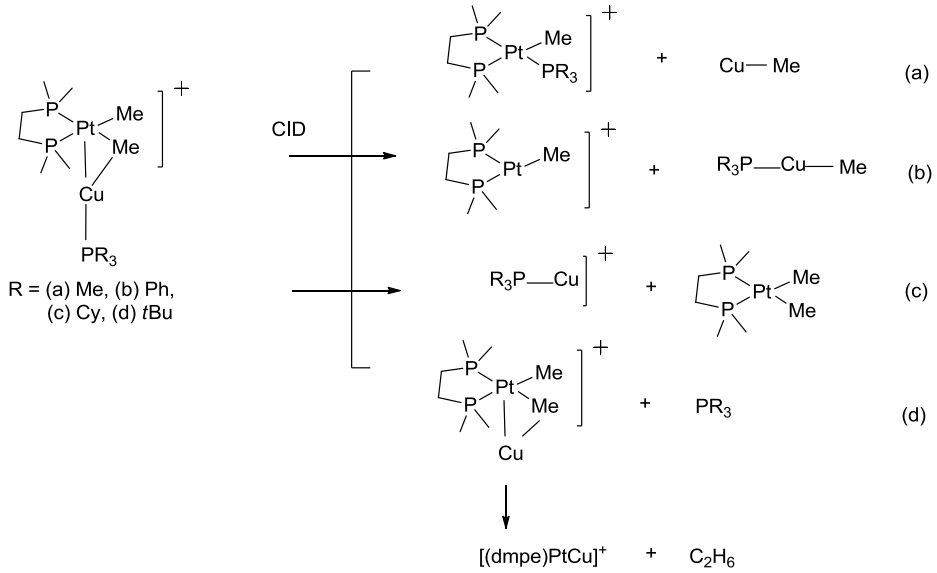

Scheme 1.9: Different dissociation pathways in bimetallic Pt-Cu complexes with analogues of phosphine ligands. Redrawn from reference 56.

Having successfully employed ESI-MS/MS technique to indicate the mechanism of transmetallation through heteroatom bimetallic between Pt and Cu, Au was employed for further investigation of transmetallation mechanism.[55] As before, the results showed that transmetallation of methyl group goes through heterobimetallic complexes. It was found that the steric effect of PR_3 ligand in cationic intermediate can define two different pathways which can be used to control different products. In order to compare the reactivity in different phases, reactions were performed in solution and monitored by ^{31}P NMR. Results were the same as what were observed in the gas phase.

1.1.2 Adventitiously-charged systems

In adventitiously-charged systems intermediates are intrinsically neutral. However, charged species arise via one or more possible ionization mechanisms. Protonation of a basic site is the main general ionization mechanism, but association of an alkali metal ion such as $[Na]^+$ or $[K]^+$ and reversible dissociation of an anionic ligand like $[I]^-$ or $[Br]^-$ are common as well (Figure 1.8). One advantage of this set of ionizations, the same as

naturally charged systems, is that alteration to the reaction mixture is usually unnecessary.

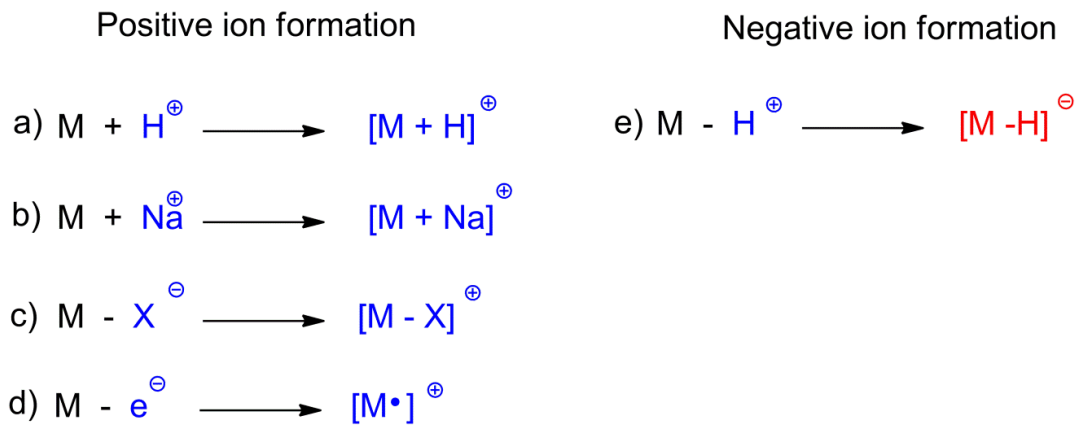

Figure 1.8: Ionization pathways: a) protonation of a basic site b) association of a alkali metal to a basic site c) halide dissociation d) oxidation e) deprotonation of an acidic site.

Loss of halide and other anionic ligands has been reported several times in palladium-catalyzed C-C bond-formations. Early investigations into these reactions revealed the formation of oxidative addition intermediates in the following examples: when bis-phosphane chelating ligands were used in the Heck arylation of methyl acrylate (loss of halide),[61] through the intramolecular cyclization of enamides to form spiro-compounds (loss of halide)[62] and in the self-coupling of arylboronic acids (loss of anionic boron ligand).[63] In the last example pertinent species were also detected by protonation of intermediates when the reaction was quenched with trifluoroacetic acid. For instance, interception of $\{Pd(H)(PPh_3)_2[B(OH)(OH_2)]\}^+$ indicates its involvement in the regeneration of the catalyst.

Cationic intermediates have been observed in the following Heck reactions of: arene diazonium salts catalyzed by triolefinic macrocycle Pd(0) complexes in which the ion formation occurred through the oxidation of analyte at the capillary or by bonding to the $[NH_4]^+$ or $[Na]^+$,[5, 64] also cationic intermediates were observed in the Heck reaction of *o*-iodophenols and enoates to form new lactones,[65] and *o*-iodophenols with olefins (the *oxa*-Heck reaction).[66] In these two cases ionization proceeded via the loss of a halide ligand.

In an ESI-MS monitoring study of Suzuki-Miyaura, using a particular Pd precatalyst (dichloro-bis(aminophosphine)) binuclear Pd complexes were detected after reaction completion presumably as the resting state. However, addition of starting reagents, resumes the reaction which may suggest the active role of the binuclear complex as the source reservoir of mononuclear active catalyst. Other interpretations propose the involvement of Pd nanoparticles in which, binuclear Pd complexes perform as the precursor or perhaps even the active catalyst, but the last possibility is less likely than other possibilities due to author's statement. A mechanism for this transformation was proposed to locate the intercepted species (Scheme 1.10). [67]

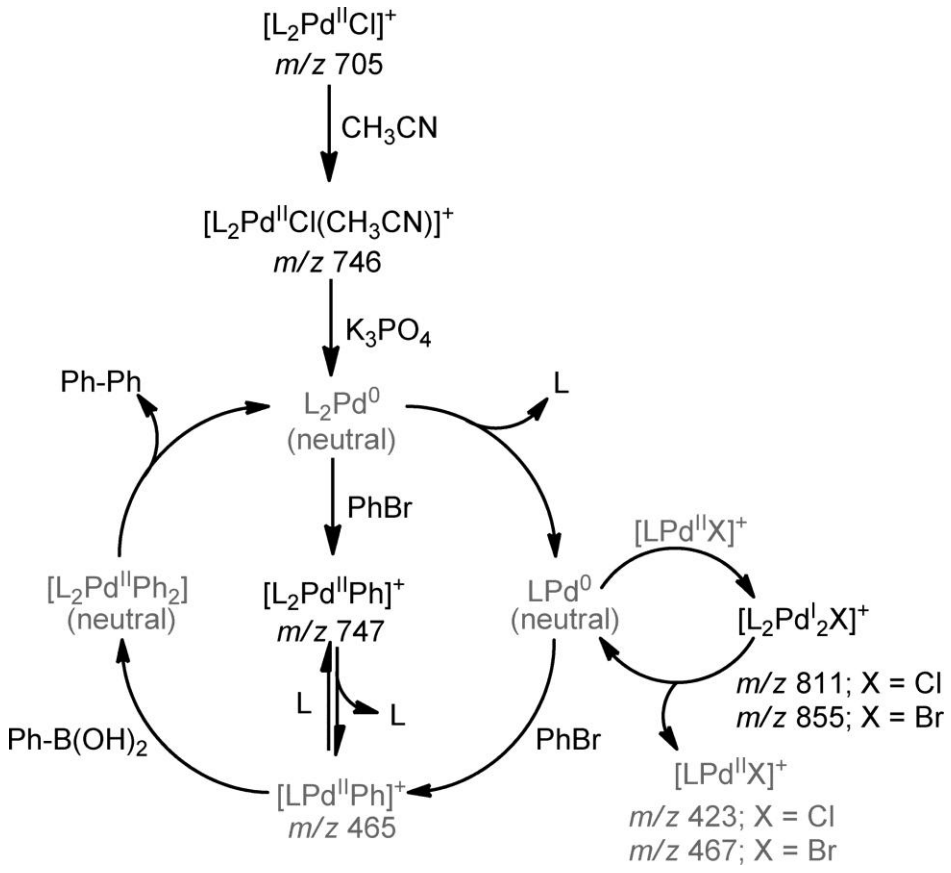

Scheme 1.10: Proposed mechanistic cycle for Suzuki–Miyaura cross-coupling based on the observation of binuclear palladium complexes. Reprinted with permission from "Observation of Binuclear Palladium Clusters upon ESI-MS Monitoring of the Suzuki–Miyaura Cross-Coupling Catalyzed by a Dichloro-bis(aminophosphine) Complex of Palladium" D. Agrawal, D. Schröder and C. M. Frech, *Organometallics*, **2011**, 30, 3579-3587. Copyright © 2011 American Chemical Society.

Reductive elimination of carbene with phenyl group from a palladium(II) N-heterocyclic carbene complex is a nice example of cationic intermediate formed in gas phase of ESI-MS.[45] This study is a complementary evidence for solution phase which represents that NHCs are not always spectator ligands, but they can afford reductive elimination to form new C-C bonds. This bond formation occurred through CID experiment (Scheme 1.11).[68, 69] Density functional calculations also reproduced the experimental data.

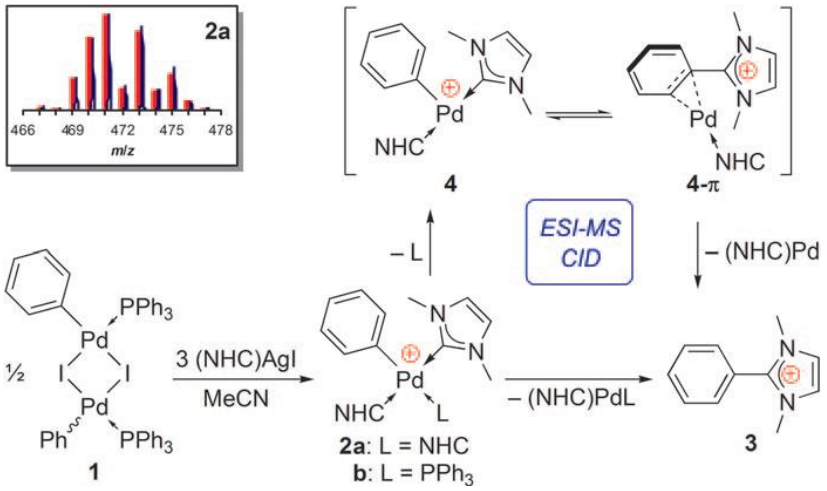

Scheme 1.11: Formation and gas-phase reactivity of Pd-NHC complexes. Reductive elimination of phenyl group and NHC ligand (**3**) occurred through CID experiment. Reprinted with permission from "Gas-Phase Energetics of Reductive Elimination from a Palladium(II) N-Heterocyclic Carbene Complex" E. P. A. Couzijn, E. Zocher, A. Bach and P. Chen, *Chem. Eur. J.*, **2010**, 16, 5408-5415. Copyright © 2010 WILEY-VCH Verlag GmbH & Co. KGaA, Weinheim.

The likely Pd^0 active species for a classic Stille reaction was indirectly observed as its molecular ion $[Pd(PPh_3)_2]^{\bullet+}$. Santos and Eberlin presented an outstanding example of a non-innocent ESI process that represents detection of otherwise neutral intermediates.[70] The molecular ion was formed by oxidation of the neutral species at the capillary through the ESI process.[70]

In another interesting reactivity investigation reported in 2013, postulated oxidized transition metal-thiolate complexes of Ru, Re and Ni were produced through the electrospray ionization process (Scheme 1.12) and the radical nature of these cationic complexes as well as their reactivity toward unsaturated hydrocarbons and ketones was examined through the formation of C-S bonds (Scheme 1.13)[71]. Reactivity of the ruthenium complex toward CH_3SSCH_3 – an addition reaction which is supposed to proceed through a radical mechanism with one or two $CH_3S^{\bullet-}$ confirmed the thiyl radical nature of this complex. Success of this study confirmed the known oxidation step of the initial complexes, $[PPN]^+[RuL_3]^-$. Finally, an ESI-made cationic Ru complex was proposed as the active intermediate in this reaction. Scheme 1.13 shows the reactivity of Ru complex with different reactants.

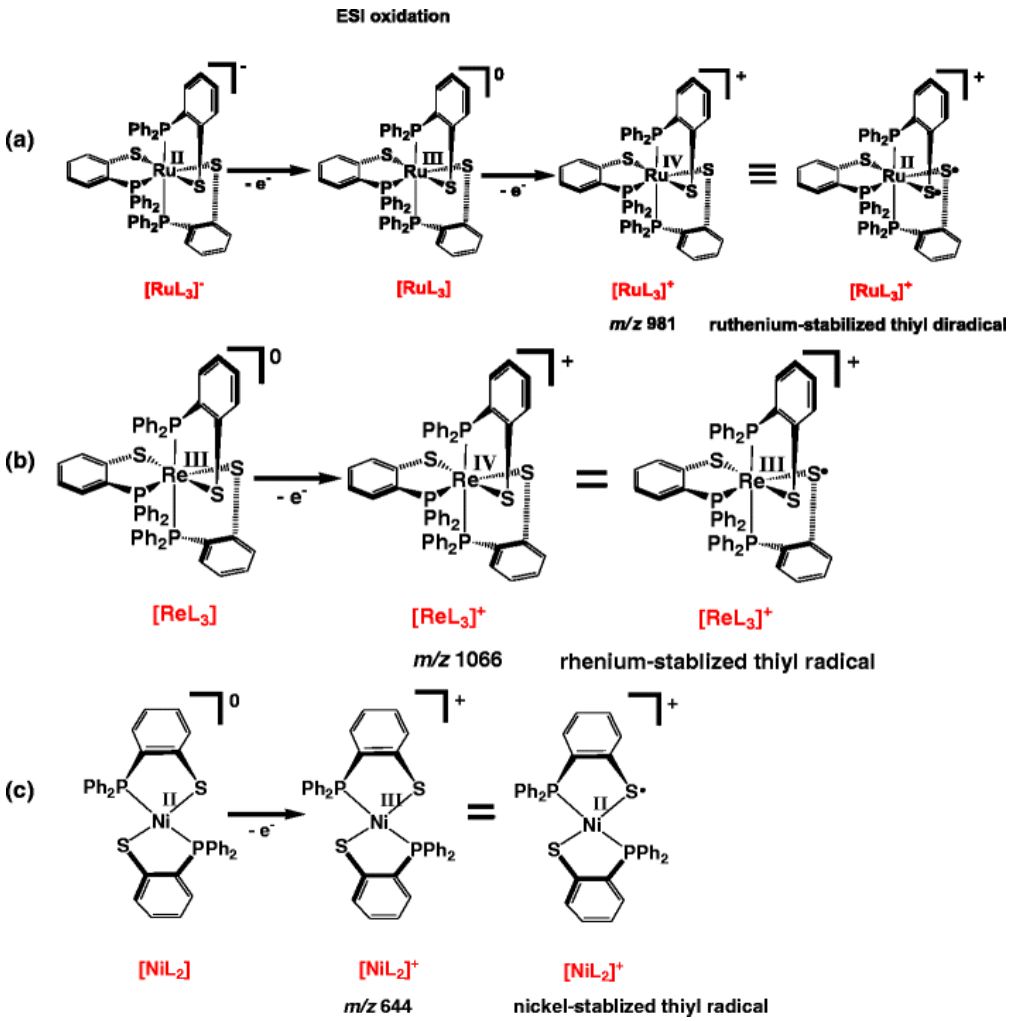

Scheme 1.12: Oxidation of $[RuL_3]^-$, ReL_3 and NiL_2 during electrospray ionization process. The observed cation in each case was regarded as metal-stabilized thiyl radical. Reprinted with permission from "Probing the Reactivity and Radical Nature of Oxidized Transition Metal-Thiolate Complexes by Mass Spectrometry" M. Lu, J. L. Campbell, R. Chauhan, C. A. Grapperhaus and H. Chen, *J. Am. Soc. Mass Spectrom.*, **2013**, 24, 502-512. Copyright © 2013, American Society for Mass Spectrometry.

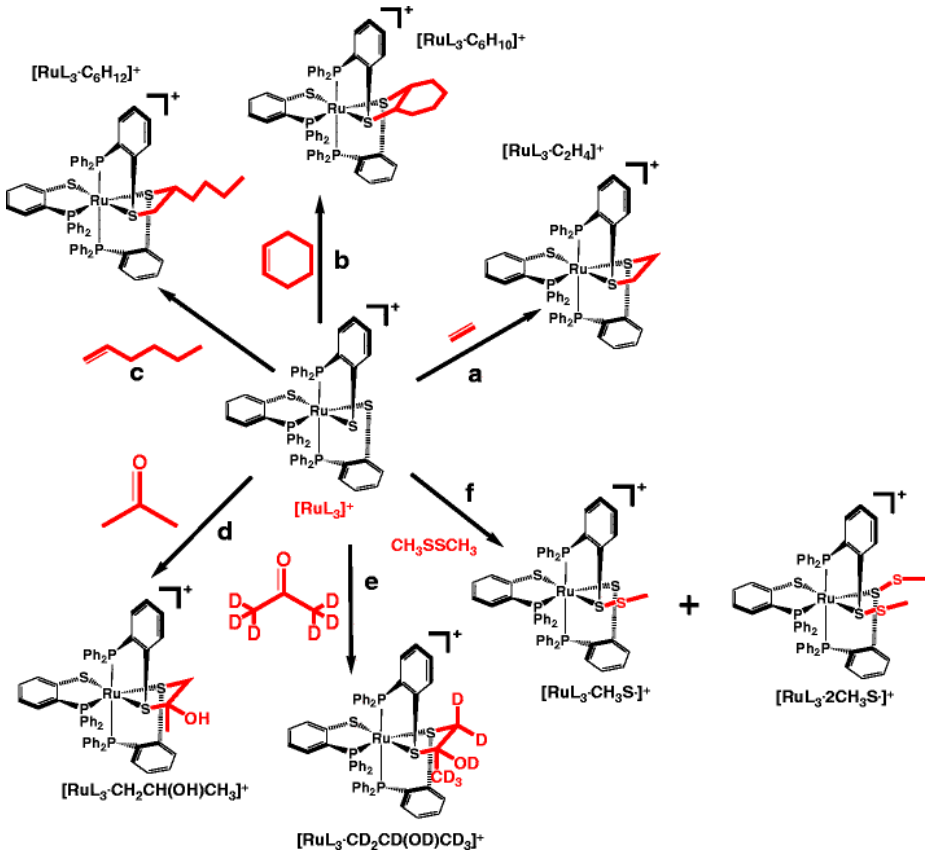

Scheme 1.13: Reactivity of $[RuL_3]^+$ with alkenes, methyl ketones and dimethyl disulfide. Ions and reactivity shown here were observed in the gas phase. Reprinted with permission from "Probing the Reactivity and Radical Nature of Oxidized Transition Metal-Thiolate Complexes by Mass Spectrometry" M. Lu, J. L. Campbell, R. Chauhan, C. A. Grapperhaus and H. Chen, *J. Am. Soc. Mass Spectrom.*, **2013**, 24, 502-512. Copyright © 2013, American Society for Mass Spectrometry.

Polymerization also has taken advantage of this type of investigation. Metzger and his coworkers used the source of alkali chloride (Me: Li, Na, K, Cs) as the additive to visualize the neutral catalysts and any other fortunate artefact in polymerization using first and second generation Grubbs catalysts.[72] In a more recent study which was supported by computational calculations,[73] they showed the advantage of using alkali metal ions in an ESI-MS study of ruthenium olefin metathesis catalysts. While the ESI-MS study of these neutral catalysts led to formation of radical cations (whose reactivities are unlike the real catalysts in solution), applying alkali metal ions allowed observation of a 14 electron active catalyst in solution, formed by dissociation of phosphane (PCy_3) from the precatalyst (Scheme 1.14). It was also found that, the concentration of the cationized

active catalyst is higher in the solution of the second generation Grubbs catalyst compared with first generation catalyst in accordance with their activities. In 2013, the same route was used to compare the activities of the first and the third generation Grubbs catalysts. Measured spectra revealed substantial amount of unreacted catalyst species in the first generation Grubbs while more active species were observed in the third generation Grubbs catalyst, again in agreement with the high efficiency of this class of catalysts.[74]

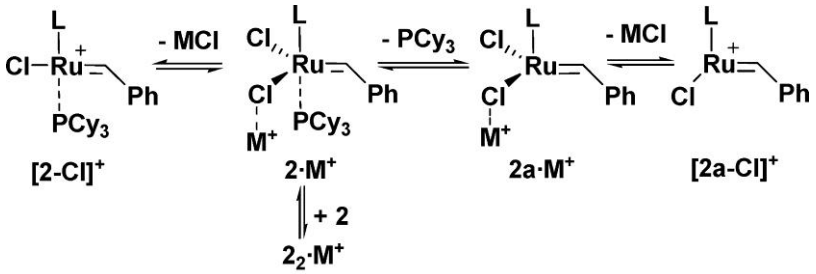

Scheme 1.14: Cationic Ru carbene complexes observed in solution of catalysts **2** in the presence of alkali metal chlorides. L :H_2IMes, M: $[Li]^+$, $[Na]^+$, $[K]^+$, $[Cs]^+$. Modified from reference 74.

1.1.3 Charged or chargeable tags

As described above, there have been good opportunities to study organometallic systems by ESI-MS, where inherently or adventitiously charged species exist in the reaction mixture. Nevertheless, many organometallic reactions proceed through neutral intermediates and/or reactants and products. Therefore, another reliable route is required to visualize such these systems in order to take advantage of the strengths of the ESI-MS as an analytical tool. To tackle this obstacle, scientists came up with a neat idea to append a charged or chargeable tag. However, concerns arise about the validity of similarity of the tag containing systems to those of neutral ones. So, the tag must not sterically and electronically interfere with the catalysis, even though alteration in polarity is inevitable.

Palladium-catalyzed reactions of pyridyl bromide with different phenylboronic acids were studied by ESI-MS by Canary et al in 1994. Ability of the ring nitrogen to bind a proton makes pyridyl bromide an appropriate choice as a chargeable tag. Oxidative addition and transmetallation intermediates were observed, thanks to this ionization mechanism (Figure 1.9).[75] The groups of Traeger,[76, 77] Dyson,[78] Nicholson[79] and Chen[80-

[82] are the major contributors to this field, nevertheless it is an underappreciated advance to some extent.

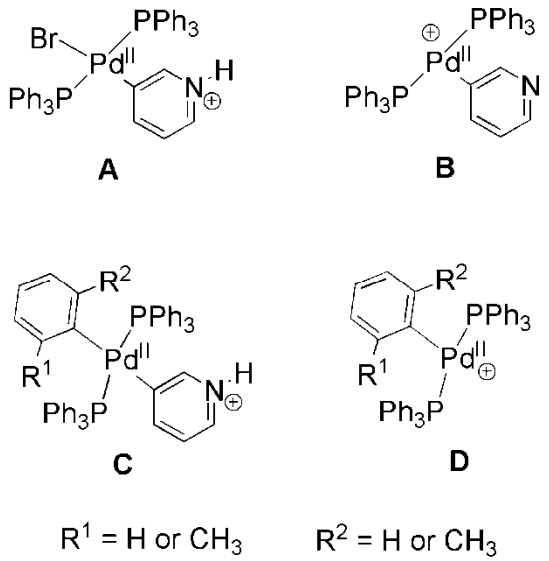

Figure 1.9: (A and B) Oxidative addition intermediates $[(pyrH)Pd(PPh_3)_2Br]^+$ and $[(pyr)Pd(PPh_3)_2]^+$, Transmetallation intermediates with (C) and without (D) pyr group in $[(pyrH)(R^1R^2C_6H_3)Pd(PPh_3)_2]^+$. Redrawn from reference 75.

Metzger [83] used the charged ligand $[P(Cy)_2(CH_2CH_2N(Me)_3)]^+[Cl]^-$, as a water-soluble ligand (Figure 1.10 A, B), to study the two first generation ruthenium olefin metathesis catalysts, initially developed by Grubbs.[84, 85] Insertion of the charged ligand proved the nature of the proposed 14-electron catalytically active Ru species (C) by direct observation of this species in the ESI. This approach confirmed many findings of the catalytic ring-closing metathesis cycle suggested earlier by Grubbs.

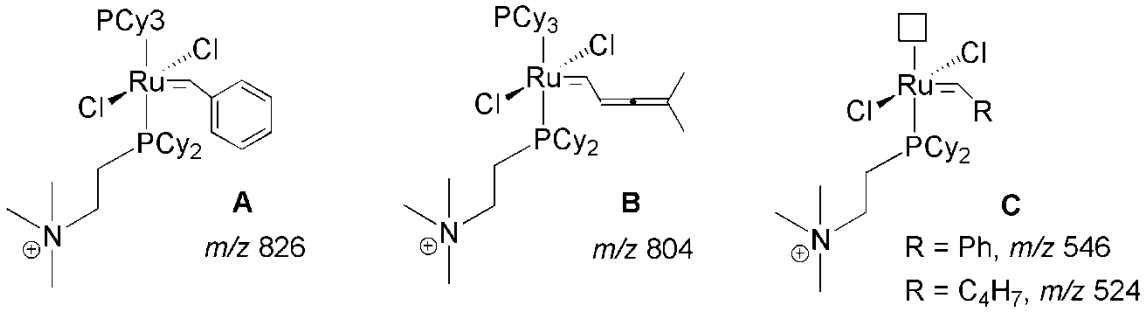

Figure 1.10: (A and B) Two charge-tagged analogues of first generation ruthenium catalysts, and (C) the related 14-electron active species detected by ESI(+)-MS. Redrawn from reference 83.

Rhodium-catalyzed hydroformylation was studied online under typical reaction conditions by connecting a pressurized autoclave directly to the mass spectrometer via a splitter. While several intermediates were characterized by this method, no attempt was made to extract kinetic data from this set-up. However, a new mechanism for self-assembling ligands was suggested based on ESI-MS studies including D_2-inclusion reactions (Scheme 1.15).[86]

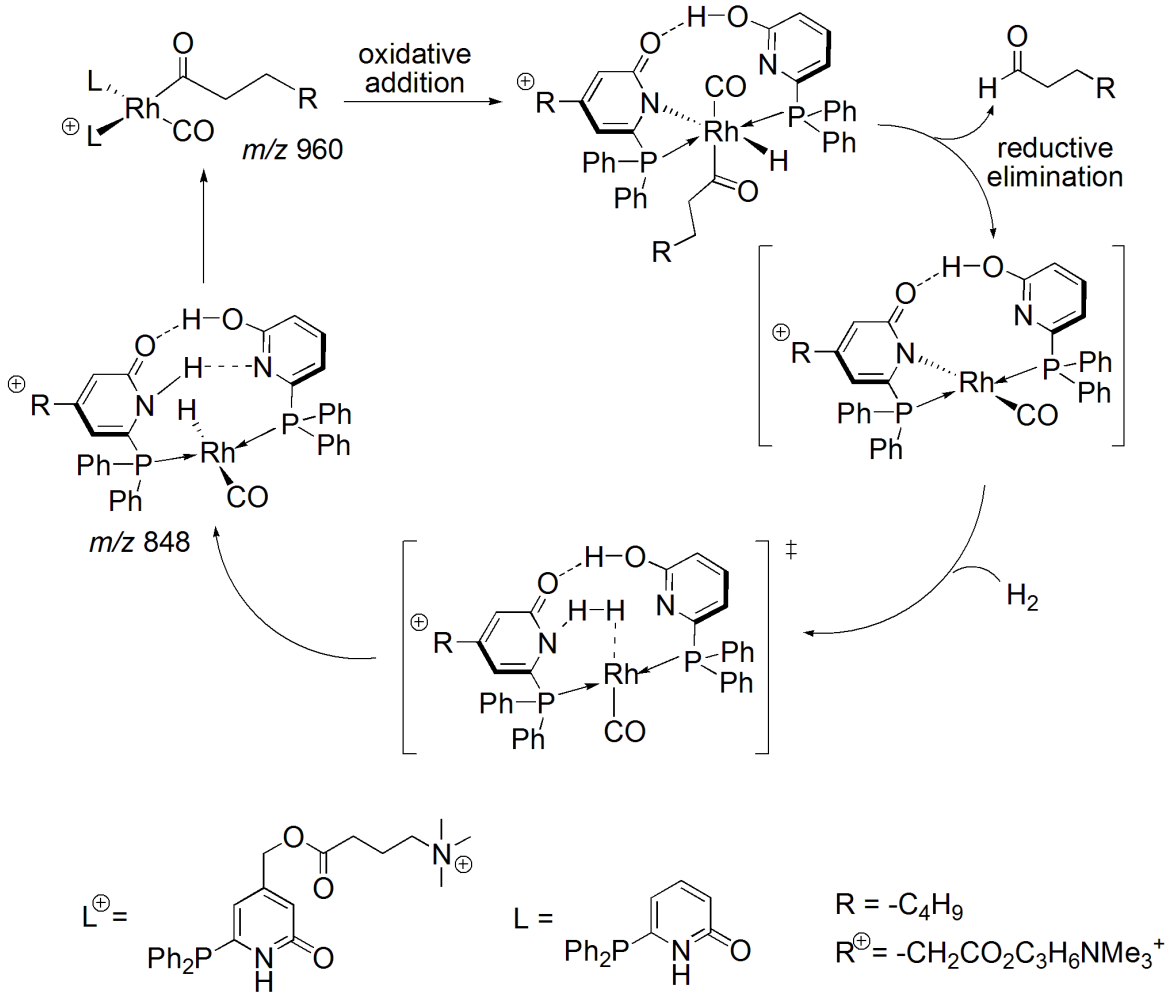

Scheme 1.15: A proposed mechanism of rhodium-catalyzed hydroformylation by ESI(+)-MS analysis. Modified from reference 86.

Eberlin and his co-workers[1] recently reported a charge-tagged acetate ligand as a probe for mass spectrometry. Nickel, copper, and palladium complexes of this ligand have been synthesized and characterized by ESI-MS (Scheme 1.16). Also, catalytic activity of a charged-tagged acetylene imidazolium salt coordinated to Pd was examined in phosphine-free Heck and Suzuki cross coupling reactions. Greater activity and yield in comparison with $Pd(OAc)_2$ precatalyst along with ability to visualize neutral species in the reaction mixture indicate the dual roles of this anionic ligand. Gas phase reactivity of the metal complexes was also performed by CID in which, rich structural and reactivity information were obtained. These findings explain some general mechanistic findings in palladium cross coupling reactions.

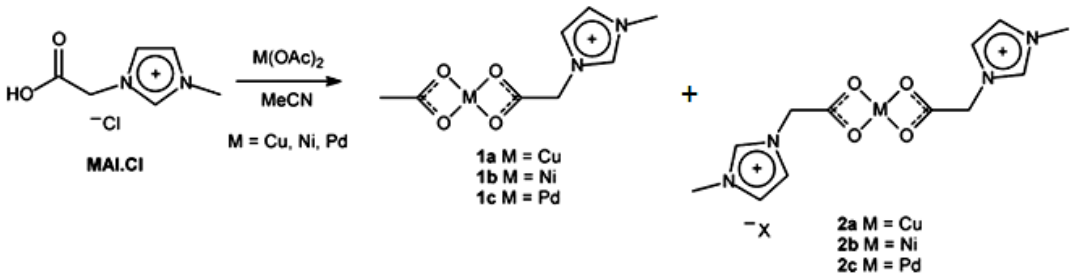

Scheme 1.16: Observation of charge-tagged complexes generated in reaction of charged-tagged acetylene imidazolium salt with neutral $M(OAc)_2$ complexes (M = Cu, Ni, Pd). Modified from reference 1.

Phosphinidene complexes [L_nM=PR] are interesting reagents due to their isoelectronic similarity to carbene complexes, [L_nM=CR_2]. So far, isolation and characterization of the nucleophilic phosphinidene type of the [Cp(L)(M=PR] have been observed reportedly.[87-89] However, there is not any report on observation of phosphinidene (Fischer-type) complex [RP=$W(CO)_5$] containing only CO, even though they have been confirmed by their reactivity investigations, there is ambiguity around the mechanism in which phosphinidene is involved.[90-92] In a gas phase study Chen and co-workers aimed to address this uncertainty.[52] When the tagged precursor (a) in Scheme 1.17 is subjected to CID, an ion corresponding to [RP=$W(CO)_5$] was observed. DFT calculations compared the reactivity of charged and neutral precursors (b) in the same scheme and concluded that both precursors had the same reactivity.

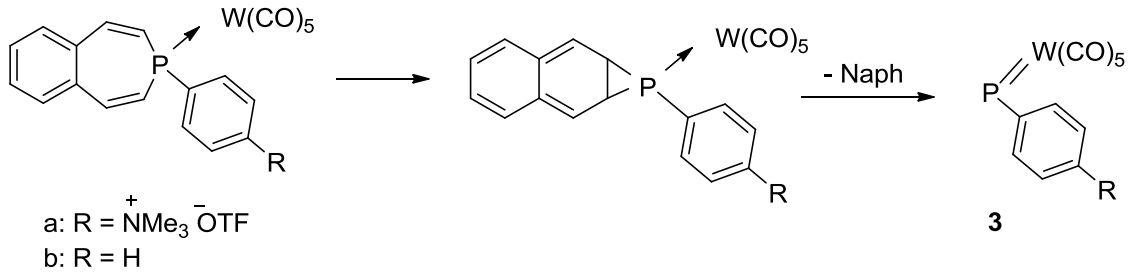

Scheme 1.17: Formation of **3a** [RP=$W(CO)_5$] in CID experiment on 3H-benzophosphepines which was proceed through loss of naphthalene. Redrawn from reference 52.

Treatment of the transient phosphinidene complex with an alkene/argon mixture in a modified mass spectrometer allowed investigation of the reactivity of this species. [1+2] cycloaddition of olefin occurred, which confirmed the reactivity and structure of the corresponding phosphinidene. Fragmentation of each adduct as well as the isotope pattern were consistent with the proposed structures (Figure 1.11).

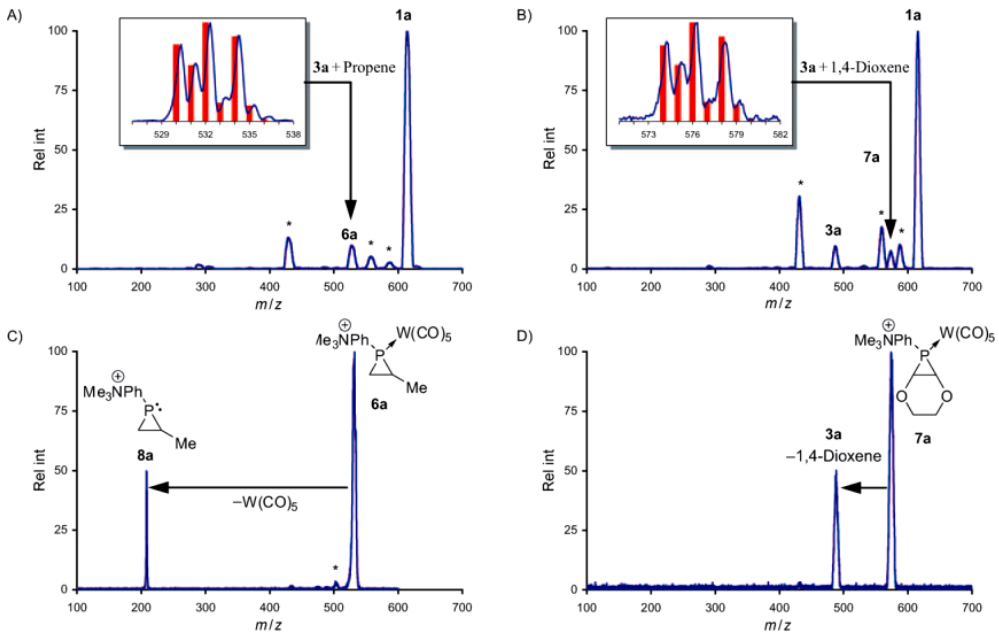

Figure 1.11: Top: (A and B) Reactivity of **3a** [RP=W(CO)$_5$] with propane and 1,4-dioxene respectively . Insets show the overly of the experimental isotope patterns of adducts **6a** and **7a** and calculated (red bars) isotope patterns. Bottom: (C and D) show CID experiments of **6a** and **7a** respectively. The marked signals (*) show fragmentation product formed by loss of CO. Reprinted with permission from "Reactive Intermediates: A Transient Electrophilic Phosphinidene Caught in the Act" H. Jansen, M. C. Samuels, E. P. A. Couzijn, J. C. Slootweg, A. W. Ehlers, P. Chen and K. Lammertsma, *Chem. --Eur. J*, **2010**, 16, 1454-1458. Copyright © 2010 WILEY-VCH Verlag GmbH & Co. KGaA, Weinheim.

McIndoe's group also have contributed to the design and employment of the charged tags. Synthesis and improvement of a series of mono and bidentante phosphine ligands;[93, 94, 95] using a tethered charged pyridinium group to study distannoxane speciation during esterification catalysis[96] and silane dehydrocoupling and olefin

hydrogenation study by using a charged analogue of Wilkinson's catalyst are some of these examples.[94,95]

Our group also recently reported a coordinating proton sponge ligand with a chargeable tag for analysis by ESI-MS.[97] It was shown that the tag 1,8-bis(dimethylamino)-2-(4-methoxyphenyl)naphthalene (Scheme 1.18) has the characteristics of a practical chargeable tag for analysis by ESI-MS. In an example it was indicated that the ligand readily coordinates to chromium in an η^6- fashion (Figure 1.12) while the proton sponge moiety abstracts proton to become charged with high efficiency. The large distance between the tag and active site guarantees innocent role of the tag on reactivity of complex.

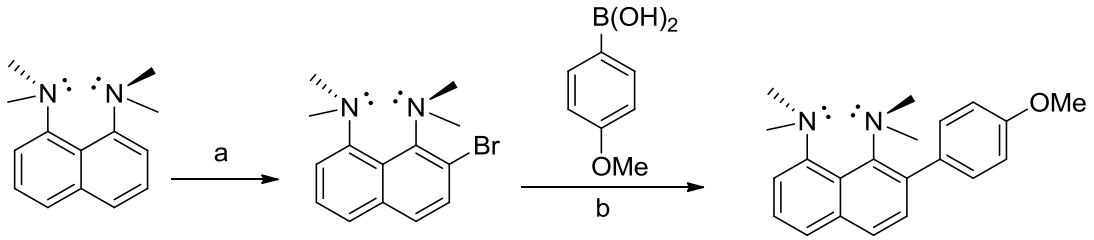

Scheme 1.18: Synthesis of **1** from a proton sponge (1,8-bis(dimethylamino)naphthalene. a) *N*-bromosuccinimide, THF and −78 ^{o}C. b) $Pd(OAc)_2$, PPh_3, $NaCO_3H$ and mixture of *n*-propanol with water. Reflux 12 h. Redrawn from reference 97.

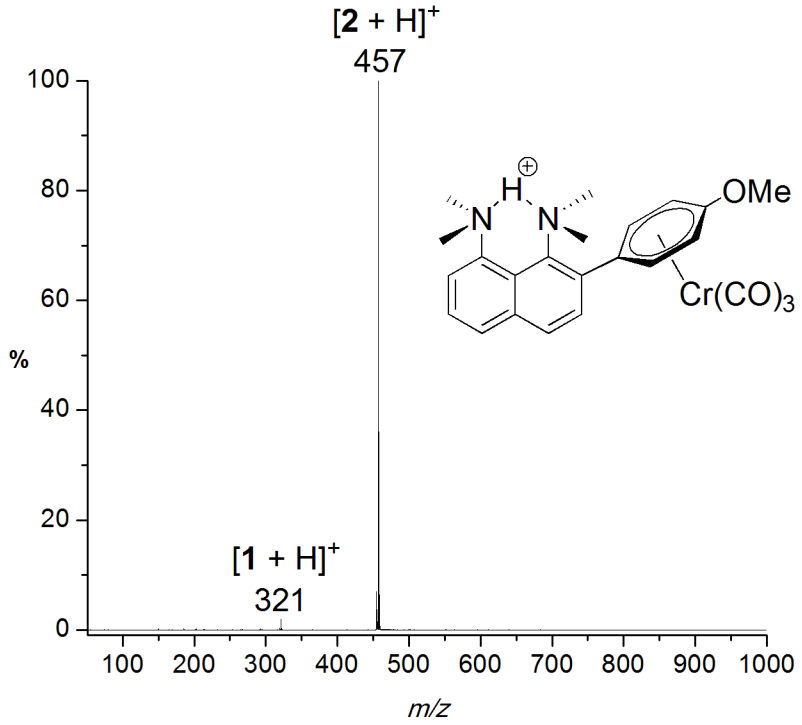

Figure 1.12: ESI(+)-MS of **2** chromium(**1**) tricarbonyl complex in methanol ([M + H]$^+$ = *m/z* 457). A small amount of free ligand **1** is also observed ([M + H]$^+$ = *m/z* 321). Reprinted with permission from "1,8-Bis(dimethylamino)-2-(4-methoxyphenyl)naphthalene: An electrospray-active analogue for η^6-coordinating ligands" K. L. Vikse, S. Kwok, R. McDonald, A. G. Oliver and J. S. McIndoe, *J. Organomet. Chem.*, **2012**, 716, 252-257. Copyright © 2012, Elsevier.

Care must be taken in designing of a tag, otherwise the tag could interfere in reaction mechanisms. Our group shows a nice example for a non-innocent proton sponge ligand. Proton sponge derivatized phosphines are appropriate ligands for ESI-MS investigation. We showed that 2-substituted proton sponge phosphane, in which the two functional groups are adjacent, is undesired ligand, because dimethylamino group can bond with metal in the complex and hence not monodentate. MS/MS experiment on the complex gave the evidence of strong N-Ru bond (Figure 1.13). Appending phosphane in the 4-position of the naphthalene ring avoids this interference. [98]

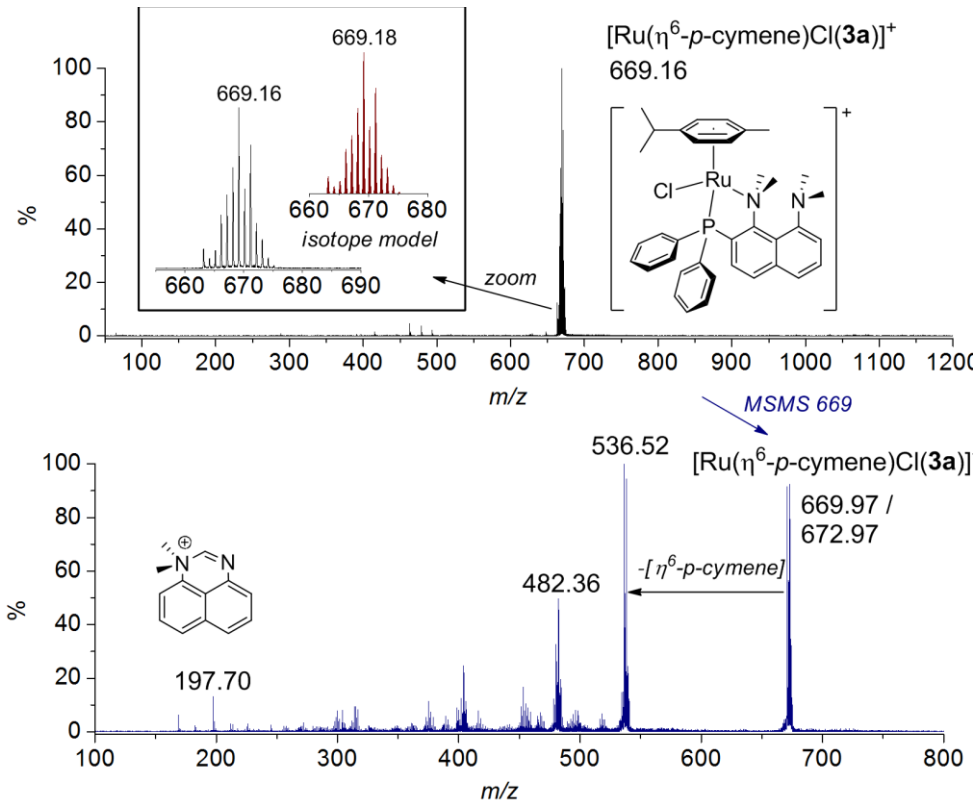

Figure 1.13: ESI(+)-MS (top) and MS/MS (bottom) of [Ru(η^6-p-cymene)Cl(**3a**)]+. Loss of *p*-cymene instead of loss of **3a** is strong evidence that **3a** is strongly bound and thus not monodentate. Modified from reference 98.

1.2 Continuous reaction monitoring

Most of studies mentioned so far involved sampling of reactions at certain intervals and injection of the sample to the ESI-MS to analyze the composition of the reaction mixture at different reaction times. One step ahead of this would be monitoring the reaction as it progresses continuously. Such an approach allows tracking the key intermediate behaviour over time but also can provide the kinetic information on the overall reaction. There are several recent organometallic studies[6, 14, 95, 99], one related micro-review[100] and a book[101] by Santos discussing online ESI-MS studies of mainly organo-catalyzed reactions but also contain organometallic examples.

One of the early studies was reported in 2006 by Enquist in which an oxidative Heck-type reaction was sampled at intervals and intensity responses of observed intermediates were plotted.[6] In 2010, the quaternary ammonium, charged substrate (*p*-iodophenyl)-

trimethyl-ammonium iodide ($[ArI]^+[I]^-$) was employed in a palladium-catalyzed Negishi reaction.[99] Reaction mixtures were drawn into a syringe and injected constantly into the mass spectrometer (Figure 1.14). The only observed species (except reactant and product) observed was $[PdL_2Bn]^+$, and no organozinc species was detected.

The graph of relative intensity against time is obtained for reactant and product for two different catalyst loadings. The high noise level is the result of inherent instability of the ESI process according to the author‘s statement. However, we have not found noise problematic in our study. In spite of low signal to noise, they managed to observe the effect of reagent concentration and catalyst loading on reaction rate.

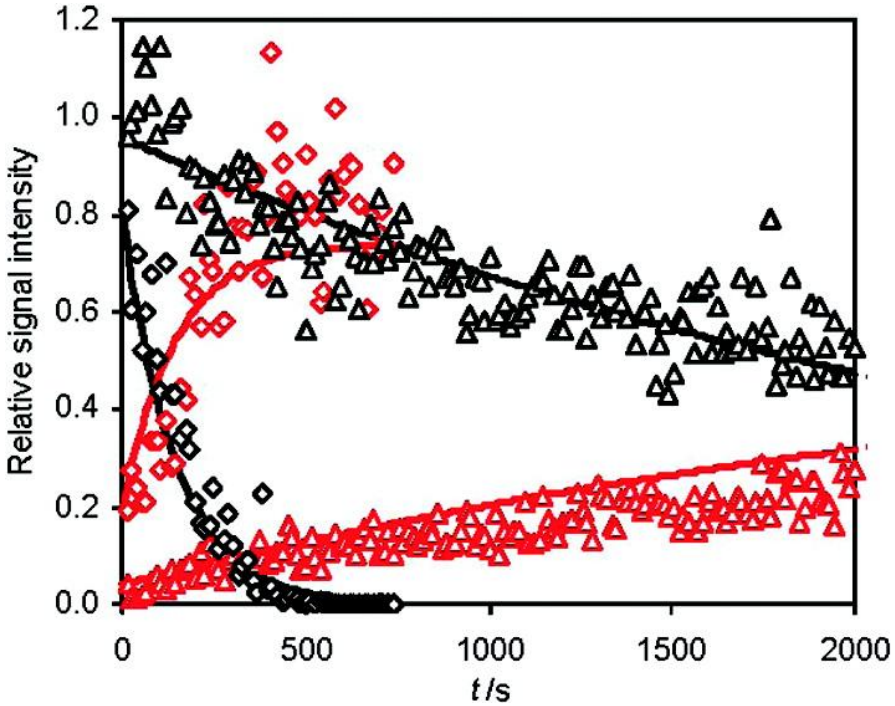

Figure 1.14: Time dependence of the normalized signal intensities of $[ArI]^+$ and $[ArBn]^+$, (red) formed in the Pd-catalyzed reaction with BnZnBr in CH_3CN at room temperature. Results of two experiments with different catalyst loadings are shown ([cat] =100 mol %, 4.5 mol%).The solid lines represent simulated time profiles based on a second-order rate constant. Reprinted with permission from “Charged Tags as Probes for Analyzing Organometallic Intermediates and Monitoring Cross-Coupling Reactions by Electrospray-Ionization Mass Spectrometry” M. A. Schade, J. E. Fleckenstein, P. Knochel and K. Koszinowski, *J. Org. Chem.*, **2010**, 75, 6848-6857. Copyright © 2010 American Chemical Society.

The mechanism of Wilkinson's catalyst action on a dialkylsilane was examined by our group in collaboration with the Dr. Lisa Rosenberg group from University of Victoria. Unlike the previous example, in which the reactant and the product were monitored, reaction intermediates were monitored by using time-resolved ESI-MS and the charged phosphine ligand $[Ph_2P(CH_2)_4PPh_2(CH_2Ph)]^+[BF_4]^-$ as an ESI lever (tag).[95] Equimolar solutions of $RhCl(PPh_3)_3$ and $(n\text{-hexyl})_2SiH_2$ containing tagged ligand were constantly introduced into the MS by a syringe from a syringe pump located in an adjacent glovebox. ESI data, not only confirmed the speciation of the reaction obtained by NMR, but also identified a few other species in the reaction. Moreover, behaviour of the species over the time (Figure 1.15) led to proposal of the dehydrocoupling mechanism of silane and competing decomposition pathway which is the result of trace water in the reaction mixture (Scheme 1.19).

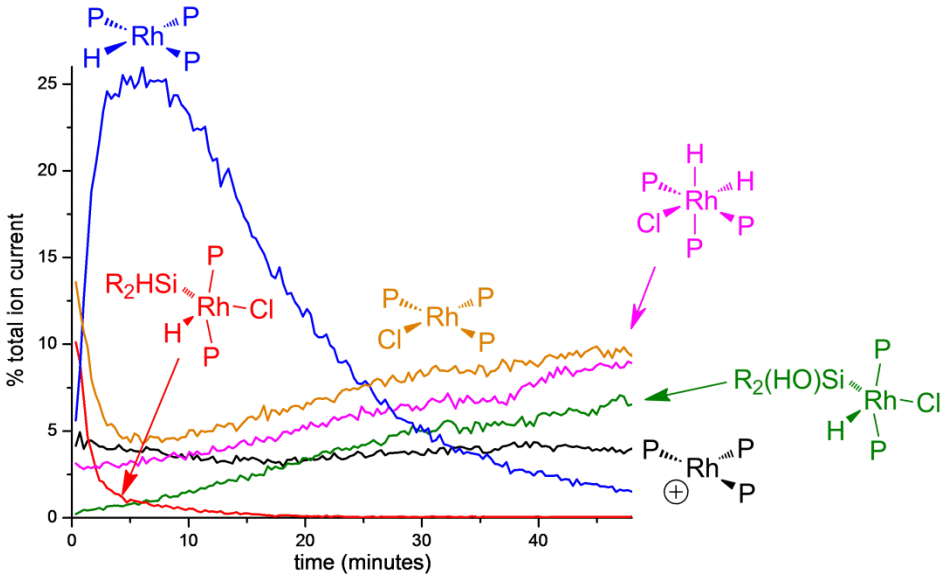

Figure 1.15: Reaction profile of the six Rh-containing species observed over time by ESI-MS. Each trace is generated by normalizing of each species to the total ion current. Inset: $\ln[RhHP_3]$ vs. time for the consumption of this species, representing first-order kinetic. Modified from reference 95.

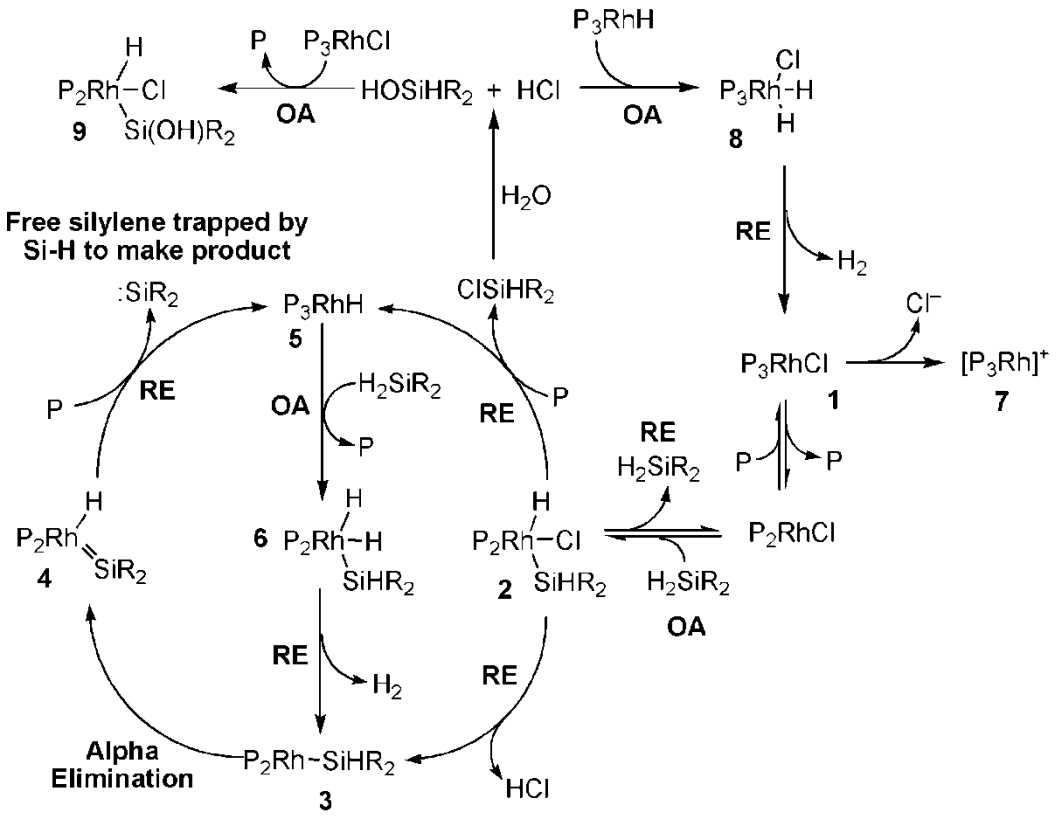

Scheme 1.19: Direct observation of numbered species by ESI(+)-MS and NMR results led to proposal of a reaction mechanism for dehydrocoupling of silane catalyzed by Wilkinson's catalyst. Modified from reference 95.

Mechanism investigation of the Pauson-Khand reaction is another example.[102] Although only one single intermediate was observed (Figure 1.16), energy dependent electrospray ionization (EDESI) as well as positive values for activation enthalpy and entropy are in good accordance with the ligand dissociation step being turnover limiting. Synthesis of the charged quaternary ammonium substrate for the intramolecular Pauson-Khand reaction and observed intermediate are shown in Scheme 1.20. The behaviour of reactant, product and intermediate is shown in Figure 1.16. Visibility of reactant and product allowed to perform the reaction at different temperatures which gave enthalpy and entropy of activation for this reaction.

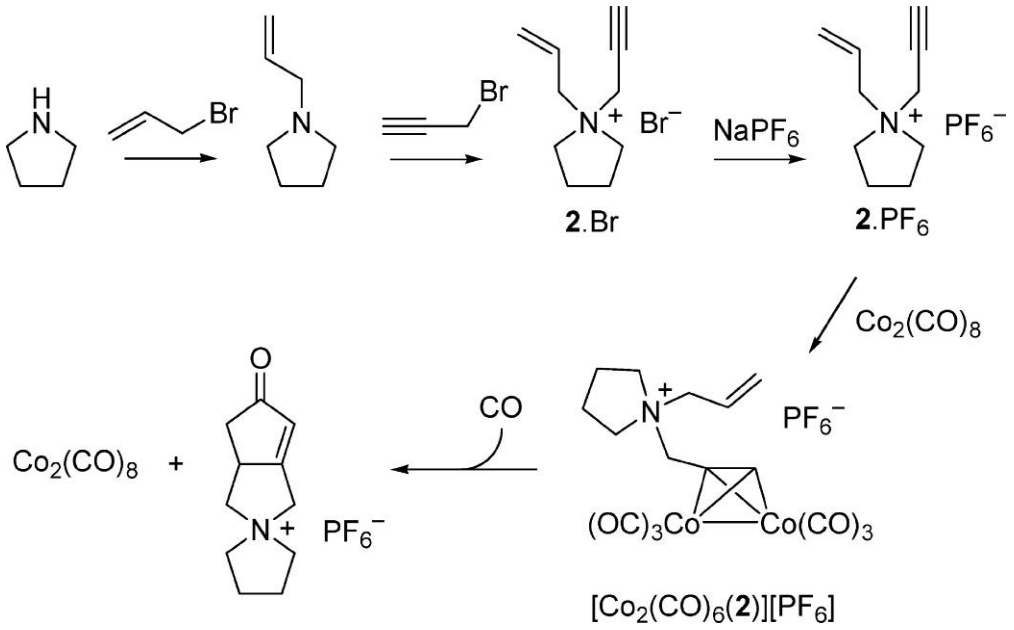

Scheme 1.20: Pathway of charged substrate for intramolecular Pauson-Khand reaction and observed intermediate by ESI(+)-MS. Reprinted with permission from “The Pauson-Khand Reaction: A Gas-Phase and Solution-Phase Examination Using Electrospray Ionization Mass Spectrometry” M. A. Henderson, J. Luo, A. Oliver and J. S. McIndoe, *Organometallics*, **2011**, 30, 5471-5479. Copyright © 2011 American Chemical Society.

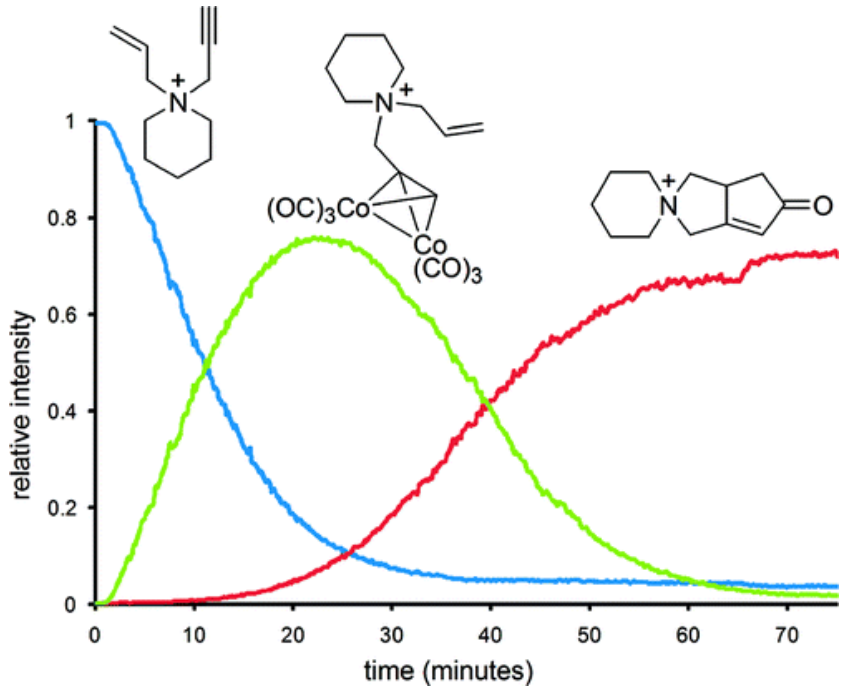

Figure 1.16: Relative intensity starting material, intermediate, and product. System was pressurized with CO gas and sample infused with online dilution with acetone to the source of ESI-MS. Reprinted with permission from "The Pauson-Khand Reaction: A Gas-Phase and Solution-Phase Examination Using Electrospray Ionization Mass Spectrometry" M. A. Henderson, J. Luo, A. Oliver and J. S. McIndoe, *Organometallics*, **2011**, 30, 5471-5479. Copyright © 2011 American Chemical Society.

1.3 Conclusion

It is clear that with recent methodological developments, ESI-MS is becoming a powerful tool to study organometallic systems. Investigation of already charged systems are straightforward and tagging methodology, online sampling and gas phase reactivity have opened new avenues to study the systems otherwise difficult to study by other means. In fact, mass spectrometry aims to fill up the gap between solution phase and theoretical studies. However, yet there are obstacles to be overcome to ensure organometallic chemists about the reliability, quantification of data, accommodating air and moisture sensitive systems and new methods to obtain kinetic data by ESI-MS. The work in this thesis aims to address these common concerns and to develop powerful new methods for studying solution-phase reaction mechanisms.

Chapter 2 Techniques and methodologies

2.1 Introduction

Catalysts transform one material to another by decreasing the energy barrier between the reactant and the product. A catalyst provides an alternative (usually more complicated) path with lower activation energy for this purpose. For each metal-catalyzed reaction a catalytic cycle is constructed which represents an educated guess about the route taken for the transformation of reactants. In many cases active intermediates are not observed since they are short-lived and their existence must be inferred based on relevant observations. Also the activity of the catalyst cannot be inferred by the cycle. For each efficient cycle several other side reactions may be involved which the sum of all only can define the portion of catalytic activity. Activation of precatalyst, catalyst solvation, product inhibition, dimerization, decomposition and agglomeration are some of these problems.[103] To have a more complete picture of a catalytic system rather than just understanding the main steps, these side reactions must be addressed. Because not all the species and interactions are detectable with one method or instrument, revealing a reaction mechanism is not straightforward and usually requires employing several methods of analysis. Fortunately there are many techniques and methodologies that lend themselves to study catalytic systems. Nuclear magnetic resonance (NMR) is probably the most important of these. Many of the elements in the periodic table have a spin-active isotope in adequate abundance to give a detectable signal. It is not hard to find an active isotope nucleus in most organometallic precatalysts, and ^{13}C, ^{1}H and ^{31}P are most commonly used. The quantitative nature of NMR as well the ability to conduct experiments across a wide range of temperatures makes it a reliable candidate for kinetic study. Chemical shifts, splitting patterns and coupling constants are the NMR tools for identification of species qualitatively whereas peak intensity is used for quantification. Isolation and characterization of intermediates by X-ray crystallography and NMR and further reactivity investigation is also a conventional method in the field. Kinetic studies using techniques that measure concentration against time (IR, UV/Vis, refractive index, volumetric gas evolution, GC/MS, etc) also greatly assist mechanistic investigations. By variation of reaction condition and concentrations important information about the

reaction mechanism can be obtained. Finally it should be noted that there is no technique which can singly illustrate a reaction mechanism completely and there are specific limitations and concern for each technique. In this thesis we aim to show the strengths of ESI-MS in the study of organometallic catalytic systems and to address some technical limitation of ESI-MS that have reduced the technique to a minor player in the field.

2.2 A brief history of mass spectrometry

Mass spectrometry has become a ubiquitous technique in the field of chemistry for both qualitative and quantitative analysis. This technique owes its maturity to many contributors over the past century. The main principle goes back to the early 1900s when Wilhelm Wien[104] controlled "negative rays" with electrical and magnetic field. He extended his work to separate positively charged rays and eventually measured their mass to charge ratios. In 1913, J.J Thomson took the initiative by showing that neon was composed of two different particles of different mass. He used the combination of electrical and magnetic field to separate the two isotopes of neon (^{20}Ne and ^{22}Ne).[105] In 1918, Arthur Dempster took one more step toward creation of the mass spectrometer by designing the first instrument which was similar to a modern instrument.[106] He used electron ionization (EI) as an ionization method in his experiment. In this method, a metal filament is heated intensively to emit continuous free electrons. Emitted electrons are accelerated by applying a voltage and the vaporized analyte is introduced to the source of instrument.[107, 108] It is the oldest and widely used method which has been improved constantly ever since. Nevertheless, a major drawback; fragmentation of ions and loss of valuable species due to collisional impact between highly energized electrons and analyte, persuaded scientists to seek for "softer" ionization methods.

Several soft ionization methods were invented and spread in the past few decades that have had huge impact in study of delicate and/or large molecules such as organometallic compounds, biomolecules, proteins and peptides. Chemical ionization (CI) was the first soft method developed by Munson and Field in 1966.[109] Instead of directly ionizing the analyte by highly energized electrons as in EI method, a reagent gas such as methane is

ionized in the source. Reaction of the resulting radical cation with further neutral gas molecules generates methyl radicals (which are pumped away) and $[CH_5]^+$, which is an exceedingly strong acid that will readily protonate almost any molecule it encounters in the gas phase (Scheme 2.1).

$$CH_4 + e^- \longrightarrow CH_4^{\bullet +} + 2e^-$$

$$CH_4^{\bullet +} + CH_4 \longrightarrow [CH_5]^+ + \dot{C}H_3$$

$$M + [CH_5]^+ \longrightarrow [MH]^+ + CH_4$$

Scheme 2.1: Mechanism of carbonium ion formation and its collision to another methane molecule leading to proton transfer in chemical ionization process.

In late 1980 two other soft ionization methods were evolved, electrospray ionization (ESI) and matrix assistance laser desorption ionization. Both quickly became popular in chemical analysis, so that two main contributors, Tanaka[110] and Fenn[111, 112] were awarded a quarter share each of the Nobel prize for Chemistry in 2002 for their achievements in this area (MALDI and ESI respectively).

In MALDI, the analyte is dissolved and co-crystallized in an organic matrix. A suitable matrix is an organic molecule with a UV chromophore (usually an aromatic acid).[113] A high intensity laser beam is focused on the matrix, which is blasted into gas phase with the analyte and matrix molecules to gas phase. In a process like CI, ionization occurs by abstraction of proton by analyte from the matrix. In fact, the matrix has a dual purpose in this process; absorption of the radiation and dilution of the analyte to avoid analyte fragmentation. MALDI has found applications in study of large molecules (masses up to >300 000 *m/z*)[114, 115] specifically for biomolecules due to softness, high sensitivity and easy sample preparation.

ESI was invented by Dole[116] in the 1960s, however it was Yamashita and Fenn who improved the technique and used it to ionize large molecules. This method of ionization conveys very little increase in internal energy to the ion itself; the energy is instead

consumed for evaporating the solvent, and hence ESI is one of the softest of ionization techniques. [117]

2.3 ESI-QToF-MS

2.3.1 The electrospray ionization process

During the ionization process analyte ions in solution are introduced to the source of instrument usually by a syringe pump. A flow of about 10 microliters per minute is sufficient for this purpose; however the process is tolerant to variation of this flow to some extent (5-50 μL min^{-1}; much lower for nanospray sources). A potential of about 3 kV is applied to the capillary which oxidizes (when positive charge is applied) or reduces (when negative charge is applied) the counterion of the analyte ion (other processes are possible: oxidation of the stainless steel capillary; oxidation or reduction of the solvent; and in some cases, oxidation or reduction of the analyte itself).[118] This electrochemical process imposes an excess of positive or negative charge to the solution, upon departing the capillary. Also, the solution is subjected to a current flow (100 L min^{-1}) of hot desolvation gas (usually N_2). The charged capillary in conjunction with the desolvation process generate a beam of mist that emerges from the Taylor cone.[119] There are two mechanisms through which single ions are formed from fine droplets: ion evaporation[120] and/or Coulombic explosion (Figure 2.1).[116] There are still debates around which mechanism generates the ions, in ion evaporation as the solvent evaporates, shrinking the surface area enforces the ions to evaporate excessively from the droplet surface, while in Coulombic explosion, exceeding the charge to surface ratio in the droplet leads to repulsion of ions in droplets repeatedly until single ions formed. A study performed in our group on lanthanide water clusters illustrated that ion evaporation is more favorable in this case.[121] Whatever the mechanism is, ESI generates ions with very little or no fragmentation. [122]

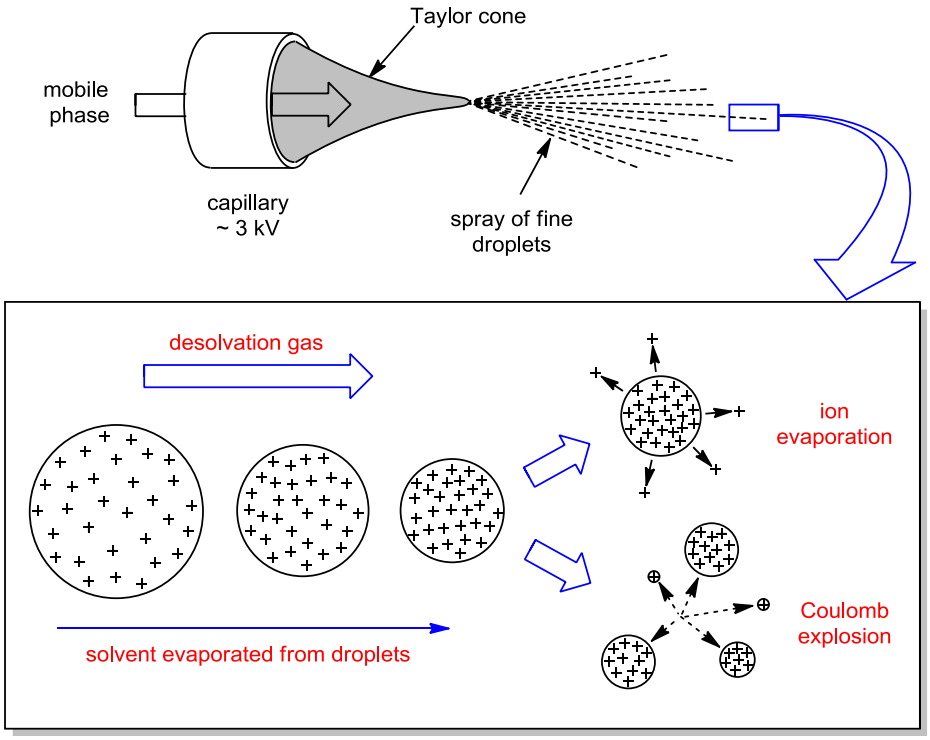

Figure 2.1: The process of electrospray ionization. Modified with permission of the author from Henderson, W., McIndoe J. S., *Mass Spectrometry of Inorganic and Organometallic Compounds*. John Wiley & Sons, Ltd. West Sussex: 2005, p. 92.

2.3.2 Q-Tof Micro

A Micromass Quadrupole Time of Flight (Q-Tof) Micro tandem mass spectrometer was the mass spectrometer used for all the research in this thesis. The source is under atmospheric pressure, but the rest of the system is differentially pumped and the analyzers and the detector are under very low pressures (~2×10^{-7} mbar for the ToF chamber).

In the source droplets produce single ions by means of solvent evaporation and high voltage. The gas phase ions are drawn into the instrument, perpendicular to the direction of the spray, through the sample and skimmer cones by means of applied voltages and pressure differential (from atmospheric pressure down to 10^{-2} torr). There is another flow of heated gas (cone gas) which is introduced to the interior of the sampling cone to ensure complete analyte desolvation. The solvent is pumped out (pressure about 1 torr) from the

inside of the first chamber and the ions are drawn into the main part of the instrument through a hexapole ion guide (Figure 2.3 c). This particular configuration is called the "Zspray™" source in Waters/Micromass mass spectrometers. The Z-shaped pathway of the ion beam ensures the minimum amount of neutral molecules and solvent entering to the instrument and hence decreases the background noise (Figure 2.2). [123] In hexapole, ions are focused into a beam that is fed into the first mass analyzer, a quadrupole. It consists of four parallel metal rods. Combinations of DC and radiofrequency AC potentials are applied to the rods in pairs. The result of this dynamic field is that only ions with specific *m/z* can be passed through the quadrupole and any ions beyond the range of interest will collide with one of the rods and be discharged (Figure 2.3).[124]

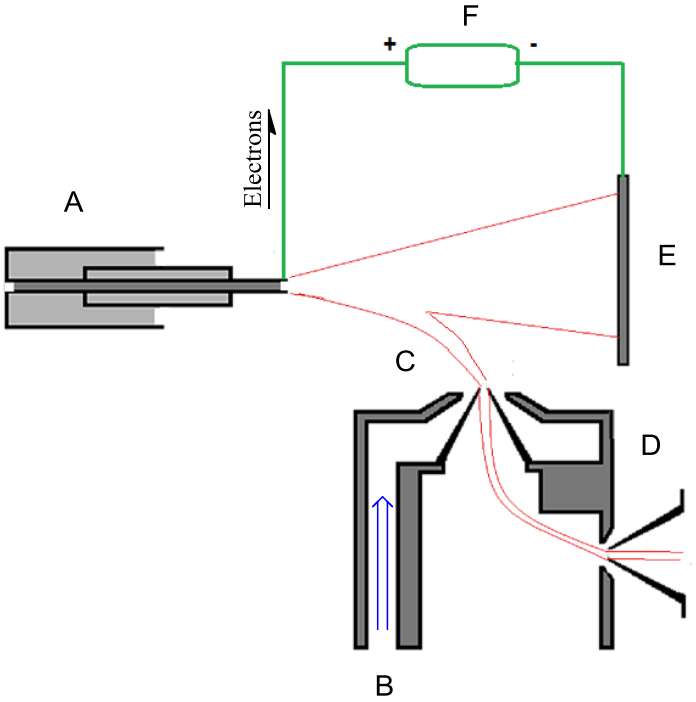

Figure 2.2: Schematic of the source of ESI-MS. **A**. ESI capillary, **B**. inlet for cone gas, **C**. sampling cone; **D**. extraction cone, **E.** baffle.; **F.** power supply. Modified from reference 123.

The range of scans is from *m/z* 50 to *m/z* 4000, however to study most of the organometallic compounds, up to *m/z* 2000 is the optimum range. There is a collision cell (at a pressure of about 10^{-3} torr) between the two analyzers that allows for fragmentation of selected ions. In normal experiments the collision cell just guides the ions to the second analyzer. In MS/MS experiments the voltage across the collision cell is increased to

fragment the ion of interest. The second analyzer is an orthogonal time of flight mass analyzer (TOF). Incoming ions are momentarily exposed to perpendicular gradient of an electric field. This process makes a "pulse" of ion beams that travels down the flight tube. To correct for differences in the initial kinetic energy of ions with same *m/z*, a reflectron (a series of gradient strong electric field acting like a mirror) repels the ions while they are reaching the end of the flight tube. This process redirects the ions toward the detector and ensures that the ions with the same mass to charge reach the detector at the same time regardless of their initial kinetic energy.[125]

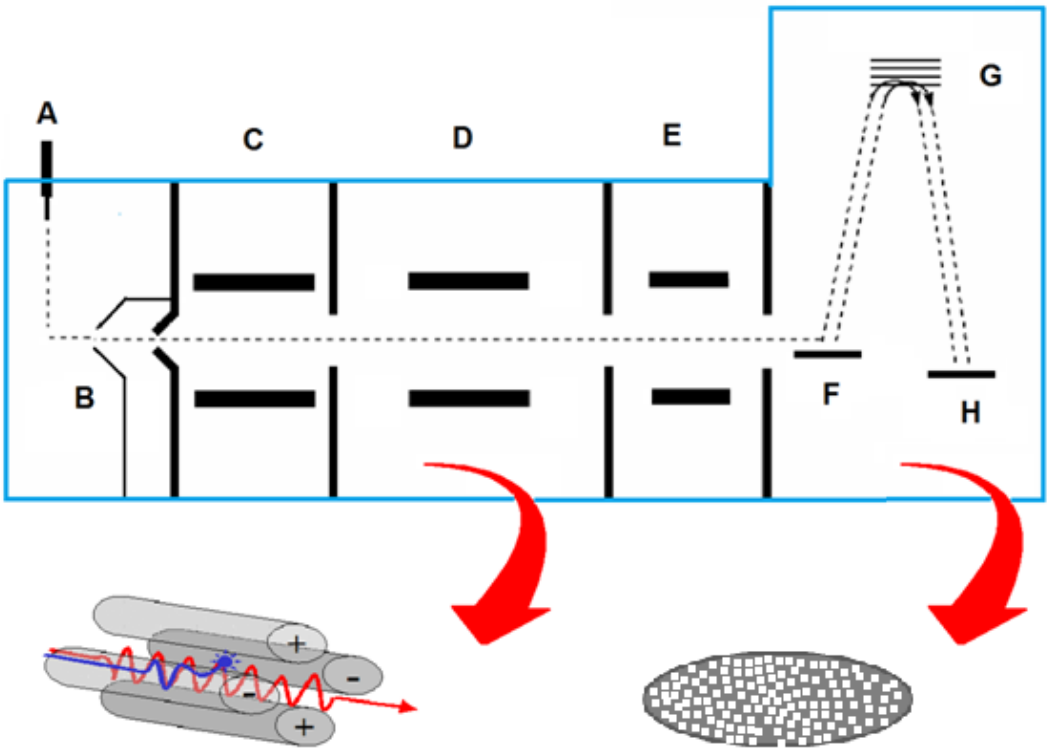

Figure 2.3: Block diagram of the Q-Tof mass spectrometer. **A**. ESI source; **B**. cone; **C**. hexapole ion guide; **D**. quadrupole mass analyser; **E**. hexapole collision cell; **F**. pusher; **G**. reflectron; **H**. MCP detector. Bottom left shows the quadrupole mass analyzer showing the trajectory of two ions with different mass-to-charge ratios. Bottom right shows a cartoon of MCP.

This correction maximizes the resolution of the final spectrum. All ions are subjected to the same amount of energy in each pulse upon arrival in TOF, so they have the same amount of kinetic energy regardless of their masses. Based on the Newtonian formula for kinetic energy ($E_k = ½mv^2$), ions with different masses will have different velocities.

Given that energy and length of flight tube (~ 1 m in this instrument) is constant, the mass to charge ratio of each ion can be determined by the time taken to reach the detector. Thus different ions are separated based on their arrival times at the detector. The microchannel plate detector (MCP) is an planar component consists of thousands of electron multipliers. When an ion impinges on any of these multipliers, a cascade of electrons is released that finally generates a greatly enhanced electrical signal. One pulse only contains a few ions. However, tens of thousands of spectra are collected per second and summed to give good overall intensities. Higher scan times gives greater signal-to-noise ratio (which increases with the square root of the number of scans).

2.3.3 Experiment types by mass spectrometry

There are several common types of MS experiment performed in our research group. First and most common is the standard MS experiment. Solution is introduced to the source of the instrument, subjected to optimized ionization condition (flow rate = 10 μL/min, cone voltage = 3 kV, collision voltage = 2 V, heated desolvation gas). These conditions vary depending on the nature of analyt. Ions enter the high vacuum area and pass through the quadrupole analyzer, no ion selection is required in this case and the analyzer lets all ions enter the collision cell and reach the TOF analyzer. Ions with different *m/z* are separated in the TOF analyzer and finally detected at the MCP. Under normal conditions we collect one spectrum per second and the inter scan time is one-tenth of a second.

In some cases the mass spectrum alone (*m/z*, isotope pattern) is not conclusive enough to identify an ion structure. In this case further information is required to assign a structure. Collision induced dissociation (CID) is another common experiment by mass spectrometer. There are two types of CID experiments. For a simple reaction mixture, when there are one or two types of analyte ions, CID can simply be performed by increasing the cone voltage in the source (in-source CID),[119] the optimal voltage lying in the range of (10 - 50 V). In this case fragmentation is the result of collision between heated nitrogen gas and excited analyte ions. In-source CID is not a suitable method for complex solutions with many ions. In this case another type of CID, a product ion MS/MS experiment is preferred. As in a normal MS experiment, ions are introduced to

the quadrupole analyzer, however this time the analyzer only allows ions of a specified *m/z* ratio to pass through the collision cell and the rest of ions are excluded from the analyzer. Ions are accelerated through the cell and collisions occur between argon gas and the energized ion. Fragments (product ions) are separated by TOF and detected at the MCP. These types of CID experiment provide useful structural information and help to assign the unknown ions.

Energy dependent electrospray ionization (EDESI) is a sophisticated CID experiment.[126] In this MS/MS experiment the full range of CID voltages is applied to the collision cell and fragments are collected as a spectrum (the experiment may also be run as an in-source CID experiment). The voltage is gradually increased over time and as a result ion fragments are collected in a plot with respect to collision voltage. The same experiment can be performed by variation of cone voltage in in-source CID experiment. This technique gives the information of required relative energy for dissociation of each fragment from the ion of interest. This sequential fragmentation gives a qualitative indication of bond strengths in an ion. The weakest bonds break first and the strongest last. Figure 2.4 shows an example of in-source EDESI study of a ruthenium carbonyl complex.

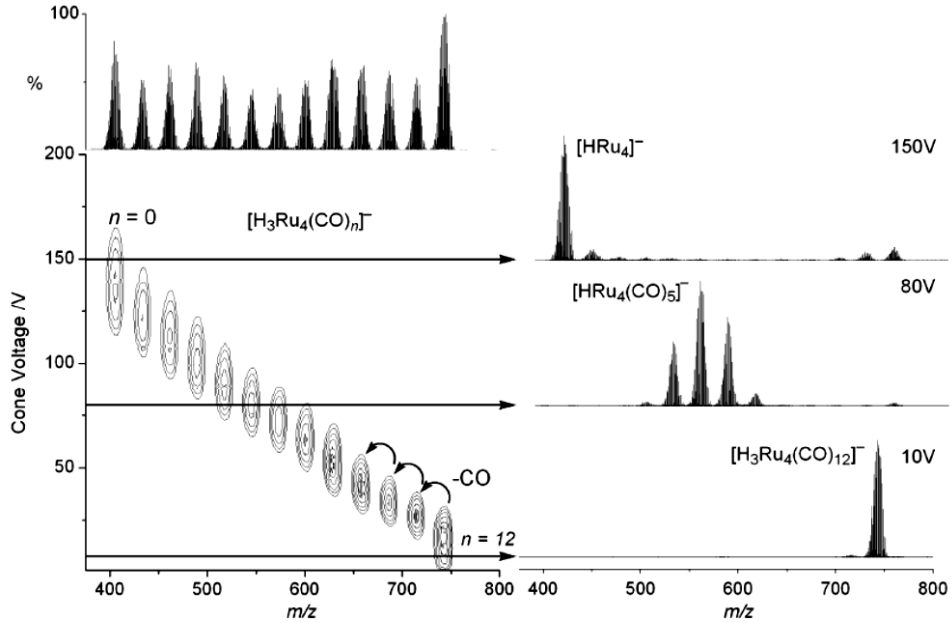

Figure 2.4: The left-hand contour plot of $[H_3Ru_4(CO)_{12}]^-$ clearly shows the loss of all CO ligands as the cone voltage is increased. Right snapshots show the ligand dissociation at three different voltages. Reprinted with permission from "Gas-phase reactivity of ruthenium carbonyl cluster anions" M. Henderson, S. Kwok and J. McIndoe, *J. Am. Soc. Mass Spectrom.*, **2009**, 20, 658-666. Copyright © 2009, American Society for Mass Spectrometry.

2.4 Numerical modeling

Powersim[a] is a program with a graphical interface for modeling nonlinear dynamics, widely used in business simulation. Although Powersim does not incorporate molecular structural information and cannot predict the molecular interactions, still it can be employed to model our kinetic information obtained by the PSI-ESI method. Instead of regarding the compounds as chemicals, blocks are considered symbolically for each species in the feature. There are a few reports using Powersim to extract kinetic data previously: alkoxyamine isomerization, addition reaction and polymerization[127], styrene polymerization[128, 129] and one report mentioned Powersim as the numerical modeling program they employed, without any details.[130] In Figure 2.5 the experimental data were determined by EPR experiments and the equilibrium rate constant was then determined by fitting the simulated data to the experimental data.[128]

[a] http://powersim.com/

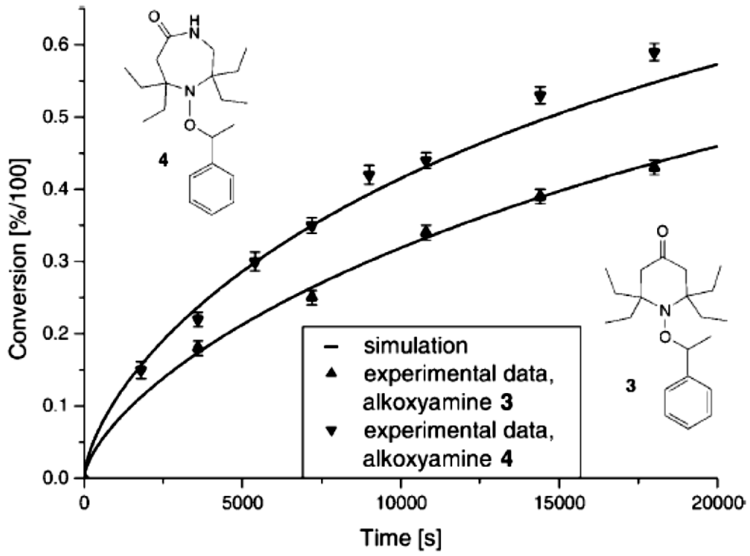

Figure 2.5: Equilibrium rate constant determination for two initiated styrene polymerization by graphical overlay of the simulated plot over the experimental one. Reprinted with permission from "A New Sterically Highly Hindered 7-Membered Cyclic Nitroxide for the Controlled Living Radical Polymerization" C.-C. Chang, K. O. Siegenthaler and A. Studer, *Helv.Chim. Acta*, **2006**, 89, 2200-2210.Copyright © 2006 Verlag Helvetica Chimica Acta AG, Zürich, Switzerland.

Previously we used Maple[a] software (version 14, Maplesoft Inc) for simulating our catalytic cycles, and then we replaced it with Powersim due to its conceptual simplicity and graphical interface which makes it more user-friendly software compared with Maple. Initially simulated results of the Sonogashira reaction (Scheme 2.2) were compared[b] in Maple and Powersim with specific rate constants to ensure the accuracy of results. This comparison represented that results are in good accordance and we can substitute Maple with Powersim confidently (Figure 2.6). Powersim has several key components for simulation of a system. These components are conceptually simple, however by increasing the number of steps in a cycle, it is converted to very complicated system and hence care must be taken to avoid uncompleted model design.

[a] Maple models were constructed by Dr. David Harrington for Sonogashira reaction.

[b]This study was performed by Wu WenZhao (Tony) as an undergraduate student 2012.

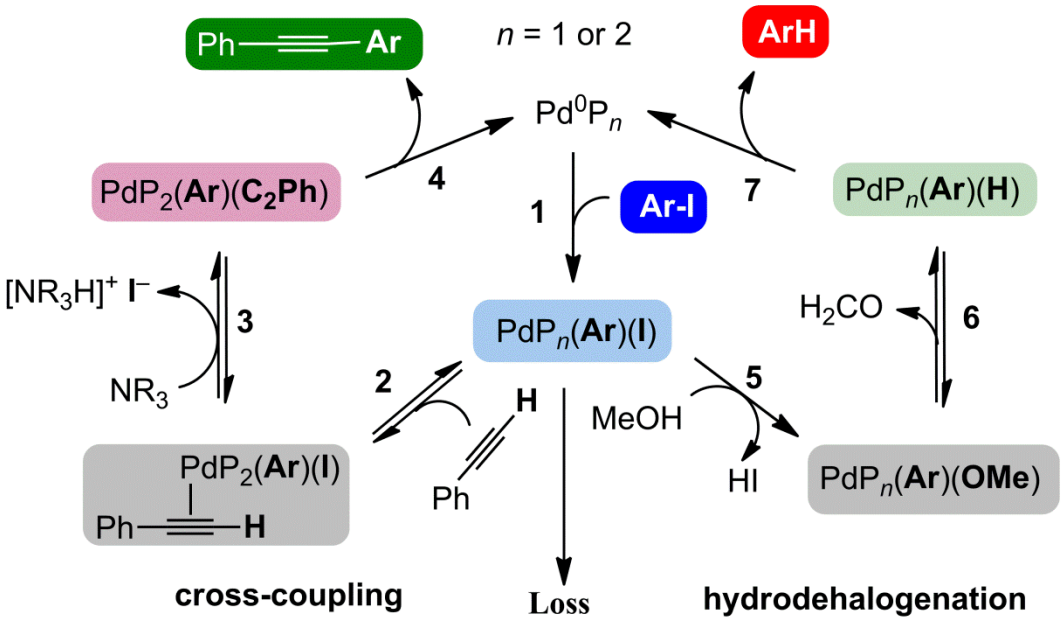

Scheme 2.2: A Sonogashira reaction and hydrodehalogenation (as the side-reaction) mechanism. A step was included as the "loss" which represents the decomposition of PdP_2ArI.

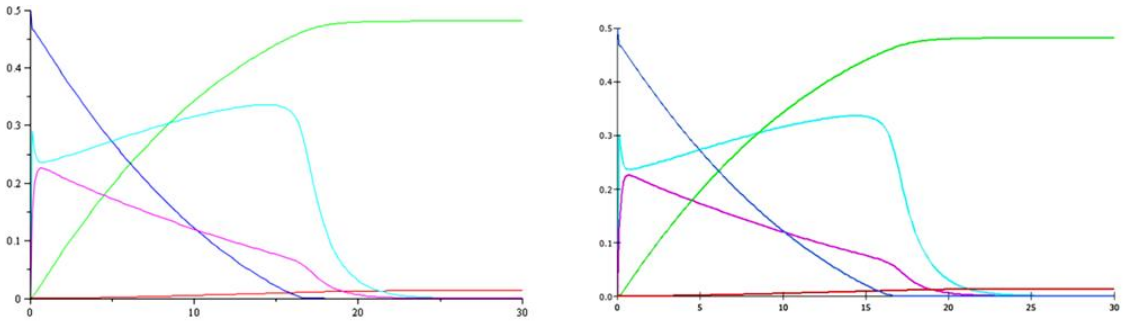

Figure 2.6: Simulated models for Sonogashira reaction constructed by: (left): Maple (right) Powersim.The same responses in both ensure the data validity obtained by Powersim software.

Level is the first key component in Powersim. Each species regardless of the nature and reactivity is defined as a level. Level can accumulate its value over time, this value can be altered by the input and output flow. We use level to represent the concentration of each species in our catalytic system. A rectangle is the symbol of this variable. It is defined in a way that its concentration cannot be lower than zero (acting as a reservoir). Since in kinetic study level represents concentration variation over time, level unit is

defined as molarity/second. Other forms of concentration and time units are applicable depending on the range of concentration, reaction rate, etc.

Another variable in this feature is flow. As its name indicates, it demonstrates the flow in and out of each level and it is symbolized by an arrow. In fact it shows the logical pathway of transportation between levels but it is unable to control the rate by itself. This function does not carry any unit.

Auxiliary (represented by a circle) is the algebraic computation zone of other inputs. From kinetic point of view, it defines the rate of reaction at each time step by multiplying the related concentration of involved species and rate constant. Data are input to auxiliary by links. Reaction rate is calculated at each time step (could be at beginning or the end of step). Unlike level variable, auxiliary does not accumulate the data. The unit of auxiliary depends on the number of levels. For one level, it corresponds to first order kinetic so the unit will be concentration over time. There is another variable named “Flow with Rate” which is the combination of a flow and an auxiliary. This variable exerts both these functions at the same time.

Constant (represented by a diamond) is a parameter which its value is constant and it is defined initially in the simulation. As opposed to level, constant value is fixed throughout. In a catalytic system, constant refers to the rate constant. Its unit also depends on the number of levels involved in the rate of that step. When no level is involved in reaction rate (zero order regime) unit of rate and rate constant are equal.

Information link or simply “link” (represented by a one way arrow) is the last key component in Powesim software. Link indicates that the variable at the tail of the line feeds the variable at the head (arrow) of the link. In the simulation of catalytic systems link essentially is used for two purposes; first to input the levels and constants values to auxiliary in order to define the reaction, second to control the flows in and out of the levels. Figure 2.7 represents an assembled model for a reaction in equilibrium where $A+B \rightleftharpoons C+D$ is applicable.

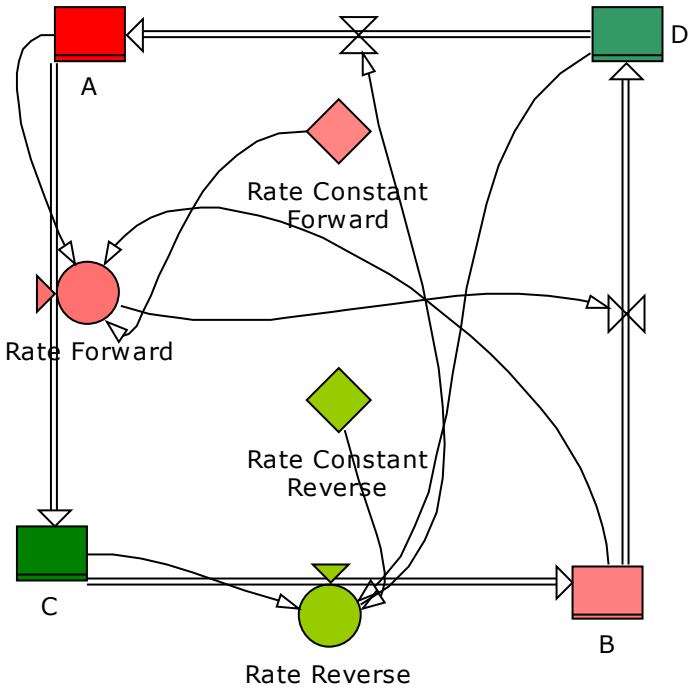

Figure 2.7: Constructed model for a generic reaction of A + B ⇌ C + D by Powersim program.

2.5 UV/Vis spectroscopy as a tool in kinetic and mechanistic study

2.5.1 Introduction

UV/Vis spectroscopy has been used for about four decades in general use and over these years it has become a standard analytical technique in research and industrial labs. No rival could be found for UV/Vis spectroscopy in terms of simplicity, accuracy, cost effectiveness and speed, even though in many other applications, other techniques may be used. UV/Vis spectroscopy has been used in variety of homogenous catalytic reactions, for characterization as well as kinetic and mechanistic studies, such as dehydrocoupling[131], Michael addition reactions,[132] hydrogenation,[133] oxidative addition,[134] and electrochemical oxidation.[135]As a part of this thesis we aimed to integrate UV/Vis spectroscopy, as a complement method with ESI-MS hoping that tandem techniques shed light into the systems where ESI-MS only is unable to provide a full assignment to homogenous catalysis.

2.5.2 From Reaction *in situ* to *Operando* methodology in catalysis study

Having an understanding of structure/activity/selectivity relationships is critical in designing of new and effective catalysts. Before jumping to study the application of "tandem" techniques in catalytic reactions, some terminology needs to be explained.

The term *in situ* (literally: in position) is used in different sciences including biology, chemistry, chemical engineering and so on. *In situ* generally means data collection in a *real environment* (i.e. no change in the medium). In chemistry specifically, it means in the reaction mixture. For instance when an intermediate is synthesized in situ it means due to its instability it can't be isolated or it is not convenient.[a]

Reaction in situ is a more specific term in chemistry that refers to *in situ* spectroscopic measurement under conditions relevant to catalytic operation. In this case, the spectra are collected under conditions relevant to catalytic operation (transient or steady state). It should be noted that many *in situ* reactor designs may not perfectly be appropriate for the kinetic study of true catalytic reaction because of many limitations in gas phase reaction, mass transfers and delay time in introducing sample into instrument.[136]

"*Operando"* methods take molecular level measurements of catalyst, reactants and products under practical conditions. Basically it means the simultaneous evaluation of structure and catalytic activity/selectivity.[137]

From different point of view operando gives a picture of catalytic structure and behavior over the course of reaction. This term was introduced in 2002 to explain a methodology that combines simultaneous *in situ* spectroscopy and kinetic measurements on the same sample at the same time. Operando is borrowed from a Latin which means *working'* or *operating* since the obtained spectra are the picture of *operating* catalyst, whereas *in situ* means *on site''*.[138] The number of papers published in the literature using the term ''operando catalysis'' since it was first proposed in 2002 shows an increasing interest in this term and techniques in catalysis study. Scifinder Scholar has 429[b] entries

---

[a] http://en.wikipedia.org/wiki/In_situ, aceess 5/20/2013.

[b] https://scifinder.cas.org, accessed on 5/20/2013

for papers employing this term, 85 papers from 2012, which shows the fast increasing popularity of this approach.

Observation of intermediates in any catalysis study could be very informative for reaction mechanism interpretation, but their lifetime is usually short. To date, NMR spectroscopy is the only commonly used method that gives simultaneous structural and kinetic information in real time for homogenous catalytic study ; but it has its own restrictions in terms of sensitivity for the observation of intermediates. So by using two or more instruments at the same time in which each method gives one part of information could compensate for the limitations of other methods and can give a better understanding of the reaction as a whole. To date, combinations of some techniques have been used with X-ray sources, such as EDE/FT-IR and EDE/Raman/UV/Vis which have proven their power in the study of heterogeneous catalysts.[139]

To see how the structural information is extracted about catalyst in real time by using UV/Vis a noteworthy example is presented here. *In situ* investigation of the oxidative addition in homogeneous Pd catalysts by synchronized time-resolved UV/Vis/EXAFS (extended X-ray absorption fine structure) is one of these examples. Oxidative addition of aryl halide is the first step of most cross coupling reactions. In a typical reaction, complex 1 (Scheme 2.3) was produced by mixing $Pd(dba)_2$ and two molar equivalents of PPh_3 in a solution of toluene and the oxidative addition reaction was initiated within the cuvette of a stopped-flow apparatus by injecting a solution of iodobenzene. The disappearance of the palladium complex was followed from the initial mixing. Figure 2.8 shows the sequential disappearance of absorption bands at 493 and 432 nm respectively that are assigned to the Pd complex. This disappearance occurs over 13 and 25 seconds respectively. Corresponding changes in the Pd K-edge of X-ray absorption near edge structure (XANES) were also measured at the same time. The results show that complementary and direct information obtained by time resolved energy dispersive (ED) is perfectly in accordance with those of UV/Vis observations. It should be noted that reaction is accelerated two times in the presence of X-ray which is confirmed by UV/Vis spectroscopy conducted with and without high energy X-ray beams. The increment of the reaction rate corresponds to a mild medium warming effect of X-ray radiation, but

doesn't damage the palladium complexes. It should be considered as a trade off for applying this technique.

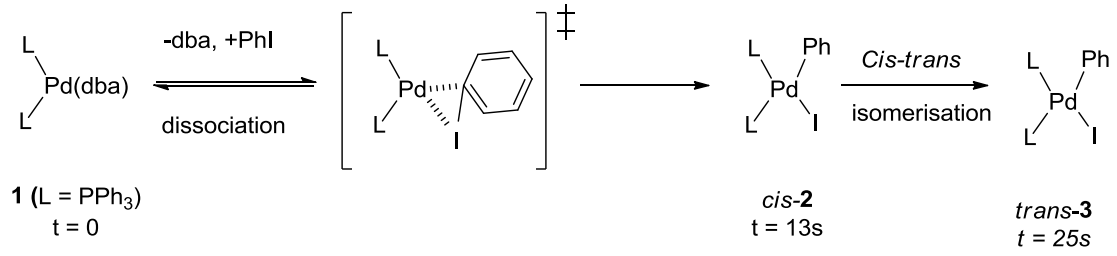

Scheme 2.3: Timescales of the oxidative addition and subsequent isomerisation. Redrawn from reference 140.

Oxidative addition of PhI to $[(PPh_3)_2Pd(0)(dba)]$ (**1**) occurred within 25 s, giving $[(PPh_3)_2PdPhI]$ (**2**) as the final product, based on changes in the XANES as well as EXAFS analysis. Other hypothetical models like triangular $[(PPh_3)_2Pd]_3$, trans-$[(PPh_3)_2PdI_2]$ or bimolecular $[(PPh_3)_2PdI]_2$, were considered in this reaction but none of them were matched with experimental spectra. So based on these evidences it is verified that mechanism has two distinct steps: first, OA of PhI on $[(PPh_3)_2Pd(dba)]$ in cis configuration, followed by *cis-trans* isomerisation. A shift in the XANES region indicated the change in oxidation state of Pd, continuous addition of PhI to the metal center, observed by EXAFS analysis and indirect UV/Vis as the loss of dba ligand, all are evidence for the OA process. The isomerisation is detected by the loss of the band based on phosphine ligand rearrangement in the UV/Vis spectrum which is qualitatively is in accordance with symmetrical change from *cis* isomer into *trans* isomer.[140]

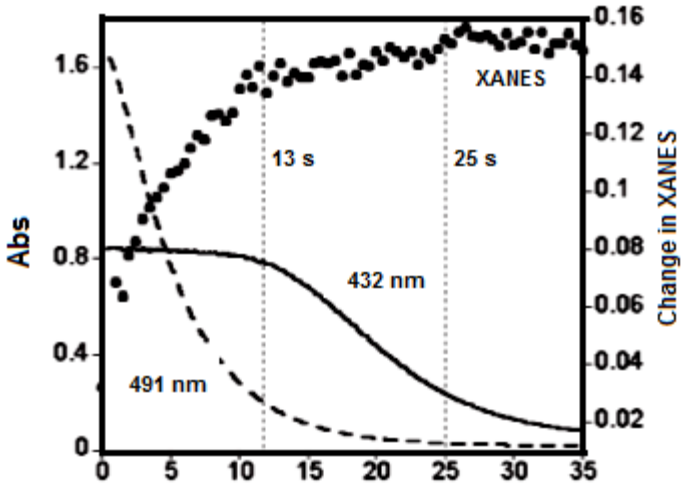

Figure 2.8: Real time monitoring of UV-Vis spectral bands (432 and 491 nm) and the related XANES data. 10 equivalents of PhI reacted with 40 mM $[(PPh_3)_2Pd(dba)]$ in toluene. Modified from reference 140.

Although the idea of tandem techniques or multi-operando seems interesting, there is challenging criticism about that. "*Why not simply doing one single experiment on different operando set-ups and then comparing the results*?" Technically speaking it is true, but we should keep this in mind that getting consistent reaction conditions may seem possible but in molecular level is very difficult. So having complementary real time information gives more confidence in interpretation of a catalyst behavior.[138]

Chapter 3 Method Development

Portions of this chapter have been previously published, and are reproduced in part with permission from "Pressurized sample infusion: an easily calibrated, low volume pumping system for ESI-MS analysis" KL Vikse, Z Ahmadi, J Luo, N van der Wal, K Daze, N Taylor and JS McIndoe, International Journal of Mass Spectrometry, **2012**, 323-324, 8-13, Copyright © 2012 Elsevier.

3.1 Introduction

Handling air and moisture sensitive reaction solutions especially for catalysis by ESI-MS has been a challenging task. Inside the MS instrument, the analyzers and the detector are located under vacuum so the inner part of instrument in not a concern. However, exposure of the solution is possible in the source and before the sample is introduced to the inlet of the ESI source. There are several methods employed by our group and others to keep the reaction mixture away from air and moisture. A conventional method is to use an airtight syringe containing the solution of the analyte and introduce it to the ESI-MS using a syringe pump. However, this system cannot be adapted to operate at different temperatures, not to mention that mixing the reaction mixture is not possible. Locating the syringe and the syringe pump into an air-tight chamber, preferably a glovebox, adjacent to the MS while solution is transferred to the source through a PEEK tubing is one solution. The Fogg group integrated a glovebox with MALDI-MS in 2008.[141] Our group has also integrated a glovebox with the ESI-MS so the sample can be introduced to the source of the instrument continuously.[142] However this method has also some limitations: the whole process is time consuming, it requires transferring the all of the reaction apparatus to the glovebox, and the method suffers from the lack of flexibility because it is hard to perform the reaction at elevated temperatures without a condenser in the glovebox.

The ESI source operates at atmospheric pressure and is not airtight. When the cone and desolvation gas is flowing, a slight negative pressure exists which can be overcome only when a very high flow of gas is running through the source (or when the exhaust vent is constricted. The source of the negative pressure is a function of the vacuum inside the

instrument and the low pressure of the waste air vent). The negative pressure implies that air and moisture can penetrate into the source and expose the analyte during the electrospray ionization process. Krista Vikse and Tyler Trefz from our group addressed this shortcoming by designing a modified source housing. An inlet and a pressure gauge were inserted into a Plexiglas source housing (a transparent cylinder approximately 15 × 15 cm). An overpressure of a few mbar prevents air leaking into the source. To confirm this approach, a very highly (pyrophoric) air- and moisture-sensitive solution of methylaluminoxane (MAO) and tetrabutylammonium chloride was run with and without the source pressurization.[a] Figure 3.1(right) shows the spectrum using the modified source while Figure 3.1(left) shows the replacement of one or two (or more) methyl groups in the methylaluminoxinate anions with –OH groups, due to the exposure to trace water in the unmodified source.

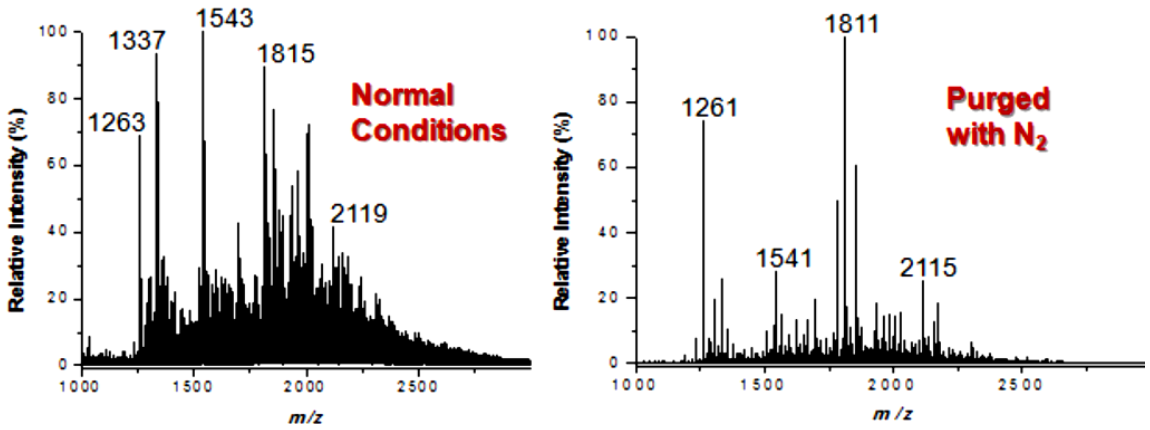

Figure 3.1: (left) MS spectrum of a fluorobenzene solution of MAO and terabutylammonium chloride under normal source conditions. (right) MS spectrum of a fluorobenzene solution of MAO and terabutylammonium chloride after purging the source with N_2 for 20 minutes.

3.2 Pressurized Sample Infusion

Our group was looking to improve a method to introduce the sample solution into ESI-MS while the reaction progresses in the flask. Although some possible methods have been reported before, none of them seemed to fit for our purpose. A small HPLC pump is

[a] This experiment was performed by Tyler Trefz (unpublished results)

the first conceivable option. But these pumps are made of stainless steel (with various plastic and rubber fittings) and designed for pure solvents and hence inappropriate for a reaction mixture due to the possible reactivity of reaction mixture with steel and mutual damage to both pump and analyte of interest. Peristaltic pumps make a pulsating flow and hence are not appropriate for ESI, since consistency of flow is important for spray quality.

Krista Vikse proposed an idea to transfer the sample solution directly to the source of the MS from the reaction flask by using a small piece of PEEK tubing whereas a neutral gas provides the driving force to guide the solution from the flask to the ESI source. This simple idea was found to be practical without complicated requirements. It provides anaerobic conditions which is suitable for the analysis of air and moisture condition but not limited to that.

Although ESI-MS is tolerant to the flow rate of introduced sample to some extent, still some investigations were required to find the relationship of overhead pressure to the flow rate and the type of solvents. In normal ESI-MS experiments, the sample solution is injected to the source of ESI by a syringe pump at the rate of 1 – 50 μL min^{-1} (in nanospray much lower than this) depending on the signal intensity of the ions of interest.

The Hagen-Poiseuille equation represents the relationship between the flow rate and the relative pressure applied as the driving force in the tubing:

$$\Delta P = (128\mu LQ)/(\pi d^4)$$

ΔP is the pressure drop, μ is the dynamic viscosity, L is the length of tube, Q is the volumetric flow rate and d is the inner diameter of the tube. In a hypothetical condition when 1 psi pressure is applied to water passing through a half of meter of a 127 μm diameter PEEK tube, a flow rate of 5.3 μL min^{-1} is obtained, which is suitable for our experiment condition. To see whether the type of solvents shows any trend with the flow rate, several overpressures were applied to the various solvents at the same experiment

conditions (constant length of the tube and temperature). As predicted, the most viscous solvent has the lowest flow rate at given pressure (Figure 3.2).[a]

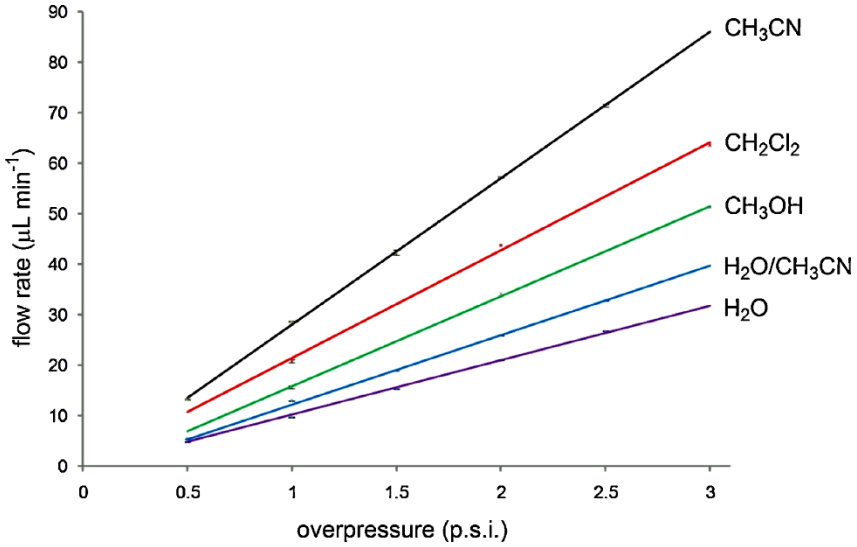

Figure 3.2: The relationship between the pressure applied to the system and the measured flow rate for a various common solvents when a 60 cm length of PEEK tubing is used. Vertical error bars shows the small range of errors.

A large amount of experimental data for the various solvents and different tube lengths were plotted against calculated data using the Hagen-Poiseuille equation to examine their relationship (Figure 3.3). The extracted results showed that no strong relationship existed between tubing length and flow rate. Since tubing length, solvent viscosity and overpressure are accurately measurable; the only potential source of error could be inner diameter of the tube. A ± 20% error for 0.005" ID PEEK tubing exists in the manufacturer's listed tolerance. Because the tube diameter is magnified by a power of four in the Hagen-Poiseuille equation this error is enough to address the most of the observed outliers. It is concluded that if a precise flow rate is required the flow rate for a given length of tubing should be measured at the first place with a constant pressure, so the Hagen-Poiseuille equation can be used to calculate an effective internal diameter, which can be used to determine the pressure required for a desired flow rate for the other solvents and pressures.

[a] These experiments were performed by students enrolled in the University of Victoria undergraduate class Chem361 during the spring of 2010 and 2011 under K. L. Vikse 's supervision.

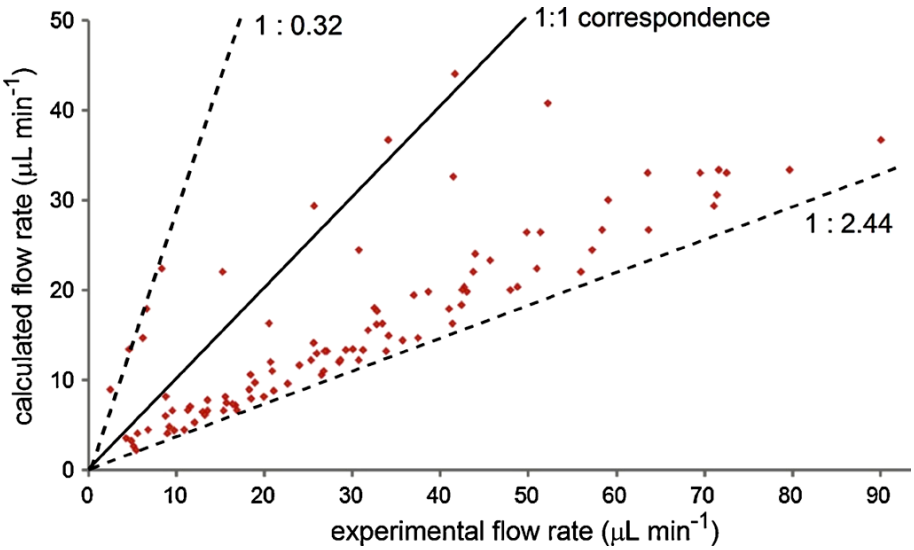

Figure 3.3: Experimental flow rates plotted against theoretical flow rates. Data points include all the data including five different solvents, four different tube lengths and five different pressures. The solid line indicates a 1:1 correspondence while the dashed lines show the expected variation if the inner diameter was 25% less (1:0.32) or 25% more (1:2.44) than the reported value.

Acid-catalyzed hydrolysis of a protected amino acid, Fmoc–Arg(Pbf)–OH using trifluoroacetic acid was studied as a practical application for online monitoring in organic mechanism investigation.

The observed mechanism pathway for this reaction is shown in Scheme 3.1 where trifluoroacetic acid breaks off the Pbf group selectively and under mild conditions. The 2,2,4,6,7-pentamethyldihydrobenzofuran-5-sulfonyl (Pbf) protecting group is more popular than the 2,2,5,7,8-pentamethylchroman-6-sulfonyl (Pmf) protecting group because in an study performed by HPLC, Pbf removal was found to be faster than removal of Pmf, so Pbf was developed as a TFA-sensitive arginine side-chain protecting group for use in Fmoc-based peptide synthesis.[143] Pbf also has the advantages of reagent availability as well as stability, both important properties for Fmoc deprotection.[144]

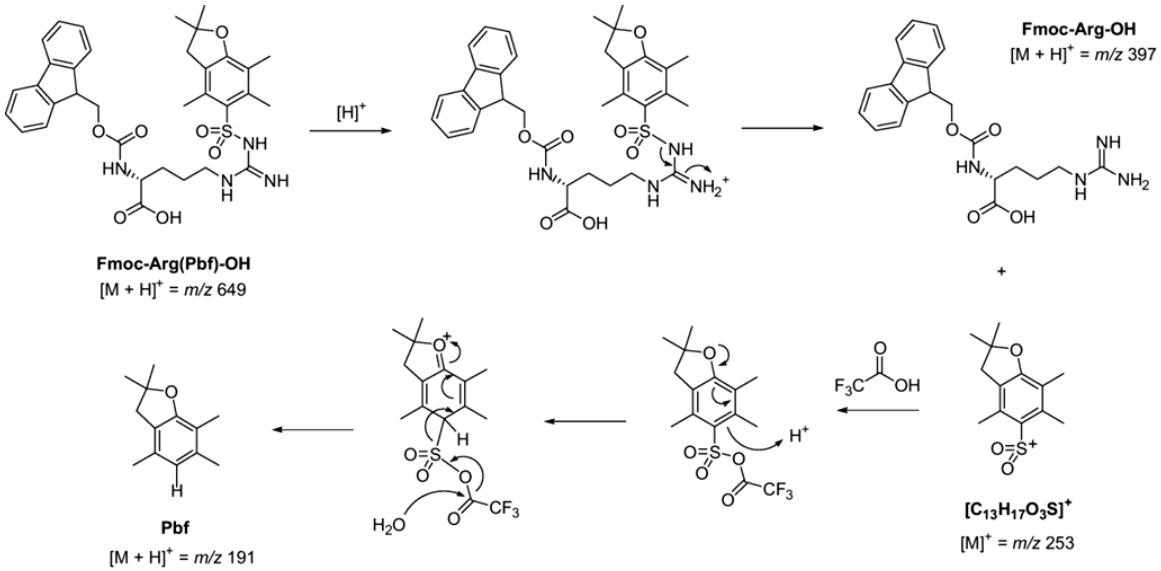

Scheme 3.1: Proposed TFA-deprotection mechanism of Fmoc-Arg(Pbf)-OH adapted from reference 144.

Here we observed Pbf cleavage from Fmoc-protected arginine under typical conditions, which proceeds as a (*pseudo*) first order kinetic. The reaction took about 20 minutes to go to completion. Figure 3.5 shows two mass spectra, one before the reaction was initiated and the second at 10 minutes.

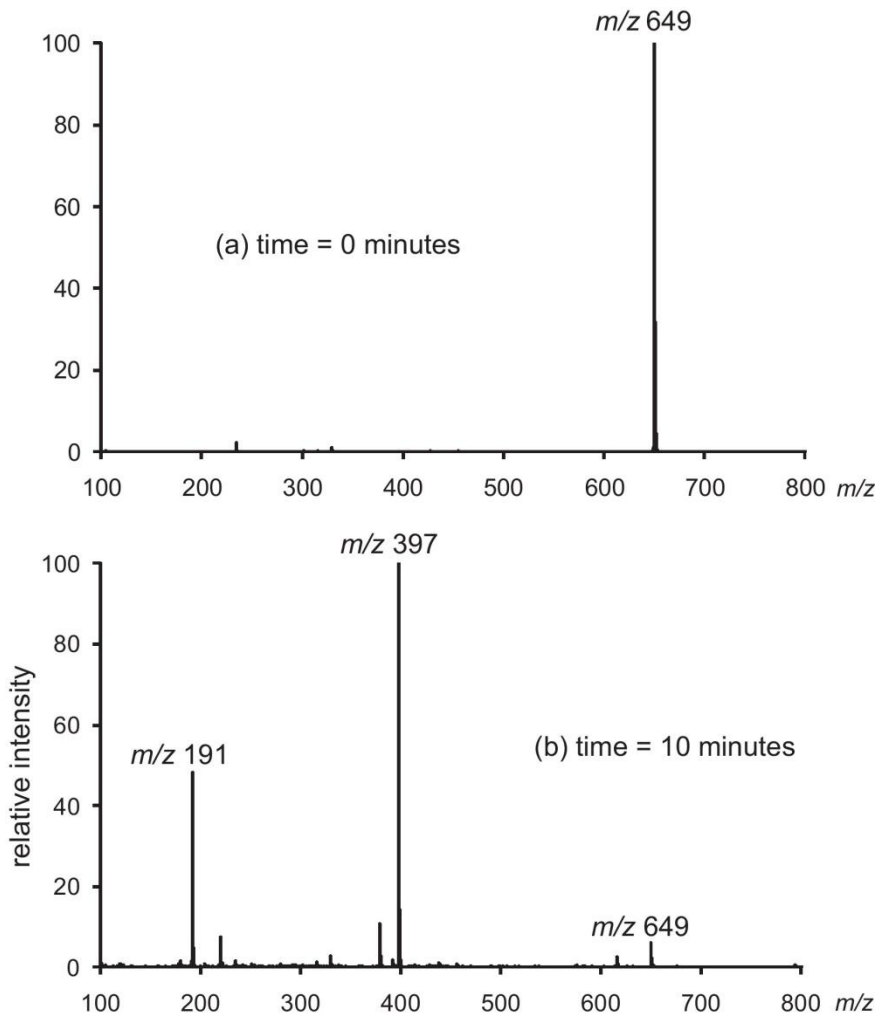

Figure 3.4: ESI(+)-MS spectra of reaction mixture (a) at t = 0, starting material at m/z 649 (b) t = 10minutes, appearance of both products at *m/z* 191 and 397 are evident.

Abundances of the species of interest were plotted versus time. In this case, reaction time is the combination of the time species spend in the flask plus the time they pass through the tube. Upon addition of trifluoroacetic acid a huge boost in ion count (at about 30 seconds) was observed which is the result of the ability of TFA to protonate neutral substrates to form $[M+H]^+$ ions. The initial ion count per spectrum jumped instantly from 3000 to 48,000 (Figure 3.6 shows only 0 –15,000 range). Over the course of hydrolysis, the protonated substrate, $[Fmoc–Arg(Pbf)–OH+H]^+$ at *m/z* 649, started to disappear and protonated forms of both fragments, $[Fmoc–Arg–OH+H]^+$ at *m/z* 397 and $[Pbf+H]^+$ at *m/z* 191 appeared. We presented the data in two different ways: first as the raw intensity and

the second normalized to total intensity of all the ions of interest including the peaks at *m*/*z* 649, 397 and 191.

Normalizing the data to the total ions of interest not only smoothed out the fluctuations of each trace but also gave a relative abundances of the ions of interest to the all ions of interest. However, when the ionization efficiencies of species are dramatically different, the shape of raw and normalized intensities will be different. Care must be taken for interpretation in this case. The disappearance of *m/z* 649 is approximately first order, with a slope of −0.21 and $R^2 = 0.96$ for a plot of ln[intensity] versus time, with $t_{½} = 3.3$ min (calculation on raw data). This number is in accordance with the assumption that the hydrolysis reaction is basically complete within 20 minutes.

From Figure 3.5 and 3.6 it is obvious that the two hydrolysis products are not produced at the same rate; the first product at *m/z* 397 is produced quickly (S-N bond cleavage), while the ion at *m/z* 191 (S-C bond cleavage) is undergone several extra steps therefore it is slightly slower. This induction time is clear at the first and second minutes of reaction in both Figures. Based on postulated mechanism pathway, we looked for the key intermediate, $[C_{13}H_{17}O_3S]^+$ at *m/z* 253. Luckily we were able to detect this species at very low intensity (a maximum of about 0.3%, Figure 3.6 inset). Overall, the observed species are in accordance with Ramage's postulated mechanism for TFA deprotection. [144] This experiment verified the ability of PSI-ESI-MS to extract necessary information for the mechanistic investigation, since it provides simultaneous monitoring of the ions (starting material, product and intermediates) across a very broad range of concentrations of approximately three orders of magnitude.

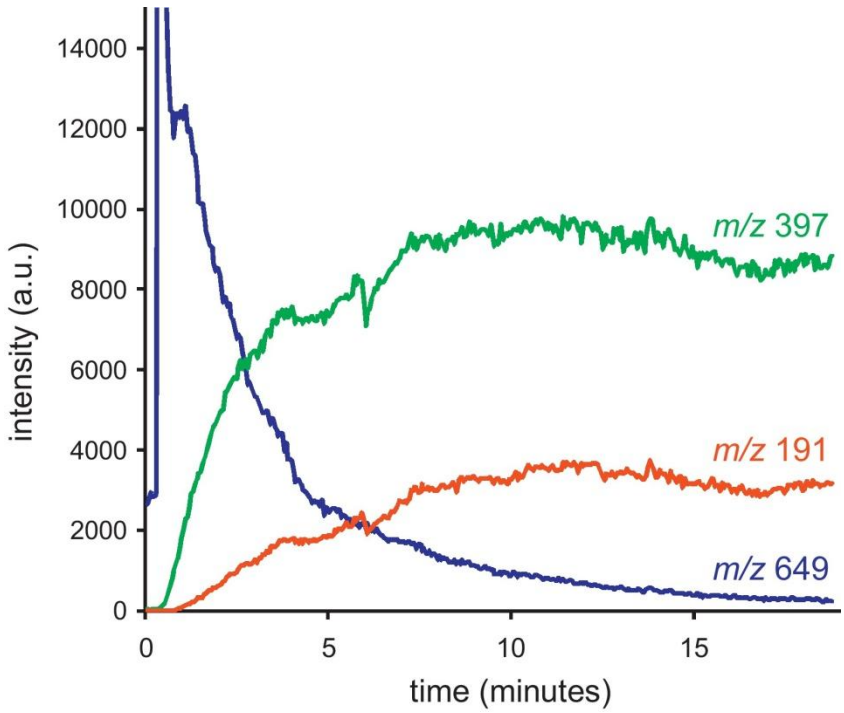

Figure 3.5: Raw intensity of the protected amino acid (*m/z* 649) and the hydrolyzed products (*m/z* 397 and 191) against time. ESI-MS spectra were collected for 3 s to generate each set of data.

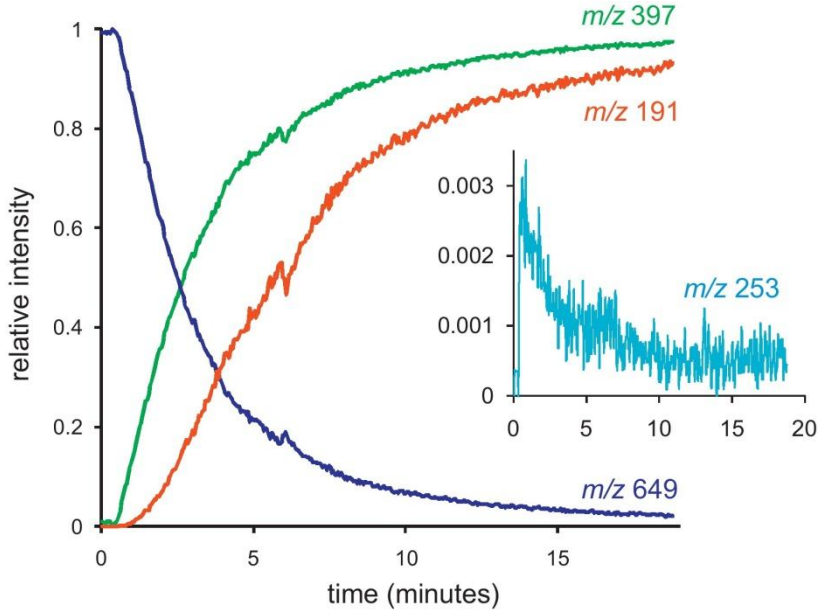

Figure 3.6: Normalized intensity for the protected amino acid (*m/z* 649) and the hydrolyzed products (*m/z* 397 and 191) against time. The inset shows the abundance of the $[C_{13}H_{17}O_3S]^+$ intermediate on different scale since its abundance is very low.

Deprotection Experiment Conditions:

2.1 mg Fmoc–Arg(Pbf)–OH (Merck Schuardt OHG) was dissolved in 1 ml acetonitrile (99.5%, CALEDON) in a 50 ml flask attached to a well-regulated supply of nitrogen (at 5 psi) and equipped with a septum and PEEK tubing (Red, 0.005 ID) leading to the mass spectrometer without further dilution. 4 ml of trifluoroacetic acid (99.9%, CALEDON) was injected in the reaction flask at appropriate time when the intensity of starting material is optimized and stabilized.

Nitrogen gas (5 psi) was used as the driving force for sample infusion in this experiment. Mass spectra were collected on a Micromass Q-ToF micro mass spectrometer in positive-ion mode using pneumatically-assisted electrospray ionization. Capillary voltage: 2900 V; cone voltage: 10 V; extraction voltage: 0.5 V; source temperature: 80 ^{0}C; desolvation temperature: 150 ^{0}C; cone gas flow: 100 L/h; desolvation gas flow: 200 L/h; scan time was 3 s and the inter scan time was 0.1 s. The reaction was continued until the amount of starting material dropped to < 5% of the initial value.

3.3 Employing PSI-ESI-MS to study metal catalyzed systems

Now that we understood the analytical aspect of the pressurized sample infusion (PSI), it was employed to study some organometallic catalytic reactions. A Schlenk flask and a piece of PEEK tubing was the only extra equipment required. As a part of my assignment, I developed this technique for more complex catalytic systems. To minimize leakage from the flask a small volume reaction flask integrated with a condenser was designed and substituted with the conventional Schlenk flask and a low flow water pump was used to circulate the cold water in and out of the condenser (Figure 3.7). The water pump was required as a supply was not conveniently available in the instrument room. A further modification was to use argon as the driving gas, as consumption is very low and argon is advantageous over nitrogen for its blanketing ability (it is heavier than air).

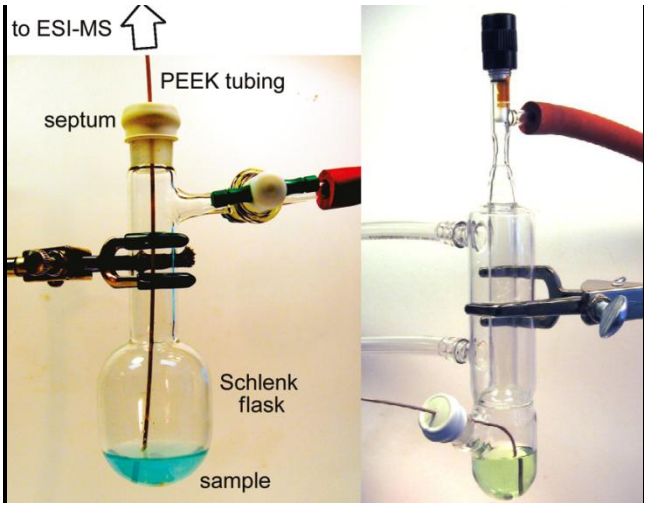

Figure 3.7: (left) Conventional Schlenk flask (right) Modified PSI-flask for running the reaction at elevated temperatures.

The copper-free Sonogashira coupling of a terminal alkyne with an aryl halide (also known as a Heck alkynylation) was chosen as the first reaction. Despite many attempts to investigate this reaction by conventional methods, the mechanism of reaction is still not entirely understood.[145-149] A charged version of an aryl iodide was synthesized as the probe for ESI-MS (Scheme 3.2). Details of this study will be explained in next chapter. Here we briefly explain some technical considerations.

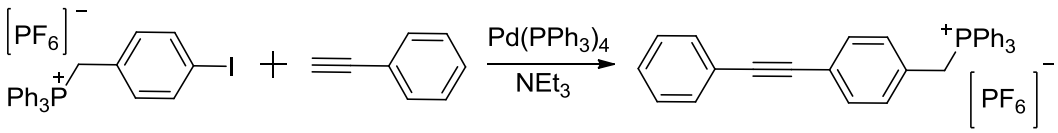

Scheme 3.2: Copper-free Sonogashira reaction between $[4\text{-I-}C_6H_4CH_2PPh_3]^+$ $[PF_6]^-$ and phenylacetylene using tetrakistriphenylphosphine as the catalyst and triethylamine as the base.

The phosphonium tag provides very low detection limits due to its high surface activity, whereas the non-coordinating counter-ion reduces ion pairing. The bulky nature of the charged group ensures that the ionization efficiency is insensitive to the remaining structure of the ion. However, we found this high surface activity a challenge due to high ion intensity even at low concentration. Saturation of MCP is likely in high ion counts hence deviation from the linearity range of the detector. To address this problem we

employed a dilution system which is essentially a T-mixer. It requires three pieces of PEEK tubing: one short tube coming out of the flask to deliver the reaction mixture to the mixer; another connecting the mixer to a syringe, while a syringe pump pushes the solvent to the mixer; and a third transfers the diluted solution to the ESI-MS. Using the same inner diameter for all three tubing caused some problems: the intensity was inconsistent, dilution factor was low and inefficient and in some cases solvent was going backward to the reaction flask instead of the ESI-MS. To overcome this barrier, the dilution system was modified in a way that the first tubing, coming from flask, was chosen as the smallest diameter to ensure lowest flow rate, to compensate for time lag, the shortest possible length was used (20 cm). Also largest diameter was chosen for the third tubing to relieve backpressure and to ensure the solution wasn't driven backwards into the reaction flask. A consistent dilution up to 1:100 was obtained while about 10 – 20× dilution was enough for the phosphonium substrate. Figure 3.8 shows the schematics of the dilution system with inner diameters used for this purpose.

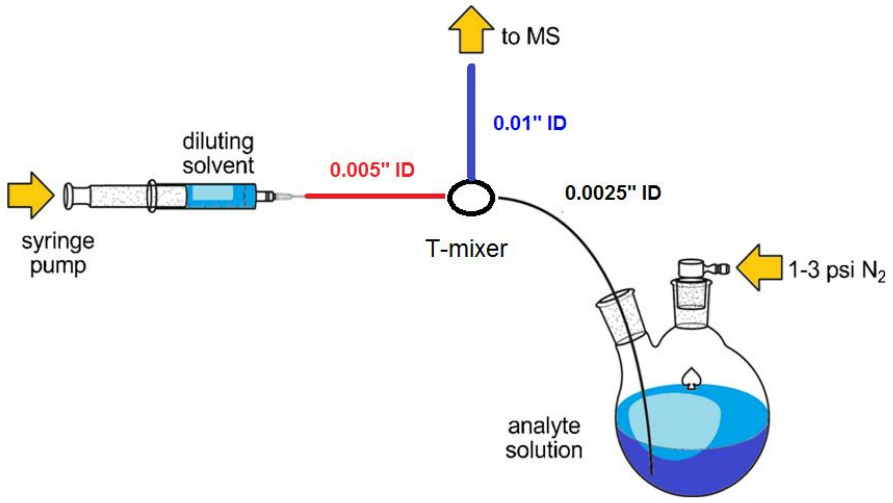

Figure 3.8: Pressurized sample infusion (PSI) with dilution system. A T-mixer is used to dilute the reaction mixture with desired solvent.

3.4 ESI-MS-UV/Vis integration

In order to integrate ESI-MS and UV/Vis techniques, three options initially were considered. The flow-through cell, the transmission dip probe and the UV/Vis detector of HPLC (or GPC) are practical methods for in situ or online studies by UV/Vis

spectroscopies. In flow-through cells the screw fitting connections easily create an open or closed system for the continuous flow reaction. For our purpose, solution can be introduced via a PEEK tubing from the reaction flask into the cell whereas a separate PEEK tubing will transfer solution form the flask into the ESI-MS (Figure 3.9 left). Another option would be transferring the same solution coming out of the outlet of the cell into the ESI-MS via another piece of PEEK tubing. In this case there will be a few seconds delay between UV/Vis and ESI-MS detections regarding to the time lag caused by the length of PEEK tubing which needs to be accounted for.

Figure 3.9: A sample of flow through cell[a] and a transmission dip probe.[b]

In transmission dip probes, light is sent through the illumination fiber to the sample compartment. Then the light reflects from a flat mirror located in tip of the probe, and it is collected by the lens into the fiber. Having a compact optical structure is the advantage of these dip probes. However, these probes cannot discriminate the transmitted light and backscattered light coming from the solution and they have internal reflections that limit the dynamic range of the measurement. Still, they could be cost-effective option for many on-line monitoring and lab applications.[150-152] Among the three options UV/Vis detector of HPLC seems to be the best option in comparison with flow through cell and dip probe. It is a UV/Vis spectrometer that has a flow through cell adapted for low concentration and continuous flow. Usually it has one or two extra cells with different volumes giving more flexibility to work with different range of concentrations. High-noise correction,

[a] http://www.chem.agilent.com/Library/catalogs/Public/Molecular_Spec_Catalog.pdf

[b] http://www.oceanoptics.com/Products/tp300transdipprobes.asp (accessed 5/24/2013)

low-loss optics, low-noise electronics and filtering make these types of detectors more sensitive with higher resolution in comparison with two other options.

With the help of Dr. Ori Granot we integrated the UV/Vis mode (Waters 996 PDA Detector) from a GPC instrument to a QTof-Micro. Both the instruments are the product of Waters Company, so MassLynx® software (ESI-MS software) can support the UV/Vis detector. Therefore controlling both machines is conveniently achieved with the same software. The two machines were integrated sequentially, so the solution is transferred to the UV/Vis first since the method is non-destructive and passed through the cell and finally leaves the cell to the ESI-MS source (Figure 3.10).

Figure 3.11 shows[a] the first graph obtained by this technique. It shows the peaks corresponding to the caffeine from both instruments.

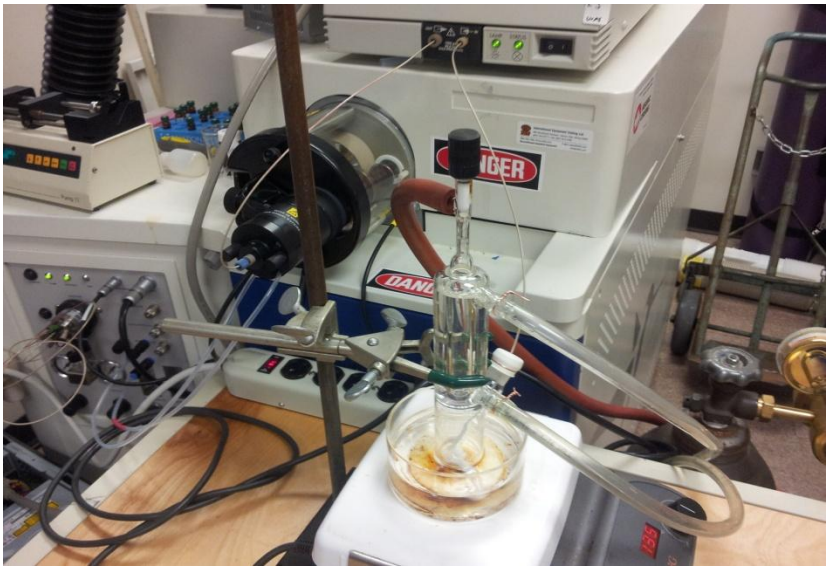

Figure 3.10: Set-up of the integrated UV/Vis with ESI-MS. Sample is introduced to the UV/Vis detector first and to the ESI-MS source via another piece of tubing.

[a] This data was recorded by Dr. Ori Granot and Eric Janusson.

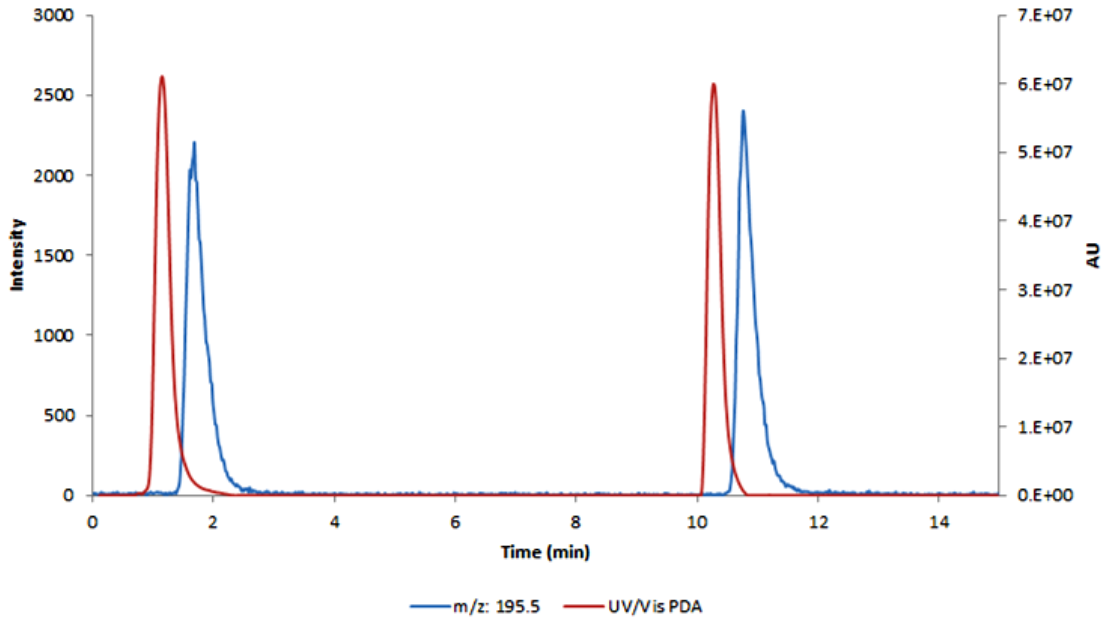

Figure 3.11: Injection of 0.2 mM of caffeine (first) without formic acid (second) with addition of 2% formic acid to protonate caffeine and hence increasing ion current in ESI-MS. Blue line corresponds to protonated caffeine and red line corresponds to PDA (photodiode array: a snapshot of the entire spectrum in less than one second). Delay time is less than 30 s when flow rate is 50 µL min^{-1}.

Success of this method has the potential to alter the way in which homogenous catalytic and organometallic reactions are conventionally studied. Neither a complicated and expensive setup nor any extra manipulation software is needed and requirements are commercially available. Besides, data collection and processing is fast and simple. The timescale for both techniques are in the range of a second or less, thus always there is a chance to observe the short-lived intermediate as well. By putting the information of both techniques together a rich profile of the time resolved reaction is extracted which can help for understanding of the kinetic and mechanism of organometallic reactions.

Chapter 4 Mechanistic investigation of the Copper-free Sonogashira reaction

Portions of this chapter are reproduced in part with permission from "Powerful insight into catalytic mechanisms through simultaneous monitoring of reactant, products and intermediates" Krista L. Vikse, Zohrab Ahmadi, Cara C. Manning, David A. Harrington and J. Scott McIndoe, *Angewandte Chemie, International Edition*, **2011**, 50, 8304-8306. Copyright © 2011 WILEY-VCH Verlag GmbH & Co. KGaA, Weinheim.

4.1 Introduction

The Heck alkynylation reaction was reported for the first time by Heck[153] and Cassar[154] independently in 1975. This palladium-catalyzed carbon-carbon bond formation is between a terminal alkyne and an aryl or vinyl halide. Shortly thereafter, Sonogashira reported that addition of a trace of CuI to the same procedure facilitates the reaction significantly; the reaction can be done at room temperature and in the most cases with a higher yield under these conditions. A primary catalytic cycle was proposed in the same report, to separate it from reaction mixture which indicated the role of CuI and suggested a mechanism for biphenylacetylene formation as the byproduct. [155]

Thereafter, this reaction became very popular for the synthesis of natural and biologically active products, heterocycles, dendrimers, conjugated polymers and nanostructures.[156] Nonetheless, the methodology has become less popular because the copper co-catalyst is not environmentally friendly and it is hard to separate it from reaction mixture. Secondly this reaction suffers from formation of homocoupling of acetylene.[157] With regard to these shortcomings, as a response for seeking a better methodology, copper-free reaction was modified and emerged from Sonogashira reaction. Perhaps a better name for this reaction would be the Heck-Cassar-Sonogashira alkynylation. However, regardless of whether copper iodide is present or not, the coupling of a terminal alkyne with an sp^2 carbon catalyzed by a palladium complex is most often called "Sonogashira reaction", perhaps because Heck (a 2010 Chemistry Nobel Prize-winner) is strongly identified with the so-called "Heck reaction", the coupling of an unsaturated halide with an alkene. Na´jera has recently documented Sonogashira reaction advances in two comprehensive reviews. [156, 158]

In spite of many advances and modifications in the application of the Sonogashira reaction, the mechanism still is not completely understood. In all proposed mechanisms three main steps are in common: oxidative addition of aryl halide to Pd catalyst, transmetallation of alkyne and reductive elimination of the final product. Transmetallation is the step which brings both carbon fragments together on the Pd centre. It is called transmetallation, since in most palladium-catalyzed cross coupling reactions the second carbon is coming from another metal (for example magnesium in the Kumada reaction and tin in the Stille reaction). This term is still used, although in the copper-free Sonogashira reaction no other metal is involved. This step is the most controversial step in the mechanism and several studies tried to understand how the alkyne is attached to the Pd catalyst. Here we intend to briefly review the related works on this mechanism.

Uncertainty mostly arises from the fact that the amines used in Sonogashira reaction are not strong enough to deprotonate the alkyne in the solution. Therefore, deprotonation is expected to occur on the metal. Leaving no other choice, it should proceed through the η^2-coordination fashion to the metal centre to pull the electron density away from acetylene, which would make the proton of acetylene more acidic and hence, enables the base to protonate the acidic *sp*-proton.[159, 160] Another possibility after formation of η^2-coordinated acetylene is a carbopalladation mechanism followed by proton abstraction by the base in the next step (base-assisted β-hydride elimination)[153, 161] (Scheme 4.1).

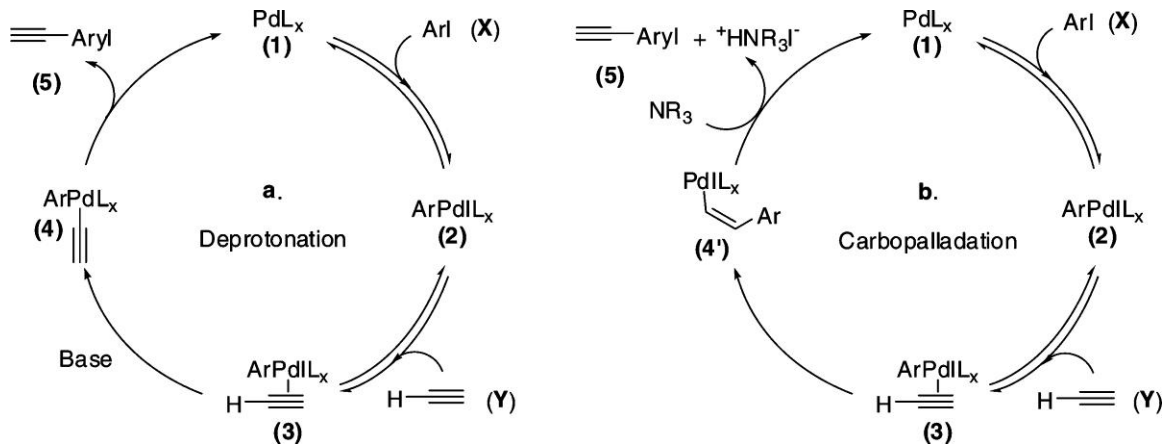

Scheme 4.1: Two proposed mechanisms for the palladium-catalyzed copper-free Sonogashira between a terminal alkyne and an aryl halide. Reprinted with permission from "Two Competing Mechanisms for the Copper-Free Sonogashira Cross-Coupling Reaction" T. Ljungdahl, T. Bennur, A. Dallas, H. Emtenäs and J. Mårtensson, *Organometallics*, **2008**, 27, 2490-2498. Copyright © 2008, American Chemical Society.

Scheme 4.2 shows carbopalladation of an arylpalladium complex with a terminal alkyne. Carbopalladation is a *syn* addition which forms the *cis* product. In case of terminal alkynes, aryl group is positioned into the less hindered place. However, a mixture of *cis* and *trans* products have been observed in carbopalladation assigned to isomerization of the first formed *cis* adducts.

In an study supported by NMR data, Amatore and Jutand investigated the reactivity of synthesized *trans*-Pd L_2PhI with EtO_2C-C≡CH. Regioselective carbopalladation was observed by initial formation of the *cis*-adduct of EtO_2C-C($PdLI_2$)=CHPh followed by *cis-trans* isomerization to make the *trans* form of this adduct.[161]

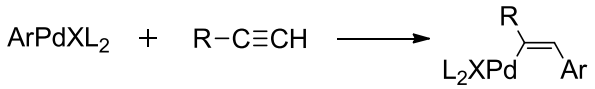

Scheme 4.2: Carbopalladation of terminal alkyne with PdL_2ArX.

Ljungdahl et al then cast doubt on whether the carbopalladation mechanism was operating under real catalytic conditions.[159] In that study, a product of carbopalladation was synthesized and was subjected to a typical catalytic reaction in the presence of

phenylacetylene with and without the base (excess Et_3N) to check the possibility of the base-assisted *trans*-elimination and intramolecular beta hydride elimination respectively. No desired product was formed in this case which excluded the possibility of carbopalladation mechanism under actual reaction conditions.

Having ruled out the carbopalladation mechanism, Ljungdahl et al proposed deprotonation functions and the turnover limiting step with two competing mechanisms depends on the electronic effects of terminal alkyne (Scheme 4.3). In a Hammett study a changeover in mechanism was observed in a series of *para*-substituted terminal alkynes. It was observed that the energy required for deprotonation is decreased by electron withdrawing groups and increased by the electron donating group. Two different pathways hence were proposed: when the proton of alkyne is acidic enough (EWG-substituents), deprotonation is facile and reaction proceeds smoothly through an anionic pathway to make coordinatively saturated palladate complex. On the other hand when *sp*-proton is not acidic enough (EDG-substituents), base assisted deprotonation is very slow and thus previous mechanism cannot compete. So further activation is required to progress in the cycle; acting in a dual role, base will initially substitute the halide to create an electronic deficient palladium complex which can subsequently undergo deprotonation more easily. This interpretation was supported by a computational study.

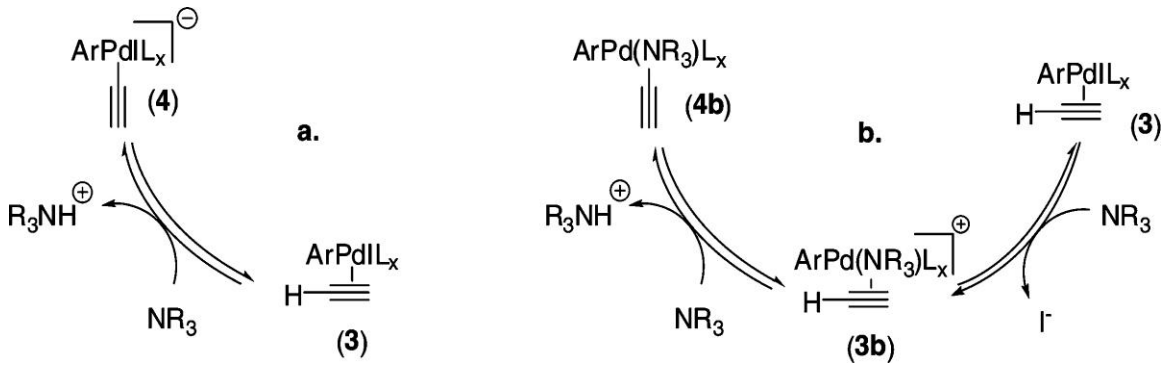

Scheme 4.3: Proposed (a) anionic pathway and (b) cationic pathway for deprotonation of para-substituent terminal alkyne. Pathway (a) is operative for EWG substituents while pathway (b) is operative for EDG substituents. Reprinted with permission from "Two Competing Mechanisms for the Copper-Free Sonogashira Cross-Coupling Reaction" T. Ljungdahl, T. Bennur, A. Dallas, H. Emtenäs and J. Mårtensson, *Organometallics*, **2008**, 27, 2490-2498. Copyright © 2008, American Chemical Society.

In a more recent work reported by Jutand et al[162], the existence of two mechanisms was inferred for the second time. This time different amines were shown to participate with multiple roles. It was suggested that base accelerates the overall reaction initially by interfering in the OA step by forming more active species of the type [Pd^0L(amine)]. Also, secondary amines can replace the ligand (L) in trans-$Pd^{II}L_2$(Ph)(X). This substitution is more favourable when L=$AsPh_3$ in comparison with PPh_3. In other words, when amine is a better ligand than the terminal alkyne it wins the competition to bond to the palladium centre first. Due to these observations two competing mechanisms were proposed for this reaction.

In a high-throughput kinetic study performed by gas chromatography (GC) in which up to 25 coupling reactions were studied in a single pot, many electronic and steric effects of substrates and ligands were studied for the copper-free Sonogashira reactions by extracting several Eyring and Hammett plots. Results of the study, which were supported by DFT calculation, denoted that aryl halide is somehow involved in the turnover limiting step (the results of Hammett plot for *para*-substituent aryl bromide will be explained in section 4.2.4).[163] Our group also contributed to this investigation previously. Several key intermediates were observed when a charged tag phosphine ligand was added to the

reaction mixture. A mechanism was proposed for the Sonogashira reaction with secondary amine based on direct observation of several key intermediates (Scheme 4.4). Also the electronic effects of *para*-substituents on the aryl iodide were investigated through an MS/MS study.[164] Results indicated that reductive elimination is most favourable for the aryl groups with electron donating substituents, which is in agreement with an theoretical study.[165]

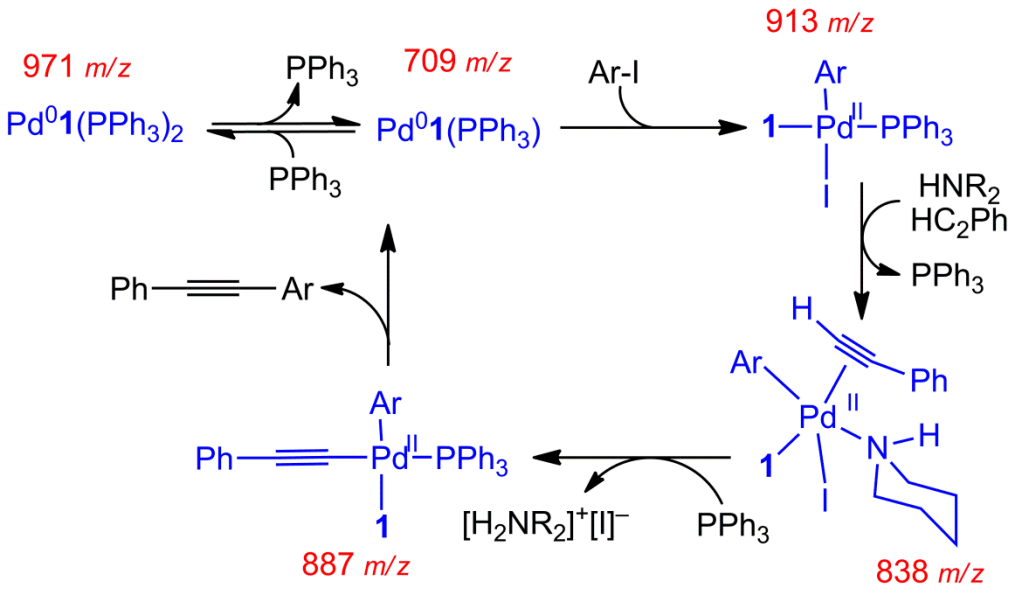

Scheme 4.4: A proposed catalytic cycle based on direct observation of intermediates on ESI(-)-MS for the copper-free Sonogashira using piperidine as the base. (**1**) is the charge tagged ligand triphenylphosphinemonosulfonate. Modified from reference 164.

So not only different studies did not completely address the mechanism of the reaction, but also disagreed with one another. In most cases, postulated intermediates were synthesized and subjected to further reactivity investigation instead of direct analysis under typical catalytic conditions. Also due to methodology limitations, most of the conclusions are the result of indirect inference of the nature of active intermediates. In previous study of Sonogashira reaction in our group, this reaction was studied by direct observation of intermediates containing a charge-tagged phosphine ligand. In this chapter, the reaction mechanism is examined from different angles to address as many questions as possible by employing the combination of substrate tagging and PSI-ESI-MS methodologies.

4.2 Sonogashira mechanism investigation by PSI-ESI-MS

4.2.1 Proof of principle

A charged tag is required to detect species otherwise invisible to ESI-MS. We functionalized the substrate, an aryl iodide, with a phosphonium hexafluorophosphate salt, $[p\text{-I-}C_6H_4CH_2PPh_3]^+[PF_6]^-$. This tag provides very low detection limits due to its high surface activity. In order to reduce ion pairing and to remove the halide (which may influence the reaction under study), we replaced halide with the non-coordinating counter-ion $[PF_6]^-$ through a salt metathesis reaction. The bulky nature of the charged group ensures that the ionization efficiency is largely insensitive to the remaining structure of the ion so the intensity of the various ions tracks very closely to their real concentrations. Scheme 4.5 shows the process in which tagged-substrate was synthesized.

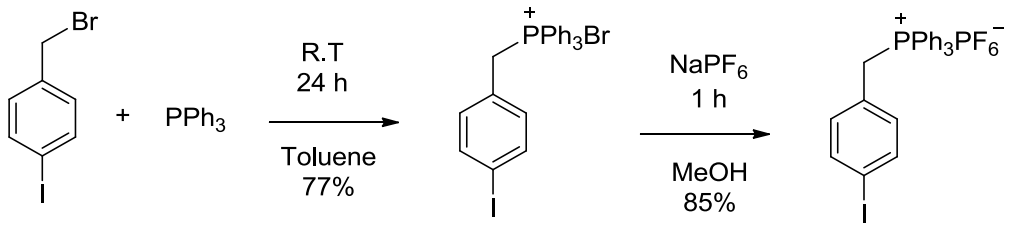

Scheme 4.5: Synthesis pattern of $[4\text{-I-}C_6H_4CH_2PPh_3]^+$ $[PF_6]^-$.

Initially as a generic condition for Sonogashira reaction we started with methanol as a polar solvent, phenylacetylene as the terminal alkyne and Et_3N as the amine. Reaction was optimized in a way that ion intensity was in an appropriate range of instrument sensitivity and the reaction went to completion in a reasonable time scale for online monitoring (Scheme 4.6). Final product of this reaction was isolated and characterized by ESI(+)-MS, ^1H and ^{31}P NMR. Also the structure was confirmed by crystallography data (Figure 4.1) (Appendix A).

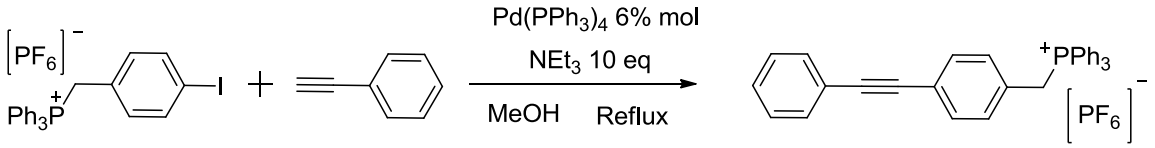

Scheme 4.6: Copper-free Sonogashira reaction with a charged aryl iodide as an ESI(+)-handle.

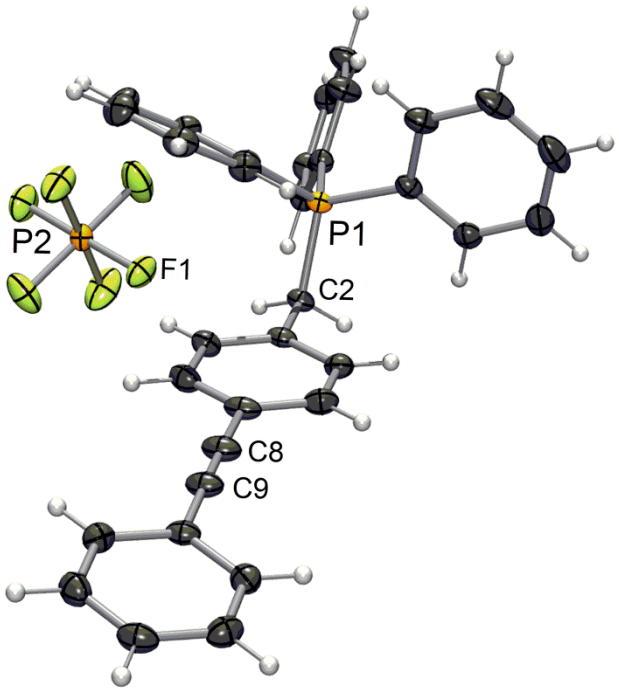

Figure 4.1:X-ray crystal structure of $Ph(C_2)C_6H_4CH_2PPh_3]^+$, including the $[PF_6]^-$ counterion.

As described in chapter 3, a dilution system was employed to adjust the intensity of species in ESI-MS. To make sure that response factor of starting material and product track with their concentration, different known rations of both were mixed and introduced to ESI-MS. As shown in Figure 4.2 linear relationship between MS intensity and concentration for these ions is evident. This predictable instrument response ensured that MS intensity data for ions in this reaction could be related to their concentration in solution.

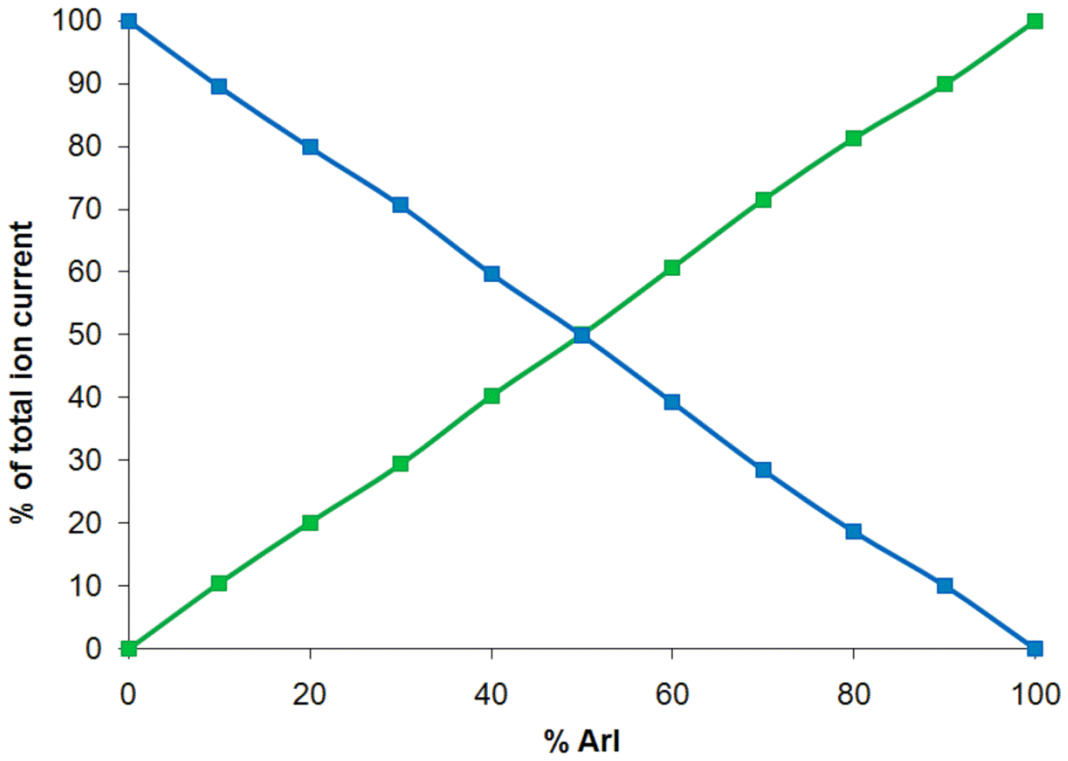

Figure 4.2: Relative intensity of starting material $[4\text{-I-}C_6H_4CH_2PPh_3]^+$ (green) and product $[Ph(C_2)C_6H_4CH_2PPh_3]^+$ (blue) as a function of mixture composition (%ArI) showing the linear relationship between intensity and concentration.

Spectra were collected in the positive-ion mode while 2.5 psi N_2 overpressure was applied. The trace of products extracted by this method tracks well with data obtained by ^{1}H NMR and UV/Vis for the same reaction (Figure 4.3). In this experiment, which required the cooperation of three experimenters, Cara Manning was responsible for extracting the samples for ^{1}H NMR and quenching the solvent. Krista Vikse and I sampled the solution for UV/Vis analysis and controlled the data acquisition in MS. Figure 4.4 shows the ^{1}H NMR data obtained after quenching the reaction mixture solution and dissolving the analyte in the $CDCl_3$. Integrals of the indicated peaks were used to generate the trace. A peak at 307 nm was grown over the course of the reaction monitored by UV/Vis which corresponds to authentic product. This peak was used to track the product with this technique (Figure 4.5).

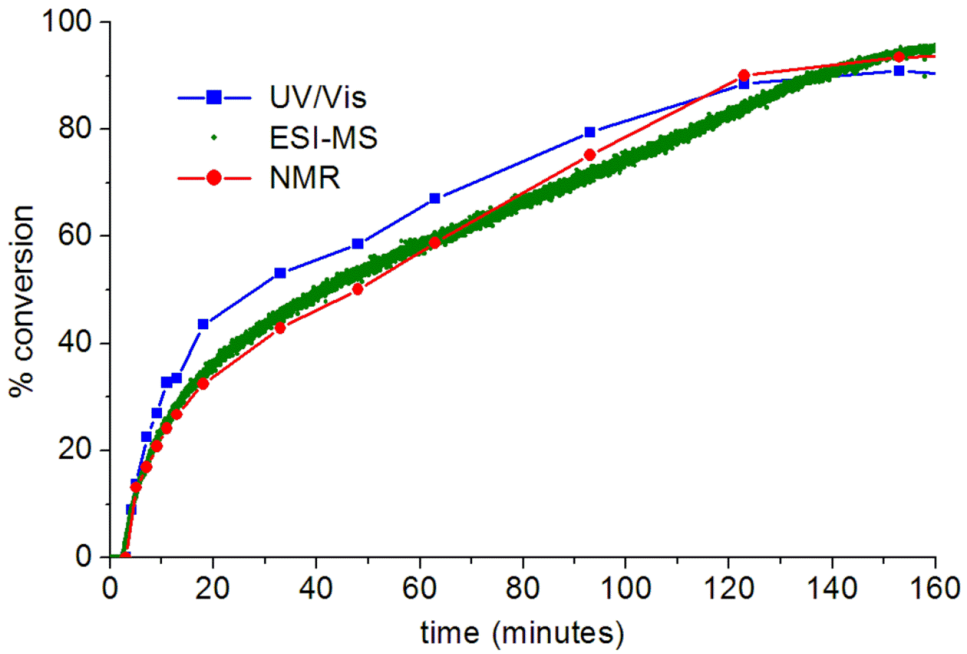

Figure 4.3: Appearance of $[PPh_3CH_2ArC_2Ar]^+$ $[PF_6]^-$ as tracked by UV/Vis, ESI-MS and ^{1}H NMR.

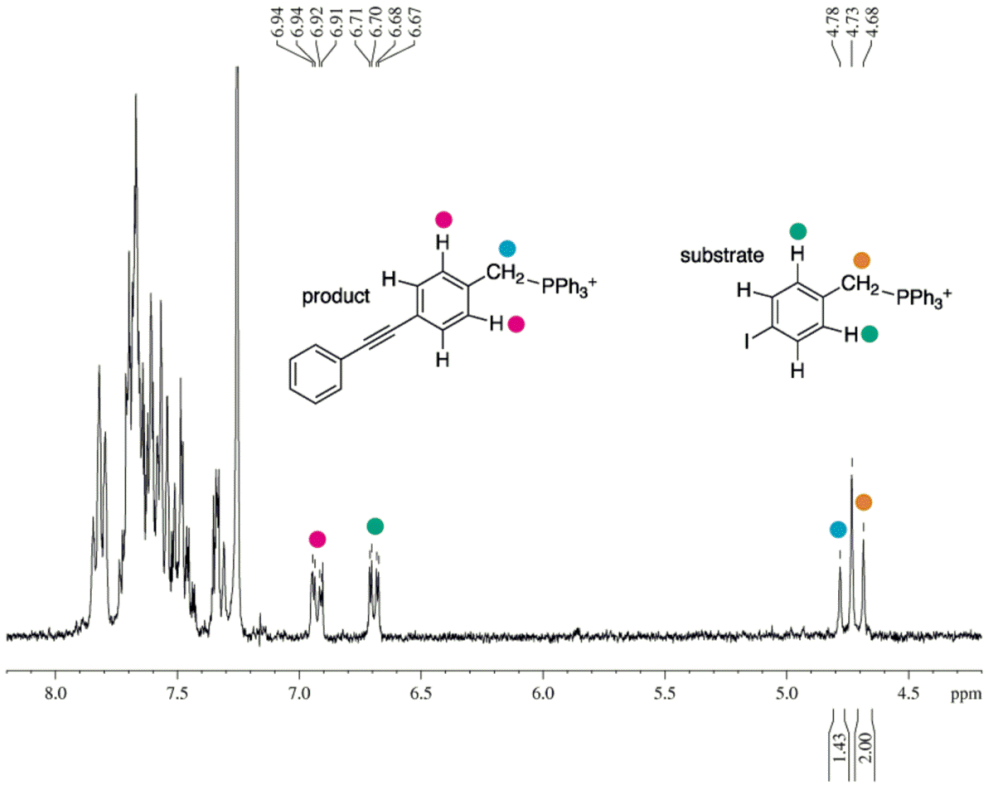

Figure 4.4: ^{1}H NMR spectrum collected during the parallel UV-Vis/NMR/MS experiment, with substrate and product peaks of interest labeled.

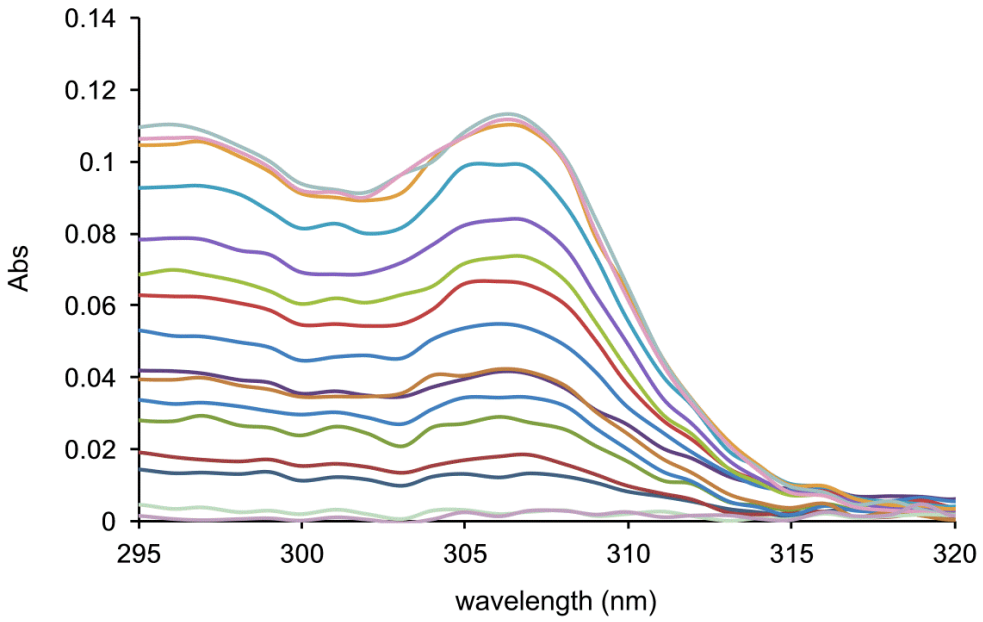

Figure 4.5: UV/Vis spectra collected during the parallel UV-Vis/NMR/MS experiment with product peaks of interest increasing at 307 nm.

Figure 4.6 shows a single ESI(+)-MS spectrum of the reaction mixture at early reaction time. It is clear that the intensities of observed intermediates are much lower than the intensity of reactant and product. The intensity of intermediates was multiplied by 100 to scale them with rest of intensities. However for some other experiments, other factors were considered for multiplication depending on the relative intensity of intermediates. The addition of an internal standard ensures the tracking of any spray instability, quality or fluctuation in the system. Also the internal standard can be used as a means to normalize the rest of data.

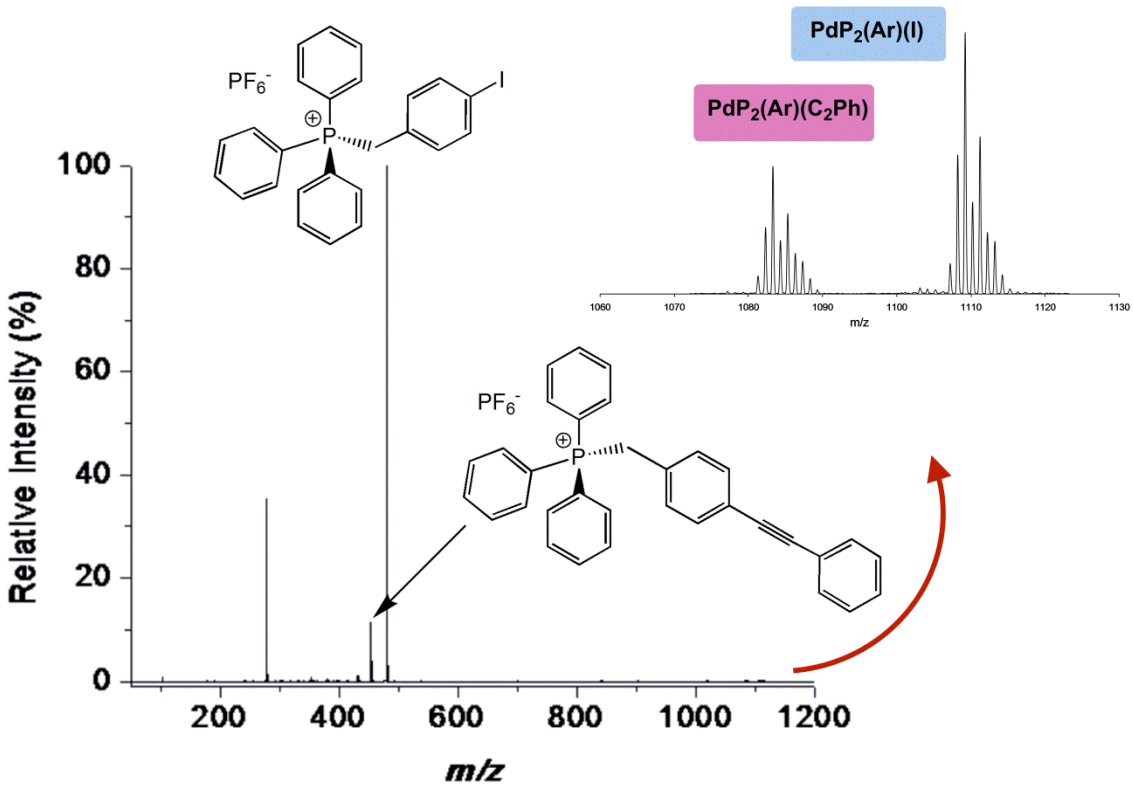

Figure 4.6: A single spectrum of the reaction. Pd-containing intermediates are lost in the baseline and require 100x magnifications to become appreciably intense with respect to reactant and product.

The relative intensities of all major tagged species are depicted: substrate (ArI, *m/z* 479.1), product (ArC_2Ph, *m/z* 453.2), byproduct (ArH, *m/z* 353.2), and under 100× magnification the oxidative addition (OA) and transmetallated (TM) intermediates $PdP_2(Ar)(I)$ (*m/z* 1109.4) and $PdP_2(Ar)(C_2Ph)$ (*m/z* 1083.4) where Ar = $[C_6H_4CH_2PPh_3]^+$, n = 1 or 2. A product ion MS/MS experiment on $PdP_2(Ar)(I)$ (*m/z* 1109.4) is shown in Figure 4.6. The most abundant fragment is the result of the loss of one PPh_3. A small peak of ArI was also observed at *m/z* 479.1. A singly charged palladium containing fragment was also observed at *m/z* 603.2 which is assigned to $Pd(Ar)(PPh_2)$ (loss of PhI). These results fully support the composition of the $PdP_2(Ar)(I)$ (though do not help us resolve the question of whether the complex is *cis* or *trans*).

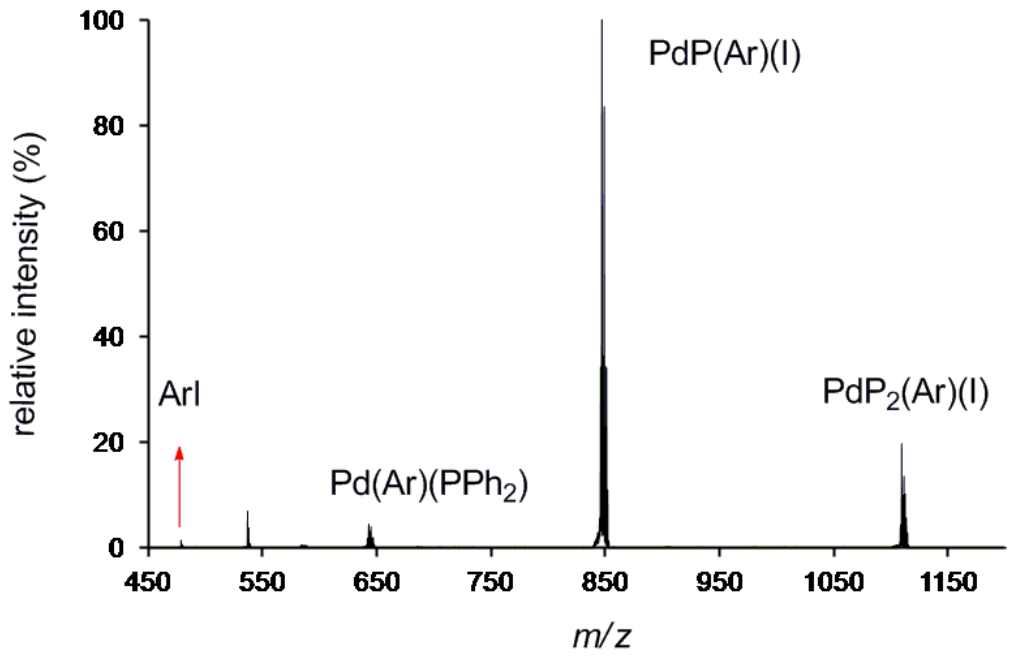

Figure 4.7: ESI(+)-MS/MS of $PdP_2(Ar)(I)$ (*m/z* 1109.4). Fragmentation occurs via loss of triphenylphosphine not loss of ArI indicating that elimination of ArI is not facile.

MS/MS experiments on $PdP_2(Ar)(C_2Ph)$ (*m/z* 1083.4) also confirmed its composition. The most abundant fragment as opposed to the previous study, is the product of RE of ArC_2Ph at *m/z* 453.2[166]. Loss of one and two PPh_3 was also observed respectively at *m/z* 821.1 and 559.1 (Figure 4.7).

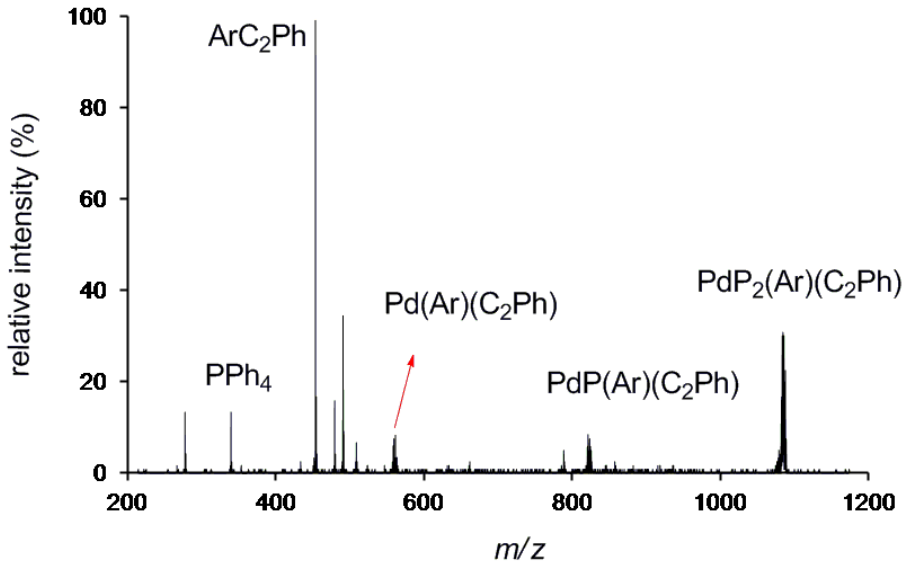

Figure 4.8: ESI(+)-MS/MS of $PdP_2(Ar)(C_2Ph)$ (*m/z* 1083.4). ArC_2Ph is the most abundant fragment which denotes that reductive elimination of the product is favourable. Loss of one and two triphenylphoshpine is observed. No attempt was made to assign all the peaks.

To make sure whether reproducibility is achieved the reaction was repeated several times within an accepted range of error. Early on, it was nearly impossible to obtain reproducible data. The main reason was that the amount of catalyst required for each reaction was very low and therefore, weighing of the low amount of it without exposure to the air was difficult. To solve this issue a stock catalyst solution was prepared and a portion of it was added to the reaction mixture at optimum time. However, the stability of the catalyst stock solution was inconsistent over time. So each portion of catalyst solution had different amount of active precatalyst and hence different reactivity. To overcome the problem, we decided to make the stock catalyst solution in the glovebox and keep it in a freezer in the glovebox between each experiment at -32°C away from light. With this method we improved the reproducibility significantly. Another problem was found when using a same reaction flask for more than one reaction. Each time that reaction was repeated in the same flask even after washing it several times with the same solvent, reaction was slower than the previous one. Perhaps it could be the result of palladium nanoparticle formation on the inside wall of the flask or built-up of the conjugate acid of the base that possibly remains even after washing the flask. To ensure reproducibility, a consistent protocol was developed for the operation and methodology

thereafter (Section 4.3). Figure 4.9 shows the reaction with the same reaction condition and the same stock solution but on two different days.

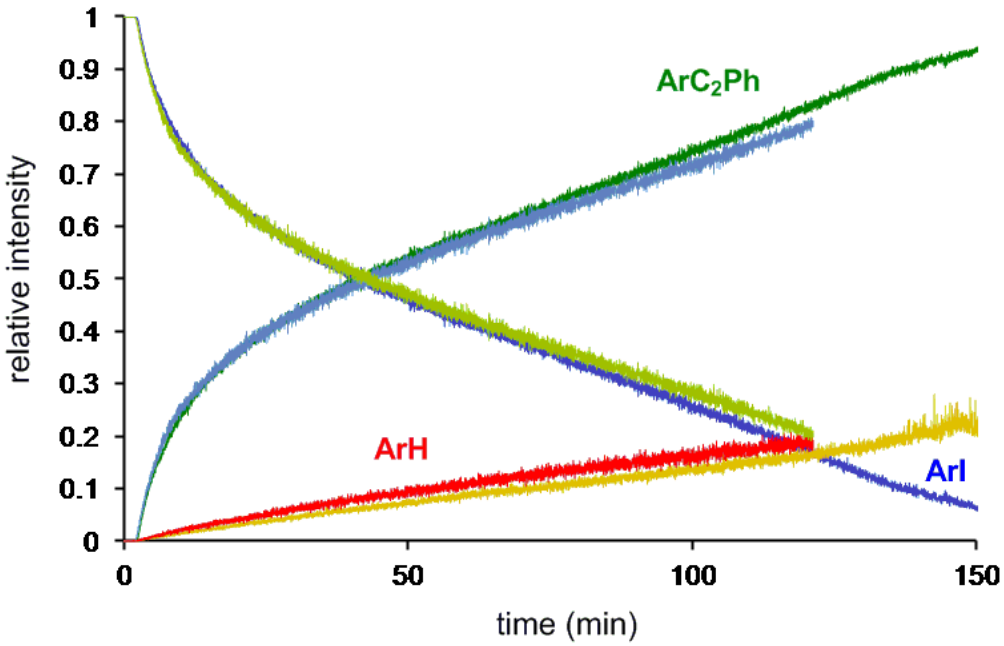

Figure 4.9: Sonogashira reaction with the same condition and same stock catalyst solution. Reactions were performed on two different days.

4.2.2 Mechanism investigation by base alteration

Figure 4.10 shows the trace of observed species over the course of the reaction under "standard conditions". Going forward, we use this term, which represents the reaction condition; MeOH as the solvent at reflux, 0.5 mM charged aryl iodide and 0.6 mM phenylacetylene, with 6% catalyst $Pd(PPh_3)_4$ and 2.5 psi N_2 as the overpressure. There are over 9500 data points represented in this plot each representing a full mass spectrum. The key point in this reaction is a distinct change in the reaction rate at about 20 minutes when the initial fast process is replaced by a slower zero-order process while the rate of byproduct formation in this situation remains unaffected with zero order throughout. Initially we hypothesized that the anionic mechanism proposed by Jutand is operating here. In that case reaction should be faster initially since cycle proceeds through typical $Pd(0)L_2$ active catalyst, whereas by increasing the amount of released halide the more stable palladium species $[PdL_2I]^-$ dominates, which might be responsible for the slower process (Scheme 4.7). However, we did not find any evidence that any such species exist.

We will explain the effort we made for direct observation of anionic species later in this chapter (Section 4.2.7).

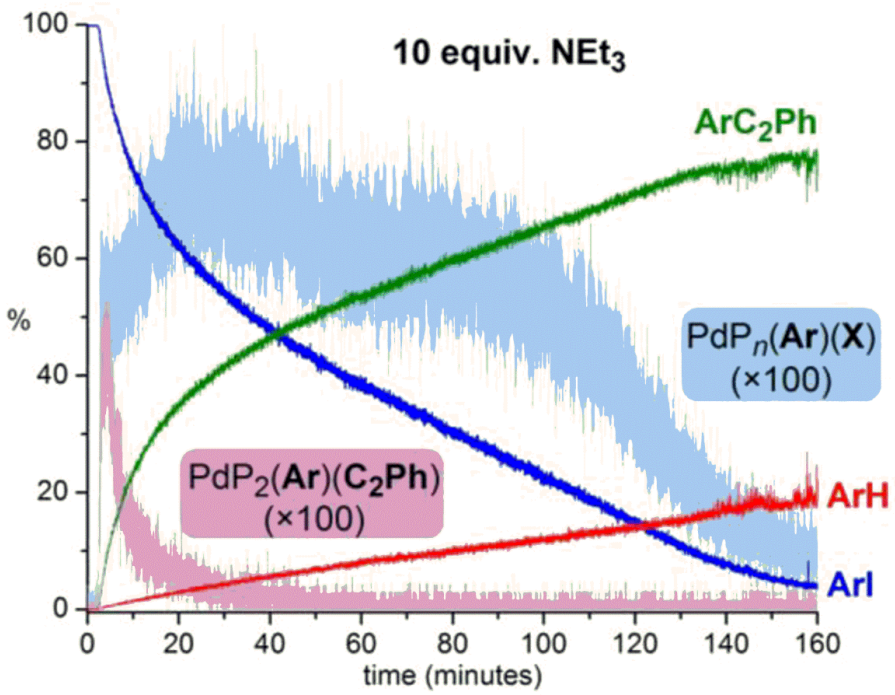

Figure 4.10: ESI(+)-MS intensities over time of all key species bearing the charged tag $[C_6H_4CH_2PPh_3]^+$ (Ar = $[C_6H_4CH_2PPh_3]^+$; P = PPh_3). The intensities of the palladium-containing intermediates have been multiplied by 100.

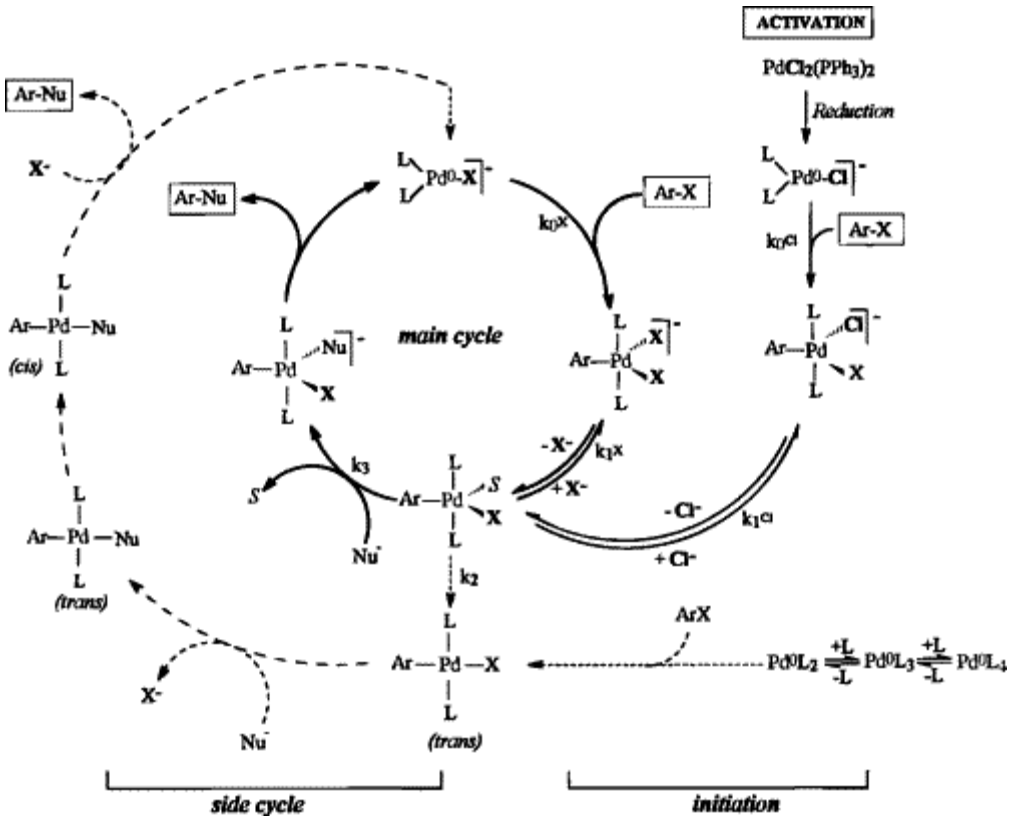

Scheme 4.7: Mechanism of palladium-catalyzed cross-coupling reactions by Jutand et al. Reprinted with permission from "Anionic Pd(0) and Pd(II) Intermediates in Palladium-Catalyzed Heck and Cross-Coupling Reactions" C. Amatore and A. Jutand, *Acc. Chem. Res.*, **2000**, 33, 314-321. Copyright © 2008, American Chemical Society.

Closer examination of the reaction profile gave us some clues about the mechanism changeover. The change in rate corresponds to the disappearance of the $PdP_2(Ar)(C_2Ph)$ while the $PdP_2(Ar)(I)$ signal reaches the maximum (then it remains approximately constant until reaction is nearly over). We assume that before $PdP_2(Ar)(C_2Ph)$ reaches the maximum, reductive elimination (RE) must be the turnover limiting and when $PdP_2(Ar)(C_2Ph)$ starts to disappear while $PdP_2(Ar)(I)$ is still in steady state, TM is taking over to become the turnover limiting step. But what causes this changeover to the mechanism? It is obvious that as the reaction progresses, HI is built up as the by-product in the reaction mixture. However, we were not confident as to whether $[H]^+$ or $[I]^-$ or maybe both caused this problem. Scheme 4.8 shows the mechanism we proposed based on direct observation of intermediates. Steps **2** and **3** are involved in production of

$PdP_2(Ar)(C_2Ph)$s, step **2** should remain unaffected by HI increase over time, but step **3** potentially can be affected by reaction progress. If build-up of $[H]^+$ or $[I]^-$ pushes this equilibrium backward, the overall reaction will be slower. To see which ion is responsible, $[NEt_4]^+[I]^-$ (one equivalent with respect to substrate) was added as a source of iodide. Although reaction was *slightly* slower, the shape of reaction did not change and it had two distinct slopes. In the second reaction one equivalent $[NEt_3H]^+$ $[I]^-$ was added as a source of protons. Interestingly, the addition of this reagent entirely shut down the initial fast reaction, and the reaction proceeded under zero-order kinetics throughout. $PdP_2(Ar)(C_2Ph)$ is almost absent and $PdP_2(Ar)(I)$ is roughly constant (Figure 4.11).

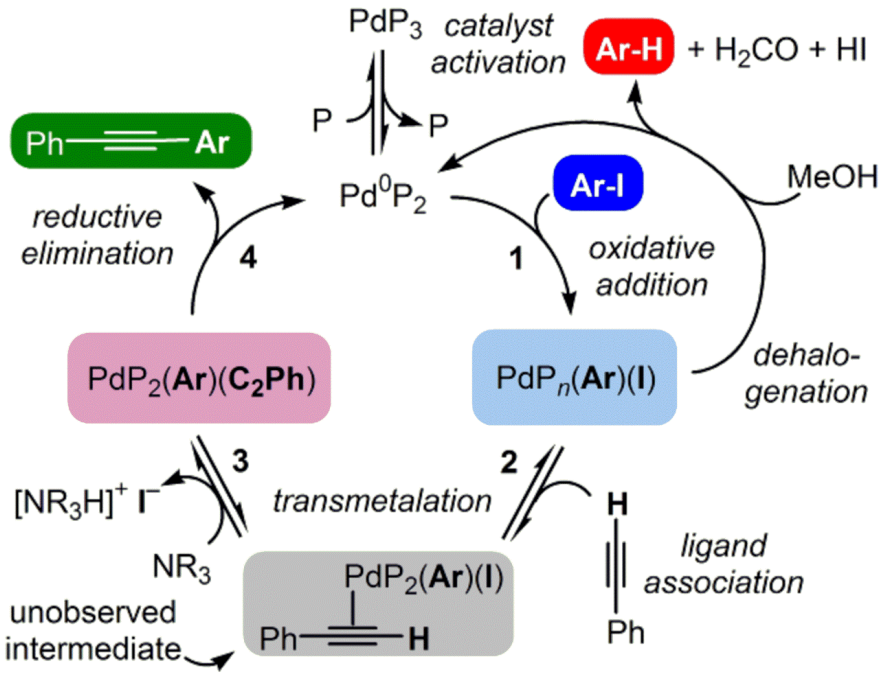

Scheme 4.8: Proposed mechanism for Sonogashira reaction based on direct observation of key intermediates as well as reaction modifications. Gray intermediate was not observed, but its existence was inferred.

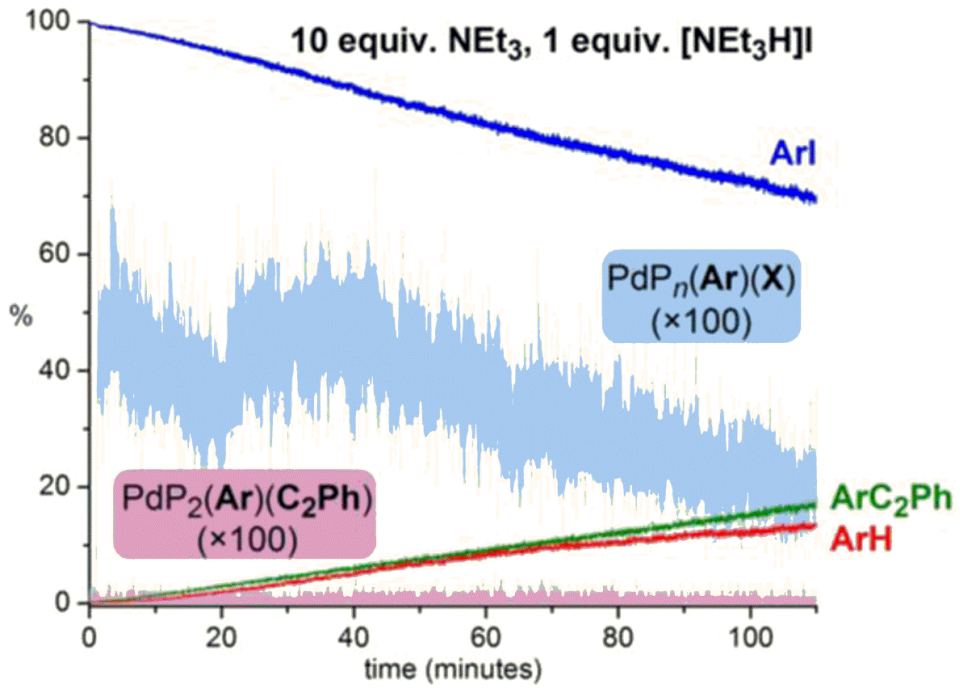

Figure 4.11: ESI(+)-MS over time for the intensity of all key species bearing the charged tag aryl iodide for the reaction with one equivalent $[Et_3NH]^+[I]^-$ as the source of protons.

This experiment also provides some insight into the side-cycle of this reaction. While addition of protons slows down the main cycle, it leaves the rate of hydrodehalogenation unaffected. It suggests that protonation/deprotonation is not turnover limiting with respect to byproduct formation.

If the addition of conjugated acid suppresses the reaction by pushing the equilibrium of the deprotonation backward, using a stronger base instead of Et_3N should sequester the proton more efficiently and hence keep up the fast initial rate. The reaction was repeated with DBU (1,8-diazabicyclo[5.4.0]undec-7-ene) as base (pK_a of ~13.9 [167] compared to 9.0 for NEt_3[168] in DMSO) and as predicted the faster first-order regime is maintained entirely.

In this case, because the dehalogenation reaction cannot compete effectively with the main cycle, not only is the reaction faster also is cleaner. Since the backwards reaction in the deprotonation step is less favourable, the amount of $PdP_2(Ar)(C_2Ph)$ is higher (almost double) and steadier so reductive elimination remains turnover limiting throughout (Figure 4.12). Figure 4.13 allows the direct comparison of the formation of product under

the three different reaction conditions. It clearly shows that how understanding the mechanism can help to improve reaction performance.

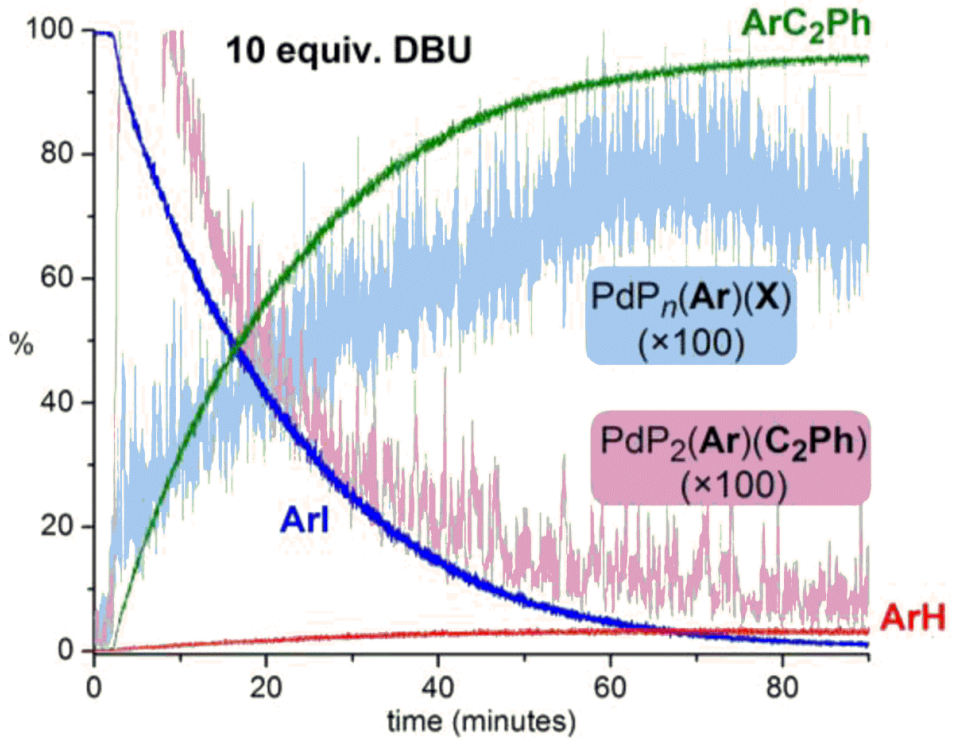

Figure 4.12: ESI(+)-MS over time for the intensity of all key species bearing the charged tag aryl iodide where DBU was used in place of NEt_3.

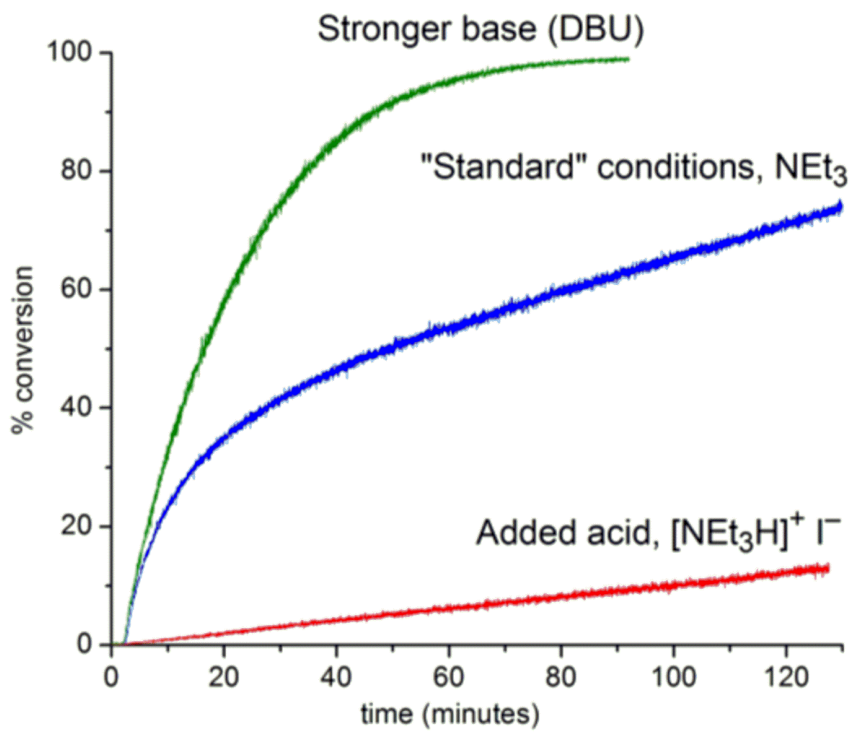

Figure 4.13: ESI(+)-MS over time for the intensity of charged tag product when using different bases and added acid (all other experimental conditions kept constant).

With respect to experimental data and observed intermediates, a numerical model of this catalytic cycle was constructed and rate constants were optimized to respond to the "standard reaction conditions". Rate constants were extracted for all involved steps. For the reaction with DBU the rate constant of deprotonation and reprotonation, were tweaked to obtain the closest match with experimental data. Figures 4.14 - 4.16 show the results. Based on extracted rate constants, reprotonation (**-3**) for the DBU experiment should be approximately ten times slower than the Et_3N experiment which overall causes the faster reaction. For $[Et_3NH]^+$ no tweaking in rate constants was necessary (this is a component of the original reaction) and simply changing the initial concentration from zero to one equivalent of the acid slows down the reaction. Approximately optimized rate constant values for each step of "standard conditions" with Et_3N reaction are reported in Scheme 4.9.

It is clear that the reactions are also affected by catalyst decomposition, as there is a tendency for concentration of the $PdL_n(Ar)(X)$ intermediate to taper off during the reaction (and the reaction to halt before completion as a result). We have not attempted to

model this behavior at this stage. However, later in this chapter we will explain this behaviour.

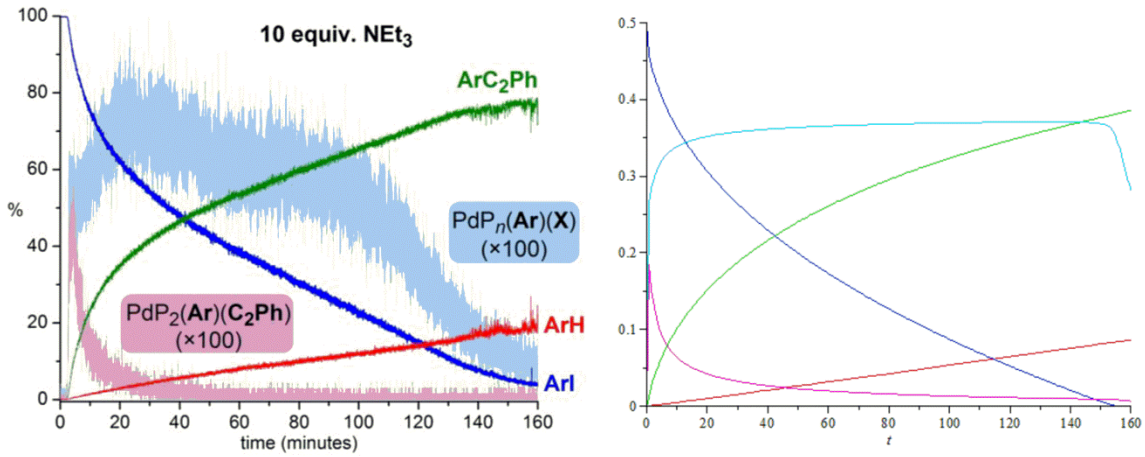

Figure 4.14: Reaction progress: experimental (left) and numerically modelled using Maple (right), under standard conditions.

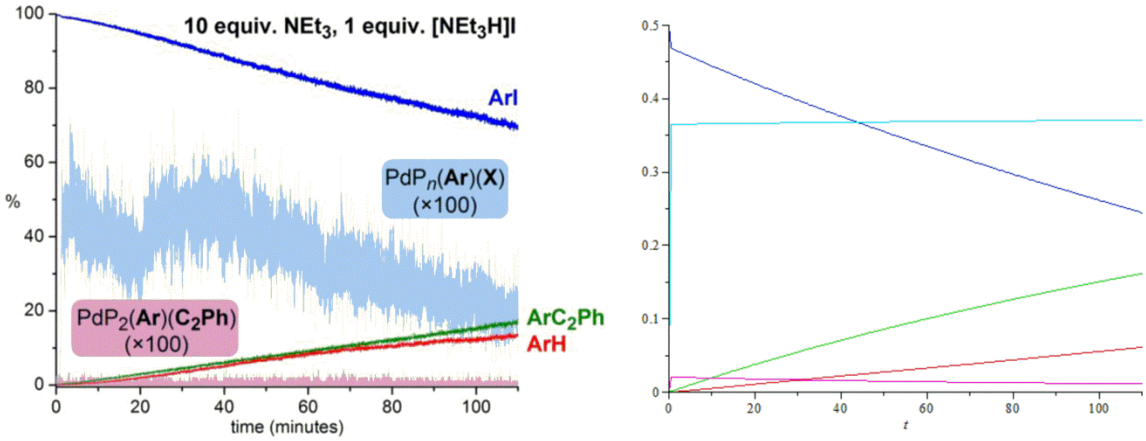

Figure 4.15: Reaction progress: experimental (left) and numerically modelled using Maple (right), under the same conditions in Figure 4.14 except for the addition of one equivalent of $[NEt_3H]^+[I]^-$ at the start of the reaction.

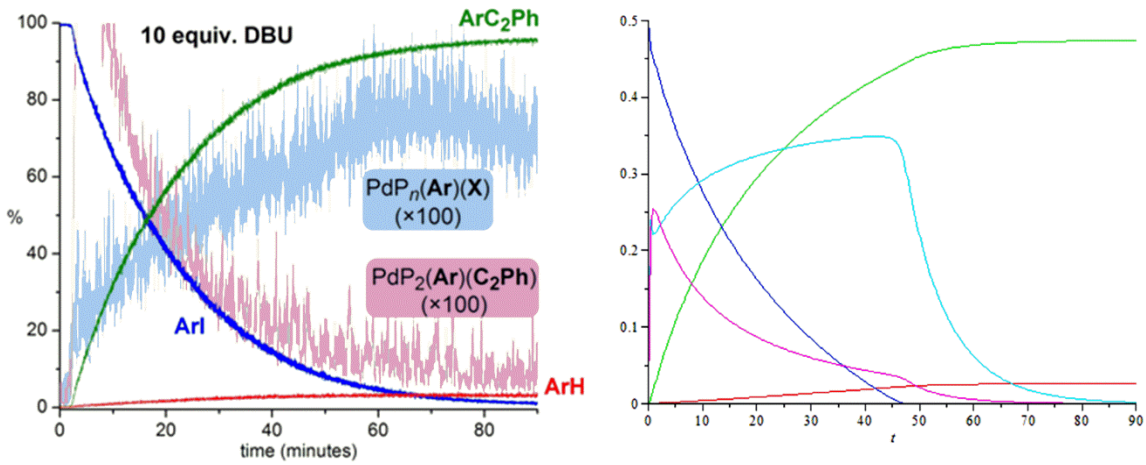

Figure 4.16: Reaction progress: experimental (left) and numerically modelled using Maple (right), under the same conditions in Figure 4.14 except NEt_3 has been substituted by DBU, and this effect was approximated by decreasing the rate constant of the reverse reaction of **3** from 100 to 10.

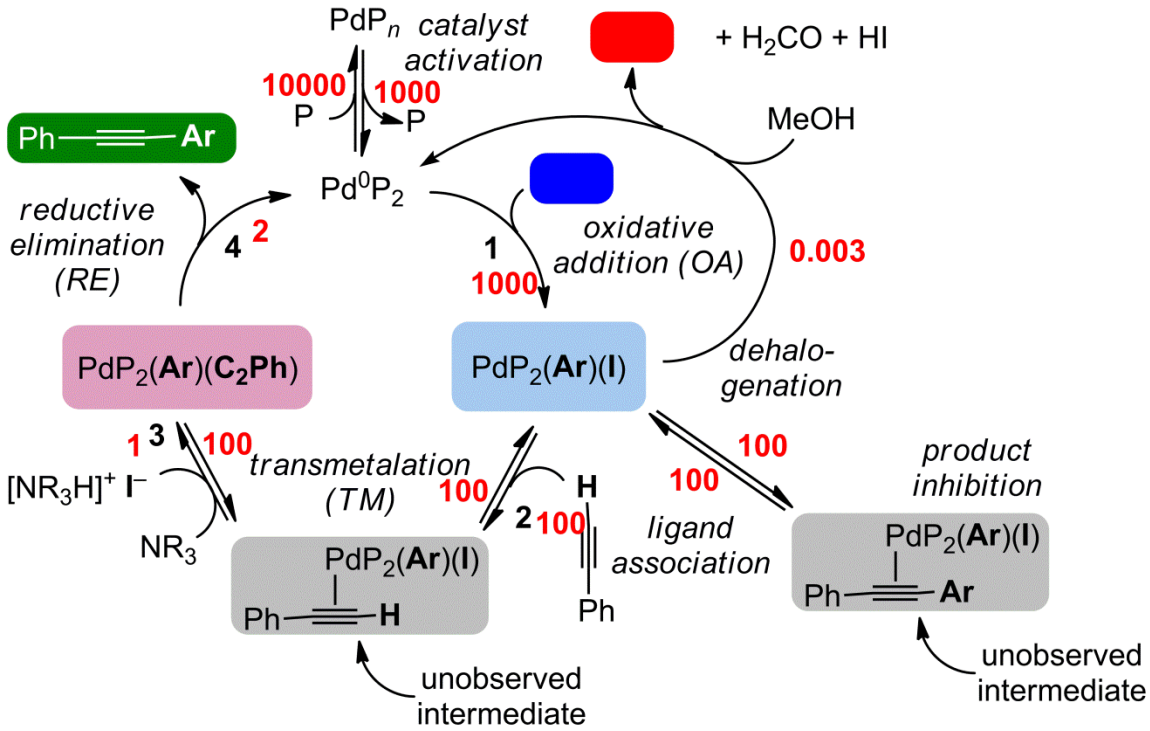

Scheme 4.9: Catalytic cycle and rate constants (red) used to simulate the reaction progress. Concentrations used were the same as employed experimentally. In this model product inhibition was hypothesized in the cycle, however further study on this part will be explained in section (4.2.6).

After establishing of the PSI-ESI-MS application in terms of reliability and accuracy of the observed data, intermediate probing, alteration in mechanism and employing numerical modeling to interpret the results, we pursued our investigation on Sonogashira reaction with variety of other experiments. So far we realized that the turnover limiting step is reductive elimination throughout, unless the base is unable to deprotonate the phenylacetylene effectively in which case, the transmetallation step becomes turnover limiting (because the reaction lies a long way towards the deprotonated alkyne). But we were unsure that what we observed so far was the whole picture of the mechanism operating here and whether any other parallel mechanism was present. There is evidence about the multiple roles of the base in the literature. As the first step, we interrogated spectra over time to try to find any amine/Pd-containing species over the course of the reaction. In case of Et_3N, no such species was observed. However, with DBU, we found two DBU-containing species. $PdP_2(Ar)(DBU)$ (doubly charged, *m/z* 567.1) and $PdP(Ar)(DBU)_2$ (doubly charged, *m/z* 512.2). MS/MS on both of these species confirmed their structures (Figure 4.17 and 4.18). Major fragments in $PdP_2(Ar)(DBU)$ is loss of one PPh_3 ligand (doubly charged, *m/z* 436.2) and one DBU (doubly charged species, *m/z* 491.5). One interesting fragment was $Pd(Ar)(PPh_2)$ (singly charged, *m/z* 643.1). In this case, in a potential reaction between two PPh_3 ligands, a phenyl group of one PPh_3 is pulled off by another PPh_3 to make a diphenylphosphido ligand. The other product is $[PPh_4]^+$, which is a common fragment in this type of spectra.

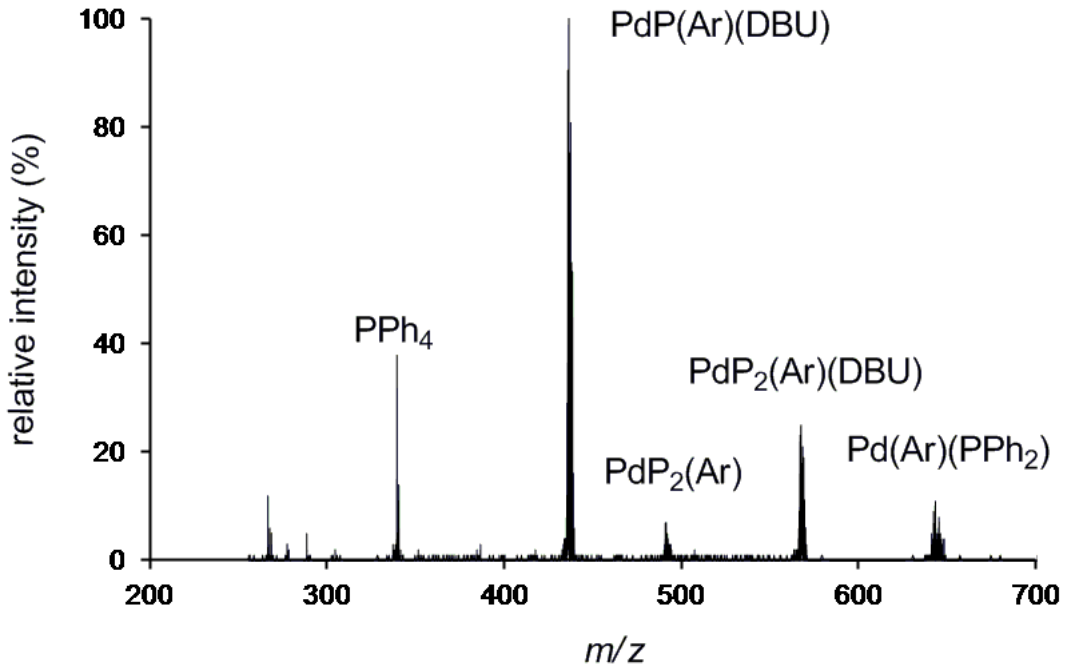

Figure 4.17: ESI(+)-MS/MS of $PdP_2(Ar)(DBU)$ (doubly charged, *m/z* 567.1). The most abundant fragment is obtained by the loss of one triphenylphoshpine (doubly charged, *m/z* 436.2). Also the loss of DBU is observed (doubly charged, *m/z* 491.5).

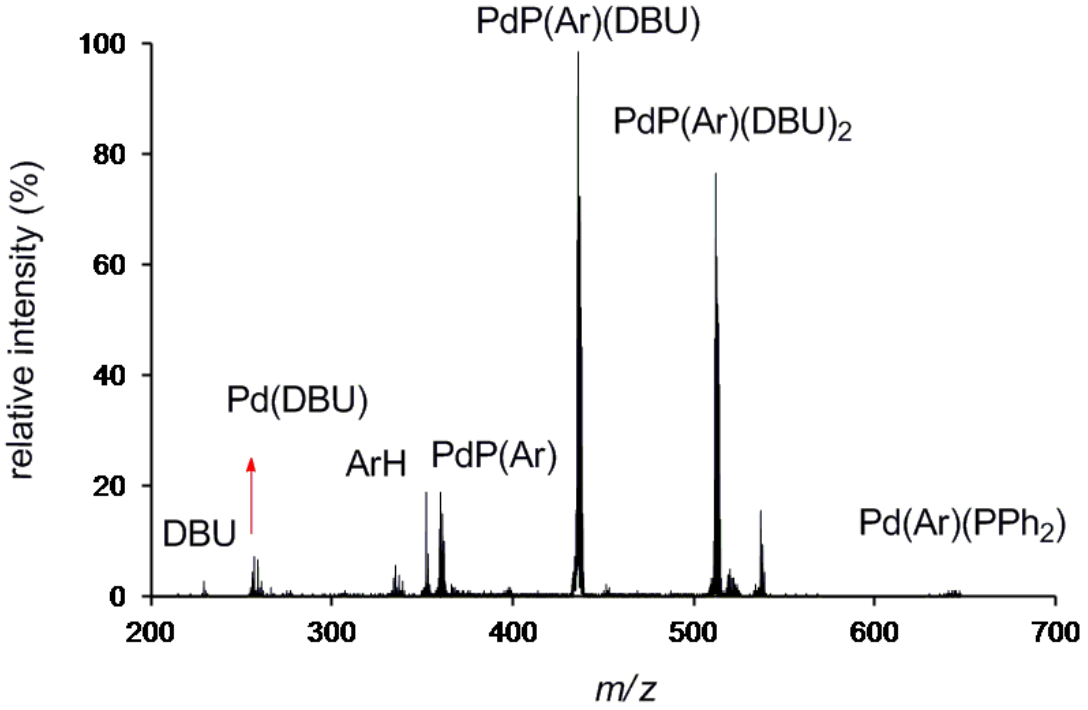

Figure 4.18: ESI(+)-MS/MS of $PdP(Ar)(DBU)_2$ (doubly charged, *m/z* 512.3). The most abundant fragment is obtained by the loss of one DBU (doubly charged, *m/z* 436.2). Also the loss of the second DBU (doubly charged, *m/z* 360.1).

The formation of base-containing species is the result of displacing iodide from PdL_nArI. In order to see how fast this substitution occurs under normal reaction conditions, as usual, ten equivalents of DBU was added to the reaction mixture in the absence of phenylacetylene at reflux. As Figure 4.19 shows, ligand replacement happened in a few seconds. Intensity of $PdL(Ar)(DBU)_2$ is about three times as the intensity of $PdL_2(Ar)(DBU)$. However we have no indication of their response factors and intensity may not be necessarily representative of their concentrations. It is also unclear whether the second DBU replacement is the result of direct substitution with second PPh_3 or it happens after PPh_3 falls off first in the solution to make PdLAr. This observation may suggest that base-containing species are involved in the mechanism as the active intermediates toward transmetallation instead of PdL_nArI.

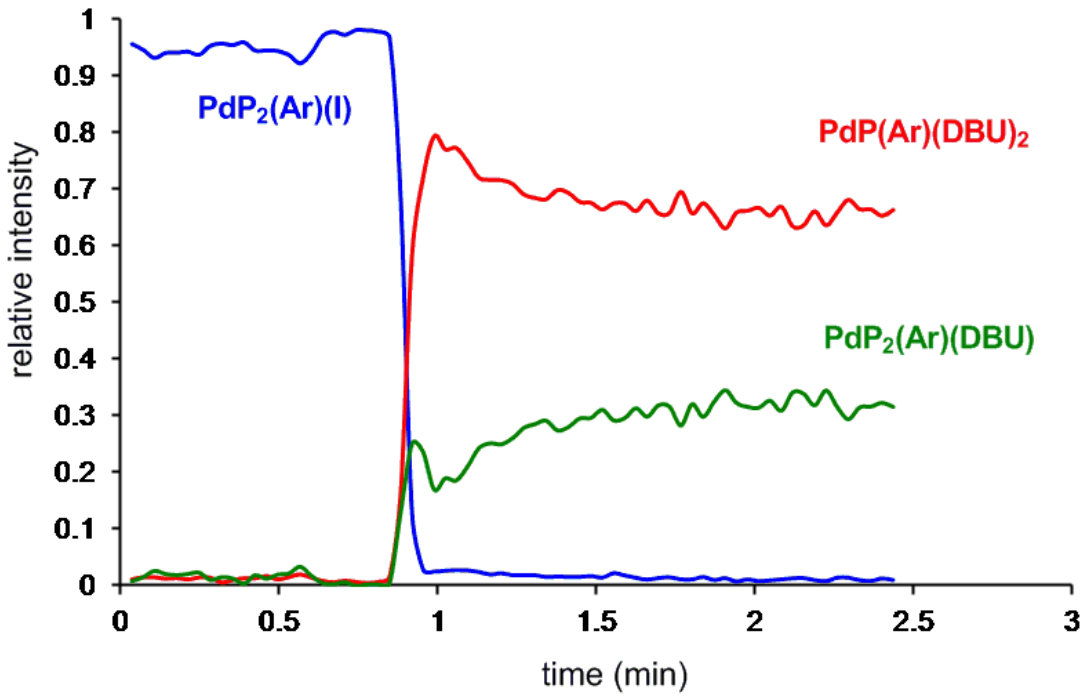

Figure 4.19: Addition of ten equivalents of DBU to the mixture of charged ArI and catalyst in standard condition at reflux.

As a separate experiment, a reaction was performed in the absence of amine to see whether any other key species were present in the reaction mixture under typical catalytic conditions. We were particularly looking for any artifact which may indicate that

carbopalladation is operating in the absence of base since formation of the related species may not require amine. Figure 4.20 shows the reaction profile. As shows reaction still progresses but very slowly and less than 1% product forms after 40 minutes. The only observed species was the $PdP_2(Ar)(I)$ and no other palladium containing species was observed.

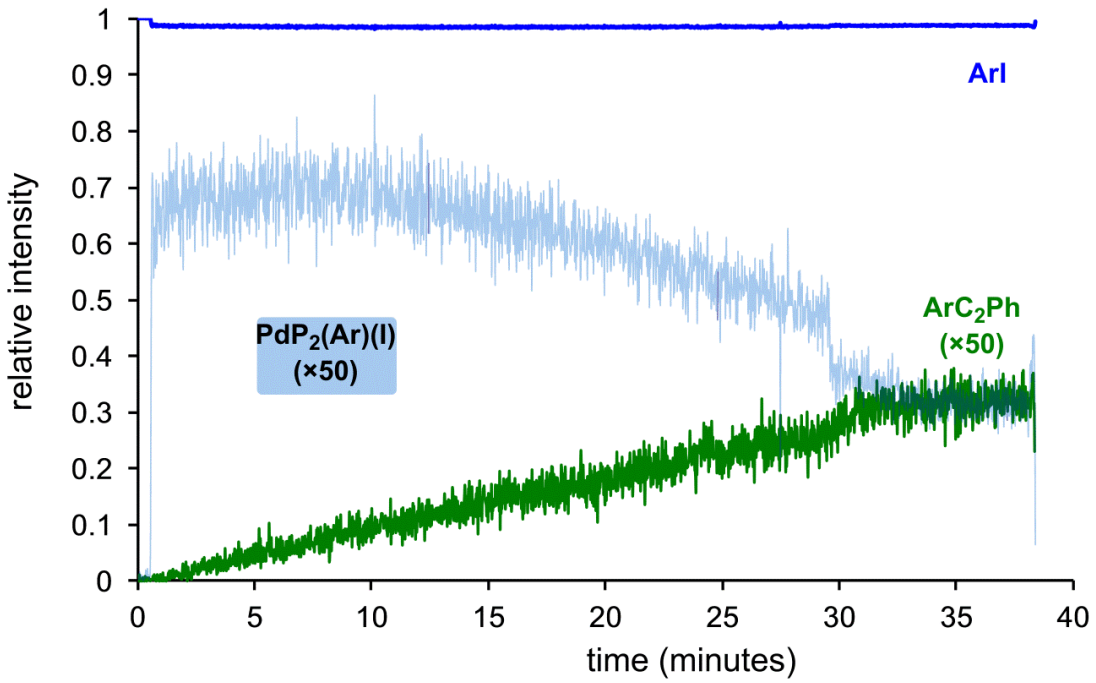

Figure 4.20: ESI(+)-MS over time for the intensity of all key species bearing the charged tag. The intensities of the product and $PdP_2(Ar)(I)$ have been multiplied by 50.

4.2.3 Reaction with a charged terminal alkyne

So far we have detected the key intermediates of Sonogashira reaction by employing the charged tag aryl iodide. For a new series of experiments charged terminal alkyne ([*p*-$HCCC_6H_4CH_2PPh_3]^+[PF_6]^-$) was synthesized and employed for monitoring purposes. This tag provided the opportunity to observe any potential alkyne-containing species that were unobservable using the charged tag aryl iodide. Again, phosphonium tag was employed to ensure reliable stability and surface activity in ESI(+)-MS. Scheme 4.10 shows the reaction pathway under the standard conditions.

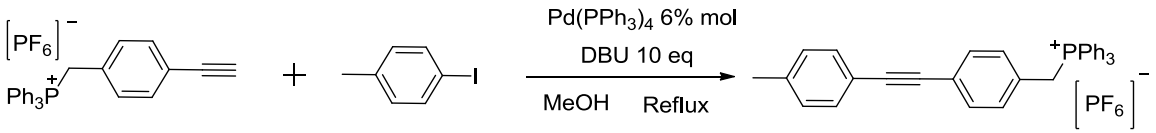

Scheme 4.10: Reaction of charged tag alkyne [p- $HCCC_6H_4CH_2PPh_3]^+$ with 1-iodo-4-methylbenzene.

In addition to the charged substrate and product, two other key intermediates were observed. These two intermediates are shown in Figure 4.21. The first intermediate is the product of substitution of base (DBU) with iodide in $PdP_2(Ar)(I)$ to form $[PdL_nAr(DBU)_n]^+$. This intermediate does not contain any tag and its charge is the result of the replacement of the anionic ligand (iodide) with a neutral ligand (DBU). Another intermediate is the $[PdL_2Ar(Ar'C_2)]^+$ (Ar'= $[C_6H_4CH_2PPh_3]^+$) and no other intermediates were observed. Given that the natures of the two intermediates are different, their surface activities in ESI-MS are not necessarily equal. We specifically searched for any hint of $[PdL_n\ (Ar'C_2)_2]^+$, which might RE a dialkyne to produce the homocoupling product $(Ar'C_2)_2$, a common byproduct in Sonogashira (with copper)[169] but no such species were observed. This observation confirms that no other side-cycle is operating in this condition and we can confidently focus on the rest of the investigation.

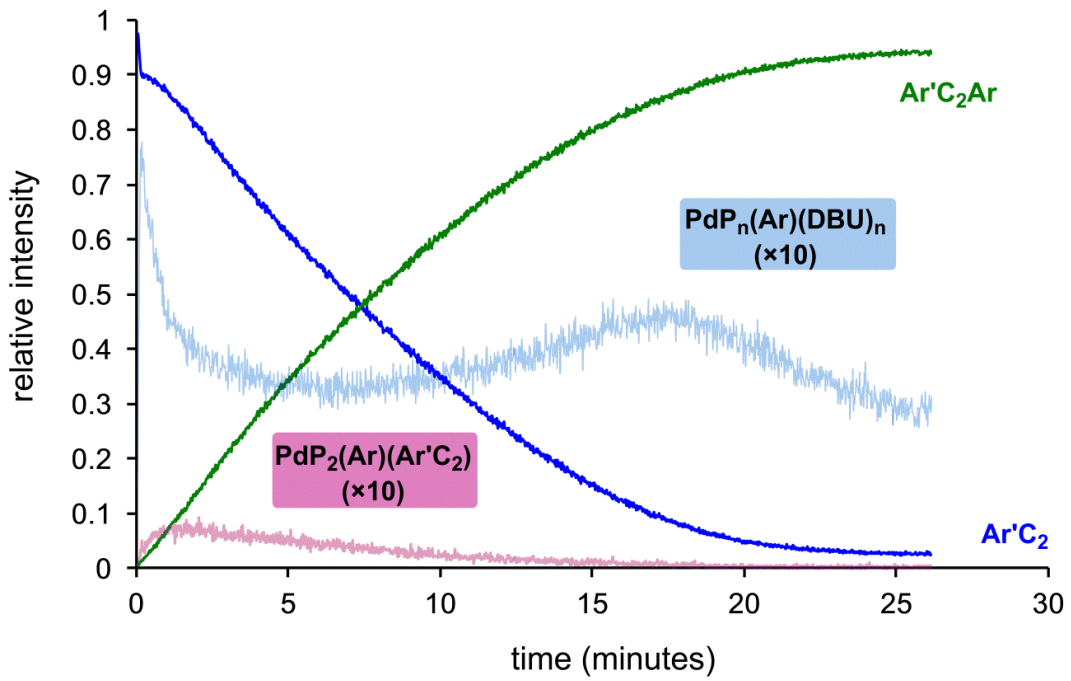

Figure 4.21: ESI(+)-MS over time for the intensity of all key species bearing the charged tag [p-$HCCC_6H_4CH_2PPh_3]^+$ (Ar' = $[C_6H_4CH_2PPh_3]^+$; P = PPh_3) (Ar = 1-iodo-4-methylbenzene). The intensities of the palladium-containing intermediates have been multiplied by 10.

4.2.4 Multisubstrates screening by PSI-ESI-MS

One approach to investigate the kinetic and mechanism of reactions is to study the influence of various structural and electronic variables on the outcome of the reaction and then identifying the key factor(s) by further analysis. For instance, Hammett plots are used to obtain mechanistic data especially about the turnover limiting step. In a Hammett plot, reactivities of aromatic reactants with different substituents are compared, which give an indication of the factors influencing the key step in the reaction. However, it is not always easy to change the substituent while keeping the rest of conditions identical. One way to solve this issue is to carry out various reactions in one vessel with only one single catalyst. This method was introduced by Kagan et al[170, 171] and called "one pot multisubstrates screening".

This method has several advantages; first, it is fast. The required time for all analyses is reduced significantly. Furthermore, condition is truly identical to the all substrates, so the result of experiment cannot be affected by bias or experimental conditions. The most

important factor is catalyst handling, which can be easily compromised by reactivity and sensitivity of stock catalyst solution over time. However, there are some limitations for this technique. The rate of formation for each product should be within two orders of magnitudes otherwise the effective catalyst concentration will not remain constant for all substrates. In fact, the production rate will be less for faster and more for slower reactions. Figure 4.22 demonstrates an example of using this technique in Sonogashira (with copper) reaction for three *para*-substituted aryl bromide.[163] The linear fit to each graph illustrates the appropriate method of slope selection for rate calculation (i.e. using initial rates).

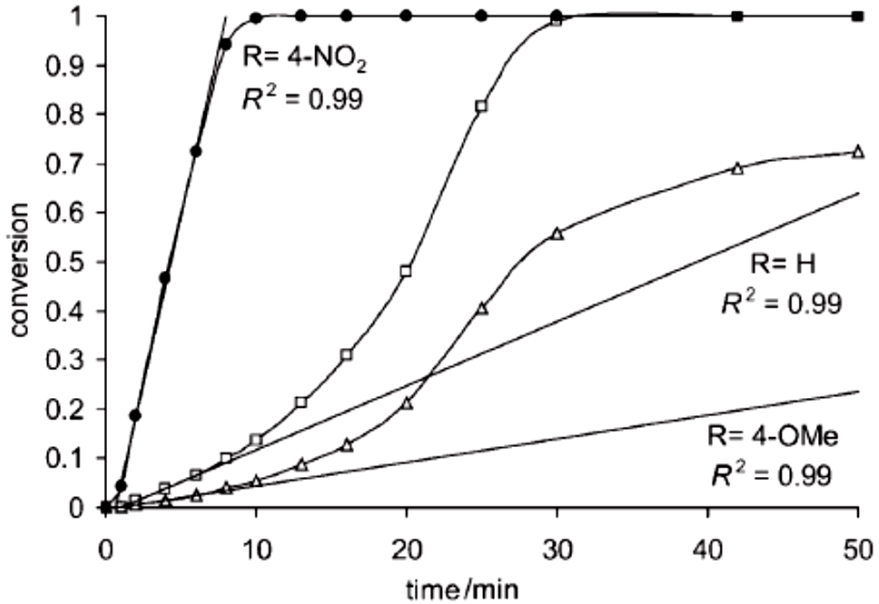

Figure 4.22: Conversion versus time curves and determination of the initial rates of the product-forming reaction. "R" symbols indicate the *para*-substituent on the aryl bromide. R^2 is the correlation coefficient of the linear fit. Reprinted with permission from "Insights into Sonogashira Cross-Coupling by High-Throughput Kinetics and Descriptor Modeling" M. R. an der Heiden, H. Plenio, S. Immel, E. Burello, G. Rothenberg and H. C. J. Hoefsloot, *Chem. --Eu. J.*, **2008**, 14, 2857-2866. Copyright © 2008 WILEY-VCH Verlag GmbH & Co. KGaA, Weinheim.

We decided to employ this technique for PSI-ESI-MS initially to test this method, where the combination of fast time resolved technique (one spectrum per second) and accurate multisubstrates screening can make a unique methodology for catalysis studies.

As the first experiment we examined the reactivity of the charged alkyne with six *para*-substituted aryl iodides under standard conditions (Scheme 4.11).

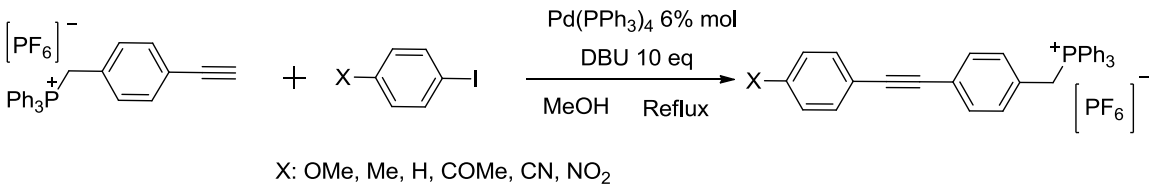

Scheme 4.11: Multisubstrates screening of the charged alkyne with six *para*- substituted aryl iodides.

Reaction was tracked for more than 90% progress and the initial linear part of each product line (Figure 4.23 and 4.24) were selected and a Hammett plot for the series generated. As shown in Figure 4.25, the data correlate nicely with σ_ρ values with R^2 = 0.96. The positive slope of the plot (ρ = 1.4) indicates that the reaction is more favourable for aryl groups with electron-withdrawing substituent in the *para*-position. Results are in good accordance with previously reported Hammett plot for Sonogashira reaction (with copper)[163] (Figure 4.26). Although the reaction conditions of these two experiments are different, still the same electronic effect is expected. The opposite results were observed for the reductive elimination. [166] However, suggesting that RE is not turnover-limiting in the reaction and instead the transmetallation is the important step. EWGs on the aryl group may be stabilizing the $PdP_2(Ar)(C_2Ar')$ intermediate and making it less prone to reprotonation.

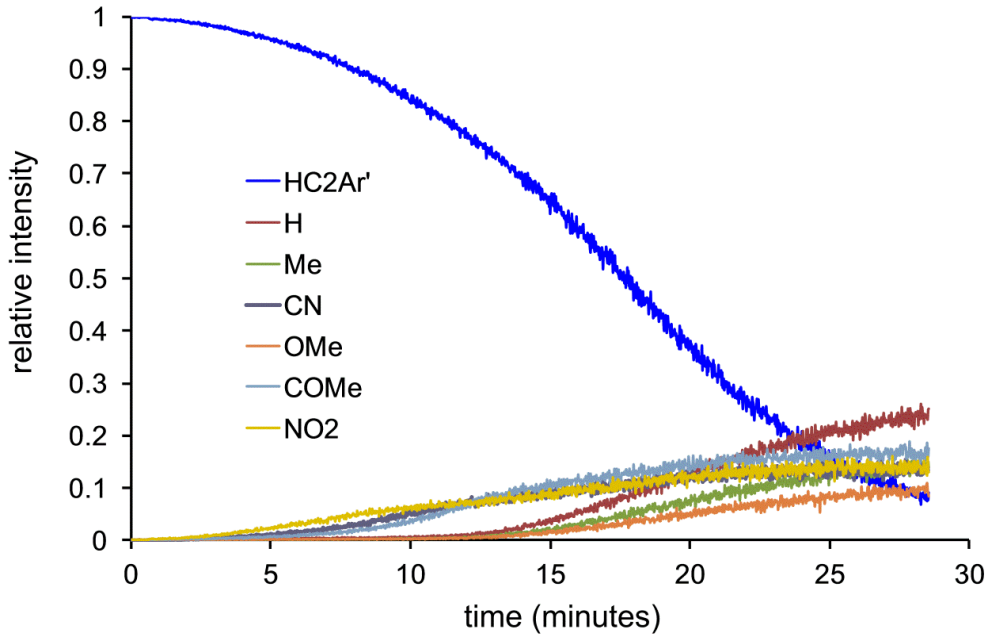

Figure 4.23: Relative intensity versus time for determination of the initial rates of the product-forming reaction. Colored (-) symbols denote the *para*-substituent on the aryl iodide and HC_2Ar' refers to charged tag alkyne as the reactant.

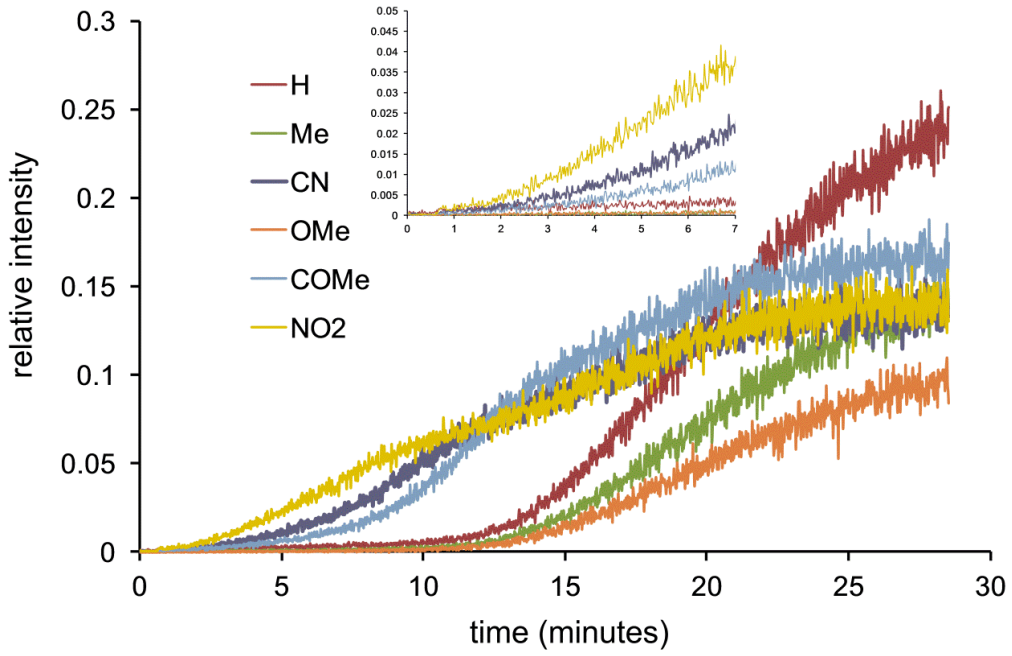

Figure 4.24: Clear formation of products with different rates. Colored (-) symbols denote the *para*-substituent on the aryl iodide and HC_2Ar' refers to charged acetylene as the reactant. Inset: Zoom on first few minutes of product formation. The best linear fit is selected for the reaction rate calculation of each product. Concentration of HC_2Ar' is 0.6 mM versus equal amount of 0.1 mM for each *para*-substituted aryl iodide.

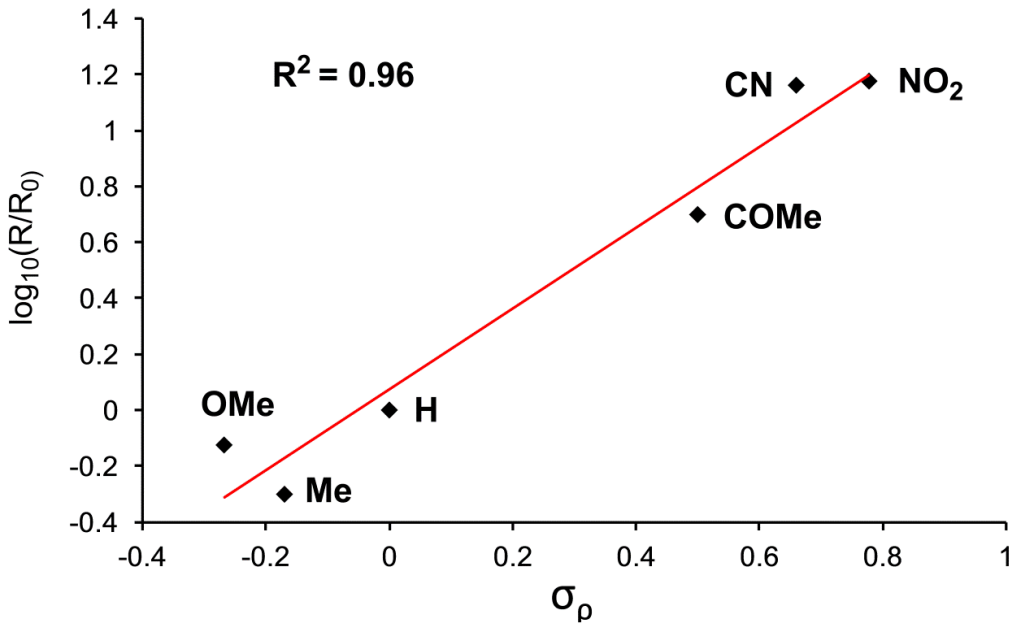

Figure 4.25: Plot of $\log_{10}(P/R)$ vs. Hammett σ_p parameter for a various of para-substituted aryl iodides. R = reaction rate for variable substituent, R_0 = reaction rate for reference substituent H.

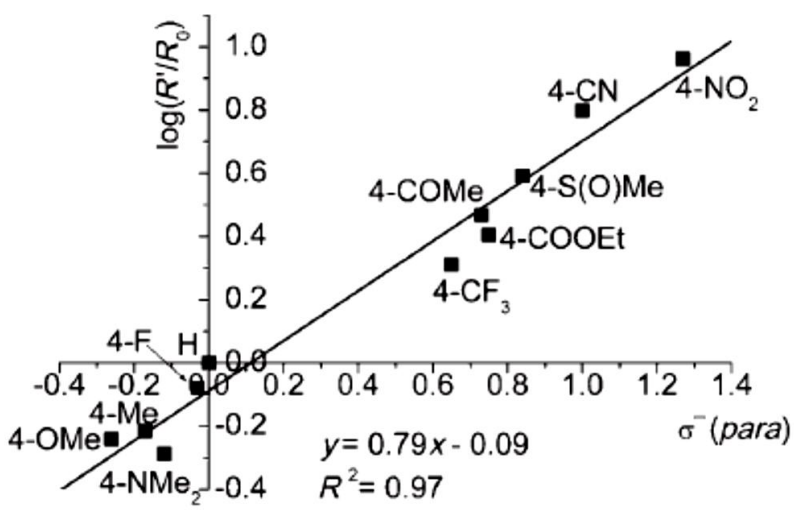

Figure 4.26: Hammett plot for Sonogashira reaction of several para-substituted aryl bromides. Conditions: HN^iPr_2, 80 °C, Na_2PdCl_4, $^tBu_3P$, CuI. Reprinted with permission from "Insights into Sonogashira Cross-Coupling by High-Throughput Kinetics and Descriptor Modeling" M. R. an der Heiden, H. Plenio, S. Immel, E. Burello, G. Rothenberg and H. C. J. Hoefsloot, *Chem. --Eu. J.*, **2008**, 14, 2857-2866. Copyright © 2008 WILEY-VCH Verlag GmbH & Co. KGaA, Weinheim.

The effect of substituent on terminal alkyne partner seems to be more important in our investigation, since the C-H bond cleavage is assumed to be the key step in Sonogashira reaction. Also a changeover in mechanism has been observed by turning from EWG to EDG on *para* position of phenylacetylene.[149] So we applied the same technique to study this effect more in depth for various substrates.

4.2.5 Kinetic isotope effect

The "isotope effect" is one the most important tools, which chemists employ to elucidate the mechanisms of the chemical reactions.[172] The kinetic isotope effect (KIE) is the term used to represent the ratio of rate constants when the two isotopes related in an equation below, where *kj* and *ki* represent the rate constants of the light and heavy isotope respectively. When an isotope of an atom such as H/D is replaced in a reaction, the reaction rate will be changed differently. When formation/cleavage of the bond involves in turnover limiting step, replacement of the isotope of the atom, significantly will alter the reaction rate. This effect is called "primary isotope effect". For instance, the reaction rate in which a C-H bond (formation/cleavage) involves will be 6-10 times slower when deuterium replaces hydrogen. However, if this bond formation/cleavage is not involved in the turnover limiting step, still a minor rate change is observed which is called "secondary isotope effect".[173] In some cases deuterated species react faster than undeuterated species. This phenomenon is called "reverse isotope effect". This phenomenon happens when the transition state is stabilized more in the presence of deuterium compared with hydrogen atom. [174]

$$KIE = \frac{kj}{ki}$$

We have found that for Sonogashira reaction, deuteration of the solvent can result in much faster and cleaner catalytic reaction, thanks to a reverse KIE. In this study methanol was replaced with two other isotopic versions CH_3OD and CD_3OD. Surprisingly both reactions in deuterated solvents were equally faster than the reaction in methanol. The reaction profiles for all three experiments are shown in Figures 4.27-29. In these figures the trace of all charged tag aryl containing Pd species including iodide and DBU ligand are represented as PdP_nArX ($X=I^-$ or DBU) for simplification (in all cases PdP_2ArX is at

very low and steady intensity and the behaviors of $PdPAr(DBU)_2$ and $PdP_2Ar(DBU)$ were almost the same). Figure 4.30 allows better comparison of reaction rates for all three sets of experiments with calculated range of errors. The only tangible difference in intermediate behaviour among these three experiments was a slightly steadier tendency of $PdP_2(Ar)(C_2Ph)$ in CH_3OD and CD_3OD. This observation implies that TM step has been facilitated somehow, but it did not provide insight about the mechanism difference, while we were looking for some other clues to interpret these behaviors.

In section 4.2.2 it was denoted that the rate constants for RE and deprotonation are close to each other. RE is the turnover limiting step throughout in DBU experiment since amine is able to pull out the proton in deprotonation step effectively. However, in Et_3N, deprotonation can compete with RE and win over the turnover limiting step. In deuterated solvents experiments, RE cannot be interfered by deuterated solvent because no hydrogen transfer is involved in this step. But in TM step, deprotonation/reprotonation is involved which can be effectively altered and hence change the reaction rate. The only conceivable option that can lead to overall faster reaction in deuterated solvent is slowing down the reprotonation step. Deprotonation step (**3**) includes the cleavage of a C_{sp}-H bond in the forward direction, but because the protonated amine $[DBUH]^+$ formed in the reaction can readily exchange its H with the deuterated solvent to form $[DBUD]^+$, the reverse reaction (-**3**) now requires the breaking of a C-D bond. As such, the reverse reaction is expected to slow down, thus the reaction overall speeds up dramatically. However, this assumption requires the proton of phenylacetylene to be unaffected before deprotonation occurs. If proton of phenylacetylene is replaced with deuterium then this assumption is not valid anymore, because both directions in deprotonation deal with deuterium not proton. To examine this hypothesis and see how fast proton exchange happens, the charge-tagged terminal alkyne was added to CH_3OD while solution was introduced to MS by PSI technique. Most of the protons were replaced with deuteriums within an hour at room temperature. This result suggests that deuterium replaces proton under standard conditions (reflux) much faster. So above mentioned assumption may not be valid and some other factor triggers the reaction rate overall. Therefore, extra investigations are required to explain these observations

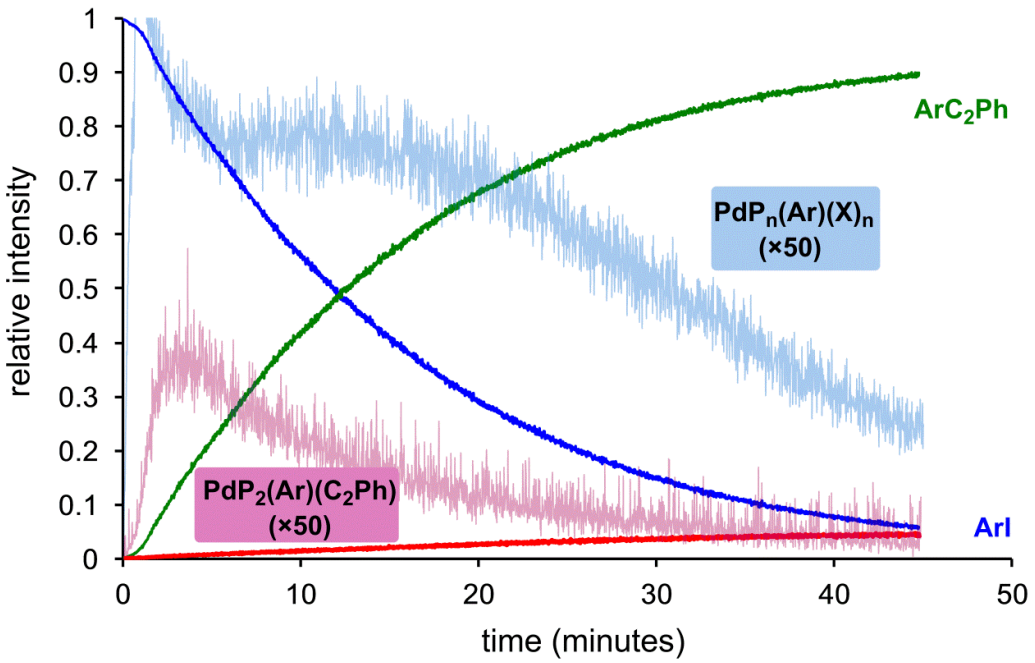

Figure 4.27: ESI(+)-MS over time for the intensity of all key species bearing the charged tag for the normal reaction in MeOH in the presence of DBU. The intensities of the PdP_nArX (X = $[I]^-$ or DBU) and $PdP_2(Ar)(C_2Ph)$ have been multiplied by 50.

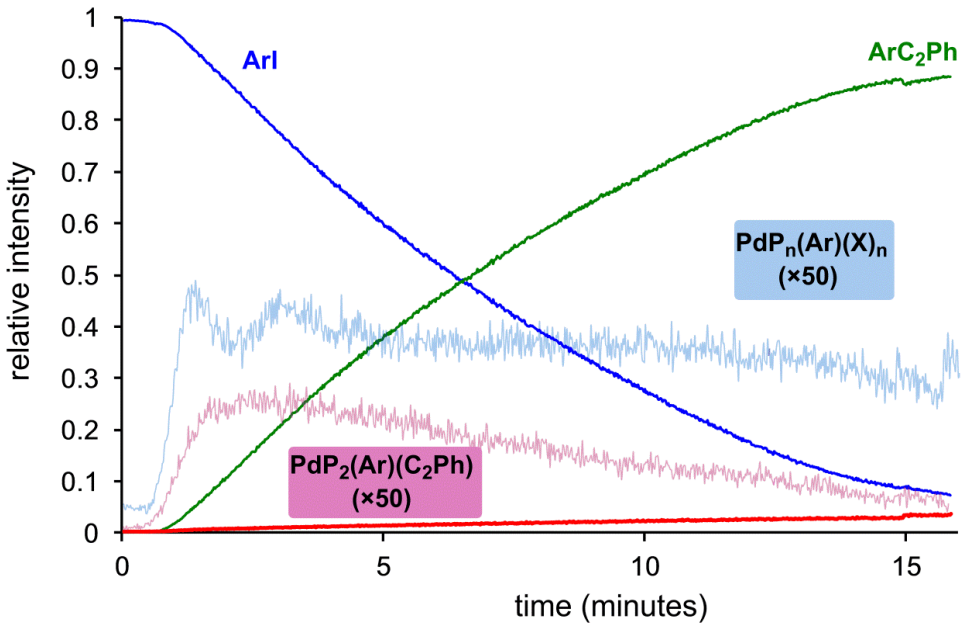

Figure 4.28: ESI(+)-MS over time for the intensity of all key species bearing the charged tag for the normal reaction in CH_3OD in the presence of DBU. The intensities of the PdP_nArX (X = $[I]^-$ or DBU) and $PdP_2(Ar)(C_2Ph)$ have been multiplied by 50.

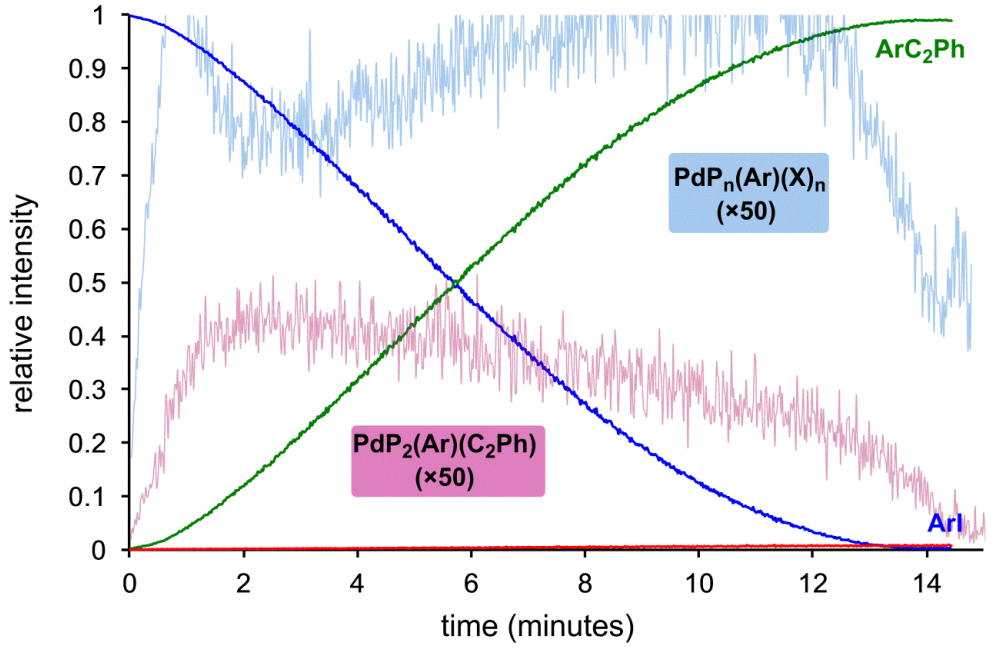

Figure 4.29: ESI(+)-MS over time for the intensity of all key species bearing the charged tag for the normal reaction in CD_3OD in the presence of DBU. The intensities of the PdP_nArX (X = $[I]^-$ or DBU) and $PdP_2(Ar)(C_2Ph)$ have been multiplied by 50.

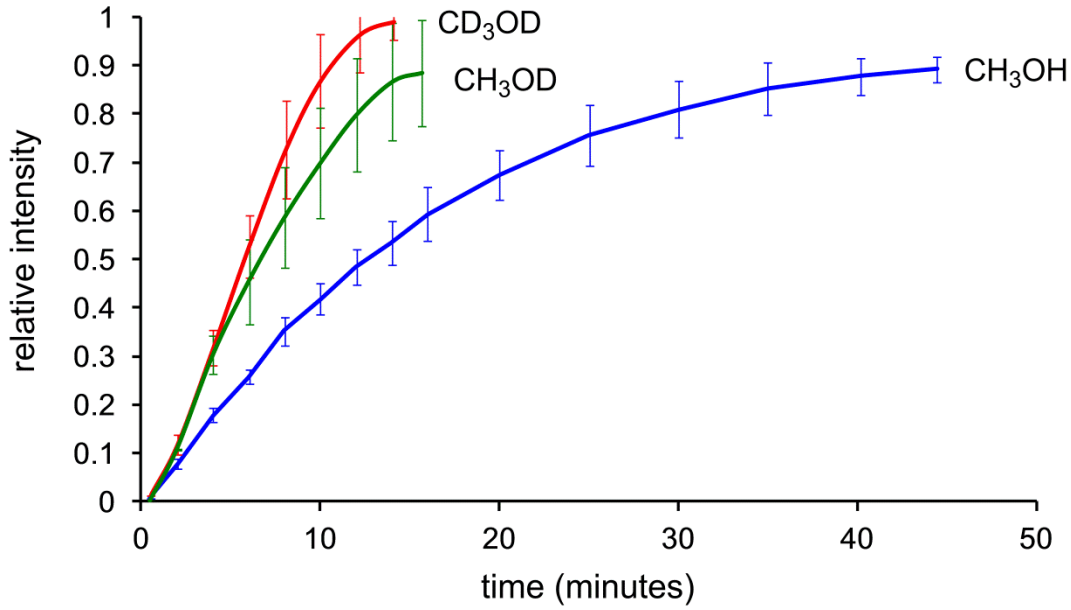

Figure 4.30: Overlay of product built-up in CH_3OH (blue), CH_3OD (green) and CD_3OD (red). Error bars are generated from triplicates (green) and quadruplicates (blue) quintuplicates (red).

To expand our approach and see how electronic effects may change the reaction rate in normal and deuterated solvents six different *para*-substituted phenylacetylenes were chosen and reacted with the charge-tagged aryl iodide in a multisubstrate reaction in both methanol and CD_3OD (Scheme 4.12).

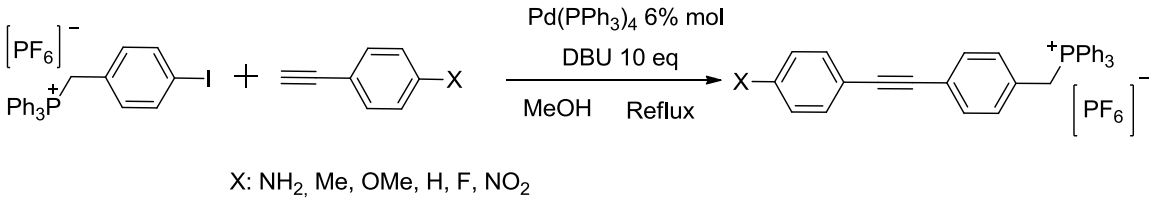

Scheme 4.12: Multisubstrate screening of six *para*-substituted phenylacetylenes with charge-tagged aryl iodide monitored by ESI(+)-MS.

Unexpected results were obtained for the two series of reactions. Figure 4.31 illustrates the one by one comparison of each substituted product appearance in both solvents. Reaction was monitored over 90% progress, but only first linear part of each graph is illustrated in here for better comparison. As shown the reactions with EWG- substituents (NO_2 and F) are faster in CD_3OD, but the reactions are faster for EDG-substituents in MeOH. In other words, more acidic terminal proton which is substituted faster in

deuterated solvent, carries out the reaction faster. Phenylacetylene (X = H) behaves like EWG, and as we already know this reaction is faster in deuterated solvent. If we compare the reactivity of substituents in the methanol only, that sounds for the electron poor phenylacetylenes, deprotonation is activated enough. So other steps in the cycle can influence the reaction rate in higher degree, we already know that RE is turnover-limiting in the Sonogashira reaction, so the parameters that facilitate this step can boost the reaction rate. Electron rich substrates accelerate the RE, thus the observed order of activity is observed. However, reaction order rate is completely upside down in deuterated methanol. Reaction is accelerated for EWG-substituted phenylacetylene and decelerated for EDG substituted ones. These results are surprising because we know deuterium exchange between phenylacetylene and CD_3OD is relatively fast under the reaction conditions, so deprotonation should happen on deuterated phenylacetylene which is assumed to be slower than phenylacetylene. These results contradict the only KIE study on Sonogashira reaction reported by Ljungdahl et al. They observed a primary KIE around 2 for nitro-substituted phenylacetylene and small inverse KIE (around 0.9) for dimethylamino-substituted phenylacetylene. However as the paper stated the results were not very accurate (reproducible in magnitude) mostly due to the sensitivity of the extremely dilute reactions.[149]

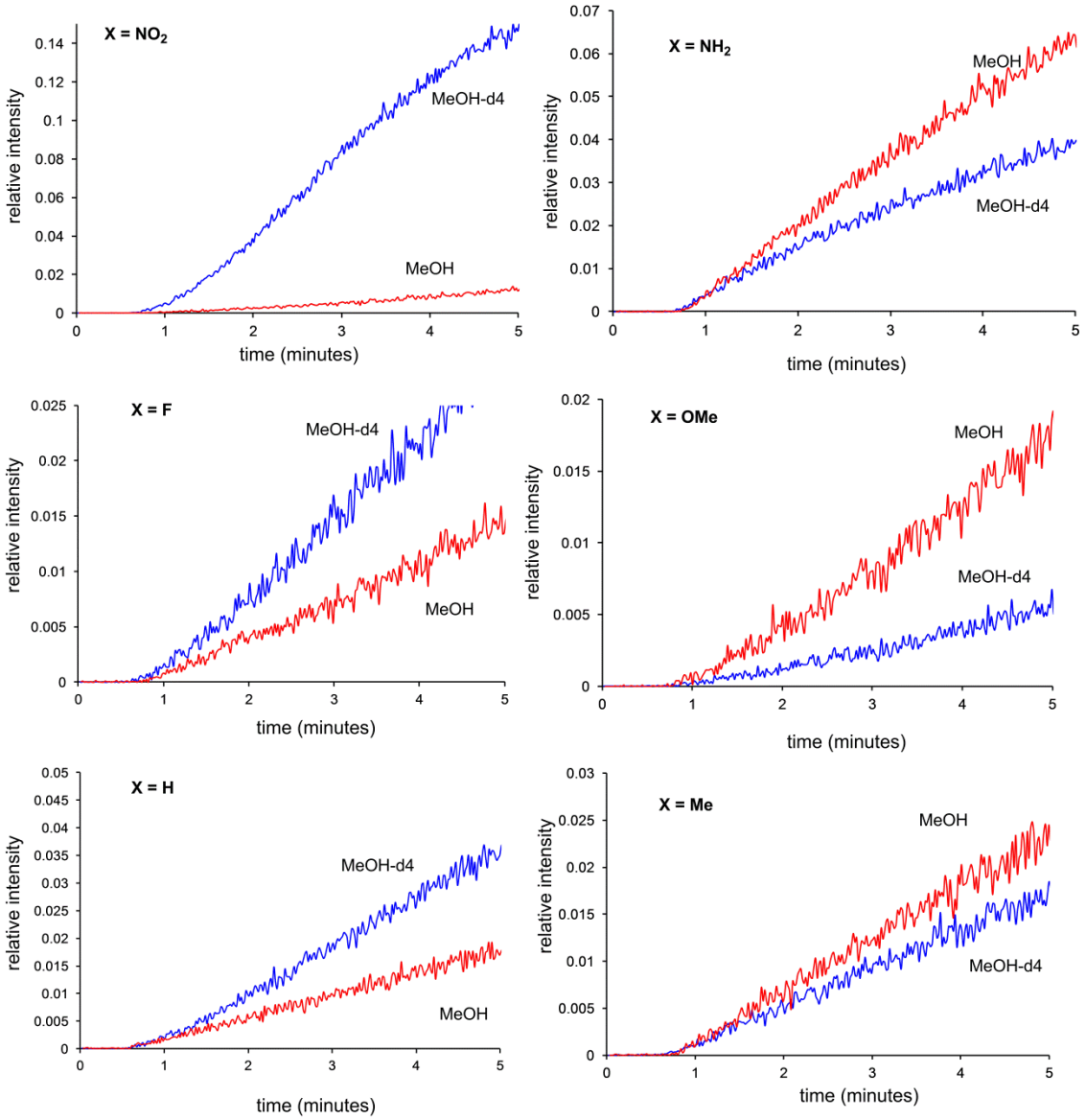

Figure 4.31 One by one comparison of conversion rate of each *para*-substituted acetylene with charged aryl iodide in MeOH (red) and CD_3OD (blue). Left figures show the EWG-substituted products whereas right figures show EDG-substituted products.

4.2.6 Effect of phenylacetylene and product inhibition on reaction rate

Phenylacetylene is involved in TM (in ligand substitution and deprotonation steps), so reaction rate should be affected by change of its concentration. Concentration alteration can provide an indication of the extent of involvement in the reaction rate. Moreover, the way intermediates behave with the changes may provide extra information about the mechanism. Under “standard conditions”, regardless of the amine type we normally use

1.2 equivalents of phenylacetylene to make sure that the reaction goes to completion. In another set of experiments primarily three equivalents phenylacetylene were used as the excess amount to see how fast reaction proceeds. As expected, the reaction accelerated significantly and finished in about 6 minutes. The only observed change in the intermediate behaviour was the steadier trend for $PdP_2(Ar)(C_2Ph)$ which implies the faster phenylacetylene addition (or substitution with another ligand) to metal centre to provide more $PdP_2(Ar)(C_2Ph)$ (Figure 4.32). Nonetheless, addition of six equivalents phenylacetylene did not enhance the reaction further and reaction was as fast as the prior experiment. The behaviour of the $PdP_2(Ar)(C_2Ph)$ did not change either compared with previous experiment (Figure 4.33). These results suggest that saturation will happen beyond the range of three equivalents of phenylacetylene which means catalyst and amine cannot afford the faster conversion anymore.

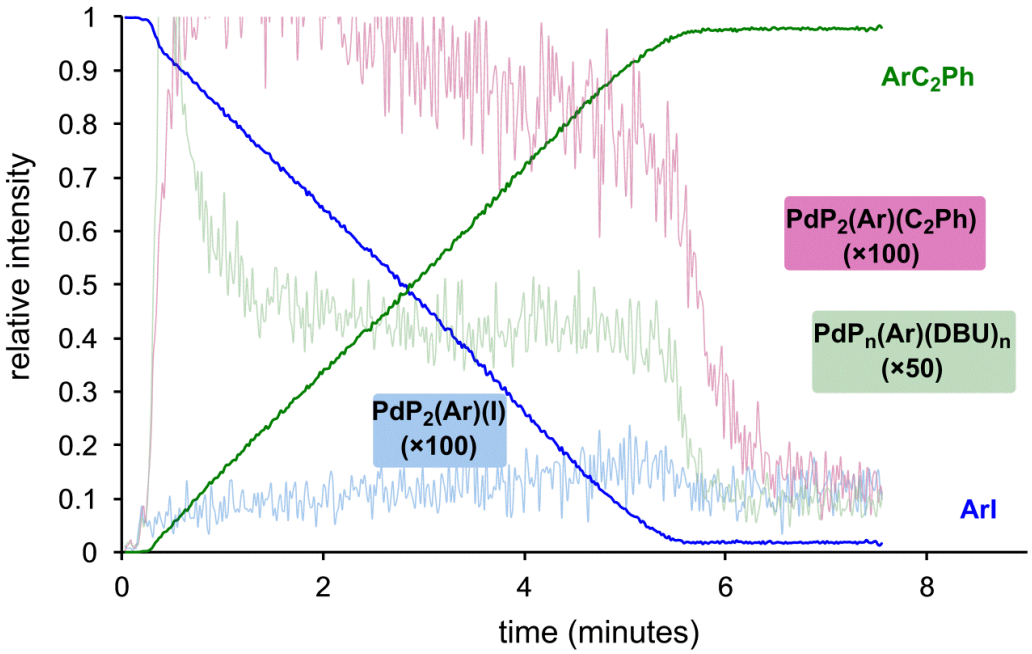

Figure 4.32: ESI(+)-MS of reaction with “standard conditions” and three equivalents of phenylacetylene.

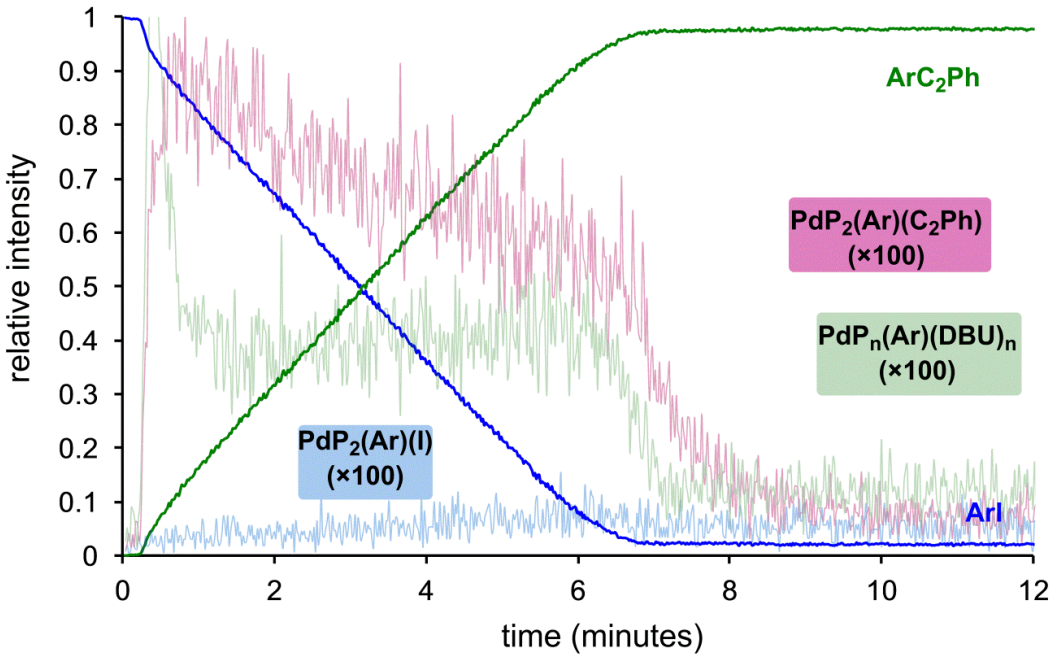

Figure 4.33: ESI(+)-MS of reaction with "standard conditions" and six equivalents of phenylacetylene.

As mentioned in chapter 2, there are several processes in which a catalyst is deactivated: agglomeration (through formation of bi, tri to multi-nuclei until formation of agglomeration)[175], irreversible bond formation to poisoning reagents such as water or oxygen and different types of inhibition. Each one of the mentioned issues will decrease the order of catalyst efficiency. In many different experiments that we have conducted so far, no evidence of species containing more than one palladium was observed, while they have been reported in some other types of cross coupling reactions as the reservoir or poisoning nuclei.[37] As another experiment we decided to see whether excess of product would "inhibit" the reaction by formation of weakly bonded η^2-acetylene to palladium centre. Biphenylacetylene was chosen as the reagent in this experiment and three equivalents with respect to phenylacetylene was added to the reaction mixture before addition of catalyst. We did not expect to see palladium-attached biphenylacetylene since η^2-bonds are inherently weak and can be broken easily through ESI process. However if product inhibition is functioning here, we would expect to conclude that by slower product formation since a part of catalyst will stay off the cycle. Figure 4.32 shows the

result of this experiment. As shown, transformation is as fast as the reaction without biphenylacetylene. Figure 4.34 summarizes the result of all three experiments in this section for a better comparison.

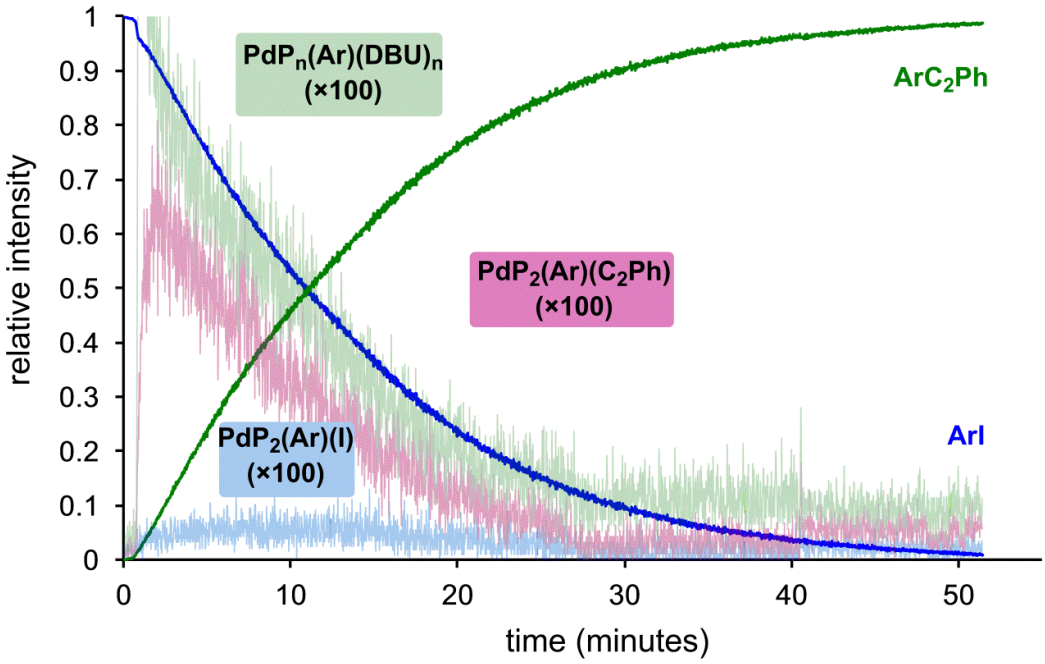

Figure 4.34: ESI(+)-MS of reaction with “standard conditions” and three equivalents of biphenylacetylene.

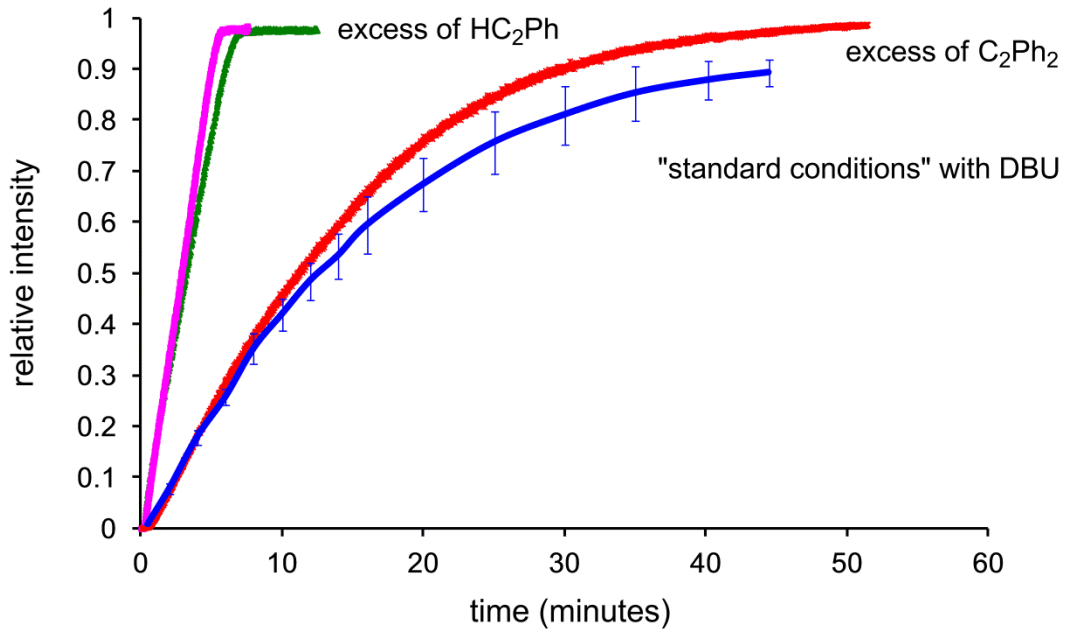

Figure 4.35: ESI-MS intensity data over time for the appearance of products when using excess of phenylacetylene (pink): three equivalents, (green): six equivalents, (red) three equivalents biphenylacetylene and (blue): standard condition (average of five runs).

In another series of experiments to see how the rate of main cycle (Sonogashira) and the side cycle (dehalogenation) are affected by the amount of the catalyst, two reactions were carried out in two other ratios of catalysts: 3 and 9 molar percentages. Ideally, reaction rate should respond linearly to the amount of catalyst when the mononuclear catalyst is responsible for transformation. However, some factors such as catalyst decomposition and bimetallic palladium formation can deviate from this relationship. The results of these experiments are illustrated in Figure 4.36. The graph on left and right show the formation rate of the product and byproduct, respectively at different amount of catalyst. In both plots curve line is obvious, which is more pronounced for the byproduct formation with 2.04 orders of magnitude compared with product with 1.72. Repeating the reaction at lower catalyst concentration (1% mol) resulted in an incomplete reaction. These observations suggest that perhaps a (constant) portion of catalyst was lost through a process, which caused the deviation. Product inhibition was ruled out already so the reason might be catalyst decomposition through the formation of an inactive resting state or an agglomeration. This phenomenon becomes important when the main cycle is unable to process the product formation effectively. For example, under “standard conditions”

with DBU, both OA step and substitution of DBU with iodide are fast. So the related intermediates form quickly at a high concentration. Because the steps which consume these intermediates are slow, intermediates should accumulate and thus, the trend must be approximately steady over time. However, for both experiments (Et_3N, DBU) slopes are slightly negative for these intermediates (Figures 4.10 and 4.12). It is inferred that the catalyst somehow is lost during this process.

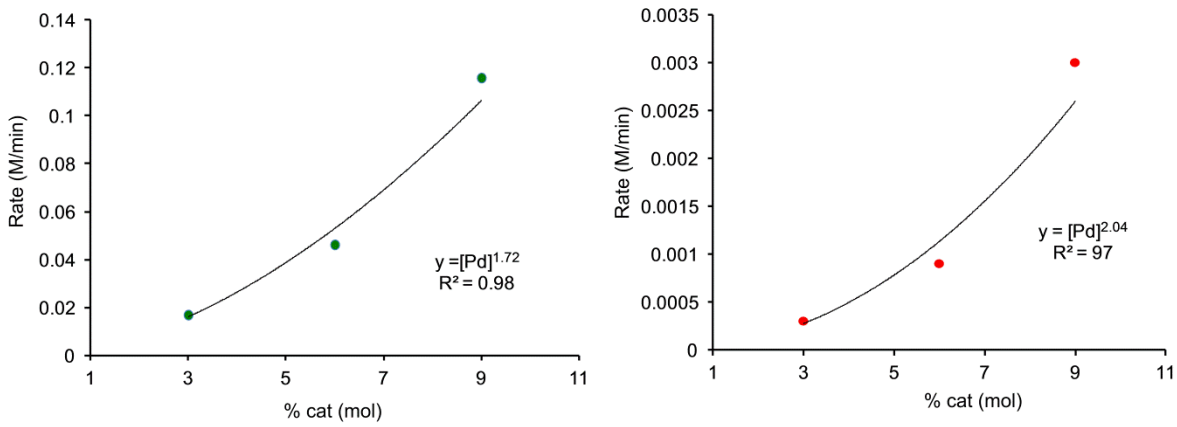

Figure 4.36: Rate of formation of product (left) and byproduct (right) using three different amounts of catalyst.

4.2.7 Reaction on ESI(-)-MS with negative tagged substrate

Much information has been obtained so far by using positively charged tag on positive mode of ESI-MS. If any anionic intermediate forms through the cycle as Jutand and others reported it would be invisible in positive mode. A possible examination is to look into reaction mechanism on negative mode of ESI. The first reaction was performed with neutral substrates (Scheme 4.13) aiming to find any anionic five coordinate intermediate such as [PdL(Et_3N)(Ar)(I)(HC_2Ph)]. In a set of experiments, several reactions were conducted in THF using a broad range of reactant concentrations (0.5 mM-4 mM) and catalyst concentrations (2-15%mol). However, no Pd species was observed, whereas the reaction progress is evident by iodide and an iodide adducts buildup (Figure 4.37). Repeating the same reaction in acetonitrile did not show any Pd species either.

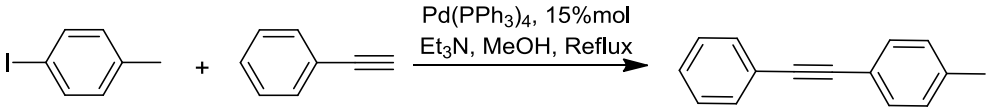

Scheme 4.13: Reaction of neutral substrates: 1-iodo-4-methylbenzene with phenylacetylene at different conditions.

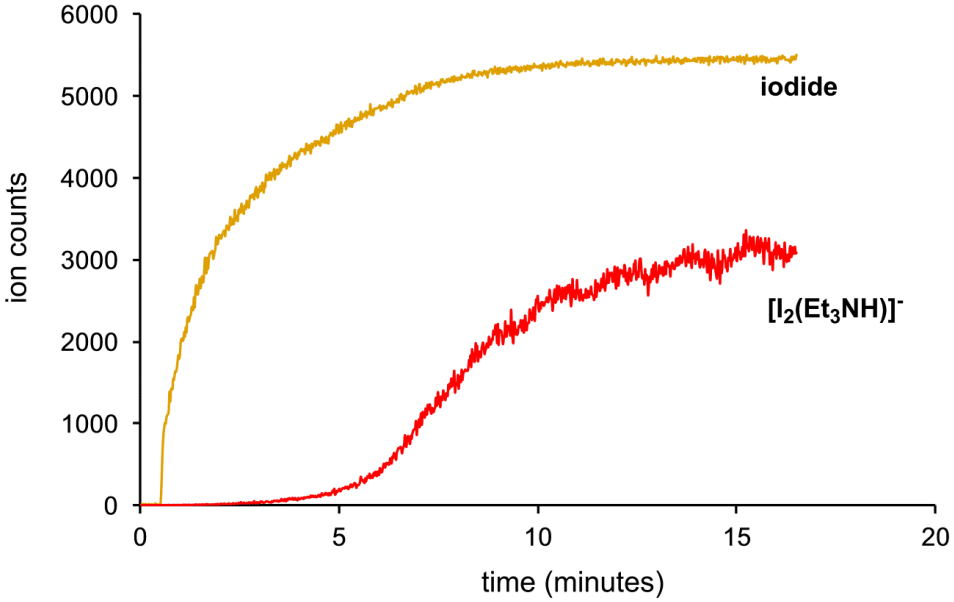

Figure 4.37: Release of the iodide and $[I_2(Et_3NH)]^-$ clearly indicates the reaction progress on ESI-(-)MS.

In another experiment, a negatively charge-tagged aryl iodide (Scheme 4.14) was used instead of neutral substrates and reaction was repeated under "standard conditions" in negative ion mode. Again the same type of OA and TM intermediates were detected and no other intermediate was observed. Figure 4.38 illustrates the structure of the observed intermediates.

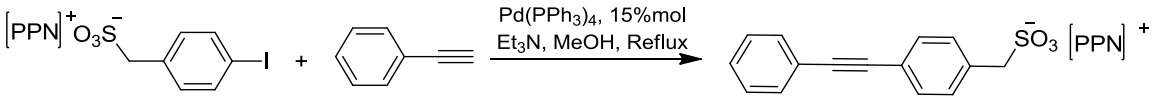

Scheme 4.14: Reaction scheme of negatively charged aryl iodide with phenylacetylene in "standard condition" on ESI(-)-MS.

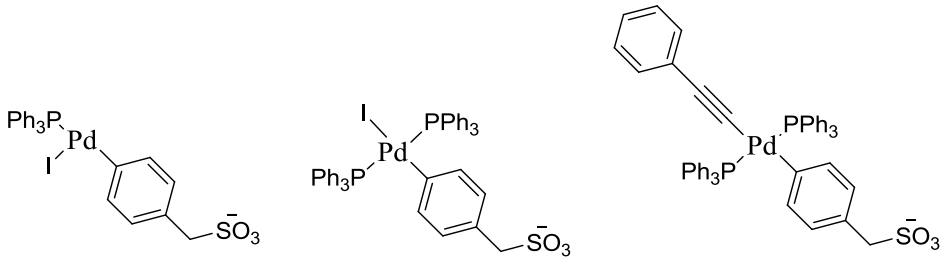

Figure 4.38: Three key intermediates observed on negative mode: (left) the first two are OA species and (right) is the TM intermediate.

4.3 Experimental

All syntheses and catalytic reactions were performed under an inert atmosphere of N_2 using standard glovebox or Schlenk procedures. Except for triphenylphosphine (Alfa Aesar), triethylamine (ACP, Montreal, Quebec) and tetrakistriphenylphosphine palladium (Pressure Chemical Co.) chemicals were obtained from Aldrich and used without further purification. Solvents were HPLC grade and purified on an MBraun solvent purification system. Gases were obtained from Airgas (Calgary, Canada).

Synthesis of $[4\text{-}IC_6H_4(CH_2)PPh_3]^+[PF_6]^-$

Triphenylphosphine (0.7 g, 2.7 mmol) and 4-iodobenzyl bromide (0.76 g, 2.6 mmol) were added to toluene (10 mL). The reaction was stirred at room temperature for 16 h. The white precipitate was filtered and washed with toluene to remove extra PPh_3 and provide the product $[4\text{-}IC_6H_4CH_2PPh_3]^+[Br]^-$ (yield: 1.1 g, 77%) (m.p. = 248 °C uncorrected). Salt metathesis with $[Na]^+[PF_6]^-$ (0.67 g, 4 mmol) gave $[4\text{-}IC_6H_4CH_2PPh_3]^+[PF_6]^-$ (yield: 1.1 g, 85%) after stirring for 1 h in methanol (5 mL). ^{1}H NMR (300 MHz, $CDCl_3$) δ = 4.53, (d, 2H, J = 14 Hz), δ= 6.7 (dd, 2H, J = 2,8 Hz) δ= 7.57-7.45 (m, 8H), δ = 7.66 (td, 6H, J = 3.5, 8 Hz), δ = 7.80 (td, 3H, J = 2, 7 Hz). ^{31}P NMR (300 MHz, $CDCl_3$) δ = 23.60(s). ESI(+)-MS *m/z* 479.1.

Synthesis of $[MePPh_3]^+[PF_6]^-$

Triphenylphosphine (2 g, 7.6 mmol) and iodomethane (0.48 mL, 7.6 mmol) were dissolved in toluene (5 mL). After 5 h a white precipitate was collected and washed with toluene then dried *in vacuo* (yield: 2.5 g, 83%). Salt metathesis was carried out by adding $[MePPh_3]^+[I]^-$ (2.5 g, 6.3 mmol) and $[Na]^+[PF_6]^-$ (2 g, 12 mmol) to MeOH (5 mL) and

stirring for 1 h. Solvent was removed by rotary evaporation and the resulting product was washed with water to remove extra $[Na]^+[PF_6]^-$ (yield: 2.3 g, 87%). ESI(+)-MS *m/z* 277.1.

Synthesis of $[4\text{-}HC_2C_6H_4(CH_2)PPh_3]^+[PF_6]^-$

$[4\text{-}HC_2C_6H_4(CH_2)PPh_3][Br]$ (1g, 1.8 mmol) and $PdCl_2(PPh_3)_2$ (0.06 g, 0.08 mmol) and trimethylsilylacetylene ($C_5H_{10}Si$) (450µL, .3.2 mmol) and copper (I) iodide (.003 g, 0.0015 mmol) and isopropylamine $(CH_3)_2CHNH_2$ (700 µL, 8.5 mmol) were dissolved in 30mL mixture of toluene/methanol (70:30 v/v). Mixture was stirred under N_2 gas at reflux for half an hour. Solution containing $[4\text{-}TMSC_2C_6H_4(CH_2)PPh_3]^+[Br\ ]^-$ (structure was confirmed by ESI(+)-MS: *m/z* 449.2) was washed through silica column. Potassium carbonate (0.57g) was dissolved in the mixture of water and methanol (25:75 v/v) and added to the filtrate. Obtained mixture was stirred for 15 min at room temperature. A yellow solution with brown precipitate was obtained. Brown precipitate was discarded after filtration and yellow solution was dried under vacuum at room temperature. 0.6g dried brown powder was obtained and subsequently washed with water. Brown powder was dissolved in 5mL methanol and $[Na]^+[PF_6]^-$ (0.045g, 2.6mmol) and stirred for one hour at room temperature. Solvent was evaporated by rotary evaporator and yellow powder was washed with water and dried under vacuum overnight. (0.4 g, 0.8 mmol product was weighted, yield: % 44. Finally product was recrystallized from hot methanol. (m.p. = 250 °C uncorrected). ^{1}H NMR (300 MHz, $CDCl_3$) δ = 3.05 (s, 1H), δ = 4.55, (d, 2H, J = 14 Hz), δ= 6.8 (dd, 2H, J = 2,8 Hz) δ= 7.22 (d, 2H, J =8 Hz), δ = 7.43- 7.52 (m, 6H), δ = 7.61 (td, 6H, J = 3, 9 Hz), δ =7.77 (td, 3H, J = 2.5, 8Hz). ^{31}P NMR (300 MHz, $CDCl_3$) δ = 23.05(s). ESI(+)-MS *m/z* 377.1.

Synthesis of $[4\text{-}IC_6H_4(CH_2)SO_3]^-[PPN]^+$

This compound was synthesized by Cara Manning from the reference: Liu, S.; Dockendorff, C.; Taylor, S. D. *Organic Letters* **2001**, *3*, 1571.

Synthesis of Et_3NHI

Et_3NHI was prepared by literature methods [J.-G. Chen, V. Suryanarayanan, K.-M. Lee, K.-C. Ho, *Solar Energy Materials and Solar Cells* **2007,** *91* (15-16), 1432-14370]. ^{1}H NMR (300 MHz, $CDCl_3$), δ=1.47 (t, 9H), δ= 3.18, (q, 6H), δ=10.1 (s, 1H).

Synthesis of Et_3NHCl

Et_3N and HCl (36.5%) were combined (1:1) and stirred for 15 min. Extra water was removed from the product by rotary evaporation. Finally, a white solid residue was obtained. The solid was recrystallized from ethyl acetate–ethanol mixture (1:1, v/v) and dried in a vacuum at 80 °C. ^{1}H NMR (300 MHz, $CDCl_3$) δ = 1.37 (t, 9H), δ-3.1 (q, 6H), δ = 11.9 (s, 1H).

^{1}NMR monitoring Experiment

Samples of the reaction mixture were removed periodically via syringe (1 mL, one sample was taken before addition of catalyst), sealed in glass vials and immediately frozen in liquid N_2. Solvent was removed by rotary evaporation and the remaining mixture was diluted with $CDCl_3$ and analyzed via ^{1}H NMR (300 MHz). The relative integrations of product and substrate peaks were used to determine the reaction progress.

Mass spectrometry Conditions

All mass spectra were collected on a Micromass Q-TOF *micro* mass spectrometer in positive-ion mode using pneumatically-assisted electrospray ionization. Capillary voltage: 2900 V. Cone voltage: 10 V. Extraction voltage: 0.5 V. Source temperature: 80°C. Desolvation temperature: 150°C. Cone gas flow: 100 L/h. Desolvation gas flow: 200 L/h. Collision voltage: 2 V (for MS experiments). Collision voltage: 15 - 25 V (for MS/MS experiments). Low and high mass resolution: 10.0. MCP voltage: 2700 V.

General experimental details

Using PSI, a solution of $[I(C_6H_4)CH_2PPh_3]^+[PF_6]^-$ (20 mL, 0.5 mM in methanol) was monitored by ESI(+)-MS. To this solution phenylacetylene (1.3 μL, 12 μmol) and base (triethylamine or 1,8-diazabicyclo[5.4.0]undec-7-ene (DBU), 0.1 mmol) were added. 6% $Pd(PPh_3)_4$ (2 mL, 17 μM stock catalyst in THF) was added by syringe through the septum to initiate the reaction. The palladium tetrakis(triphenylphosphine) stock solution was stored in an inert atmosphere glovebox at -32°C between uses. Overpressure in the flask was held at 2.5 psi throughout the reaction and the temperature was held at reflux throughout. The reaction mixture was diluted online by a T-mixer and introduced to the MS with methanol at 10 -20 μL/min. PSI flask was put in the base bath after only

experiment and extra acid bath treatment was avoided. Dry flask was washed with hot solvent before each experiment.

Chapter 5 A mechanism investigation of dehalogenation using palladium catalyst

5.1 Introduction

The replacement of a C-X (X = halide) bond with a C-H bond (dehalogenation) is a frequent competing reaction in palladium-catalyzed cross-coupling reactions, and is responsible for diminished yields and unwanted byproducts. An early mechanism for catalytic dehalogenation of aryl halides was proposed by Zask[176], and then extended by Nolan[177, 178] involving oxidative addition of aryl halide (Ar-X) to a Pd(0) complex, followed by displacement of the halide ligand by methoxide, β-elimination of formaldehyde (when solvent is methanol) and reductive elimination of Ar-H to regenerate the Pd(0) species.

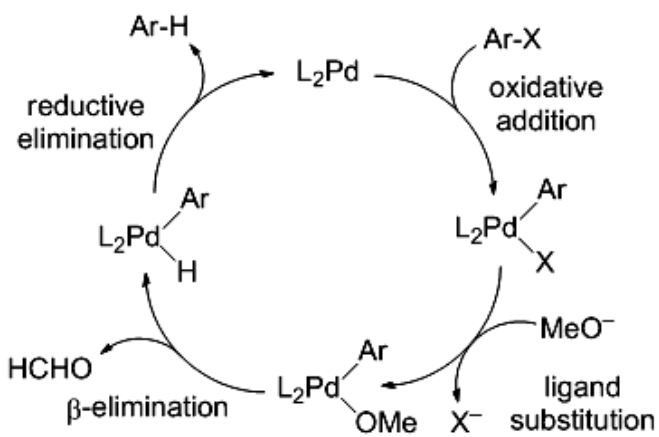

Scheme 5.1: A possible mechanism of dehalogenation of aryl halides. Redrawn from reference 178.

The same mechanism also was reported using Ni(0)/imidazolium chloride[179] and Ru(II)[180] catalysts. Oxidation of the alcohol solvent has been reported by Zhang[181] in homocoupling as well as hydrodehalogenation of aryl halides. Recently, another report[182] on equivalent oxidation of solvent during dehalogenation also supports the involvement of β-hydride elimination as a key step in the reaction. Our interest in the reaction stemmed from our observation that dehalogenation was the major side reaction in the copper-free Sonogashira reaction/Heck alkynation when conducted in methanol,[183] and

we decided to study it in its own right by the simple expedient of leaving out the other coupling partner, the terminal alkyne.

5.2 Reaction review

We started the investigations first by simply leaving out the other coupling partner, the terminal alkyne from Sonogashira reaction in "standard conditions" with Et_3N or DBU as the base. We realized that dehalogenation is slow in the presence of weak bases, but is greatly accelerated by using the relatively strong base potassium *tert*-butoxide. Examination of the reaction of the charge-tagged aryl iodide $[Ph_3PCH_2C_6H_4I]^+[PF_6]^-$ (ArI) in methanol using $Pd(PPh_3)_4$ as the catalyst and ^{t}BuOK as the base allowed us to follow the abundance of starting material product, byproduct (in this case the biphenyl product of homocoupling) and all intermediates containing the charged tag that are present in reasonable abundance (Figure 5.1). Overall, the reaction proceeds with *pseudo* first-order kinetics (k = 0.0292 s^{-1}) (Figure 5.2). The reaction proceeds quite slowly in CH_3OH, taking about 100 minutes to go to completion even at quite high catalyst loadings (6 % mole). In addition to the product (ArH), the homocoupling byproduct (ArAr) also forms in low yield (~2% based on relative intensity). The main palladium-containing species observed over the course of the reaction are $PdP_2(Ar)(I)$, $PdP_2(Ar)(H)$, and $PdP_2(Ar)_2$. Figure 5.1 shows intensity vs. time traces for ArI, ArH, ArAr, $PdP_2(Ar)(I)$ and $PdP_2(Ar)(H)$ and $PdP_2(Ar)_2$ (the three Pd-containing species have been multiplied by 100 to get them on the same scale as the other species). Because two different plausible intermediates are observed, the reactions that consume these compounds are both relatively slow, and both reactions are likely to contribute to the overall rate of the reaction. Both of these species appear in the mechanism in Scheme 5.1, suggesting that it was reasonable. The low yield of this byproduct means we have neglected it as contributing significantly to the overall process.

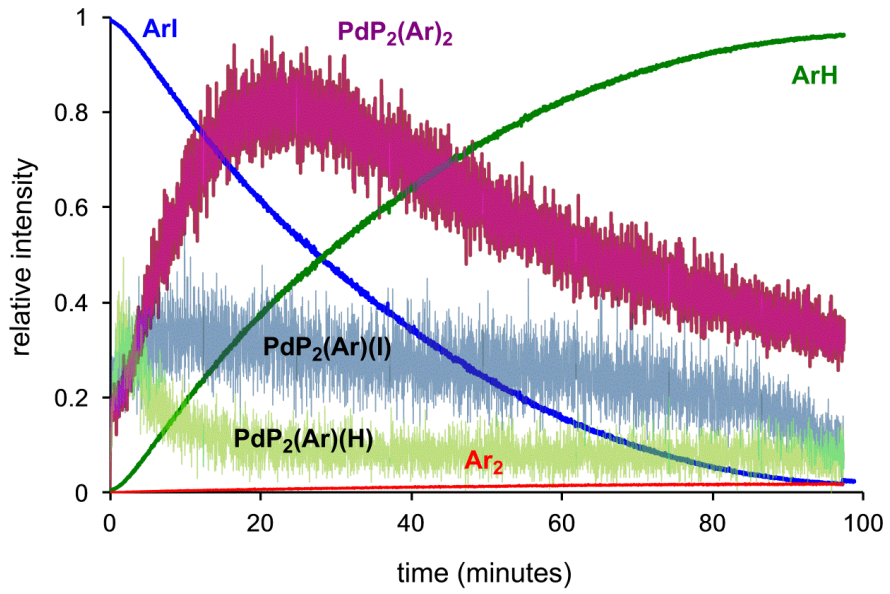

Figure 5.1: Normalized relative abundance of all charged tag containing species in MeOH. Intensity of intermediates were multiplied to hundred for better demonstration.

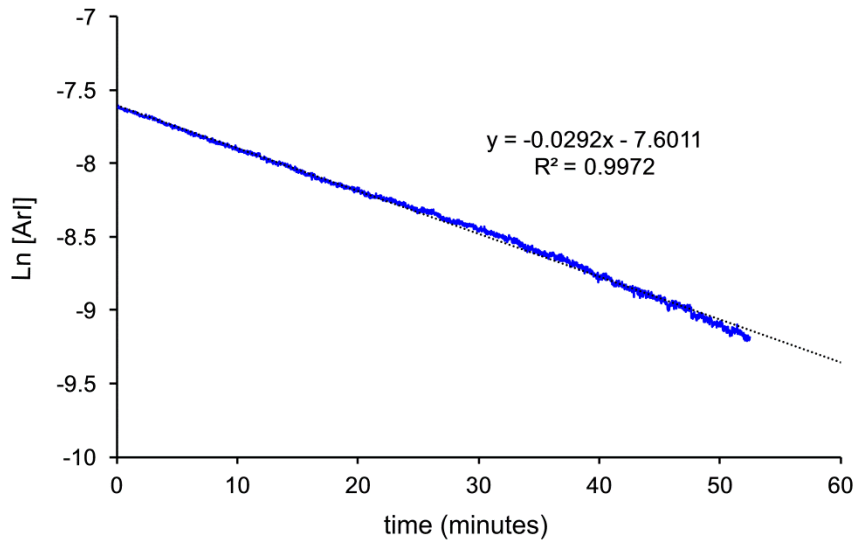

Figure 5.2: *Pseudo* first-order kinetics of dehalogenation of aryl iodide in methanol.

The appearance of the $PdP_2(Ar)_2$ intermediate is interesting; it grows in slowly throughout the reaction and starts to goes away only very slowly once about half of the ArI is consumed. In a cross-coupling reaction (Suzuki reaction) we have studied involving formation of biphenyls [*unpublished*] in which reductive elimination of the product is very fast. It suggests that the high abundance of this intermediate throughout implies that it is the *trans* rather than the *cis* complex. As it is observed the abundance of PdP_2Ar_2 reaches even more than the combination of both active intermediates at

maximum (doubly charged species usually show higher intensity in ESI-MS than singly charged species), but it only produces about 2% Ar-Ar overall.

MS/MS allows us to easily probe this assumption, by subjecting the ion to collision-induced dissociation (CID). If the two groups are *cis* to one another, we would expect the reductive elimination of Ar-Ar to be facile. The $PdP_2(Ar)(H)$ ion, for example, cleanly eliminates ArH (at *m/z* 353) even at low voltages (below 10V) and at higher voltage, 20V, ArH is the most dominant fragment (Figure 5.3, 5.4). Conversely, the $PdP_2(Ar)_2$ ion (a doubly charged ion at *m/z* 668) decomposes incoherently to a range of fragments, including $[PPh_4]^+$ (*m/z* 339), $[Pd(Ar)(CHPPh_3)]^+$ (*m/z* 733) but only a very small amount of $[Ar\text{-}Ar]^{2+}$ (at *m/z* 352) (Figure 5.5, 5.6).

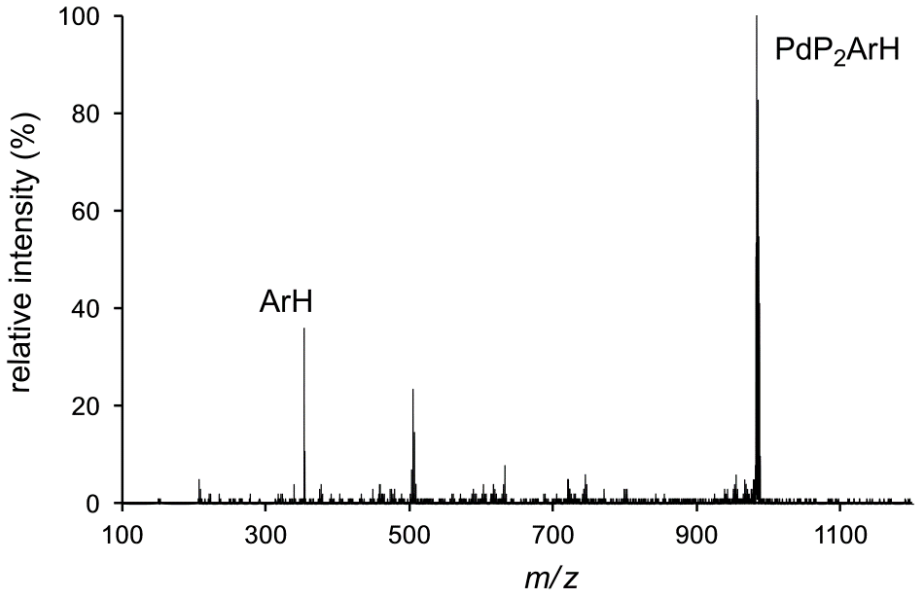

Figure 5.3: MS/MS on $PdP_2(Ar)(H)$ (*m/z* at 983). Average of 17 spectra at voltages lower than 10V.

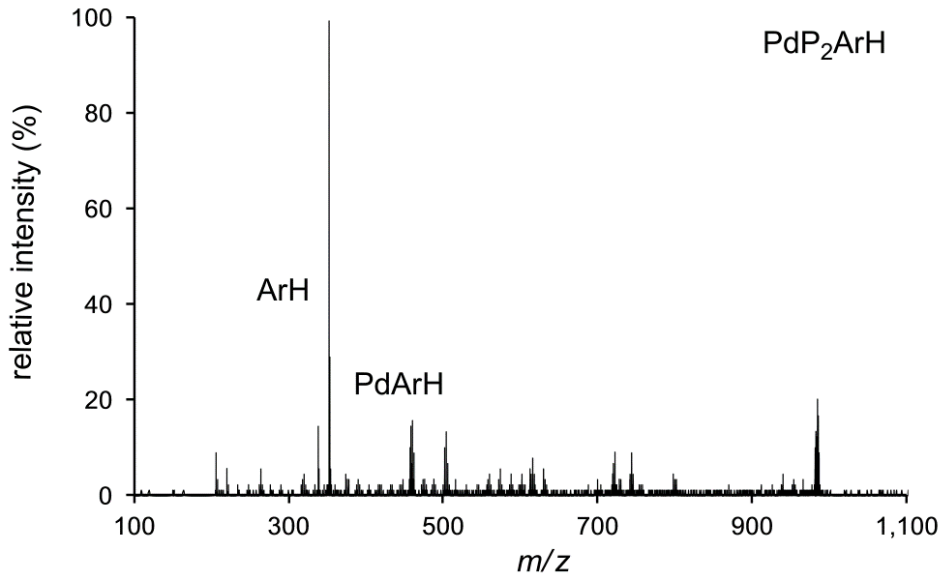

Figure 5.4: MS/MS on $PdP_2(Ar)(H)$ (*m/z* at 983). Average of 30 spectra at voltages between 15 - 20.

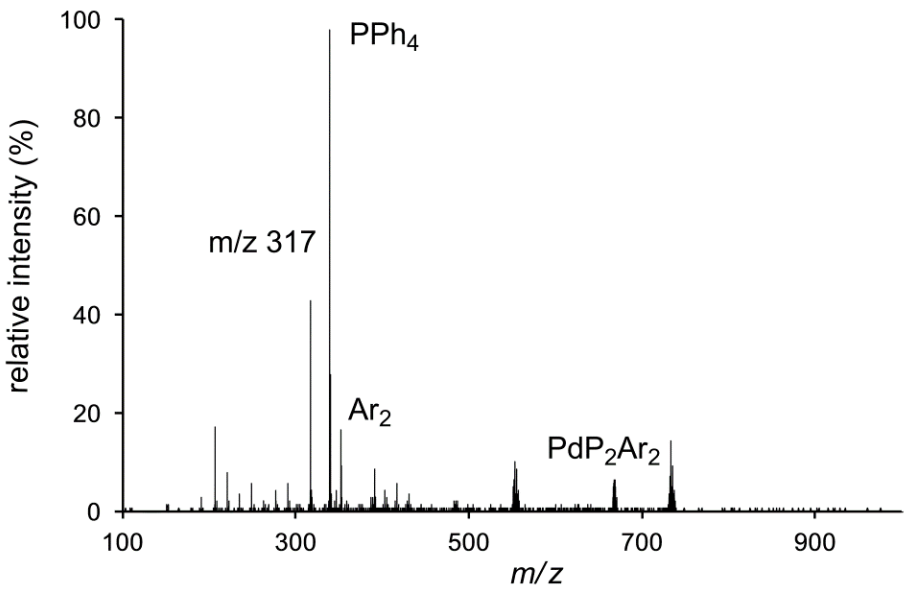

Figure 5.5: MS/MS on $PdP_2(Ar)_2$ (*m/z* at 668). Average of 16 spectra at voltages lower than 10 V.

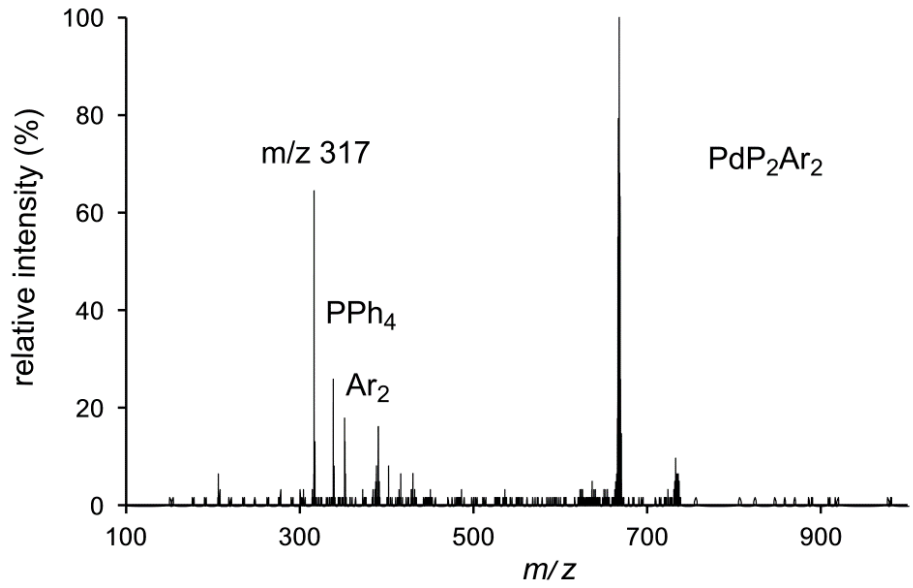

Figure 5.6: MS/MS on $PdP_2(Ar)_2$ (*m/z* at 668). Average of 12 spectra at voltages between 15 - 20V.

5.3 Kinetic isotope effect

Given the involvement of the solvent in the reaction, the opportunity for isotopic labelling promised to give us additional insight into the key elementary steps. Both the β-elimination and the reductive elimination involve breaking of a bond to H, so we can expect these steps to be slowed if CH_3 is replaced with CD_3, thanks to the primary kinetic isotope effect (KIE).[184-188] Accordingly, the reaction was repeated in CD_3OD, and it was, as expected, considerably slower. However, when the reaction was repeated in CH_3OD, the reaction was equally slow (Figure 5.7). The intermediate behaviour in all three cases was qualitatively similar: a steady state for $PdP_2(Ar)(I)$, and a jump at the start for $PdP_2(Ar)(H)$. However, relative intensities of key intermediates were lower than those observed in the Sonogashira reaction (Chapter 4). The CH_3OD experiment was particularly informative. If the turnover limiting step involved β-elimination or reductive elimination, we would expect the rate to be essentially unaffected compared to CH_3OH.

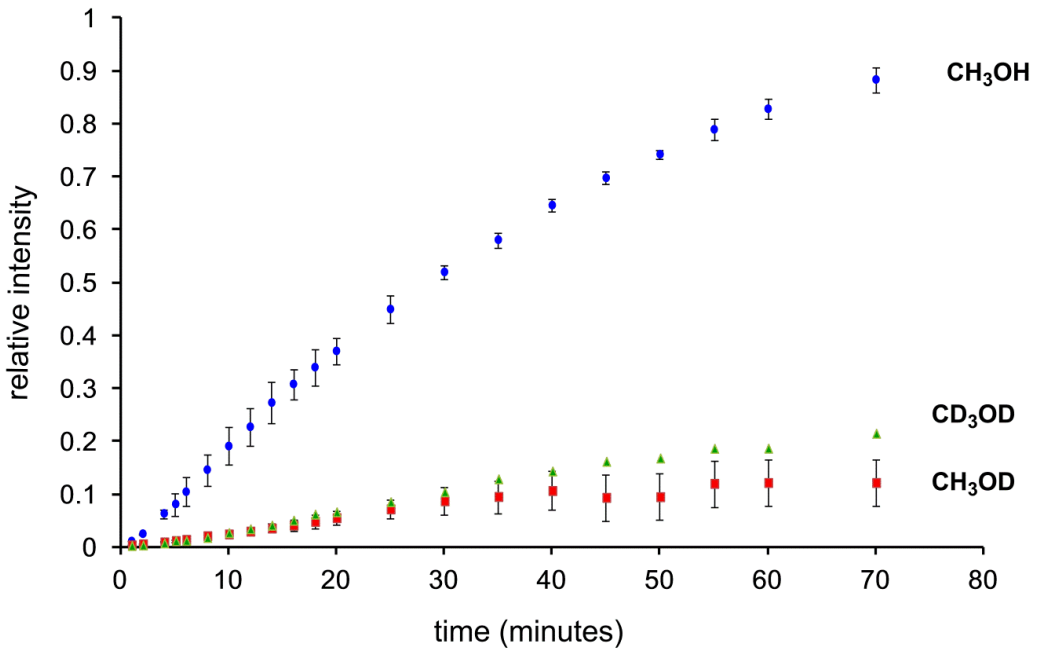

Figure 5.7: Overlay of product built-up in CH_3OH (blue), CH_3OD (red) and CD_3OD (green). Error bars are generated from triplicates (red and blue). Green is generated from duplicates.

The monitoring of the reaction in CH_3OD revealed that as the reaction progresses some hydrogen is replaced by deuterium in $PdP_2(Ar)(H)$ (Scheme 5.2), which results the formation of a mixture of ArH and ArD products. Given that about 50:50 of products formed overall, if the reductive elimination is responsible for the slower rate in CH_3OD, we would expect this reaction to be faster than the reaction CD_3OD but slower than that of in CH_3OH. The fact that it is as slow as CD_3OD experiment rules out this hypothesis.

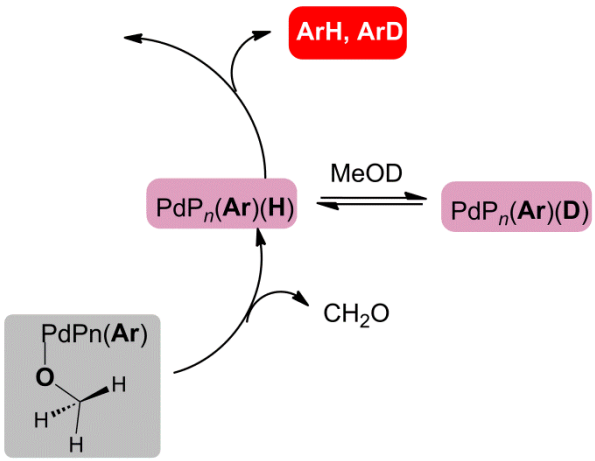

Scheme 5.2: H/D exchange and formation of a mixture of products.

The fact that the rate was just as slow for CH_3OD as for CD_3OD suggests that the key step was actually deprotonation. If the deprotonation happens off the metal to make $[RO]^-$, the amount of $[RO]^-$ will be determined by the position of the ROH + KO^{t}Bu ↔ ROK + HO^{t}Bu equilibrium in solution, which will be approximately the same for R = CD_3 as it is for R = CH_3. So we assume that the deprotonation instead occurs when the methanol is bound to the metal, and that it is methanol as opposed to methoxide that displaces the iodide ligand to make $[PdP_2(Ar)(MeOH)]^+$. However, this intermediate is not observed, so how can the deprotonation therefore be turnover limiting? This possibility arises if an equilibrium $PdP_2(Ar)(I)$ + MeOH ↔ $[PdP_2(Ar)(MeOH)]^+$ + $[I]^-$ exists and lies mostly to the left. This assumption is reasonable given that we detect only $PdP_2(Ar)(I)$ in a methanol solution of this compound and no $[PdP_2(Ar)(MeOH)]^+$ + $[I]^-$. If we run the catalytic reaction *without* a charged tag (i.e. with PhI or $MeOC_6H_4I$ rather than ArI), we see roughly equal amounts of $[PdP_2(Ar)(I) + K]^+$ and $[PdP_2Ar]^+$. The potassium ion adduct appears because of the presence of the KO^{t}Bu base, despite the fact that the interaction between the complex and $[K]^+$ is typically a weak one. The $[PdP_2Ar]^+$ ion is not a fragment of the potassium adduct (Figure 5.8), so represents an independent species, although it is present in very low concentration.

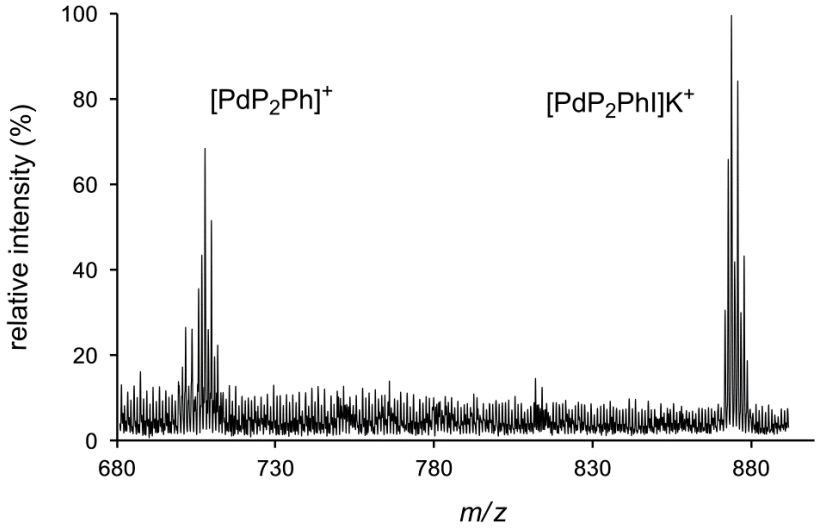

Figure 5.8: Isotope patterns of $[PdP_2PhI+K]^+$ and $[PdP_2Ph]^+$. Average of about 500 spectra over the course of reaction.

Scheme 5.3 shows the modified mechanism. Assuming this mechanism is functioning; it suggests a couple of ideas for explorations. If dissociation of iodide is crucial, its removal must accelerate the reaction and addition of iodide must slow it down. Both of these experiments were conducted, by adding $AgNO_3$ at the start of the reaction to precipitate out any iodide that is released, and by adding one equivalent to $[I]^-$ to the reaction. The predicted effects indeed played out (Figure 5.9):

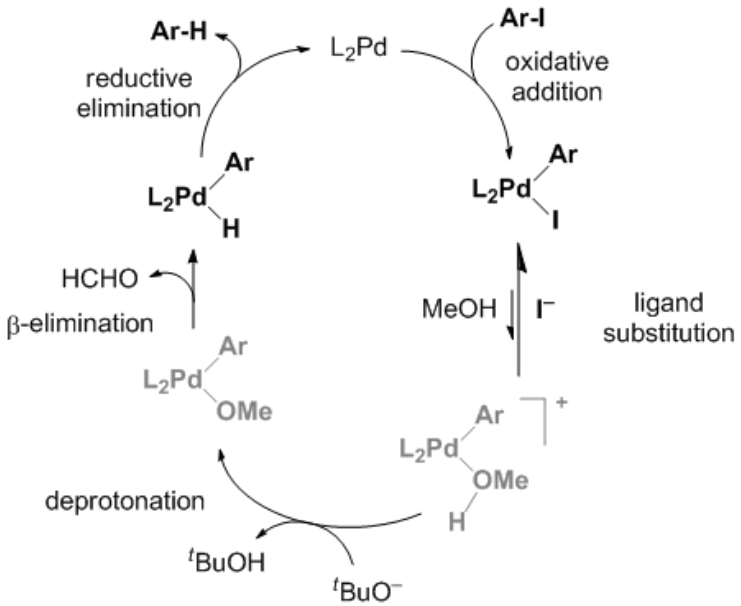

Scheme 5.3: Catalytic cycle and rate constants used to simulate the reaction progress. Concentrations used were the same as employed experimentally.

The $AgNO_3$ experiment was especially interesting because the reaction was initially very fast but after conversion of about 25% it slows down dramatically. We think this is due to removal of the catalyst somehow, perhaps a combination of oxidation of Pd(0) by Ag(I), and co-precipitation of remaining Pd(0) with the Ag(0) so formed. The solution discoloured considerably when the catalyst precursor was combined with $AgNO_3$ and black particles precipitated out. Whatever is going on to slow the reaction, the initial fast reaction rapidly ceases, so $AgNO_3$ is not a helpful reagent in terms of overall yield. The slow reaction in the presence of $[I]^-$ is predictable given that we expect the iodide dissociation to be suppressed in the presence of high concentrations of $[I]^-$. Addition of halide has been reported to decelerate the reaction of PdP_2ArBr with $PhB(OH)_2$ in Suzuki

cross coupling reactions which suggest that PdP_2ArBr is in equilibrium with more reactive species.[189]

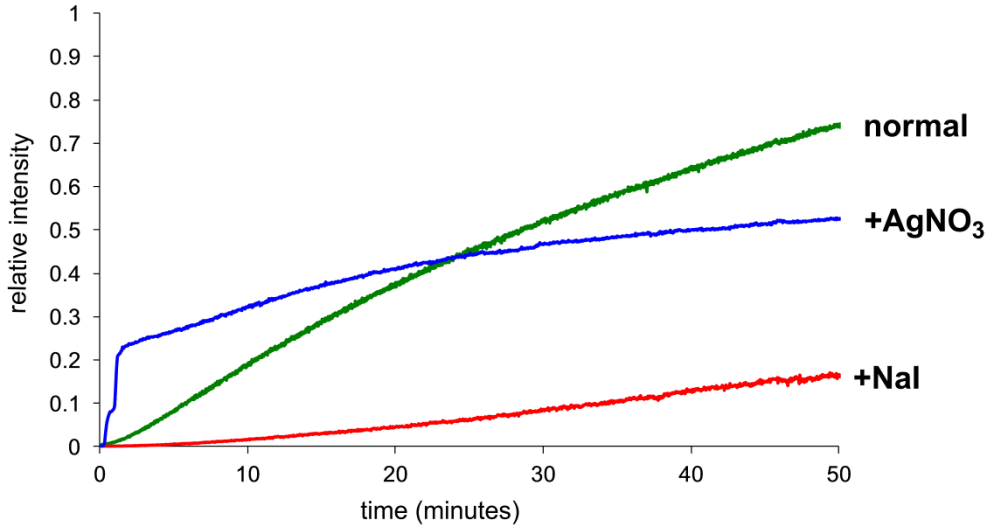

Figure 5.9: A comparison of the "normal" reaction (green) and after addition of one equivalent of $AgNO_3$ (blue) or $[I]^-$ (red). Blue and red are generated from duplicates.

5.4 Numerical modelling of the proposed mechanism

Using the modified mechanism in Scheme 5.3, a numerical model was constructed using Powersim and tested it to see if there exists a combination of rate constants that allow us to approximate the experimental traces, including the qualitative behaviour of the intermediates. Colors are the same in all figures. Concentrations of intermediates are multiplied by 100 in the experimental plot but by 20 in the simulation; as we don't know the relative response factor for the intermediates versus the substrate, we have paid attention to the relative abundances between intermediates and changes with time rather than the absolute abundances. The initial experimental concentrations after addition of all components were used as initial conditions. Units are min^{-1} for first order rate constants and mM^{-1} min^{-1} for second order rate constants. Reverse reactions were considered in every single step for the flexibility purpose in the model. However the rate constants were considered as zero for those steps which are known to be effectively non reversible (reductive elimination and β-hydride elimination) (Scheme 5.4).

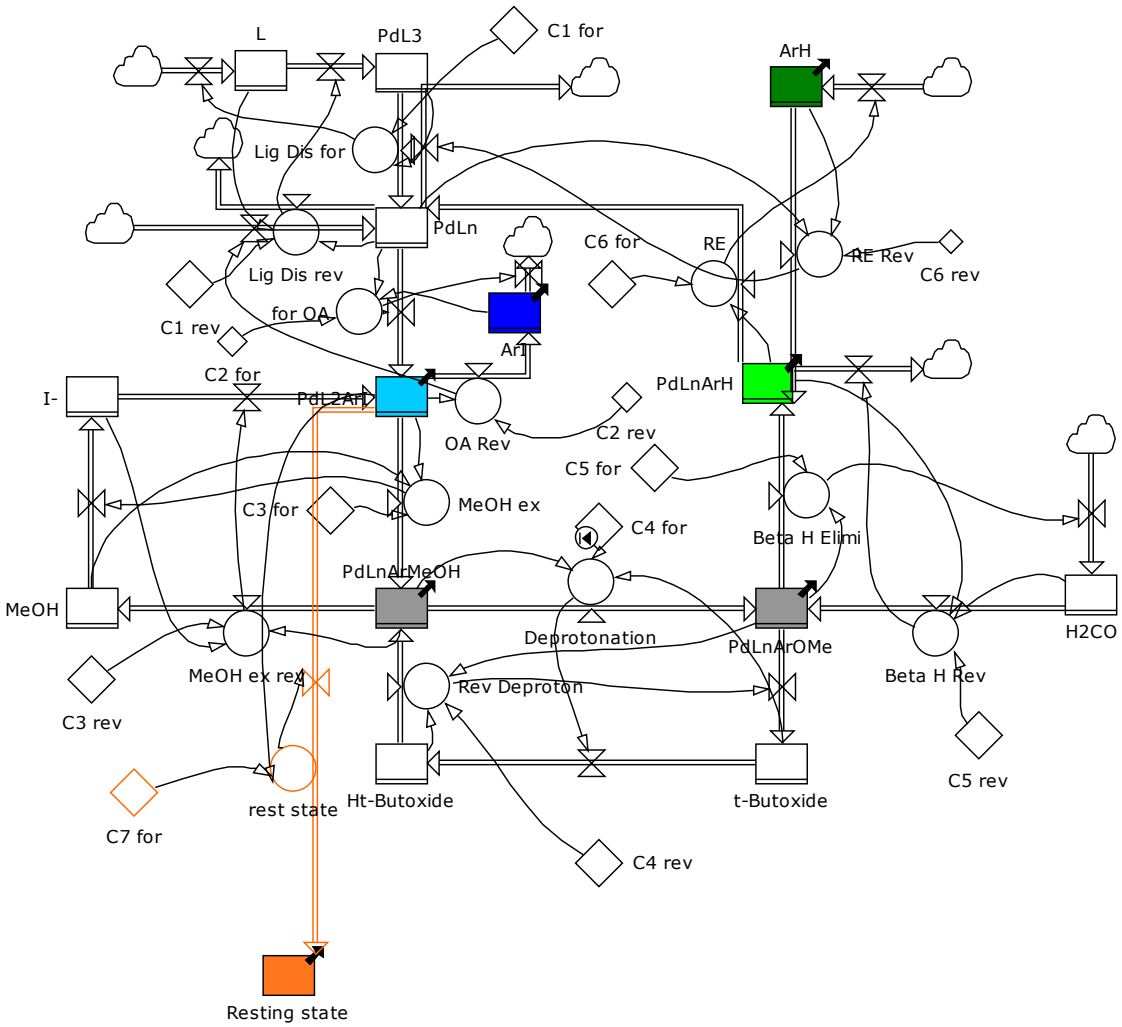

Scheme 5.4: Numerical model of hydrodehalogenation (applied for the reactions in MeOH, CH_3OD, CD_3OD and iodide addition).

While ESI-MS has a high dynamic range, it is still quite plausible for intermediates to have a low enough abundance that they do not appear above the noise; nonetheless, their abundance in the numerical model should be lower than the other intermediates that are observed. In this case, the $PdP_2(Ar)(OMe)$ intermediate is *not* observed, which suggests that the reaction that consumes it - the β-elimination - is not turnover limiting. The numerical model had substantial constraints: it needed to emulate the normal behaviour of the system, as well as predict how the reaction changes when the various perturbations (d_1 and d_4 deuteration, addition of iodide, addition of $AgNO_3$) are made. As a starting point it was assumed that the primary kinetic isotope effect would slow all reactions

involving the breaking of a bond to hydrogen by a factor of 7, and that $AgNO_3$ would remove any iodide formed immediately. We also added an undefined catalyst decomposition process, but did not try to model the homocoupling pathway explicitly, since it only involved approximately 2% of the final product (Figure 5.10).

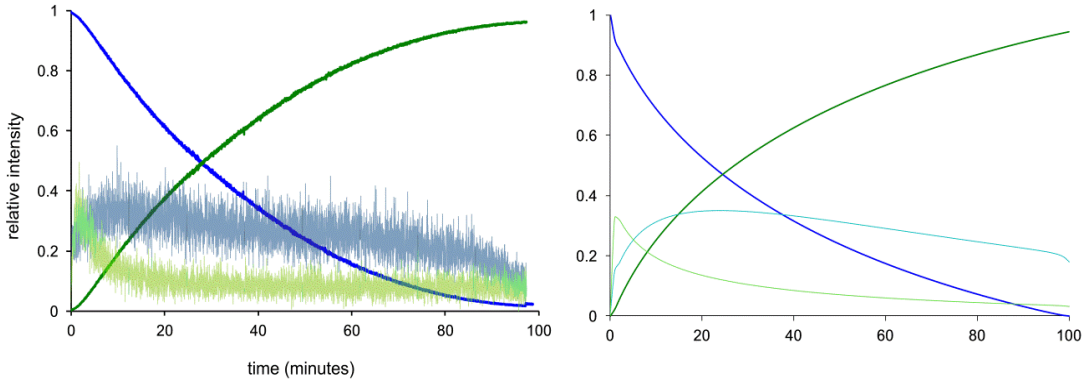

Figure 5.10: Experimental (left) and numerically modelled dehalogenation (right). Intermediate intensity has been multiplied by 20 to get them on the same scale.

On optimization, it seems that the KIE for the deprotonation step needs to be >7 to account for the dramatic change in reactivity, and the best fit is obtained if modelled at k_H/k_D = 16 for that particular transformation. This value is relatively high, and may indicate that tunnelling is involved. Given the reaction is a deprotonation, tunnelling of the proton is plausible, though further work would be required to prove this hypothesis. The optimized model closely matches the observed behaviour of the system in CH_3OD (Figure 5.11).

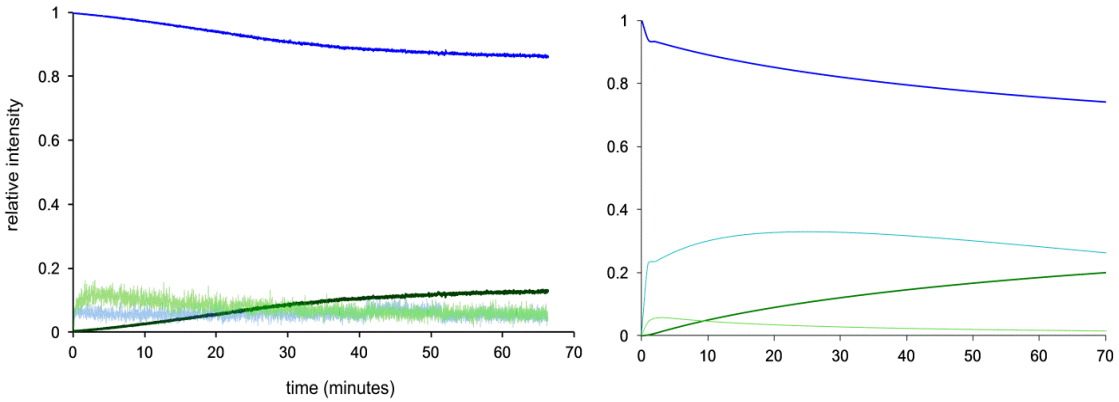

Figure 5.11: Reaction progress in CH_3OD: experimental (left) and numerically modeled using Powersim (right), under standard conditions.

To address all the perturbations in CD_3OD model should respond properly to two more steps to confirm the proposed mechanism. In addition to deprotonation, β-hydride elimination and reductive elimination are involved in deuterium bond formation-cleavage respectively. A typical KIE is expected for both these steps, thus both steps were slowed down 7 times and the system closely responded to the changes (Figure 5.12).

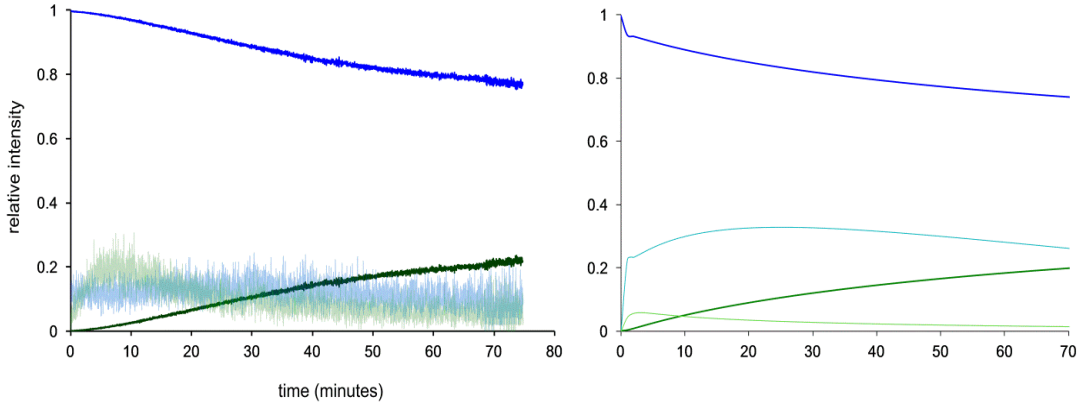

Figure 5.12: Reaction progress in CD_3OD: experimental (left) and numerically modeled using Powersim (right), under standard conditions.

For the sodium iodide addition experiment, 0.5 mM iodide (1 equivalent) was input as the initial concentration and no change in rate constants were required. The model closely matched with the experimental data (Figure 5.13). For the $[Ag]^+$ addition experiment,

some changes in the constructed model were required to include the involvement of the fast irreversible reaction between $[Ag]^+$ and $[I]^-$ (Scheme 5.5). As was discussed earlier the reaction does not go to completion due to catalyst deactivation, however initial fast product formation qualitatively matches with numerical model (Figure 5.14).

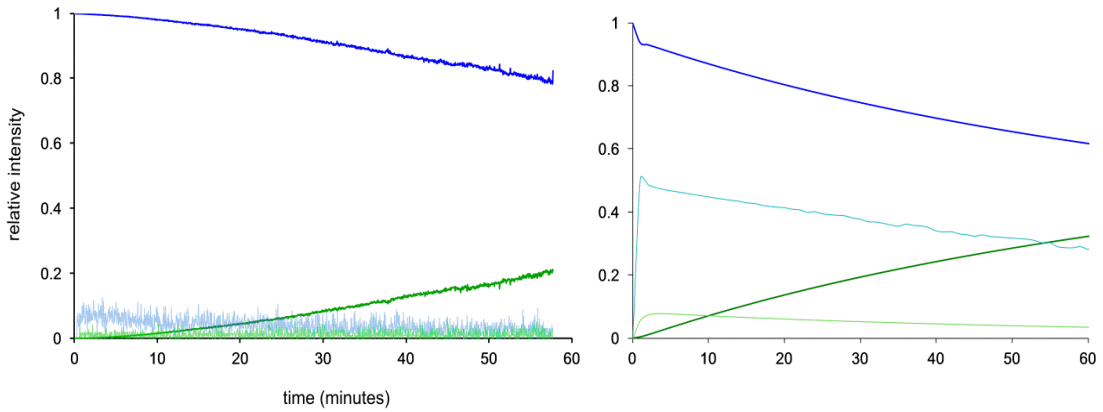

Figure 5.13: Reaction progress in CH_3OH with addition of 1 equivalent $[I]^-$: experimental (left) and numerically modeled using Powersim (right), under standard conditions.

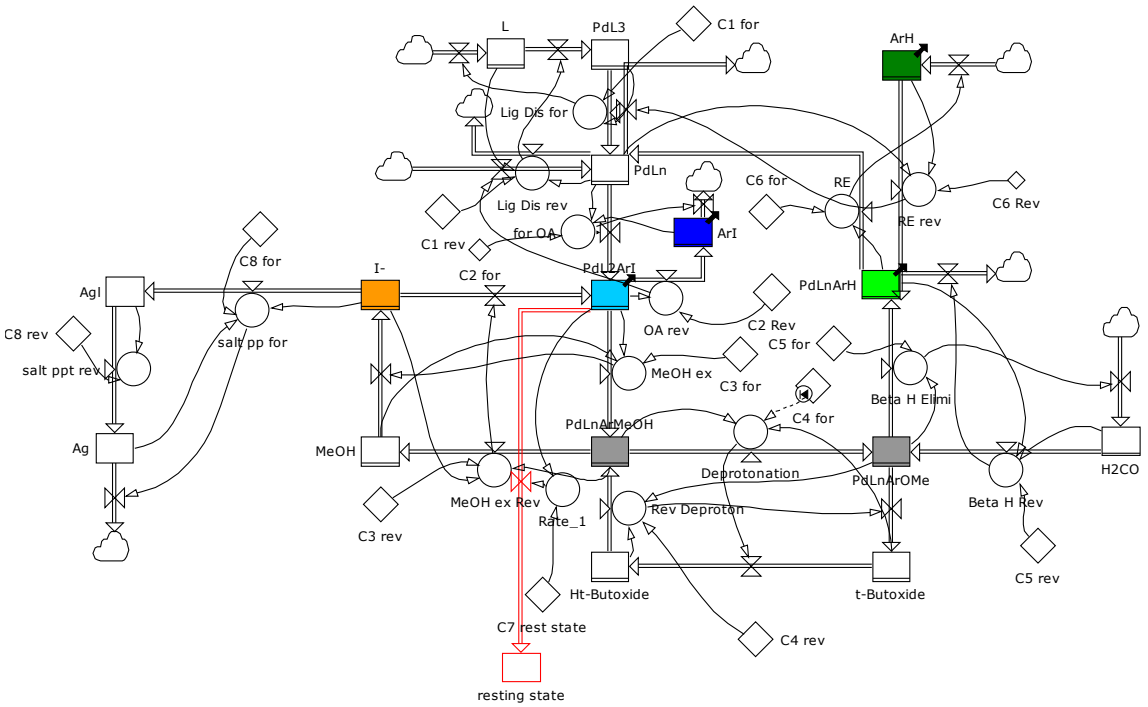

Scheme 5.5: Numerical model of hydrodehalogenation including $[Ag]^+$ reaction with $[I]^-$.

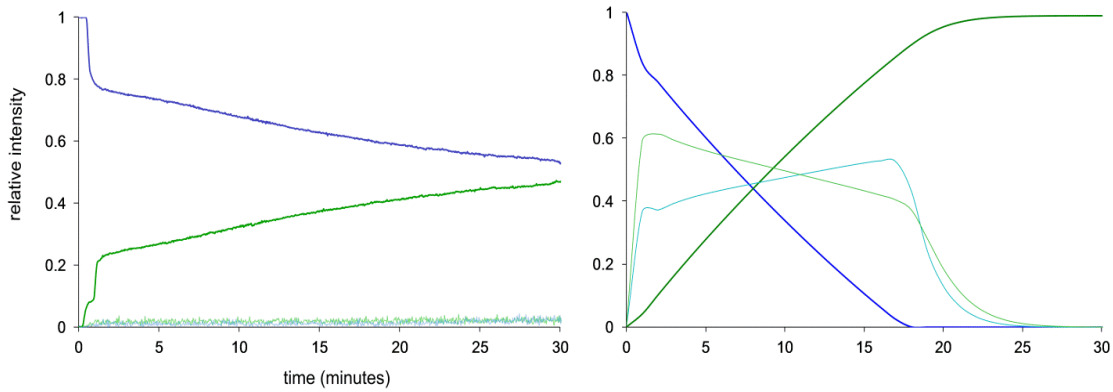

Figure 5.14: Reaction progress in CH_3OH with addition of 1 equivalent $[Ag]^+$: experimental (left) and numerically modeled using Powersim (right), under standard conditions.

Table 5.1 summarizes the rate constants of different steps in all the simulated reactions. The variable rate constants in different reactions were represented in black color for better comparison.

Table 5.1: Rate constant values in different experiments.

Rate constants	Experiments				
	MeOH	**MeOH-D1**	**MeOH-D4**	**Iodide**	**$[Ag]^+$**
C1 for	10,000	10,000	10,000	10,000	10,000
C1 rev	10,000	10,000	10,000	10,000	10,000
C2 for	1000	1000	1000	1000	1000
C2 rev	0	0	0	0	0
C3 for	1	1	1	1	1
C3 rev	3500	3500	3500	3500	3500
C4 for	0.6	0.04	0.04	0.6	0.6
C4 rev	100	6.25	6.25	100	100
C5 for	2000	2000	285	2000	2000
C5 rev	0	0	0	0	0
C6 for	1	1	1	1	1
C6 rev	0	0	0	0	0
C7 for	0.012	0.012	0.012	0.012	0.012
C8 for	-	-	-	-	1
C8 rev	-	-	-	-	0

5.5 Enthalpy and entropy of activation

The reaction was repeated at four different temperatures (306.2, 307.6, 316.5 and 339.6 K) to allow the measurement of $\Delta H^{\ddagger}$ = 72 ± 8 kJ mol^{-1} and $\Delta S^{\ddagger}$ = -60 ± 170 J mol^{-1} via the construction of an Eyring plot (below). The large error in the entropy of activation is due to the fact that at the low concentrations used in these experiments (0.5 mM), getting the near-perfect data required for measuring a precise intercept is in practice is very difficult. However, the temperature-sensitive behaviour does nicely illustrate the point that the reaction studied is clearly taking place in the solution, as opposed to being an artefact of the ESI-MS process somehow (Figure 5.15).

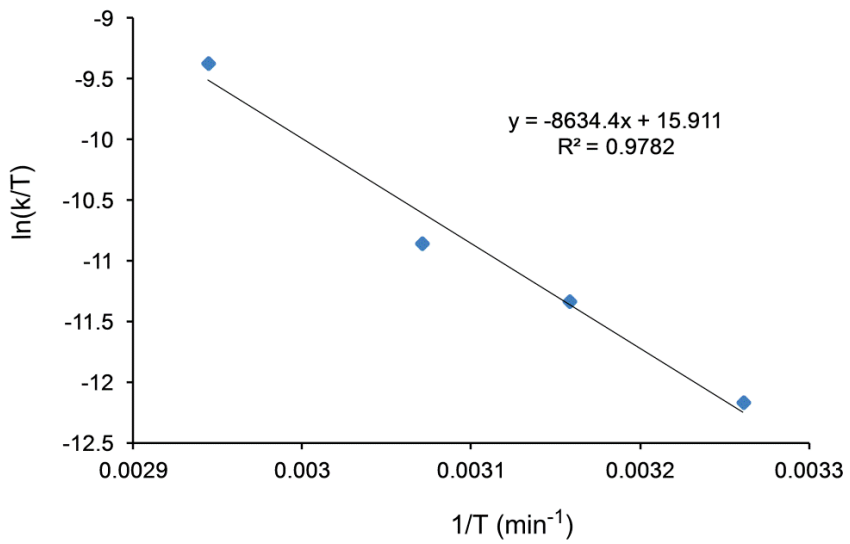

Figure 5.15: Eyring plot of hydrodehalogenation in MeOH.

5.6 Experimental

All syntheses and catalytic reactions were performed under an inert atmosphere of N_2 using standard glovebox or Schlenk procedures. All chemicals were obtained from Aldrich and used without further purification. Solvents were HPLC grade and purified on an MBraun solvent purification system. Gases were obtained from Airgas (Calgary, Canada). All mass spectra were collected on a Micromass Q-ToF *micro* mass spectrometer in positive ion mode using pneumatically assisted electrospray ionization. Capillary voltage: 2900 V. Cone voltage: 10 V. Extraction voltage: 0.5 V. Source

temperature: 70°C. Desolvation temperature: 150°C. Cone gas flow: 100 L/h. Desolvation gas flow: 100 L/h. Collision voltage: 2 V (for MS experiments). Collision voltage: 10 - 25 V (for MS/MS experiments). During PSI experiments, overpressure in the flask was held at 2.5 psig (Ar). The reaction mixture was transferred to MS without further dilution through PEEK tubing (200 mm in length, i.d. 0.055 mm). Data was processed without any normalization for Eyring plots, but all other plots were normalized after applying a correction for variable ionization efficiency (dividing the measured response factors of each specie including ArI (Ar = $[C_6H_4CH_2PPh_3]^+$), ArH, Ar-Ar and observed intermediates over sum of all tag-containing species). For the monitoring 10 ml 0.5 mM of ArI in methanol was degassed and transferred to a Schlenk flask with integrated condenser and 2 mg of $[Ph_3PMe]^+[PF_6]^-$ added as the internal standard. 6% $Pd(PPh_3)_4$ (2 mL, 17 μM stock catalyst in THF) was added by syringe through the septum to initiate the reaction. The tetrakistriphenylphosphine palladium stock solution was stored in an inert atmosphere glovebox at -32°C between uses. Potassium tert-butoxide (10 equivalents, stock solution in MeOH) was added by syringe through the septum after addition of catalyst solution. For the reaction using excess iodide, 1 equivalent (to ArI) of $[Ph_3PMe]^+[I]^-$ was added as the source of iodide. For silver ion experiment, 1 equivalent (to ArI) $AgNO_3$ was added.

Chapter 6 An unexpected pathway for ligand substitution in an aryl halide complex of palladium

Portions of this chapter are reproduced in part with permission from "An Unexpected Pathway for Ligand Substitution in an Aryl Halide Complex of Palladium" Zohrab Ahmadi, Allen G. Oliver and J. Scott McIndoe, *ChemPlusChem,* **2013**, 78, 632-635.

6.1 Introduction

Aryl halide complexes of palladium are interesting because they are intermediates in many palladium-catalyzed cross-coupling reactions.[190-192] The reactivity of these complexes has been extensively studied toward different reagents such as alkynes, carbon monoxide and isocyanide to give new organopalladium or organic compounds.[193-196] In spite of many reports on the synthesis and reactivity of these complexes, [197-199] the mechanism by which they are formed has not received much attention. For example the the only mechanistic suggestion for synthesis of $Pd(PPh_3)_2(Ar)(I)$ from Pd(TMEDA)(Ar)(I) (Ar = aryl ligand, TMEDA = tetramethylethylenediamine) has been described as "by replacement of the chelating N^N ligand by PPh_3 and an isomerization process that is probably promoted by the great transphobia of the Ph_3P/Ar ligand pair".[200] The *trans* effect of a ligand is an important parameter for its ability to labilize the other ligand coordinated to its trans position, and this effect is most significant in square planar complexes.[201] In the Pd(TMEDA)(Ph)(I) complex, TMEDA is expected to be activated more than I^- group since TMEDA is in opposite side of $[Ph]^-$ which has stronger *trans* effect compared with the a nitrogen donor of TMEDA in *trans* position of $[I]^-$.

Oxidative addition of an aryl iodide to $Pd^0(dba)_2$ in the presence of TMEDA, followed by displacement of TMEDA by two equivalents of phosphine is an easy and efficient way to synthesize $Pd(PR_3)_2(Ar)(I)$ complexes. However this reaction works only for aryl iodide complexes, not for the other halides.[202] We used this reaction to make a charge-tagged version of $Pd(PR_3)_2(Ar)(I)$, with a positive charge appended to the aryl group. This intermediate plays a role in many cross-coupling reactions and its isolation can provide the opportunity of further mechanistic study by ESI-MS.

6.2 Mechanism investigation of the ligand substitution

Through synthesis of $Pd(PR_3)_2(Ar)(I)$ we realized that the charge-tagged analogue itself provides an opportunity to study a ligand substitution reaction in detail, because both the precursor, $[Pd(TMEDA)(Ar)(I)]^+$ (**1**, Ar = $[C_6H_4CH_2PPh_3]^+$ $[PF_6]^-$) and product, $[Pd(PPh_3)_2(Ar)(I)]^+$ (**4**), are themselves charged.

We expected that addition of PPh_3 to $[Pd(TMEDA)(Ar)(I)]^+$ proceeded through a slow substitution of PPh_3 with one of the TMEDA donors which subsequently should , follow by faster displacement of the other TMEDA donor with a second PPh_3 (left side of Scheme 6.1). However, the first PSI-ESI-MS reaction resulted some unpredicted observation. Upon addition of PPh_3 a doubly-charged palladium-containing peak jumped up rapidly in (+)ESI-MS which was followed by its disappearance with semi-first order kinetics over the course of reaction. This intermediate was assigned to $[Pd(TMEDA)(Ar)(PPh_3)]^{2+}$. This finding was quite interesting because it suggested that the reaction proceeded quite differently from what had been assumed by others; there was a very fast displacement of I^- by PPh_3 to form $[Pd(TMEDA)(Ar)(PPh_3)]^{2+}$ (**2**), followed by a much slower displacement of TMEDA and recoordination of $[I]^-$ to form the product (**4**). Since this displacement consists of separation and recoordination of iodide, we would expect to see the same behavior for iodide but in the negative ion mode. Figure 6.1 summarizes the observation of both modes of ESI-MS. As it is clear formation of **2** and I^- is almost identical and very fast under these conditions, and is complete in less time than it takes for the solution to move from reaction flask to mass spectrometer (~10 seconds). To obtain the relative intensity in Sonogashira and hydrodehalogenation, normalizations were processed by normalizing each species of interest to the all tag containing species, since the response factor of species specially substrates and products were close to one another due to equal charge to mass and the big size of charged tag in comparison with the rest of the structure. However this method is not applicable due to the formation of doubly-charged complex **2.** A doubly-charged species has better detector response at multi-channel plates compared with a singly-charged species with similar *m/z* and hence higher ion counts. So the same type of normalization is misleading in this case. To solve this problem, the maximum intensity reached by each species was considered as a unit in

the figure and the intensity at different times was normalized to the maximum intensity to obtain Figure 6.1. Figure 6.2 and 6.3 were duplicated for better demonstration of $[I]^-$ and **2** formations with *pseudo*-first order fitting for each one as the insets.

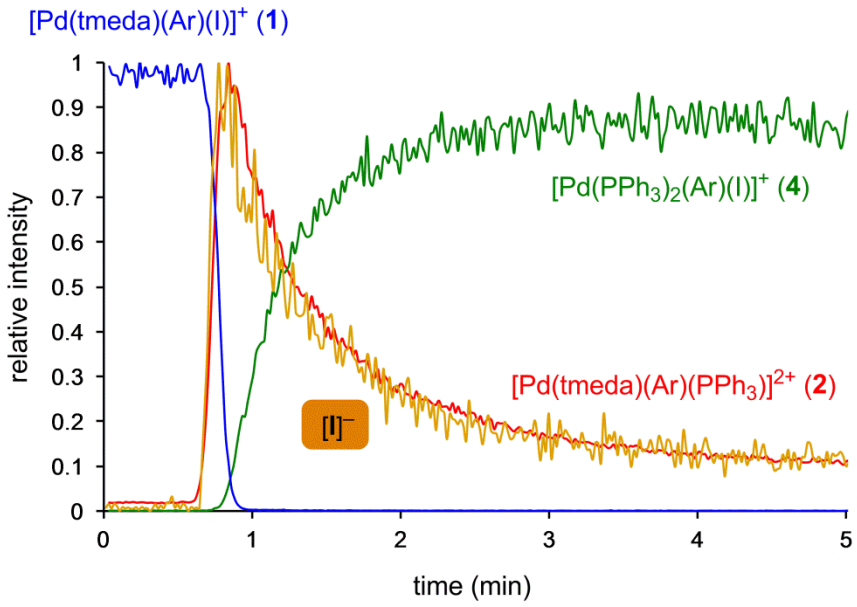

Figure 6.1*:* Reaction progress in methanol at 55 °C, as measured by positive-ion (traces for blue **1**, red **2** and green **4**) and negative-ion mode (orange $[I]^-$, from a duplicate experiment) PSI-ESI-MS.

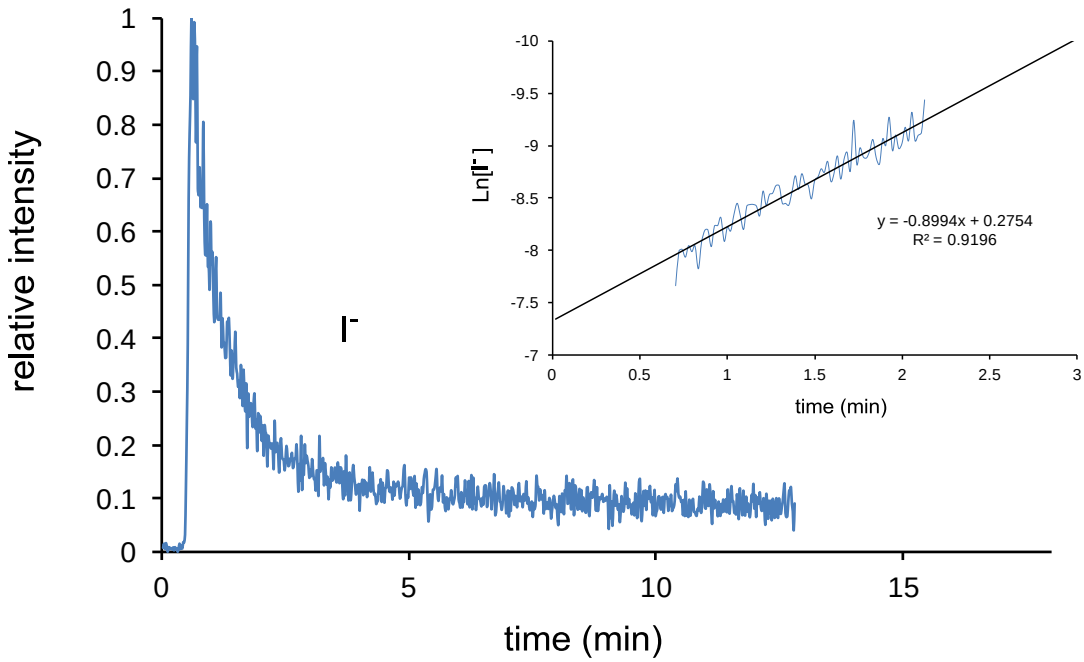

Figure 6.2: *Pseudo*-first order kinetics for the first couple of minutes after addition of PPh_3 gives k = 0.9 ± 0.1 s^{-1}. These data are duplicated in Figure 6.1.

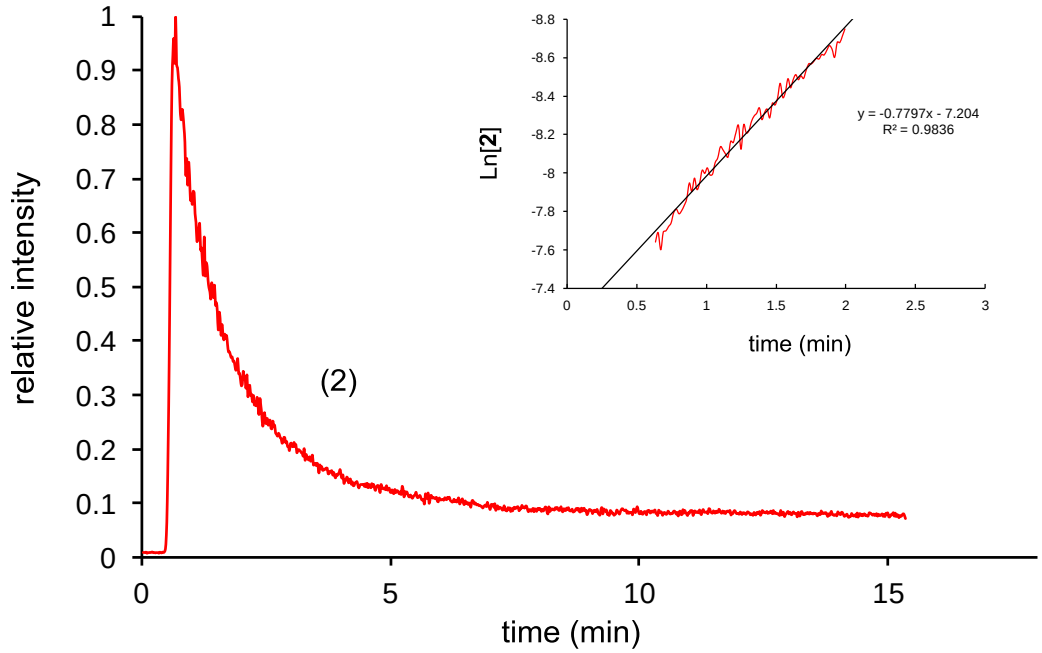

Figure 6.3: *Pseudo*-first order kinetics for the first couple of minutes after addition of PPh_3 gives k = 0.8 ± 0.1 s^{-1}. These data are duplicated in Figure 6.1.

To see whether the tagging has compromised the mechanism somehow which resulted the observed pathway, a neutral complex of Pd(TMEDA)(Ph)(I) was synthesized and

subjected to the same reaction conditions. In this case only $[Pd(TMEDA)(Ph)(PPh_3)]^+$ intermediate should be visible by ESI-MS. The formation and consumption of this charged intermediate over the course of reaction at two different temperatures was appeared in Figure 6.4 which is in accordance with previous results.

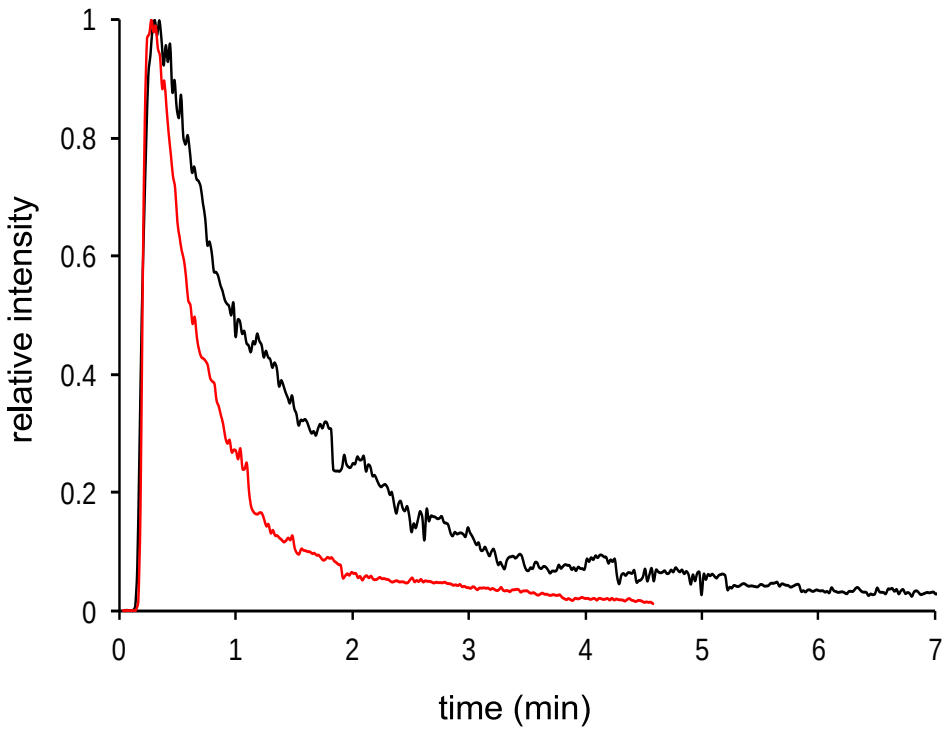

Figure 6.4: Appearance and disappearance of charged $[Pd(TMEDA)(Ph)(PPh_3)]^+$ in conversion of neutral Pd(TMEDA)PhI to $Pd(PPh_3)_2(Ph)I$ observed by positive ion PSI-ESI-MS at 327 (black) and 338 K (red).

In a separate experiment to make sure that the electrospray process does not compromise the observed mechanism and that the mechanism can be inferred by other methods, the reaction of neutral complex Pd(TMEDA)(Ph)(I) was monitored by ^{1}H NMR at room temperature. While ^{31}P NMR failed to provide useful information due to the very low concentration of substrate and long relaxation time, ^{1}H NMR provided informative data which confirmed the same observed mechanism (Figure 6.5 and 6.6).

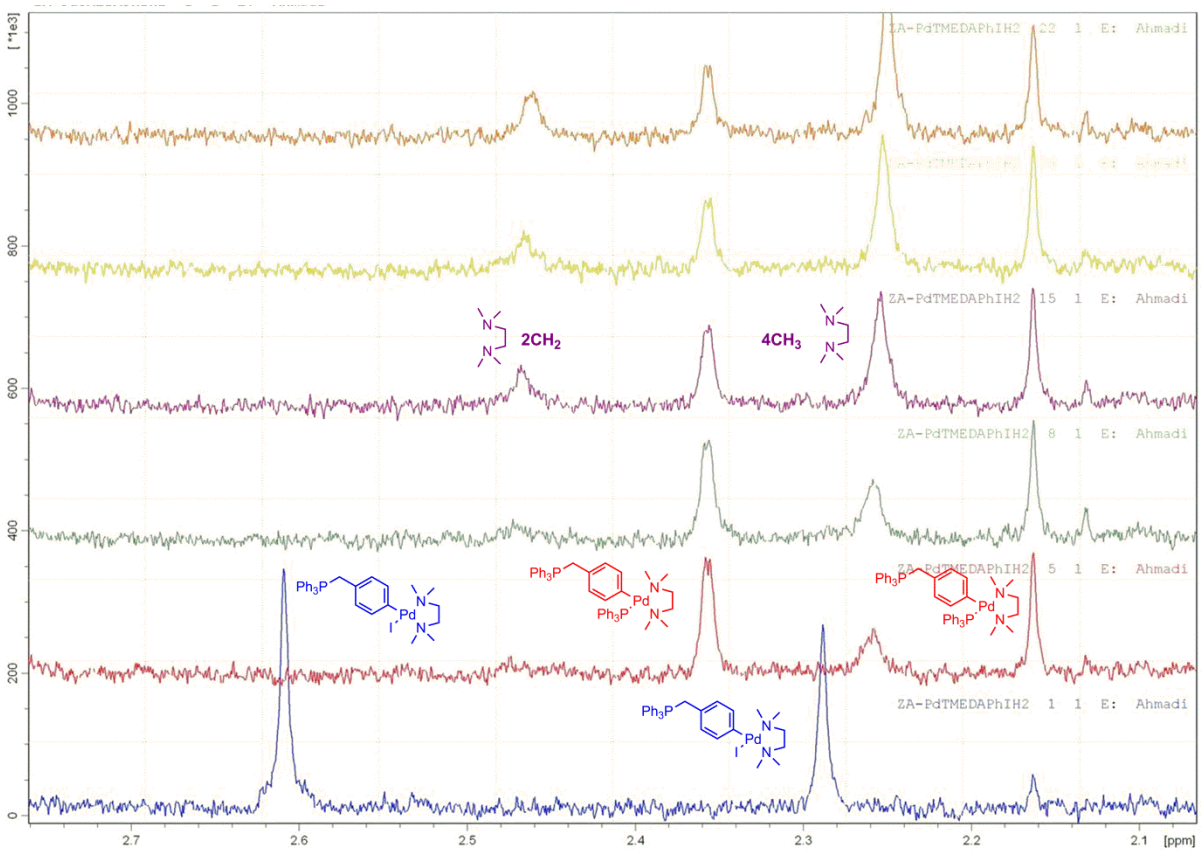

Figure 6.5: ^{1}H NMR monitoring experiment. The bottom spectrum shows two siglets of Me groups of TMEDA in Pd(TMEDA)PhI before addition of PPh_3. Second spectrum from the bottom shows the formation of Pd(TMEDA)PhPPh_3 at 25 minute. Downfield shift in chemical shift of methyl groups is observed due to replacement of PPh_3 with TMEDA in Pd complex. Appearance of free TMEDA is evident at δ 2.26. Spectra were collected every five minutes but only a few of them are show in this figure.

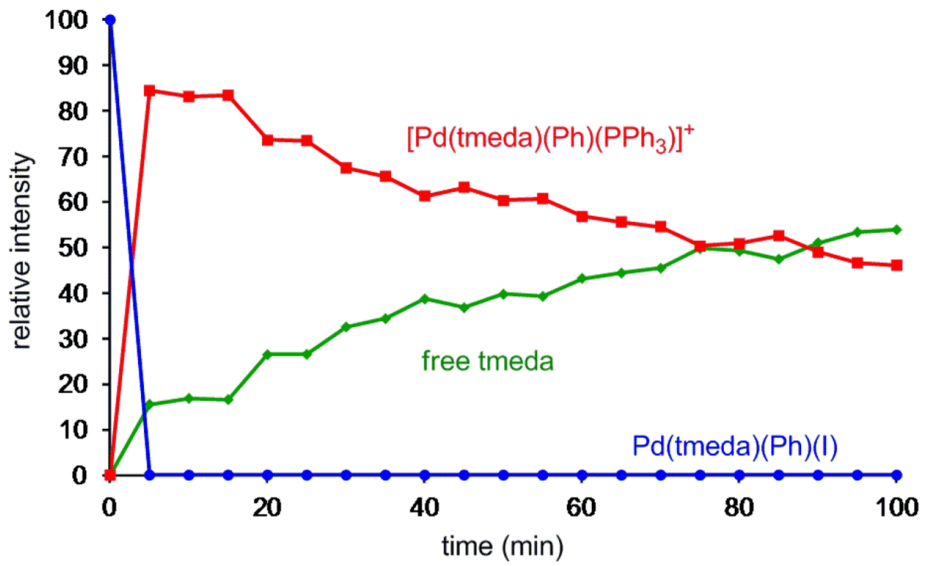

Figure 6.6: Reaction progress in CD_3OD at 22°C, as measured by ^1H NMR using the methyl groups of the TMEDA ligand.

To see whether the structural analysis can provides extra information about fast replacement of iodide, crystal structure of **1** was obtained (Figure 6.7). The strong *trans* influence of the aryl ligand is obvious, elongating the *trans* Pd-N bond to 2.20 Å compared to 2.14 Å for the Pd-N bond *trans* to the iodide ligand. However, the Pd-I bond length of 2.58 Å is ordinary; Pd-I bond lengths in square planar complexes range from 2.41-3.14 Å, with an average of 2.64 Å and a standard deviation of 0.05 Å, (Data extracted from the CCDB on 1289 square planar structures containing Pd-I and three other ligands of any type. The range is much smaller for the 57 square planar complexes with Pd I, two nitrogen donors and one other ligand: 2.55 to 2.60 Å) so if anything, the Pd-I bond length in **1** is on the short side.

.

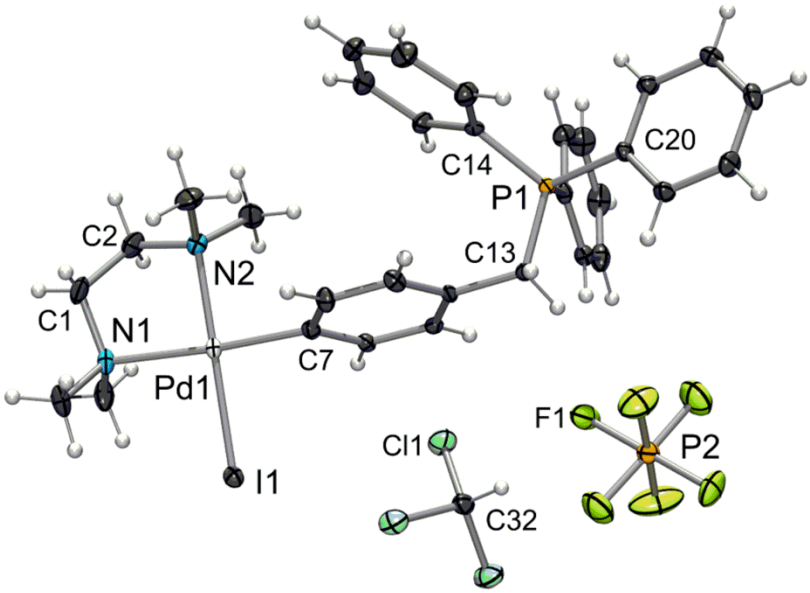

Figure 6.7: X-ray crystal structure of **1**, including the $[PF_6]^-$ counterion and $CDCl_3$ of crystallization. Selected bond lengths (Å): Pd1-I1 2.5807(2); Pd1-N1 2.2009(15); Pd1-N2 2.1411(17); Pd1-C7 1.9842(17). Selected bond angles (°): C7-Pd1-N2 92.62(7); C7-Pd1-11 87.54(5); N2-Pd1-N1 83.72(6); N1-Pd1-I1 96.12(5).

We continued to investigate the reaction mechanism in more detail since the crystal structure did not provide extra insight. As it was clear in Figure 6.1 some information is lost in very initial fast step of the reaction. We could probe the fast initial step with more time resolution than in the initial experiment, simply by applying dilution without fear of approaching the detection limit since sensitivity is not a problem when studying charge-tagged compounds by ESI-MS. The reaction was repeated with ten times the dilution of the prior concentration of **1**, and the amount of PPh_3 was reduced to one equivalent (down from ten). Accordingly, the first replacement was greatly slowed (by a factor of 1000), and also *pseudo*-first order kinetics were replaced with a second order regime (Figure 6.8) and the reaction overall took over 15 minutes to complete at 55°C, so much more time is available to calculate the second-order rate constant as $k_2 = 143 \pm 1$ L mol^{-1} s^{-1} (Figure 6.8, inset). The second-order kinetics suggests an associative mechanism, as is typical for square planar metal complexes.[203]

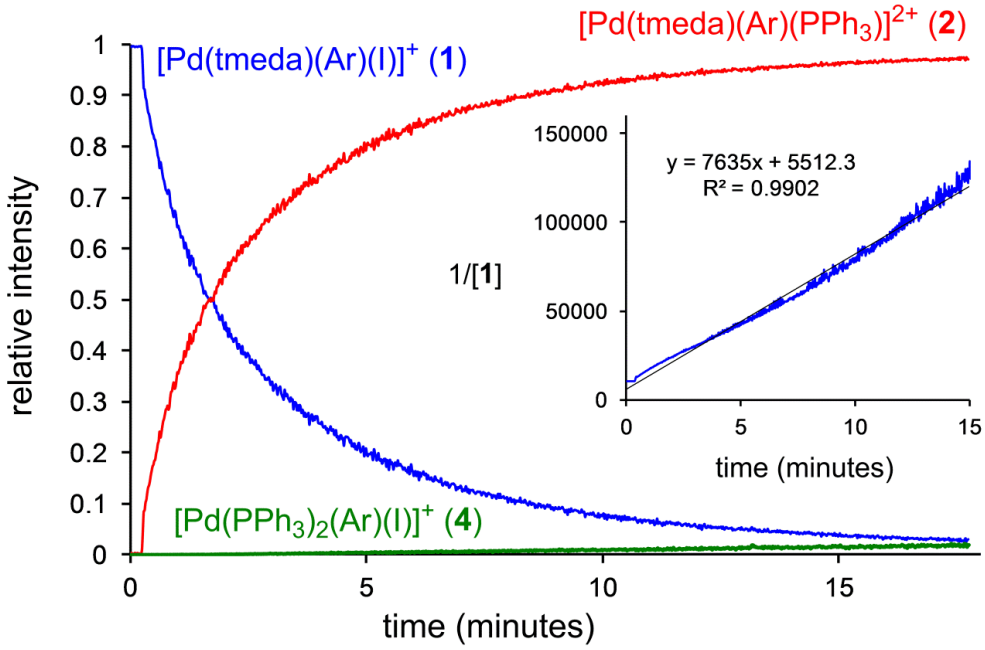

Figure 6.8: Reaction progress in methanol at 55°C, as measured by positive-ion PSI-ESI-MS. The reaction has been greatly lowered in rate by reducing the concentration of both reactants. Inset: fit of 1/[**1**] vs time confirming a good match to second-order kinetics.

Two pathways are conceivable for formation of **4** from **2** which is the slow step of this reaction: through formation of $[Pd(\kappa^1\text{-TMEDA})(PPh_3)(Ar)(I)]^+$ (**3a**) and/or $[Pd(\kappa^1\text{-TMEDA})(PPh_3)_2(Ar)]^{2+}$ (**3b**) (Scheme 6.1). Neither **3a** nor **3b** could be observed during the reaction, meaning that the rate of formation of **3a/b** from **2** is much slower than the consumption of **3a/b** to form **4**. The kinetics of the transformation of **2** into **4** are *pseudo* first order, with k_{obs} = 1.08 s^{-1} at 55°C with a 5-fold excess of PPh_3. To see which of **3a** or **3b** is the real intermediate in the mechanism, two experiments were considered to examine the effect of iodide and PPh_3, respectively, on the second substitution reaction. Addition of 10 extra equivalents of PPh_3 after formation of **2** had no effect on the rate of reaction (Figure 6.9). On the other hand, addition of 10 equivalents of $[I]^-$ after the initial ligand substitution (**1** to **2**) speeds up the reaction significantly, proposing that the pathway through **3a** contributes the most in the mechanism.

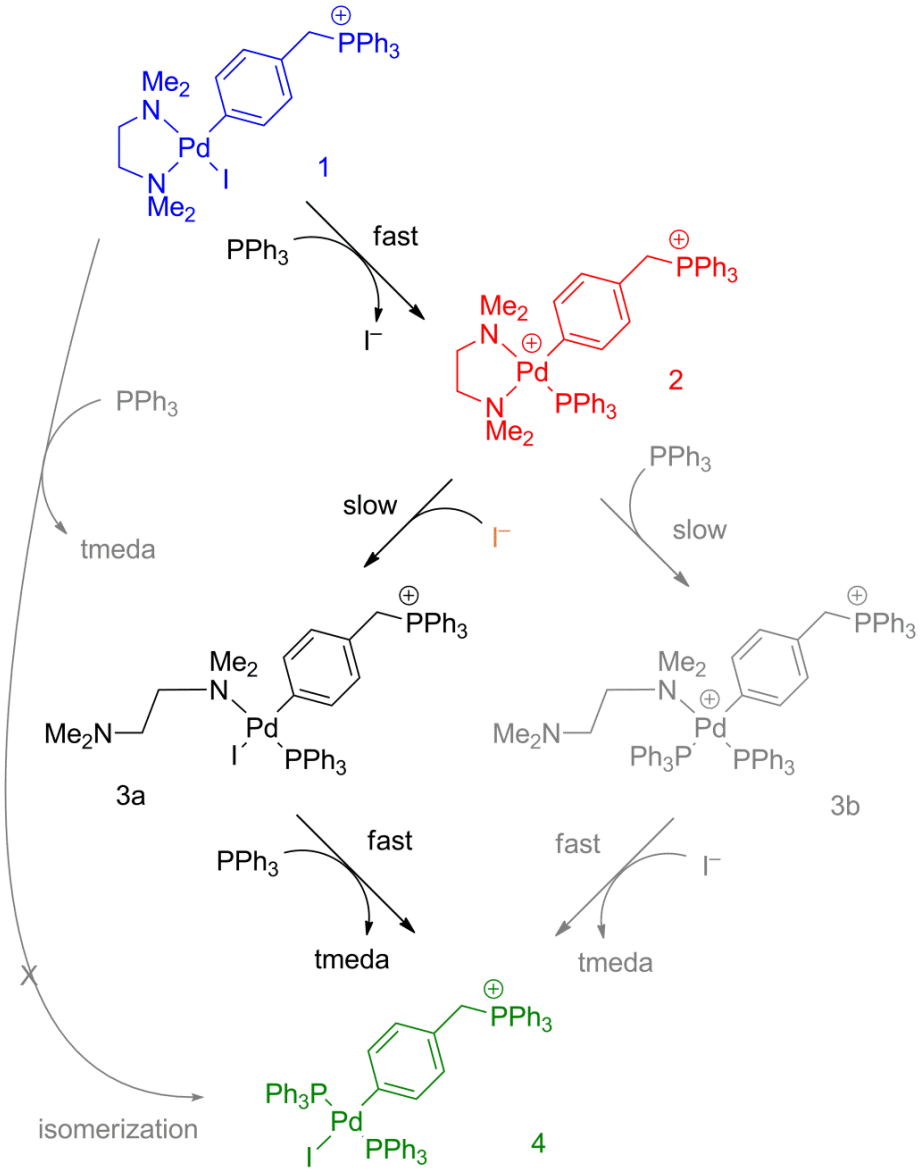

Scheme 6.1: Possible reaction pathways for the substitution of TMEDA for 2 × PPh_3. PSI-ESI-MS reveals the reaction to proceed via **1** → **2** → **3a** → **4**. Of these four complexes, only **3a** is not directly observed, but its involvement can be inferred by the effect of $[I]^-$ vs. PPh_3 on the reaction **2** → **4**.

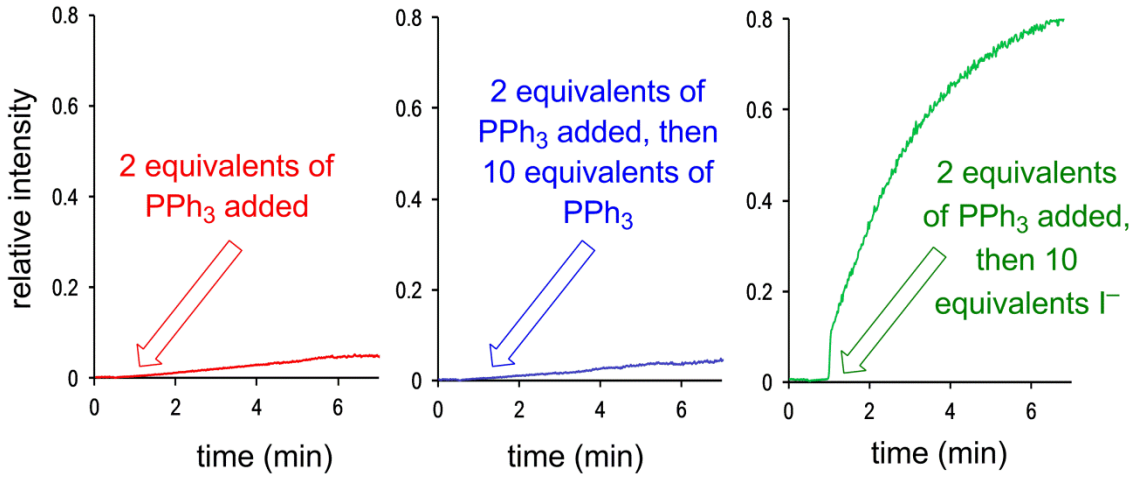

Figure 6.9: Rate of formation of **4** from **1** under different experimental conditions. Additional PPh_3 does not affect the rate, but additional $[I]^-$ does.

The fact that the substitution occurs via **3a** is interesting, as it opens a new avenue for the synthesis of the halide analogue of $Pd(PR_3)(Ar)(X)$ (X = Br, Cl, F, pseudohalide) simply by addition of an excess of their salt. In another set of experiments, addition of NaBr and NaCl resulted in formation of the expected new halide complex. However, in each reaction the remaining $[I]^-$ released from the complex competes with the other halide to form a mixture of products (Figure 6.10 and 6.11 for $[Cl]^-$ and $[Br]^-$ addition respectively). As is obvious in these figures, because $[I]^-$ is a better nucleophile than $[Br]^-$, which is better than $[Cl]^-$ thus $[Br]^-$ competes better to replace $[I]^-$ in the complex than $[Cl]^-$. A solution for this issue is the addition of one equivalent of $AgNO_3$[204] to precipitate out AgI, followed by addition of the desired halide, and this reaction completes very quickly in yields of >98% by ESI-MS for $Pd(PR_3)(Ar)(Br)$ (Figure 6.12).

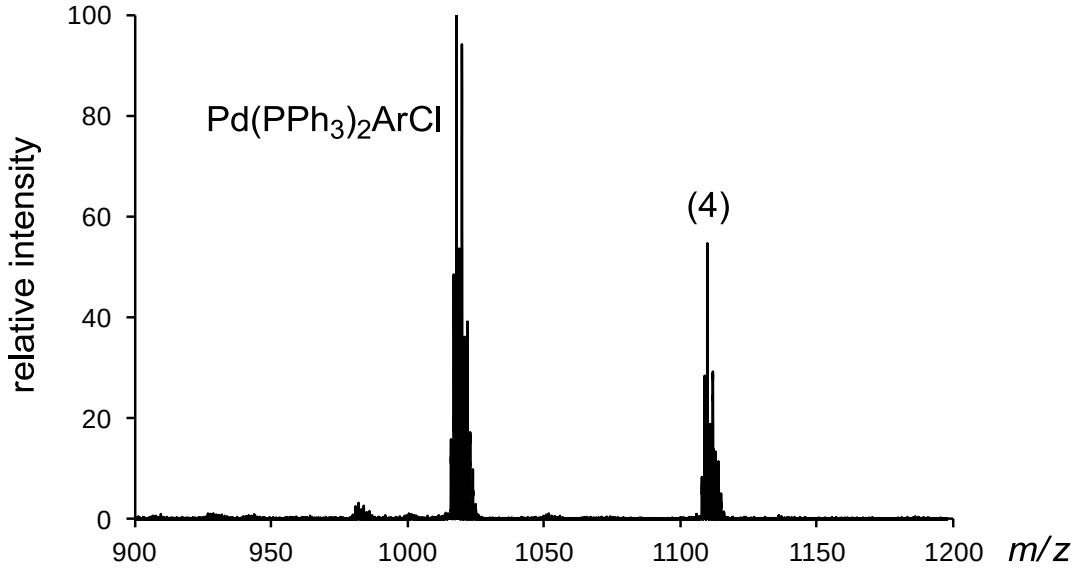

Figure 6.10: A single spectrum of the reaction after 16 minutes of addition NaCl into reaction.

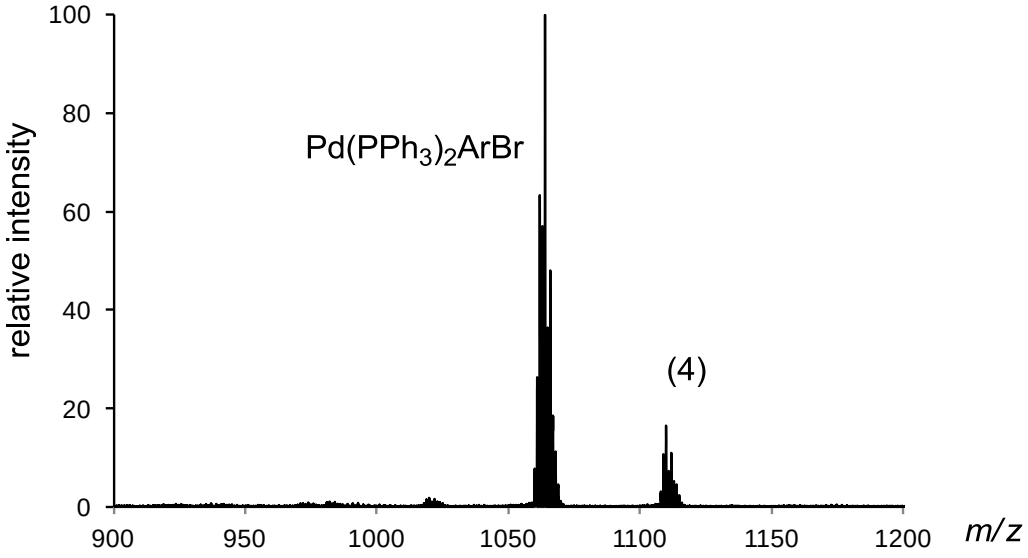

Figure 6.11: A single spectrum of the reaction after 18 minutes of addition KBr into reaction.

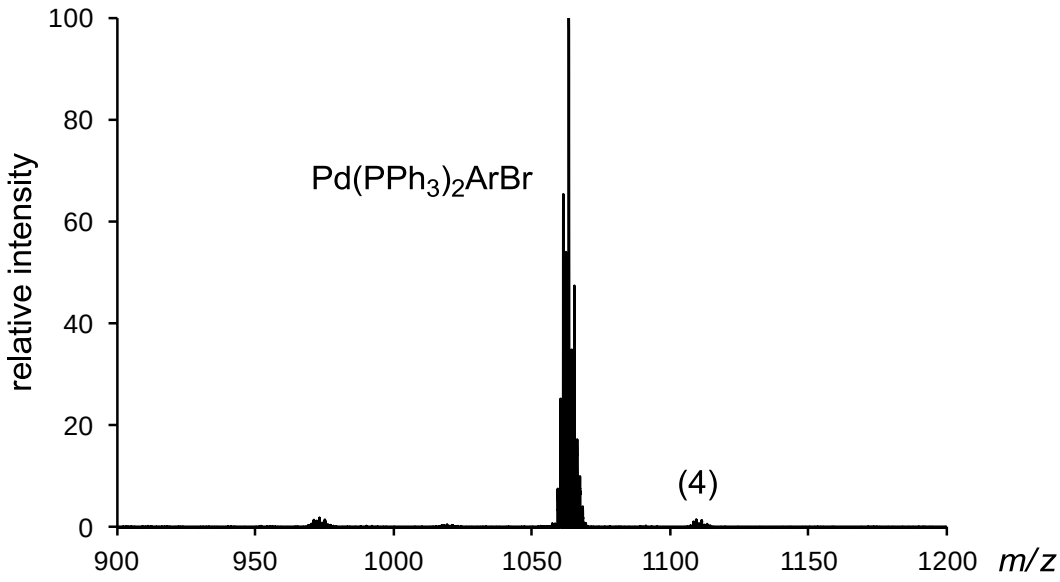

Figure 6.12: A single spectrum of the reaction at 30 minutes after addition of $AgNO_3$ followed by addition of 10eq KBr. The amount of $Pd(PPh_3)_2(Ar)(I)$ is less than 3% (based on the intensity) compared to the bromide analogue.

6.3 Enthalpy and Entropy of activation

In order to see how enthalpy and entropy of activation track with mechanistic data, both conversion including **1** → **2** and **1** → **4** were repeated under the same conditions but different temperatures. **1** → **4** (303.5, 317.3, 323.5 and 332.6 K) to allow the measurement of $\Delta H^{\ddagger} = 20 \pm 2$ kJ mol^{-1} and $\Delta S^{\ddagger} = -80 \pm 200$ J mol^{-1} via the construction of an Eyring plot (Figure 6.13). The large error in the entropy of activation is due to the fact that at the low concentrations used in these experiments, getting the near-perfect data required for measuring a precise intercept is very difficult.

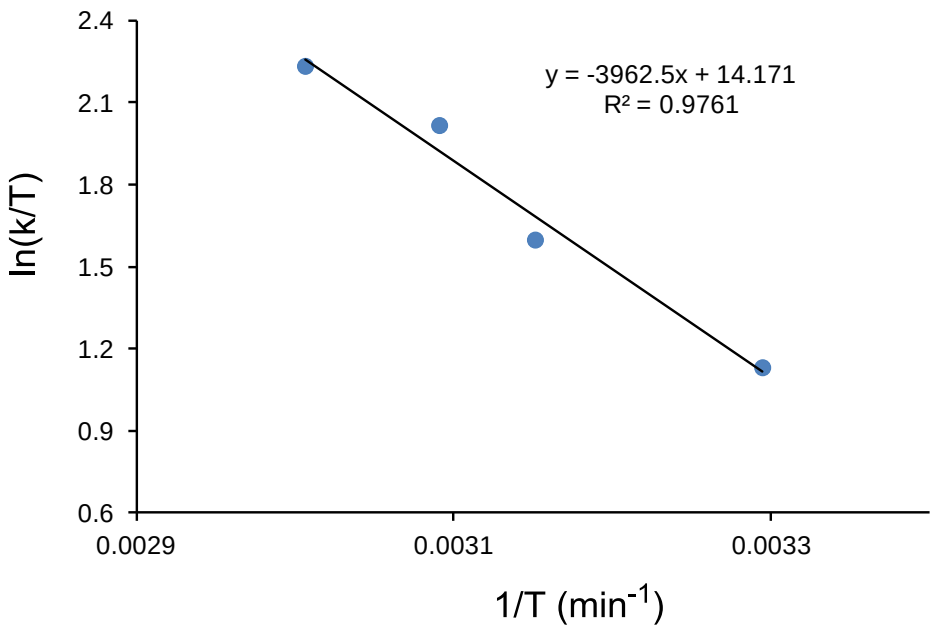

Figure 6.13: Eyring plot for the reaction of **1** to **2** at same conditions but different temperatures.

An Eyring plot for the conversion of **1** → **4** provided similarly high uncertainty in the $\Delta S^{\ddagger}$ value (10 ± 170 J mol^{-1}), but a substantially higher $\Delta H^{\ddagger}$ of 78 ± 8 kJ mol^{-1} (Figure 6.14). That this ligand substitution is slower than the first is perhaps unsurprising, as it involves the displacement of a chelating ligand, as opposed to just displacing the monodentate iodide ligand.

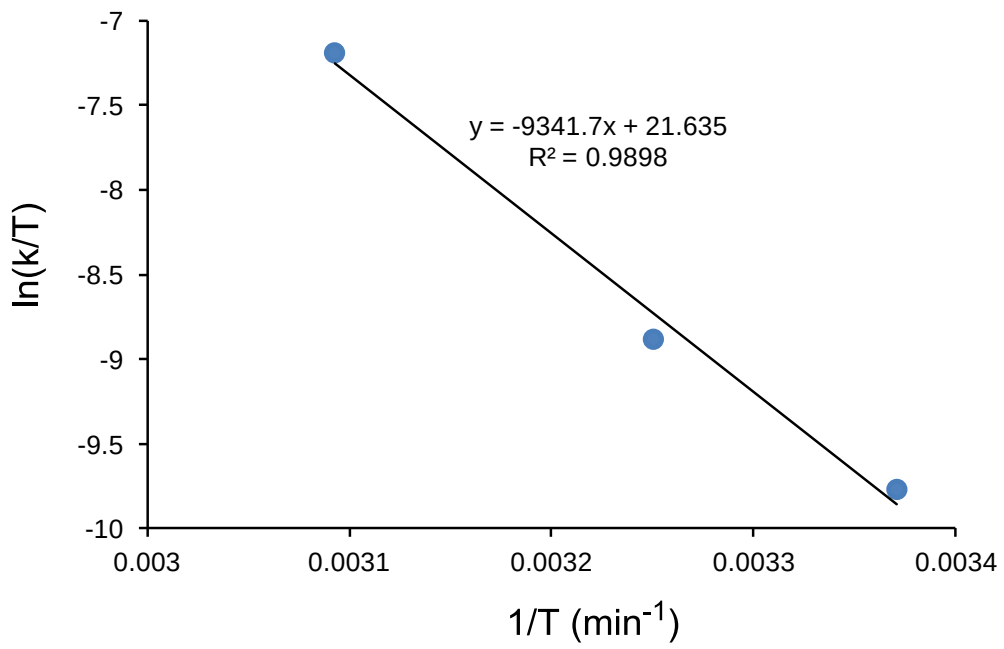

Figure 6.14: Eyring plot for the reaction of **1** to **4** at the same conditions but different temperatures.

6.4 Conclusion

The extent in which PSI-ESI-MS sheds light into this mechanism is promising for further investigation of homogenous catalysis. It demonstrates that a profound understanding of a mechanism allows for the modification of a reaction in a rational way. Particularly the unpredicted behavior of iodide in dissociation and recoordination suggested a neat method to intercept this halide and replace it with other halides to make $Pd(PR_3)_2(Ar)(X)$ (X = I, Br, Cl, F). Although these complexes have been made before, they usually require forcing conditions such as high temperature, activated ArCl and long reaction times[205], and while some improved methods have been reported for specific halides[206, 207], a fast, efficient and general approach to this group of compounds has not been forthcoming.

6.5 Experimental

All syntheses and catalytic reactions were performed under an inert atmosphere of N_2 using standard glovebox or Schlenk procedures. All chemicals were obtained from Aldrich and used without further purification. Solvents were HPLC grade and purified on an MBraun solvent purification system. Gases were obtained from Airgas (Calgary, Canada). All mass spectra were collected on a Micromass Q-ToF *micro* mass spectrometer in positive and negative-ion mode using pneumatically assisted electrospray ionization. Further details are available in the supporting information.

Synthesis of $[Pd(TMEDA)(C_6H_4CH_2PPh_3)(I)]^+[PF_6]^-$ (1)

$[4\text{-}IC_6H_4CH_2PPh_3]^+[PF_6]^-$ (0.13 g, 0.2 mmol), tetramethylethylenediamine (TMEDA) (37 µL, 0.25 mmol) and $Pd(dba)_2$ (0.12 g, 0.1 mmol) were dissolved in acetone (8 mL) and stirred for 30 min at 30 °C until the solution changed colour from red to yellow. The product was filtered and washed with cold diethylether and dried in vacuum overnight at 60 °C. Yield 72% (0.12 g, 0.14 mmol). Single crystals were grown from a solution of $CDCl_3$. M.p: 97 °C. ^{1}H NMR (300 MHz, $CDCl_3$): δ 2.27 (s, 6H, NCH_3), 2.60 (s, 6H, NCH_3), 2.69 (m, 2H, NCH_2), 2.52 (m, 2H, NCH_2), 4.32 (d, 2H, PCH_2, J = 14 Hz), 6.28 (dd, 2H, C_6H_4, $^3J_{HH}$ = 8 Hz, $^4J_{HP}$ = 2 Hz), 6.99 (d, 2H, C_6H_4, J=8 Hz), 7.3-7.8 (m, C_6H_5, 15H). ^{31}P NMR (300 MHz, $CDCl_3$): δ 22.96 (s). ESI(+)-MS (solvent: MeOH): *m/z* 701.1(Figure 6.15) Appropriate crystals for X-ray analysis was grown in $CDCl_3$ (Appendix B).

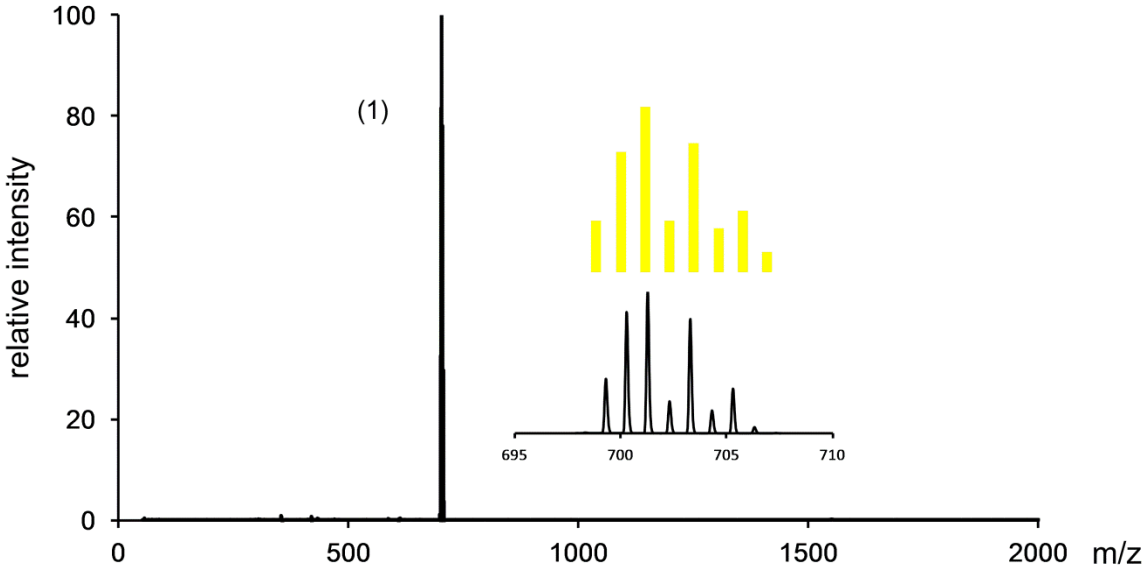

Figure 6.15: Positive ion ESI-MS of **1** along with its experimental and calculated isotope pattern.

Synthesis of Pd(TMEDA)(Ph)(I)

Pd(TMEDA)(Ph)(I) was prepared by a literature method.[208] To a purple solution of 1.0 g (1.6 mmol) of $Pd(dba)_2$ in 30 ml of benzene were added 230 µl (2.3 mmol) of TMEDA and 230 µl (2.5 mmol) of iodobenzene. The mixture was slowly heated to 50°C under N_2 gas during which the colour changed to orange. The solution was filtered and the solvent removed. Rest of the residue was washed with cold diethyl ether (3 × 5 ml). Yield: 0.7 g (95%). Pure product was obtained by recrystallization from boiling benzene. ^{1}H NMR (300 MHz) ($CDCl_3$): δ 2.28 (6H, s, NMe,), δ 2.61 (4H, AA'BB', 2 CH_2), δ 2.64 (6H, s, NMe), δ 6.75 (lH, t, J= 7.2 Hz, *p*-Ph), δ 6.87 (2H, dd, J= 6.9, 7.4 Hz, *m*-ph), δ 7.18 (2H, d, J= 7.4 Hz, *o*-Ph).

^{1}H NMR monitoring experiment

For the ^{1}H NMR monitoring experiment, 1 mM of Pd(TMEDA)PhI was made in 1 ml CD_3OD in the NMR tube and was degassed and sealed with a rubber septum. 2.2 equivalents of PPh_3 (65 ul of 0.0088 g PPh_3 in 1 ml $CDCl_3$) was injected in the tube at the beginning of the reaction. NMR spectrum were collected (32 scans, delay time (D1): 5s) every 5 minutes using a 500 MHz Bruker instrument.

Additional mass spectrometric and experimental details:

Capillary voltage: 2900 V. Cone voltage: 10 V. Extraction voltage: 0.5 V. Source temperature: 70 °C. Desolvation temperature: 150°C. Cone gas flow: 100 L/h. Desolvation gas flow: 200 L/h. Collision voltage: 2 V (for MS experiments). Collision voltage: 15 - 25 V (for MS/MS experiments). During PSI experiments, overpressure in the flask was held at 3.5 psig (Ar) throughout the reaction and the temperature was controlled by a digital thermometer mounted inside the flask. The reaction mixture was transferred to MS without further dilution through PEEK tubing (200 mm in length, i.d. 0.055 mm). Data was processed without any normalization for Eyring plots, but all other plots were normalized after applying a correction for variable ionization efficiency (using the measured response factors of **1** and **4**, and by estimating that of **2** based on the quantitative transformation of **1** into **2**). About 3600 spectra were collected per hour of monitoring (1 s^{-1}). For the monitoring of **1** to **2**, 5 ml 0.1 mM of **1** in methanol was degassed and transferred to PSI flask and 0.2 mg of $[Ph_3PMe]^+[PF_6]^-$ added as the internal standard. 1 equivalent of PPh_3 (dissolved in 5:95 toluene/methanol) was added and the reaction was monitored for about 20 min at different temperatures. For the monitoring of **1** to **4**, 5ml 1mM of **1** in methanol was degassed and transferred to the flask and 2 mg $[Ph_3PMe]^+[PF_6]^-$ added as an internal standard. 10 equivalents of PPh_3 (dissolved in 5:95 toluene/methanol) were added and the reaction monitored for about 20 minutes at different temperatures

Chapter 7 Conclusion

This thesis described the application of pressurized sample infusion (PSI) in homogenous catalytic study. Details of the implementation were described and technical barriers were addressed. Also an integration of UV/Vis spectroscopy with ESI-MS was proposed which can be used to obtain complementary information of catalytic systems where ESI-MS only is not informative enough.

PSI-ESI-MS was used to study several palladium catalytic systems including: Sonogashira cross coupling reaction, hydrodehalogenation of aryl iodide and a ligand substitution in an arylpalladium complex. Other techniques such as NMR, UV-Vis, X-ray crystallography and numerical modeling were used to validate the data. Rich kinetic and mechanistic information were obtained which led to a proposal of mechanistic pathway for each of these transformations.

Bibliography

1. F. F. D. Oliveira, M. R. dos Santos, P. M. Lalli, E. M. Schmidt, P. Bakuzis, A. A. M. Lapis, A. L. Monteiro, M. N. Eberlin and B. A. D. Neto, *J. Org. Chem.*, **2011**, 76, 10140-10147.

2. K. W. M. Siu, R. Guevremont, J. C. Y. Le Blanc, G. J. Gardner and S. S. Berman, *J. Chromatogr. A*, **1991**, 554, 27-38.

3. A. J. Canty, P. R. Traill, R. Colton and I. M. Thomas, *Inorg. Chim. Acta*, **1993**, 210, 91-97.

4. J. Masllorens, I. Gonzalez and A. Roglans, *Eur. J. Org. Chem.*, **2007**, 158-166.

5. A. A. Sabino, A. H. L. Machado, C. R. D. Correia and M. N. Eberlin, *Angew. Chem., Int. Ed.*, **2004**, 43, 2514-2518.

6. P. A. Enquist, P. Nilsson, P. Sjoberg and M. Larhed, *J. Org. Chem.*, **2006**, 71, 8779-8786.

7. A. Svennebring, P. J. R. Sjoberg, M. Larhed and P. Nilsson, *Tetrahedron*, **2008**, 64, 1808-1812.

8. C. Chevrin, J. Le Bras, A. Roglans, D. Harakat and J. Muzart, *New J. Chem.*, **2007**, 31, 121-126.

9. C. Markert, M. Neuburger, K. Kulicke, M. Meuwly and A. Pfaltz, *Angew. Chem. Int. Ed. Engl.*, **2007**, 46, 5892-5895.

10. C. Raminelli, M. H. G. Prechtl, L. S. Santos, M. N. Eberlin and J. V. Comasseto, *Organometallics*, **2004**, 23, 3990-3996.

11. M. Bonchio, G. Licini, G. Modena, O. Bortolini, S. Moro and W. A. Nugent, *J. Am. Chem. Soc.*, **1999**, 121, 6258-6268.

12. Z. Li, Z. H. Tang, X. X. Hu and C. G. Xia, *Chem.--Eur. J.*, **2005,** 11, 1210-1216.

13. B. C. Gilbert, J. R. Lindsay Smith, A. Mairata i Payeras, J. Oakes and R. Pons i Prats, *J. Mol. Catal. A: Chem.*, **2004**, 219, 265-272.

14. H. Chen, R. Tagore, G. Olack, J. S. Vrettos, T.-C. Weng, J. Penner-Hahn, R. H. Crabtree and G. W. Brudvig, *Inorg. Chem.*, **2007**, 46, 34-43.

15. P. J. Dyson, K. Russell and T. Welton, *Inorg. Chem. Commun.*, **2001**, 4, 571-573.

16. P. Pelagatti, M. Carcelli, F. Calbiani, C. Cassi, L. Elviri, C. Pelizzi, U. Rizzotti and D. Rogolino, *Organometallics*, **2005**, 24, 5836-5844.

17. C. Daguenet, R. Scopelliti and P. J. Dyson, *Organometallics*, **2004**, 23, 4849-4857.

18. C. Vicent, M. Viciano, E. Mas-Marza, M. Sanau and E. Peris, *Organometallics*, **2006**, 25, 3713-3720.

19. A. Roglans and A. Pla-Quintana, in *Reactive Intermediates: MS Investigations in Solution*, ed. L. S. Santos, Wiley-VCH Verlag GmbH & Co. KGaA, **2010**, pp. 229-275.

20. R. A. J. O'Hair, in *Reactive Intermediates: MS Investigations in Solution*, ed. L. S. Santos, Wiley-VCH Verlag GmbH & Co. KGaA, **2010**, pp. 199-227.

21. J. S. McIndoe, in *Spectroscopic Properties of Inorganic and Organometallic Compounds*, ed. R. D. Jack Yarwood, Simon Duckett, Royal Society of Chemistry, **2010**, pp. 288-308.

22. M. Bonchio, O. Bortolini, V. Conte and S. Primon, *J. Chem. Soc., Perkin Trans. 2*, **2001**, 763-765.

23. M. Bonchio, G. Licini, G. Modena, O. Bortolini, S. Moro and W. A. Nugent, *J. Am. Chem. Soc.*, **1999**, 121, 6258-6268.

24. M. Bonchio, G. Licini, G. Modena, S. Moro, O. Bortolini, P. Traldi and W. Nugent, *Chem. Commun.*, **1997**, 869-870.

25. O. Bortolini, M. Carraro, V. Conte and S. Moro, *Eur. J. Inorg. Chem.*, **2003**, 42-46.

26. B. C. Gilbert, N. W. J. Kamp, J. R. Lindsay Smith and J. Oakes, *J. Chem. Soc., Perkin Trans. 2: Phys.Org. Chem.*, **1998**, 1841-1844.

27. B. C. Gilbert, J. R. Lindsay Smith, A. Mairata i Payeras, J. Oakes and R. Pons i Prats, *J. Mol. Catal. A: Chem.*, **2004**, 219, 265-272.

28. B. C. Gilbert, J. R. Lindsay Smith, M. S. Newton, J. Oakes and R. Pons i Prats, *Org. Biomol. Chem.*, **2003**, 1**,** 1568-1577.

29. C. Kim, K. Chen, J. Kim and L. Que, Jr., *J. Am. Chem. Soc.*, **1997**, 119, 5964-5965.

30. D. Feichtinger and D. A. Plattner, *Angew. Chem., Int. Ed. Engl.*, **1997**, 36, 1718-1719.

31. Z. O. Oyman, W. Ming and R. Van der Linde, *Appl. Catal., A*, **2007**, 316, 191-196.

32. E. F. Wilson, H. N. Miras, M. H. Rosnes and L. Cronin, *Angew. Chem., Int. Ed. Engl.*, **2011**, 50, 3720-3724.

33. C.-X. Yin and R. G. Finke, *J. Am. Chem. Soc.*, **2005**, 127, 9003-9013.

34. A. Fujii, E. Hagiwara and M. Sodeoka, *J. Am. Chem. Soc.*, **1999**, 121, 5450-5458.

35. M. Tromp, J. R. A. Sietsma, S. A. v. Bokhoven, G. P. F. v. Strijdonck, R. J. v. Haaren, A. M. J. v. d. Eerden, P. W. N. M. v. Leewen and D. C. Koningsberger, *Chem. Commun.*, **2003**, 128-129.

36. D. Harakat, J. Muzart and J. Le Bras, *RSC Advances*, **2012**, 2, 3094-3099.

37. R. S. Paton and J. M. Brown, *Angew. Chem., Int. Ed. Engl.*, **2012**, 51, 10448-10450.

38. W. Zhu, H. Wang, H. Peng, G. Liu and Y. Guo, *Chin. J. Chem.*, **2013**, 31, 371-376.

39. J. Lindh, P. J. R. Sjöberg and M. Larhed, *Angew. Chem., Int. Ed. Engl.*, **2010**, 49, 7733-7737.

40. M. Parera, A. Dachs, M. Solà, A. Pla-Quintana and A. Roglans, *Chem.--Eur. J.*, **2012**, 18, 13097-13107.

41. J. Hyvl, D. Agrawal, R. Pohl, M. Suri, F. Glorius and D. Schröder, *Organometallics*, **2013**, 32, 807-816.

42. S.-W. Cheng, M.-C. Tseng, K.-H. Lii, C.-R. Lee and S.-G. Shyu, *Chem. Commun.*, **2011**, 47, 5599-5601.

43. K. Jiang, G. Bian, Y. Chai, H. Yang, Q. Lai and Y. Pan, *Int. J. Mass. Spectrom.*, **2012**, 321–322, 40-48.

44. A. Fedorov, L. Batiste, E. P. A. Couzijn and P. Chen, *ChemPhysChem*, **2010**, 11, 1002-1005.

45. E. P. A. Couzijn, E. Zocher, A. Bach and P. Chen, *Chem.--Eur. J.*, **2010**, 16, 5408-5415.

46. L. Batiste, A. Fedorov and P. Chen, *Chem. Commun.*, **2010**, 46, 3899-3901.

47. Y.-Y. Lai, M. Bornand and P. Chen, *Organometallics*, **2012**, 31, 7558-7565.

48. M.-E. Moret and P. Chen, *Eur. J. Inorg. Chem.*, **2010**, 2010, 438-446.

49. F. Rouholahnejad, D. b. Mathis and P. Chen, *Organometallics*, **2009**, 29, 294-302.

50. M. Jović, S. Torker and P. Chen, *Organometallics*, **2011**, 30, 3971-3980.

51. A. Fedorov, L. Batiste, A. Bach, D. M. Birney and P. Chen, *J. Am. Chem. Soc.*, **2011**, 133, 12162-12171.

52. H. Jansen, M. C. Samuels, E. P. A. Couzijn, J. C. Slootweg, A. W. Ehlers, P. Chen and K. Lammertsma, *Chem.Eur. J.*, **2010**, 16, 1454-1458.

53. A. Fedorov, E. P. A. Couzijn, N. S. Nagornova, O. V. Boyarkin, T. R. Rizzo and P. Chen, *J. Am. Chem. Soc.*, **2010**, 132, 13789-13798.

54. D. b. Mathis, E. P. A. Couzijn and P. Chen, *Organometallics*, **2011**, 30, 3834-3843.

55. D. Serra, M.-E. Moret and P. Chen, *J. Am. Chem. Soc.*, **2011**, 133, 8914-8926.

56. M.-E. Moret, D. Serra, A. Bach and P. Chen, *Angew. Chem., Int. Ed. Engl.*, **2010**, 49, 2873-2877.

57. S. Torker, A. Müller, R. Sigrist and P. Chen, *Organometallics*, **2010**, 29, 2735-2751.

58. C. Adlhart and P. Chen, *Helv. Chim. Acta*, **2003**, 86, 941-949.

59. S. Torker, D. Merki and P. Chen, *J. Am. Chem. Soc.*, **2008**, 130, 4808-4814.

60. G. J. Arsenault, C. M. Anderson and R. J. Puddephatt, *Organometallics*, **1988**, **7**, 2094-2097.

61. J. M. Brown and K. K. Hii, *Angew. Chem., Int. Ed. Engl.*, **1996**, 35, 657-659.

62. L. Ripa and A. Hallberg, *J. Org. Chem.*, **1996**, 61, 7147-7155.

63. M. A. Aramendia, F. Lafont, M. Moreno-Manas, R. Pleixats and A. Roglans, *J. Org. Chem.*, **1999**, 64, 3592-3594.

64. A. R. Anna Pla-Quintana, *Arkivoc*, **2005**, 51-62.

65. T. d. A. Fernandes, V. B. Gontijo, M. N. Eberlin, S. A. J. M. da and P. R. R. Costa, *J. Org. Chem.*, **2010**, 75, 7085-7091.

66. C. D. Buarque, V. D. Pinho, B. G. Vaz, M. N. Eberlin, S. A. J. M. da and P. R. R. Costa, *J. Organomet. Chem.*, **2010**, 695, 2062-2067.

67. D. Agrawal, D. Schröder and C. M. Frech, *Organometallics*, **2011**, 30, 3579-3587.

68. D. S. McGuinness, N. Saendig, B. F. Yates and K. J. Cavell, *J. Am. Chem. Soc.*, **2001**, 123, 4029-4040.

69. N. D. Clement and K. J. Cavell, *Angew. Chem., Int. Ed. Engl*, **2004**, 116, 3933-3935.

70. L. S. Santos, G. B. Rosso, R. A. Pilli and M. N. Eberlin, *J. Org. Chem.*, **2007**, 72, 5809-5812.

71. M. Lu, J. L. Campbell, R. Chauhan, C. A. Grapperhaus and H. Chen, *J. Am. Soc. Mass Spectrom.*, **2013**, 24, 502-512.

72. H.-Y. Wang, W.-L. Yim, T. Klüner and J. O. Metzger, *Chem. Eur. J.*, **2009**, 15, 10948-10959.

73. H.-Y. Wang, W.-L. Yim, Y.-L. Guo and J. O. Metzger, *Organometallics*, **2012**, 31, 1627-1634.

74. S. Kurzhals, C. Enders and W. H. Binder, *Macromolecules*, **2013**, 46, 597-607.

75. A. O. Aliprantis and J. W. Canary, *J. Am. Chem. Soc.*, **1994**, 116, 6985-6986.

76. R. Colton and J. C. Traeger, *Inorg. Chim. Acta.*, **1992**, 201, 153-155.

77. I. Ahmed, A. M. Bond, R. Colton, M. Jurcevic, J. C. Traeger and J. N. Walter, *J. Organomet. Chem.*, **1993**, 447, 59-65.

78. D. J. F. Bryce, P. J. Dyson, B. K. Nicholson and D. G. Parker, *Polyhedron*, **1998**, 17, 2899-2905.

79. C. Decker, W. Henderson and B. K. Nicholson, *J. Chem. Soc., Dalton Trans.*, **1999**, 3507-3513.

80. C. Hinderling, C. Adlhart and P. Chen, *Angew. Chem., Int. Ed.* , **1998**, 37, 2685-2689.

81. C. Adlhart, C. Hinderling, H. Baumann and P. Chen, *J. Am. Chem. Soc.*, **2000**, 122, 8204-8214.

82. P. Chen, *Angew. Chem., Int. Ed.* , **2003**, 42, 2832-2847.

83. H. Wang and J. O. Metzger, *Organometallics*, **2008**, **27**, 2761-2766.

84. T. A. Kirkland, D. M. Lynn and R. H. Grubbs, *J. Org. Chem.*, **1998**, 63, 9904-9909.

85. B. Mohr, D. M. Lynn and R. H. Grubbs, *Organometallics*, **1996**, 15, 4317-4325.

86. C. H. Beierlein, B. Breit, S. R. A. Paz and D. A. Plattner, *Organometallics*, **2010**, 29, 2521-2532.

87. A. W. Ehlers, E. J. Baerends and K. Lammertsma, *J. Am. Chem. Soc.*, **2002**, 124, 2831-2838.

88. F. E. Hahn and M. C. Jahnke, *Angew. Chem., Int. Ed. Engl*, **2008**, 120, 3166-3216.

89. P. B. Hitchcock, M. F. Lappert and W.-P. Leung, *J. Chem. Soc., Chem. Commun.*, **1987**, 0, 1282-1283.

90. M. A. Iron, H. C. Lo, J. M. L. Martin and E. Keinan, *J. Am. Chem. Soc.*, **2002**, 124, 7041-7054.

91. M. A. Iron, J. M. L. Martin and M. E. van der Boom, *J. Am. Chem. Soc.*, **2003**, 125, 11702-11709.

92. M. M. Quintal, A. Karton, M. A. Iron, A. D. Boese and J. M. L. Martin, *J. Phys. Chem. A*, **2005**, 110, 709-716.

93. N. J. Farrer, R. McDonald and J. S. McIndoe, *Dalton Trans.*, **2006**, 4570-4579.

94. D. M. Chisholm, A. G. Oliver and J. S. McIndoe, *Dalton Trans.*, **2010**, 39, 364-373.

95. S. M. Jackson, D. M. Chisholm, J. S. McIndoe and L. Rosenberg, *Eur. J. Inorg. Chem.*, **2011**, 2011, 327-330.

96. E. Crawford, T. Lohr, E. M. Leitao, S. Kwok and J. S. McIndoe, *Dalton Trans.*, **2009**, 9110-9112.

97. K. L. Vikse, S. Kwok, R. McDonald, A. G. Oliver and J. S. McIndoe, *J. Organomet. Chem.*, **2012**, 716, 252-257.

98. N. J. Farrer, K. L. Vikse, R. McDonald and J. S. McIndoe, *Eur. J. Inorg. Chem.*, **2012**, 2012, 733-740.

99. M. A. Schade, J. E. Fleckenstein, P. Knochel and K. Koszinowski, *J. Org. Chem.*, **2010,** 75, 6848-6857.

100. L. S. Santos, *J. Org. Chem.*, **2008**, 235-253.

101. L. S. Santos, in *Reactive Intermediates: MS Investigations in Solution*, ed. L. S. Santos, Wiley-VCH Verlag GmbH & Co. KGaA, **2010**, pp. 133-198.

102. M. A. Henderson, J. Luo, A. Oliver and J. S. McIndoe, *Organometallics*, **2011**, 30, 5471-5479.

103. J. Halpern, *Inorg. Chim. Acta.*, **1981**, 50, 11-19.

104. M. A. Grayson, ed., *Measuring Mass: From Positive Rays to Proteins*, Chemical Heritage Press, Philadelphia, **2002**.

105. J. J. Thomson, *Proceedings of the Royal Society of London. Series A*, **1913**, 89, 1-20.

106. A. J. Dempster, *Phys. Rev.*, **1918**, 11, 316.

107. A. J. Dempster, *Philos. Mag.*, **1916**, 31, 438-443.

108. J. C. Traeger, in *The Encyclopedia of Mass Spectrometry*, ed. M. L. G. a. R. M. Caprioli, Elsevier Ltd., Amsterdam, **2007**, p. 119.

109. M. S. B. Munson and F. H. Field, *J. Am. Chem. Soc.*, **1966**, 88, 2621-2630.

110. K. Tanaka, H. Waki, Y. Ido, S. Akita, Y. Yoshida and T. Yohida, *Rapid Commun. Mass Spectrom.*, **1988**, 2, 151-153.

111. M. Yamashita and J. B. Fenn, *J. Phys. Chem.*, **1984**, 88, 4451-4459.

112. J. B. Fenn, M. Mann, C. K. Meng, S. F. Wong and C. M. Whitehouse, *Science*, **1989**, 246, 64-71.

113. R. Zenobi and R. Knochenmuss, *Mass Spectrom. Rev.*, **1999**, 17, 337-366.

114. M. Karas, U. Bahr, A. Ingendoh and F. Hillenkamp, *Angew. Chem., Int. Ed. Engl.* , **1989**, 28, 760-761.

115. U. Bahr, M. Karas and F. Hillenkamp, *Z. Anal. Chem.*, **1994**, 348, 783-791.

116. M. Dole, L. L. Mack, R. L. Hines, R. C. Mobley, L. D. Ferguson and M. B. Alice, *J. Chem. Phys.*, **1968**, 49, 2240-2249.

117. l. M. J. F. De, B. G. J. Van, C. G. Enke, R. B. Cole, M. Martinez-Sanchez and J. B. Fenn, *J. Mass Spectrom.*, **2000**, 35, 939-952.

118. M. G. Ikonomou, A. T. Blades and P. Kebarle, *Anal. Chem.*, **1991**, 63, 1989-1998.

119. B. B. Schneider and D. D. Y. Chen, *Anal. Chem.*, **2000**, 72, 791-799.

120. J. V. Iribarne and B. A. Thomson, *J. Chem. Phys.*, **1976**, 64, 2287-2294.

121. K. McQuinn, F. Hof and J. S. McIndoe, *Chem. Commun.*, **2007**, 4099-4101.

122. V. B. Di Marco and G. G. Bombi, *Mass Spectrom. Rev.*, **2006**, 25, 347-379.

123. I. Manisali, D. D. Y. Chen and B. B. Schneider, *Trends Anal. Chem.*, **2006**, 25, 243-256.

124. E. de Hoffmann, V. Stroobant and Editors, in *Mass Spectrometry: Principles and Applications, Third Edition*, John Wiley & Sons, Ltd., **2007**, pp. 88-100.

125. B. A. Mamyrin, *Int. J. Mass. Spectrom. and Ion Processes*, **1994**, 131, 1-19.

126. P. J. Dyson, B. F. G. Johnson, J. S. McIndoe and P. R. R. Langridge-Smith, John Wiley & Sons, Ltd., **2000**, pp. 311-313.

127. A. Studer, *Chem. Soc. Rev.*, **2004**, 33, 267-273.

128. C.-C. Chang, K. O. Siegenthaler and A. Studer, *Helv. Chim. Acta.*, **2006**, 89, 2200-2210.

129. C.-C. Chang and A. Studer, *Macromolecules*, **2006**, 39, 4062-4068.

130. N. Bentenitis, *J. Chem. Edu.*, **2008**, 85, 1146.

131. C. A. Jaska and I. Manners, *J. Am. Chem. Soc.*, **2004**, 126, 9776-9785.

132. M. Bauer, T. Kauf, J. Christoffers and H. Bertagnolli, *Phys. Chem. Chem. Phys*, **2005**, **7**, 2664-2670.

133. M. V. Joshi, S. Vaidya, R. Pandey and D. Mukesh, *J. Catal.*, **1999**, 183, 102-106.

134. C. Amatore and A. Jutand, *J. Organomet. Chem.*, **1999**, 576, 254-278.

135. N. Matyasovszky, M. Tian and A. Chen, *J. Phys. Chem. A*, **2009**, 113, 9348-9353.

136. M. A. Bañares, *Catal. Today*, **2005**, 100, 71-77.

137. B. M. Weckhuysen, *Chem. Commun.*, **2002**, 0, 97-110.

138. M. O. Guerrero-Perez and M. A. Banares, *Chem. Commun.*, **2002**, 0, 1292-1293.

139. M. A. Newton, B. Jyoti, A. J. Dent, S. G. Fiddy and J. Evans, *Chem. Commun.*, **2004**, 0, 2382-2383.

140. G. Guilera, M. A. Newton, C. Polli, S. Pascarelli, M. Guino and K. K. Hii, *Chem. Commun.*, **2006**, 4306-4308.

141. M. D. Eelman, J. M. Blacquiere, M. M. Moriarty and D. E. Fogg, *Angew. Chem., Int. Ed. Engl.*, **2008**, 47, 303-306.

142. A. T. Lubben, J. S. McIndoe and A. S. Weller, *Organometallics*, **2008**, 27, 3303-3306.

143. L. A. Carpino, H. Shroff, S. A. Triolo, E.-S. M. E. Mansour, H. Wenschuh and F. Albericio, *Tetrahedron Lett.*, **1993**, 34, 7829-7832.

144. R. Ramage, J. Green and A. J. Blake, *Tetrahedron*, **1991**, 47, 6353-6370.

145. C. Amatore and A. Jutand, *J. Organomet. Chem.*, **1999**, 576, 254-278.

146. L. J. Goossen, D. Koley, H. L. Hermann and W. Thiel, *Organometallics*, **2005**, 24, 2398-2410.

147. A. Tougerti, S. Negri and A. Jutand, *Chem.--Eur. J.*, **2007**, 13, 666-676.

148. A. Jutand, S. Négri and A. Principaud, *Eur. J. Inorg. Chem.*, **2005**, 2005, 631-635.

149. T. Ljungdahl, T. Bennur, A. Dallas, H. Emtenäs and J. Mårtensson, *Organometallics*, **2008**, 27, 2490-2498.

150. P. Reiss, S. Carayon, J. Bleuse and A. Pron, *Synth. Met.*, **2003**, 139, 649-652.

151. H. Jung, H. Choi, J. Kim and F. W. Schwartz, *J. Contam. Hydrol.*, **2006**, 82, 133-144.

152. J. R. Lizotte and T. E. Long, *Macromol. Chem. Phys.*, **2003**, 204, 570-576.

153. H. A. Dieck and F. R. Heck, *J. Organomet. Chem.*, **1975**, 93, 259-263.

154. L. Cassar, *J. Organomet. Chem.*, **1975**, 93, 253-257.

155. K. Sonogashira, Y. Tohda and N. Hagihara, *Tetrahedron Lett.*, **1975**, 16, 4467-4470.

156. R. Chinchilla and C. Najera, *Chem. Soc. Rev.*, **2011**, 40, 5084-5121.

157. P. Siemsen, R. C. Livingston and F. Diederich, *Angew. Chem., Int. Ed. Engl.*, **2000**, 39, 2632-2657.

158. R. Chinchilla and C. Najera, *Chem. Rev.*, **2007**, 107, 874-922.

159. T. Ljungdahl, T. Bennur, A. Dallas, H. Emtenaes and J. Maartensson, *Organometallics*, **2008**, 27, 2490-2498.

160. A. Soheili, J. Albaneze-Walker, J. A. Murry, P. G. Dormer and D. L. Hughes, *Organic Lett.*, **2003**, 5, 4191-4194.

161. C. Amatore, S. Bensalem, S. Ghalem and A. Jutand, *J. Organomet. Chem.*, **2004**, 689, 4642-4646.

162. Asma Tougerti, Serge Negri and Anny Jutand, *Chem-- Eur. J.* , **2007**, 13, 666-676.

163. M. R. an der Heiden, H. Plenio, S. Immel, E. Burello, G. Rothenberg and H. C. J. Hoefsloot, *Chem.--Eur. J.*, **2008**, 14, 2857-2866.

164. K. L. Vikse, M. A. Henderson, A. G. Oliver and J. S. McIndoe, *Chem. Commun.*, **2010**, 46, 7412-7414.

165. J. J. Low and W. A. Goddard, III, *J. Am. Chem. Soc.*, **1986**, 108, 6115-6128.

166. K. L. Vikse, M. A. Henderson, A. G. Oliver and J. S. McIndoe, *Chem. Commun.*, **2010**, 46, 7412-7414.

167. S. D. Lepore, A. Khoram, D. C. Bromfield, P. Cohn, V. Jairaj and M. A. Silvestri, *J. Org. Chem.*, **2005**, 70, 7443-7446.

168. I. M. Kolthoff, M. K. Chantooni, Jr. and S. Bhowmik, *J. Am. Chem. Soc.*, **1968**, 90, 23-28.

169. J.-H. Li, Y. Liang and Y.-X. Xie, *J. Org. Chem.*, **2005**, 70, 4393-4396.

170. X. Gao and H. B. Kagan, *Chirality*, **1998**, 10, 120-124.

171. T. Satyanarayana and H. B. Kagan, *Adv. Synth. Catal.*, **2005**, 347, 737-748.

172. W. W. Cleland, *Arch. Biochem. Biophys.*, **2005**, 433, 2-12.

173. C. Hennig, R. B. Oswald and S. Schmatz, *The J. Phys. Chem. A*, **2005**, 110, 3071-3079.

174. D. G. Churchill, K. E. Janak, J. S. Wittenberg and G. Parkin, *J. Am. Chem. Soc.*, **2003**, 125, 1403-1420.

175. M. Tromp, J. R. A. Sietsma, J. A. van Bokhoven, G. P. F. van Strijdonck, R. J. van Haaren, A. M. J. van der Eerden, P. W. N. M. van Leeuwen and D. C. Koningsberger, *Chem. Commun.*, **2003**, 0, 128-129.

176. A. Zask and P. Helquist, *J. Org. Chem.*, **1978**, 43, 1619-1620.

177. M. S. Viciu, G. A. Grasa and S. P. Nolan, *Organometallics*, **2001**, 20, 3607-3612.

178. O. Navarro, H. Kaur, P. Mahjoor and S. P. Nolan, *J. Org. Chem.*, **2004**, 69, 3173-3180.

179. C. Desmarets, S. Kuhl, R. Schneider and Y. Fort, *Organometallics*, **2002**, 21, 1554-1559.

180. M. E. Cucullu, S. P. Nolan, T. R. Belderrain and R. H. Grubbs, *Organometallics*, **1999**, 18, 1299-1304.

181. M. Zeng, Y. Du, L. Shao, C. Qi and X.-M. Zhang, *J. Org. Chem.*, **2010**, 75, 2556-2563.

182. J. Moon and S. Lee, *J. Organomet. Chem.*, **2009**, 694, 473-477.

183. K. L. Vikse, Z. Ahmadi, C. C. Manning, D. A. Harrington and J. S. McIndoe, *Angew. Chem., Int. Ed. Engl.*, **2011**, 50, 8304-8306.

184. Olsson, M. H. M.; Siegbahn, P. E. M.; Warshel, A. *J. Am. Chem. Soc.* **2004**, *126*, 2820-2828.

185. G. Parkin, *J. Labelled Comp. Radiopharm.*, **2007**, 50, 1088-1114.

186. W. D. Jones, *Accounts of Chemical Research*, **2002**, 36, 140-146.

187. E. Rosenberg, E. V. Anslyn, C. Barner-Thorsen, S. Aime, D. Osella, R. Gobetto and L. Milone, *Organometallics*, **1984**, 3, 1790-1795.

188. O. Matsson and K. C. Westaway, in *Advances in Physical Organic Chemistry*, ed. D. Bethell, Academic Press, **1999**, pp. 143-248.

189. C. Amatore, A. Jutand and G. Le Duc, *Chem.--Eur. J.*, 2011, 17, 2492-2503.

190. J. K. Stille and K. S. Y. Lau, *Acc. Chem. Res.*, **1977**, 10, 434-442.

191. J. Tsuji, in *Palladium Reagents and Catalysts*, John Wiley & Sons, Ltd, **2005**, pp. i-xiv.

192. A. Suzuki, *Angew. Chem., Int. Ed. Engl.*, **2011**, 50, 6722-6737.

193. J. Vicente, J.-A. Abad and J. Gil-Rubio, *Organometallics*, **1996**, 15, 3509-3519.

194. J. Vicente, J.-A. Abad, K. F. Shaw, J. Gil-Rubio, M. C. Ramírez de Arellano and P. G. Jones, *Organometallics*, **1997**, 16, 4557-4566.

195. J. Vicente, I. Saura-Llamas, J. Turpín, M. C. Ramírez de Arellano and P. G. Jones, *Organometallics*, **1999**, 18, 2683-2693.

196. J. Vicente, I. Saura-Llamas, C. Grünwald, C. Alcaraz, P. G. Jones and D. Bautista, *Organometallics*, **2002**, 21, 3587-3595.

197. D. Solé, S. Díaz, X. Solans and M. Font-Bardia, *Organometallics*, **2006**, 25, 1995-2001.

198. J. Dupont, C. S. Consorti and J. Spencer, *Chem. Rev.*, **2005**, 105, 2527-2572.

199. J. Dupont, M. Pfeffer and J. Spencer, *Eur. J. Inorg. Chem.*, **2001**, 2001, 1917-1927.

200. J. Vicente, J.-A. Abad, R. Fernández-de-Bobadilla, P. G. Jones and M. C. Ramírez de Arellano, *Organometallics*, **1996**, 15, 24-34.

201. F. R. Hartley, *Chemical Society Reviews*, **1973**, 2, 163-179.

202. T. I. Wallow, F. E. Goodson and B. M. Novak, *Organometallics*, **1996**, 15, 3708-3716.

203. R. B. Jordan, *Reaction Mechanisms of Inorganic and Organometallic Systems, 3rd Ed*, **2007**.

204. K. Karabelas, C. Westerlund and A. Hallberg, *J. Org. Chem.*, **1985**, 50, 3896-3900.

205. P. Fitton and E. A. Rick, *J. Organomet. Chem.*, **1971**, 28, 287-291.

206. S. L. Fraser, M. Y. Antipin, V. N. Khroustalyov and V. V. Grushin, *J. Am. Chem. Soc.*, **1997**, 119, 4769-4770.

207. L. K. Hwang, Y. Na, J. Lee, Y. Do and S. Chang, *Angew. Chem., Int. Ed. Engl.*, **2005**, 44, 6166-6169.

208. B. A. Markies, A. J. Canty, W. de Graaf, J. Boersma, M. D. Janssen, M. P. Hogerheide, W. J. J. Smeets, A. L. Spek and G. van Koten, *J. Organomet. Chem.*, **1994**, 482, 191-199.

Appendix A Crystallographic details for [*p*-$Ph(C_2)C_6H_4CH_2PPh_3]^+[PF_6]^-$

DISCUSSION

The compound crystallizes as colourless block-like crystals from a methanol solution. There are four molecules of the phosphonium cation and associated PF_6 anion and two molecules of methanol in the unit cell of the primitive, centrosymmetric, monoclinic space group $P2_1/c$.

The phosphonium cation exhibits the expected structure. The bond distances and angles within the molecules are as expected.

The methanol of crystallization was found to have partial occupancy. Refinement of the site occupancy yielded an occupancy of very close to 50%, thus in the final refinement the methanol was model at a fixed 50% occupancy. The hydroxyl of the methanol forms H-bonds to neighbouring fluorines of the PF_6 anion (see Table of Hydrogen-bonds for details).

CRYSTAL SUMMARY

Crystal data for $C_{33.50}H_{28}F_6O_{0.50}P_2$; M_r = 614.50; Monoclinic; space group $P2_1/c$; *a* = 9.7820(12) Å; *b* = 15.0655(19) Å; *c* = 20.388(3) Å; α = 90°; β = 99.581(2)°; γ = 90°; V = 2962.7(6) $Å^3$; Z = 4; T = 120(2) K; λ(Mo-Kα) = 0.71073 Å; μ(Mo-Kα) = 0.209 mm^{-1}; d_{calc} = 1.378g.cm^{-3}; 39492 reflections collected; 6151 unique (R_{int} = 0.0353); giving R_1 = 0.0352, wR_2 = 0.0853 for 5112 data with [I>2σ(I)] and R_1 = 0.0450, wR_2 = 0.0914 for all 6151 data. Residual electron density ($e^-.Å^{-3}$) max/min: 0.456/-0.333.

An arbitrary sphere of data were collected on a colorless block-like crystal, having approximate dimensions of 0.30 × 0.21 × 0.14 mm, on a Bruker APEX-II diffractometer using a combination of ω- and φ-scans of 0.5°. Data were corrected for absorption and polarization effects and analyzed for space group determination. The structure was solved by direct methods and expanded routinely. The model was refined by full-matrix least-squares analysis of F^2 against all reflections. All non-hydrogen atoms were refined with anisotropic thermal displacement parameters. Unless otherwise noted, hydrogen atoms were included in calculated positions. Thermal parameters for the hydrogens were tied to the isotropic thermal parameter of the atom to which they are bonded (1.5 × for methyl, 1.2 × for all others).

Table 1. Crystal data and structure refinement for [*p*-Ph(C_2)$C_6H_4CH_2PPh_3$]$^+$[PF_6]$^-$

Identification code	jsm20a	
Empirical formula	$C_{33.50}H_{28}F_6O_{0.50}P_2$	
Formula weight	614.50	
Temperature	120(2) K	
Wavelength	0.71073 Å	
Crystal system	Monoclinic	
Space group	$P2_1/c$	
Unit cell dimensions	*a* = 9.7820(12) Å	α = 90°
	b = 15.0655(19) Å	β = 99.581(2)°
	c = 20.388(3) Å	γ = 90°
Volume	2962.7(6) Å^3	
Z	4	
Density (calculated)	1.378 g.cm^{-3}	
Absorption coefficient (μ)	0.209 mm^{-1}	
F(000)	1268	
Crystal size	0.30 × 0.21 × 0.14 mm^3	
θ range for data collection	1.69 to 26.56°	
Index ranges	$-12 \leq h \leq 12$, $-18 \leq k \leq 18$, $-25 \leq l \leq 25$	
Reflections collected	39492	
Independent reflections	6151 [R_{int} = 0.0353]	
Completeness to θ = 26.56°	99.4 %	
Absorption correction	Semi-empirical from equivalents	
Max. and min. transmission	0.7454 and 0.6975	
Refinement method	Full-matrix least-squares on F^2	
Data / restraints / parameters	6151 / 0 / 390	
Goodness-of-fit on F^2	1.030	
Final R indices [I>2σ(I)]	R_1 = 0.0352, wR_2 = 0.0853	
R indices (all data)	R_1 = 0.0450, wR_2 = 0.0914	
Largest diff. peak and hole	0.456 and -0.333 e$^-$.Å^{-3}	

Table 2. Atomic coordinates and equivalent isotropic displacement parameters ($Å^2$) for $[p\text{-}Ph(C_2)C_6H_4CH_2PPh_3]^-[PF_6]^-$. U(eq) is defined as one third of the trace of the orthogonalized U_{ij} tensor.

	x	y	z	U(eq)
P(1)	0.09124(4)	0.76798(2)	0.33423(2)	0.018(1)
C(1)	0.08273(16)	0.72780(10)	0.41760(7)	0.021(1)
C(2)	0.04226(16)	0.63087(10)	0.41671(7)	0.021(1)
C(3)	-0.09624(17)	0.60503(11)	0.40599(8)	0.025(1)
C(4)	-0.13121(18)	0.51577(11)	0.40437(8)	0.028(1)
C(5)	-0.02842(18)	0.45072(10)	0.41342(8)	0.027(1)
C(6)	0.11077(18)	0.47663(11)	0.42481(8)	0.029(1)
C(7)	0.14522(17)	0.56598(11)	0.42626(8)	0.026(1)
C(8)	-0.06596(19)	0.35828(11)	0.41299(8)	0.031(1)
C(9)	-0.09951(19)	0.28194(11)	0.41299(8)	0.028(1)
C(10)	-0.13961(17)	0.19023(10)	0.41574(7)	0.023(1)
C(11)	-0.27807(17)	0.16757(11)	0.41565(8)	0.026(1)
C(12)	-0.31541(18)	0.07990(11)	0.42116(8)	0.029(1)
C(13)	-0.21611(18)	0.01358(11)	0.42614(8)	0.029(1)
C(14)	-0.07891(18)	0.03537(11)	0.42540(8)	0.029(1)
C(15)	-0.03978(17)	0.12309(11)	0.42058(8)	0.026(1)
C(16)	-0.07967(15)	0.77860(10)	0.28618(7)	0.021(1)
C(17)	-0.09801(18)	0.76897(11)	0.21714(8)	0.029(1)
C(18)	-0.2271(2)	0.78514(12)	0.17923(9)	0.036(1)
C(19)	-0.33737(19)	0.81007(12)	0.20990(10)	0.039(1)
C(20)	-0.31938(18)	0.81971(12)	0.27839(10)	0.034(1)
C(21)	-0.19054(16)	0.80453(10)	0.31686(8)	0.026(1)
C(22)	0.19071(16)	0.69072(10)	0.29509(7)	0.022(1)
C(23)	0.12985(17)	0.61146(10)	0.26871(8)	0.026(1)
C(24)	0.21073(19)	0.54777(11)	0.24525(8)	0.030(1)
C(25)	0.35119(19)	0.56212(12)	0.24787(9)	0.034(1)
C(26)	0.41202(18)	0.64016(12)	0.27403(9)	0.034(1)
C(27)	0.33210(17)	0.70502(11)	0.29788(8)	0.027(1)
C(28)	0.17289(15)	0.87528(10)	0.33859(7)	0.020(1)
C(29)	0.17368(18)	0.92210(11)	0.27924(8)	0.031(1)
C(30)	0.23532(19)	1.00486(12)	0.28138(9)	0.034(1)
C(31)	0.29531(17)	1.04160(11)	0.34177(9)	0.029(1)
C(32)	0.29419(17)	0.99581(11)	0.40014(8)	0.027(1)
C(33)	0.23375(16)	0.91207(10)	0.39889(8)	0.023(1)
P(2)	0.59346(4)	0.76111(3)	0.47368(2)	0.024(1)
F(1)	0.43262(10)	0.73436(7)	0.46690(5)	0.035(1)
F(2)	0.60260(11)	0.70679(9)	0.40716(5)	0.048(1)
F(3)	0.75378(10)	0.78796(8)	0.47966(6)	0.042(1)
F(4)	0.63657(12)	0.67388(7)	0.51574(6)	0.049(1)
F(5)	0.58458(12)	0.81380(8)	0.54027(6)	0.052(1)

F(6)	0.55051(12)	0.84731(8)	0.43053(7)	0.060(1)
O(1S)	0.4247(3)	0.5958(2)	0.58424(17)	0.051(1)
C(1S)	0.4987(5)	0.5174(3)	0.5813(4)	0.079(2)
H(1A)	0.1742	0.7357	0.4461	0.026
H(1B)	0.0140	0.7632	0.4369	0.026
H(3A)	-0.1672	0.6488	0.3997	0.031
H(4A)	-0.2261	0.4988	0.3970	0.034
H(6A)	0.1818	0.4330	0.4316	0.034
H(7A)	0.2400	0.5831	0.4338	0.031
H(11A)	-0.3468	0.2127	0.4118	0.031
H(12A)	-0.4096	0.0650	0.4215	0.035
H(13A)	-0.2421	-0.0467	0.4301	0.035
H(14A)	-0.0111	-0.0102	0.4282	0.035
H(15A)	0.0547	0.1377	0.4206	0.031
H(17A)	-0.0225	0.7514	0.1962	0.034
H(18A)	-0.2398	0.7791	0.1322	0.044
H(19A)	-0.4258	0.8206	0.1838	0.046
H(20A)	-0.3955	0.8368	0.2991	0.040
H(21A)	-0.1780	0.8117	0.3638	0.031
H(23A)	0.0334	0.6016	0.2670	0.031
H(24A)	0.1699	0.4939	0.2273	0.036
H(25A)	0.4064	0.5180	0.2316	0.040
H(26A)	0.5086	0.6494	0.2757	0.041
H(27A)	0.3736	0.7586	0.3159	0.032
H(29A)	0.1322	0.8972	0.2379	0.037
H(30A)	0.2366	1.0368	0.2413	0.041
H(31A)	0.3373	1.0985	0.3429	0.034
H(32A)	0.3348	1.0215	0.4414	0.032
H(33A)	0.2341	0.8802	0.4391	0.028
H(1S)	0.4416	0.6307	0.5545	0.061
H(1SA)	0.4855	0.4960	0.5352	0.095
H(1SB)	0.4652	0.4724	0.6095	0.095
H(1SC)	0.5975	0.5284	0.5969	0.095

Table 3. Anisotropic displacement parameters (Å^2) for [*p*-Ph(C_2)$C_6H_4CH_2PPh_3$]$^+$[PF_6]$^-$. The anisotropic displacement factor exponent takes the form: $-2\pi^2[h^2a^{*2}U_{11} + ... + 2hka^*b^*U_{12}]$

	U_{11}	U_{22}	U_{33}	U_{23}	U_{13}	U_{12}
P(1)	0.0226(2)	0.0164(2)	0.0155(2)	-0.0004(1)	0.0028(1)	-0.0026(2)
C(1)	0.0284(8)	0.0189(8)	0.0164(7)	0.0008(6)	0.0030(6)	-0.0005(6)
C(2)	0.0320(8)	0.0188(7)	0.0138(7)	0.0005(6)	0.0054(6)	-0.0018(6)
C(3)	0.0303(8)	0.0236(8)	0.0240(8)	0.0019(6)	0.0084(6)	0.0003(7)
C(4)	0.0343(9)	0.0253(9)	0.0269(8)	-0.0001(7)	0.0092(7)	-0.0077(7)
C(5)	0.0448(10)	0.0190(8)	0.0179(7)	-0.0006(6)	0.0102(7)	-0.0044(7)
C(6)	0.0394(10)	0.0210(8)	0.0258(8)	0.0028(6)	0.0057(7)	0.0038(7)
C(7)	0.0292(8)	0.0232(8)	0.0240(8)	0.0024(6)	0.0026(6)	-0.0013(6)
C(8)	0.0478(11)	0.0249(9)	0.0214(8)	-0.0003(7)	0.0110(7)	-0.0039(7)
C(9)	0.0425(10)	0.0229(9)	0.0209(8)	-0.0009(6)	0.0112(7)	-0.0024(7)
C(10)	0.0330(8)	0.0197(8)	0.0160(7)	-0.0018(6)	0.0065(6)	-0.0035(6)
C(11)	0.0299(8)	0.0266(8)	0.0224(8)	-0.0012(6)	0.0059(6)	0.0045(7)
C(12)	0.0279(8)	0.0338(9)	0.0262(8)	-0.0029(7)	0.0064(7)	-0.0070(7)
C(13)	0.0433(10)	0.0193(8)	0.0257(8)	0.0000(6)	0.0074(7)	-0.0060(7)
C(14)	0.0351(9)	0.0242(9)	0.0287(9)	0.0007(7)	0.0054(7)	0.0060(7)
C(15)	0.0256(8)	0.0279(9)	0.0244(8)	-0.0007(7)	0.0052(6)	-0.0021(6)
C(16)	0.0233(8)	0.0180(8)	0.0218(7)	0.0031(6)	0.0008(6)	-0.0042(6)
C(17)	0.0343(9)	0.0283(9)	0.0219(8)	0.0019(7)	0.0010(7)	-0.0073(7)
C(18)	0.0444(11)	0.0332(10)	0.0262(9)	0.0066(7)	-0.0085(8)	-0.0114(8)
C(19)	0.0314(9)	0.0311(10)	0.0471(11)	0.0143(8)	-0.0115(8)	-0.0083(8)
C(20)	0.0253(8)	0.0284(9)	0.0462(11)	0.0113(8)	0.0043(7)	-0.0020(7)
C(21)	0.0280(8)	0.0203(8)	0.0287(8)	0.0043(6)	0.0053(6)	-0.0027(6)
C(22)	0.0282(8)	0.0207(8)	0.0165(7)	-0.0008(6)	0.0049(6)	-0.0007(6)
C(23)	0.0312(8)	0.0234(8)	0.0236(8)	-0.0027(6)	0.0050(6)	-0.0047(7)
C(24)	0.0423(10)	0.0227(8)	0.0252(8)	-0.0056(7)	0.0060(7)	-0.0030(7)
C(25)	0.0415(10)	0.0287(9)	0.0327(9)	-0.0066(7)	0.0119(8)	0.0044(8)
C(26)	0.0306(9)	0.0349(10)	0.0395(10)	-0.0074(8)	0.0117(8)	-0.0004(7)
C(27)	0.0301(8)	0.0243(8)	0.0265(8)	-0.0039(7)	0.0060(7)	-0.0036(7)
C(28)	0.0211(7)	0.0157(7)	0.0236(8)	0.0006(6)	0.0034(6)	-0.0006(6)
C(29)	0.0395(10)	0.0278(9)	0.0225(8)	0.0024(7)	0.0001(7)	-0.0084(7)
C(30)	0.0419(10)	0.0268(9)	0.0317(9)	0.0100(7)	0.0013(7)	-0.0073(7)
C(31)	0.0260(8)	0.0195(8)	0.0393(9)	0.0018(7)	0.0036(7)	-0.0035(6)
C(32)	0.0275(8)	0.0229(8)	0.0289(8)	-0.0049(7)	0.0030(6)	-0.0038(6)
C(33)	0.0251(8)	0.0217(8)	0.0221(8)	-0.0003(6)	0.0033(6)	-0.0011(6)
P(2)	0.0209(2)	0.0246(2)	0.0266(2)	0.0001(2)	0.0025(2)	0.0024(2)
F(1)	0.0240(5)	0.0419(6)	0.0404(6)	-0.0056(5)	0.0082(4)	-0.0054(4)
F(2)	0.0304(6)	0.0774(9)	0.0352(6)	-0.0196(6)	0.0036(4)	0.0010(5)
F(3)	0.0225(5)	0.0503(7)	0.0516(7)	-0.0059(5)	0.0025(4)	-0.0041(5)
F(4)	0.0548(7)	0.0335(6)	0.0524(7)	0.0122(5)	-0.0105(6)	0.0028(5)
F(5)	0.0415(6)	0.0592(8)	0.0561(8)	-0.0326(6)	0.0117(5)	-0.0051(6)

F(6)	0.0429(7)	0.0439(7)	0.0906(10)	0.0342(7)	-0.0002(6)	0.0010(5)
O(1S)	0.0415(16)	0.0453(17)	0.066(2)	0.0113(15)	0.0115(14)	-0.0046(13)
C(1S)	0.043(3)	0.041(3)	0.155(6)	0.024(3)	0.022(3)	0.002(2)

Table 4. Bond lengths [Å] for jsm20a.

atom-atom	distance	atom-atom	distance
P(1)-C(22)	1.7879(16)	P(1)-C(16)	1.7986(15)
P(1)-C(28)	1.7987(15)	P(1)-C(1)	1.8191(15)
C(1)-C(2)	1.512(2)	C(2)-C(3)	1.391(2)
C(2)-C(7)	1.394(2)	C(3)-C(4)	1.387(2)
C(4)-C(5)	1.394(2)	C(5)-C(6)	1.398(2)
C(5)-C(8)	1.440(2)	C(6)-C(7)	1.387(2)
C(8)-C(9)	1.196(2)	C(9)-C(10)	1.440(2)
C(10)-C(11)	1.397(2)	C(10)-C(15)	1.398(2)
C(11)-C(12)	1.380(2)	C(12)-C(13)	1.385(2)
C(13)-C(14)	1.384(2)	C(14)-C(15)	1.384(2)
C(16)-C(21)	1.395(2)	C(16)-C(17)	1.397(2)
C(17)-C(18)	1.388(2)	C(18)-C(19)	1.386(3)
C(19)-C(20)	1.386(3)	C(20)-C(21)	1.388(2)
C(22)-C(27)	1.392(2)	C(22)-C(23)	1.401(2)
C(23)-C(24)	1.379(2)	C(24)-C(25)	1.383(3)
C(25)-C(26)	1.384(2)	C(26)-C(27)	1.389(2)
C(28)-C(33)	1.389(2)	C(28)-C(29)	1.402(2)
C(29)-C(30)	1.382(2)	C(30)-C(31)	1.388(2)
C(31)-C(32)	1.377(2)	C(32)-C(33)	1.392(2)
P(2)-F(6)	1.5855(12)	P(2)-F(4)	1.5875(11)
P(2)-F(5)	1.5875(12)	P(2)-F(2)	1.5990(11)
P(2)-F(3)	1.6044(11)	P(2)-F(1)	1.6077(10)
O(1S)-C(1S)	1.392(5)	C(1)-H(1A)	0.9900
C(1)-H(1B)	0.9900	C(3)-H(3A)	0.9500
C(4)-H(4A)	0.9500	C(6)-H(6A)	0.9500
C(7)-H(7A)	0.9500	C(11)-H(11A)	0.9500
C(12)-H(12A)	0.9500	C(13)-H(13A)	0.9500
C(14)-H(14A)	0.9500	C(15)-H(15A)	0.9500
C(17)-H(17A)	0.9500	C(18)-H(18A)	0.9500
C(19)-H(19A)	0.9500	C(20)-H(20A)	0.9500
C(21)-H(21A)	0.9500	C(23)-H(23A)	0.9500
C(24)-H(24A)	0.9500	C(25)-H(25A)	0.9500
C(26)-H(26A)	0.9500	C(27)-H(27A)	0.9500
C(29)-H(29A)	0.9500	C(30)-H(30A)	0.9500
C(31)-H(31A)	0.9500	C(32)-H(32A)	0.9500
C(33)-H(33A)	0.9500	O(1S)-H(1S)	0.8400
C(1S)-H(1SA)	0.9800	C(1S)-H(1SB)	0.9800
C(1S)-H(1SC)	0.9800		

Symmetry transformations used to generate equivalent atoms:

Table 5. Bond angles [°] for jsm20a.

atom-atom-atom	angle	atom-atom-atom	angle
C(22)-P(1)-C(16)	109.90(7)	C(22)-P(1)-C(28)	109.69(7)
C(16)-P(1)-C(28)	108.17(7)	C(22)-P(1)-C(1)	108.26(7)
C(16)-P(1)-C(1)	110.83(7)	C(28)-P(1)-C(1)	109.99(7)
C(2)-C(1)-P(1)	111.27(10)	C(3)-C(2)-C(7)	119.19(14)
C(3)-C(2)-C(1)	121.21(14)	C(7)-C(2)-C(1)	119.60(14)
C(4)-C(3)-C(2)	120.33(15)	C(3)-C(4)-C(5)	120.59(16)
C(4)-C(5)-C(6)	119.12(15)	C(4)-C(5)-C(8)	120.10(16)
C(6)-C(5)-C(8)	120.76(16)	C(7)-C(6)-C(5)	120.07(15)
C(6)-C(7)-C(2)	120.70(16)	C(9)-C(8)-C(5)	178.7(2)
C(8)-C(9)-C(10)	177.78(17)	C(11)-C(10)-C(15)	119.29(15)
C(11)-C(10)-C(9)	120.33(15)	C(15)-C(10)-C(9)	120.35(15)
C(12)-C(11)-C(10)	120.24(15)	C(11)-C(12)-C(13)	120.29(16)
C(14)-C(13)-C(12)	119.83(15)	C(15)-C(14)-C(13)	120.49(16)
C(14)-C(15)-C(10)	119.84(15)	C(21)-C(16)-C(17)	120.12(15)
C(21)-C(16)-P(1)	120.15(12)	C(17)-C(16)-P(1)	119.44(12)
C(18)-C(17)-C(16)	119.70(17)	C(19)-C(18)-C(17)	120.06(17)
C(20)-C(19)-C(18)	120.34(16)	C(19)-C(20)-C(21)	120.21(17)
C(20)-C(21)-C(16)	119.56(16)	C(27)-C(22)-C(23)	120.23(15)
C(27)-C(22)-P(1)	119.48(12)	C(23)-C(22)-P(1)	119.88(12)
C(24)-C(23)-C(22)	119.65(15)	C(23)-C(24)-C(25)	120.09(16)
C(24)-C(25)-C(26)	120.55(16)	C(25)-C(26)-C(27)	120.11(16)
C(26)-C(27)-C(22)	119.37(15)	C(33)-C(28)-C(29)	120.01(14)
C(33)-C(28)-P(1)	121.59(12)	C(29)-C(28)-P(1)	118.41(12)
C(30)-C(29)-C(28)	119.45(15)	C(29)-C(30)-C(31)	120.36(16)
C(32)-C(31)-C(30)	120.26(15)	C(31)-C(32)-C(33)	120.17(15)
C(28)-C(33)-C(32)	119.75(15)	F(6)-P(2)-F(4)	179.02(8)
F(6)-P(2)-F(5)	91.02(8)	F(4)-P(2)-F(5)	89.96(7)
F(6)-P(2)-F(2)	89.76(8)	F(4)-P(2)-F(2)	89.26(7)
F(5)-P(2)-F(2)	179.21(8)	F(6)-P(2)-F(3)	90.07(6)
F(4)-P(2)-F(3)	89.95(6)	F(5)-P(2)-F(3)	90.04(6)
F(2)-P(2)-F(3)	90.09(6)	F(6)-P(2)-F(1)	89.57(6)
F(4)-P(2)-F(1)	90.40(6)	F(5)-P(2)-F(1)	90.39(6)
F(2)-P(2)-F(1)	89.48(6)	F(3)-P(2)-F(1)	179.44(7)
C(2)-C(1)-H(1A)	109.4	P(1)-C(1)-H(1A)	109.4
C(2)-C(1)-H(1B)	109.4	P(1)-C(1)-H(1B)	109.4
H(1A)-C(1)-H(1B)	108.0	C(4)-C(3)-H(3A)	119.8
C(2)-C(3)-H(3A)	119.8	C(3)-C(4)-H(4A)	119.7
C(5)-C(4)-H(4A)	119.7	C(7)-C(6)-H(6A)	120.0
C(5)-C(6)-H(6A)	120.0	C(6)-C(7)-H(7A)	119.7
C(2)-C(7)-H(7A)	119.7	C(12)-C(11)-H(11A)	119.9
C(10)-C(11)-H(11A)	119.9	C(11)-C(12)-H(12A)	119.9
C(13)-C(12)-H(12A)	119.9	C(14)-C(13)-H(13A)	120.1

Table 6. Torsion angles [°] for jsm20a.

atom-atom-atom-atom	angle	atom-atom-atom-atom	angle
C(22)-P(1)-C(1)-C(2)	-48.47(13)	C(16)-P(1)-C(1)-C(2)	72.13(12)
C(28)-P(1)-C(1)-C(2)	-168.31(11)	P(1)-C(1)-C(2)-C(3)	-86.62(16)
P(1)-C(1)-C(2)-C(7)	92.85(15)	C(7)-C(2)-C(3)-C(4)	-0.4(2)
C(1)-C(2)-C(3)-C(4)	179.03(14)	C(2)-C(3)-C(4)-C(5)	0.0(2)
C(3)-C(4)-C(5)-C(6)	0.6(2)	C(3)-C(4)-C(5)-C(8)	178.74(15)
C(4)-C(5)-C(6)-C(7)	-0.7(2)	C(8)-C(5)-C(6)-C(7)	-178.85(15)
C(5)-C(6)-C(7)-C(2)	0.3(2)	C(3)-C(2)-C(7)-C(6)	0.3(2)
C(1)-C(2)-C(7)-C(6)	-179.16(14)	C(4)-C(5)-C(8)-C(9)	-25(9)
C(6)-C(5)-C(8)-C(9)	153(9)	C(5)-C(8)-C(9)-C(10)	-66(12)
C(8)-C(9)-C(10)-C(11)	84(5)	C(8)-C(9)-C(10)-C(15)	-94(5)
C(15)-C(10)-C(11)-C(12)	0.8(2)	C(9)-C(10)-C(11)-C(12)	-177.22(15)
C(10)-C(11)-C(12)-C(13)	-0.7(2)	C(11)-C(12)-C(13)-C(14)	-0.2(2)
C(12)-C(13)-C(14)-C(15)	0.8(2)	C(13)-C(14)-C(15)-C(10)	-0.6(2)
C(11)-C(10)-C(15)-C(14)	-0.2(2)	C(9)-C(10)-C(15)-C(14)	177.87(15)
C(22)-P(1)-C(16)-C(21)	154.35(12)	C(28)-P(1)-C(16)-C(21)	-85.92(13)
C(1)-P(1)-C(16)-C(21)	34.73(15)	C(22)-P(1)-C(16)-C(17)	-31.72(15)
C(28)-P(1)-C(16)-C(17)	88.02(14)	C(1)-P(1)-C(16)-C(17)	-151.33(12)
C(21)-C(16)-C(17)-C(18)	-0.1(2)	P(1)-C(16)-C(17)-C(18)	-174.07(13)
C(16)-C(17)-C(18)-C(19)	-0.5(3)	C(17)-C(18)-C(19)-C(20)	0.5(3)
C(18)-C(19)-C(20)-C(21)	0.0(3)	C(19)-C(20)-C(21)-C(16)	-0.7(2)
C(17)-C(16)-C(21)-C(20)	0.7(2)	P(1)-C(16)-C(21)-C(20)	174.60(12)
C(16)-P(1)-C(22)-C(27)	144.74(12)	C(28)-P(1)-C(22)-C(27)	25.94(15)
C(1)-P(1)-C(22)-C(27)	-94.09(13)	C(16)-P(1)-C(22)-C(23)	-42.63(14)
C(28)-P(1)-C(22)-C(23)	-161.43(12)	C(1)-P(1)-C(22)-C(23)	78.55(14)
C(27)-C(22)-C(23)-C(24)	-0.3(2)	P(1)-C(22)-C(23)-C(24)	-172.83(13)
C(22)-C(23)-C(24)-C(25)	0.1(2)	C(23)-C(24)-C(25)-C(26)	0.1(3)
C(24)-C(25)-C(26)-C(27)	-0.1(3)	C(25)-C(26)-C(27)-C(22)	-0.1(3)
C(23)-C(22)-C(27)-C(26)	0.3(2)	P(1)-C(22)-C(27)-C(26)	172.87(13)
C(22)-P(1)-C(28)-C(33)	-111.45(13)	C(16)-P(1)-C(28)-C(33)	128.68(13)
C(1)-P(1)-C(28)-C(33)	7.51(15)	C(22)-P(1)-C(28)-C(29)	68.79(14)
C(16)-P(1)-C(28)-C(29)	-51.07(15)	C(1)-P(1)-C(28)-C(29)	-172.25(13)
C(33)-C(28)-C(29)-C(30)	0.0(3)	P(1)-C(28)-C(29)-C(30)	179.73(14)
C(28)-C(29)-C(30)-C(31)	-0.3(3)	C(29)-C(30)-C(31)-C(32)	0.1(3)
C(30)-C(31)-C(32)-C(33)	0.5(3)	C(29)-C(28)-C(33)-C(32)	0.6(2)
P(1)-C(28)-C(33)-C(32)	-179.13(12)	C(31)-C(32)-C(33)-C(28)	-0.8(2)

Symmetry transformations used to generate equivalent atoms:

Table 7. Hydrogen bonds for [*p*-Ph(C_2)$C_6H_4CH_2PPh_3$]$^+$[PF_6] [Å and °]$^-$.

D-H...A	d(D-H)	d(H...A)	d(D...A)	<(DHA)
O(1S)-H(1S)...F(1)	0.84	2.36	3.186(3)	166.6
O(1S)-H(1S)...F(4)	0.84	2.28	2.931(3)	135.0

Symmetry transformations used to generate equivalent atoms:

Appendix B Crystallographic details for $[Pd(TMEDA)(C_6H_4CH_2PPh_3)(I)]^+[PF_6]^-$ (1)

DISCUSSION

The complex crystallizes as colorless block-like crystals from $CDCl_3$ solution. There are one molecule of the Pd cation, associated PF_6 anion and on deuterochloroform of crystallization in the asymmetric unit of the primitive, centrosymmetric triclinic space group P-1.

The cation consists of a Pd atom ligated in a slightly distorted, four-coordinate square-planar geometry by an idodine, the two nitrogens of a tetramethyl ethylene diamine ligand and one phosphorus of the $Ph_2PCH_2PPh_3$ moeity. The τ-4 value for the Pd center is: 0.003. Tau-4 is a metric that indicates the geometry of a four coordinate center. It is derived from [360-(α+β)/141], where α and β are the two largest angles about the center. A value of zero indicates a square planar coordination environment and a value of one a tetrahedral geometry (see additional reference for details). The primary distortion away from ideal is the bond distances to the ligating atoms. The bond angles about the Pd are all close to ideal.

The structure displays no unusual behaviour and is otherwise as expected.

CRYSTAL SUMMARY

Crystal data for $C_{32}H_{38}Cl_3F_6IN_2P_2Pd$; M_r = 966.23; Triclinic; space group P-1; *a* = 12.2931(7) Å; *b* = 13.3600(8) Å; *c* = 13.7475(8) Å; α = 99.5490(10)°; β = 114.9930(10)°; γ = 106.3080(10)°; V = 1856.03(19) $Å^3$; Z = 2; T = 120(2) K; λ(Mo-Kα) = 0.71073 Å; μ(Mo-Kα) = 1.690 mm^{-1}; d_{calc} = 1.729g.cm^{-3}; 44375 reflections collected; 9174 unique (R_{int} = 0.0244); giving R_1 = 0.0212, wR_2 = 0.0511 for 8075 data with [I>2σ(I)] and R_1 = 0.0266, wR_2 = 0.0535 for all 9174 data. Residual electron density ($e^-.Å^{-3}$) max/min: 1.059/-0.485.

An arbitrary sphere of data were collected on a colourless block-like crystal, having approximate dimensions of 0.17 × 0.14 × 0.10 mm, on a Bruker Kappa X8-APEX-II diffractometer using a combination of ω- and φ-scans of 0.5°. Data were corrected for absorption and polarization effects and analyzed for space group determination. The structure was solved by direct methods and expanded routinely. The model was refined by full-matrix least-squares analysis of F^2 against all reflections. All non-hydrogen atoms were refined with anisotropic thermal displacement parameters. Unless otherwise noted, hydrogen atoms were included in calculated positions. Thermal parameters for the hydrogens were tied to the isotropic thermal parameter of the atom to which they are bonded (1.5 × for methyl, 1.2 × for all others).

REFERENCES

Bruker AXS. (2008). *APEX-2*. Bruker-Nonius AXS, Madison, Wisconsin, USA.

G. M. Sheldrick, *Acta Cryst.*, **2008**, *A64*, 112.

Table 1. Crystal data and structure refinement for $[Pd(TMEDA)(C_6H_4CH_2PPh_3)(I)]^+[PF_6]^-$

Identification code	uvic1230	
Empirical formula	$C_{32}H_{38}Cl_3F_6IN_2P_2Pd$	
Formula weight	966.23	
Temperature	120(2) K	
Wavelength	0.71073 Å	
Crystal system	Triclinic	
Space group	P-1	
Unit cell dimensions	*a* = 12.2931(7) Å	α = 99.5490(10)°
	b = 13.3600(8) Å	β = 114.9930(10)°
	c = 13.7475(8) Å	γ = 106.3080(10)°
Volume	1856.03(19) $Å^3$	
Z	2	
Density (calculated)	1.729 $g.cm^{-3}$	
Absorption coefficient (μ)	1.690 mm^{-1}	
F(000)	956	
Crystal color, habit	colourless, block	
Crystal size	0.17 × 0.14 × 0.10 mm^3	
θ range for data collection	1.68 to 28.34°	
Index ranges	$-16 \leq h \leq 16$, $-17 \leq k \leq 17$, $-18 \leq l \leq 18$	
Reflections collected	44375	
Independent reflections	9174 [R_{int} = 0.0244]	
Completeness to θ = 28.34°	98.8 %	
Absorption correction	Numerical	
Max. and min. transmission	0.8991 and 0.8153	
Refinement method	Full-matrix least-squares on F^2	
Data / restraints / parameters	9174 / 0 / 428	
Goodness-of-fit on F^2	1.023	
Final R indices [I>2σ(I)]	R_1 = 0.0212, wR_2 = 0.0511	
R indices (all data)	R_1 = 0.0266, wR_2 = 0.0535	
Largest diff. peak and hole	1.059 and -0.485 $e^-.Å^{-3}$	

Table 2. Atomic coordinates and equivalent isotropic displacement parameters (Å^2) for $[Pd(TMEDA)(C_6H_4CH_2PPh_3)(I)]^+[PF_6]^-$. U(eq) is defined as one third of the trace of the orthogonalized U_{ij} tensor.

	x	y	z	U(eq)
I(1)	1.02292(1)	0.85186(1)	0.86736(1)	0.019(1)
Pd(1)	0.85308(1)	0.76782(1)	0.92569(1)	0.014(1)
P(1)	0.27801(4)	0.82056(4)	0.53005(4)	0.012(1)
N(1)	0.98322(16)	0.72610(13)	1.06609(13)	0.019(1)
N(2)	0.71290(16)	0.69887(14)	0.97509(14)	0.021(1)
C(1)	0.9138(2)	0.70315(19)	1.13115(17)	0.026(1)
C(2)	0.7696(2)	0.63843(19)	1.05171(18)	0.029(1)
C(3)	1.1132(2)	0.81608(18)	1.14242(17)	0.028(1)
C(4)	1.0010(2)	0.62734(18)	1.02207(17)	0.028(1)
C(5)	0.6959(2)	0.78978(19)	1.03741(19)	0.030(1)
C(6)	0.5831(2)	0.62081(19)	0.88019(19)	0.029(1)
C(7)	0.72813(17)	0.80489(15)	0.80390(15)	0.015(1)
C(8)	0.70778(18)	0.90082(15)	0.83203(15)	0.018(1)
C(9)	0.61463(18)	0.92645(15)	0.75046(16)	0.017(1)
C(10)	0.54169(17)	0.85764(15)	0.63779(15)	0.014(1)
C(11)	0.56408(17)	0.76359(15)	0.60775(15)	0.014(1)
C(12)	0.65629(17)	0.73773(15)	0.69014(15)	0.015(1)
C(13)	0.44074(17)	0.88817(15)	0.55175(15)	0.015(1)
C(14)	0.29106(17)	0.82702(15)	0.66572(15)	0.014(1)
C(15)	0.30733(19)	0.74245(16)	0.71092(16)	0.020(1)
C(16)	0.3312(2)	0.75586(19)	0.82161(18)	0.027(1)
C(17)	0.3412(2)	0.8520(2)	0.88653(18)	0.030(1)
C(18)	0.3277(2)	0.93663(19)	0.84231(18)	0.029(1)
C(19)	0.3016(2)	0.92455(16)	0.73191(16)	0.021(1)
C(20)	0.17760(17)	0.89126(14)	0.46353(14)	0.014(1)
C(21)	0.05027(18)	0.85474(15)	0.44425(16)	0.018(1)
C(22)	-0.03272(19)	0.90341(16)	0.38764(16)	0.020(1)
C(23)	0.01236(19)	0.98814(16)	0.35008(16)	0.020(1)
C(24)	0.1387(2)	1.02456(16)	0.36934(17)	0.021(1)
C(25)	0.22203(19)	0.97662(16)	0.42659(16)	0.019(1)
C(26)	0.20376(18)	0.67966(14)	0.43958(15)	0.015(1)
C(27)	0.0954(2)	0.60606(16)	0.43671(17)	0.021(1)
C(28)	0.0319(2)	0.49931(17)	0.36020(19)	0.028(1)
C(29)	0.0756(2)	0.46548(17)	0.28867(18)	0.030(1)
C(30)	0.1830(2)	0.53856(17)	0.29128(16)	0.025(1)
C(31)	0.24638(19)	0.64597(16)	0.36535(15)	0.019(1)
P(2)	0.46912(5)	0.74365(4)	0.21657(5)	0.022(1)
F(1)	0.46676(14)	0.66569(13)	0.29329(14)	0.045(1)
F(2)	0.45060(17)	0.83024(13)	0.29760(14)	0.048(1)
F(3)	0.31541(14)	0.68191(14)	0.14147(14)	0.053(1)

F(4)	0.62339(14)	0.80424(14)	0.29413(15)	0.051(1)
F(5)	0.4888(2)	0.65663(13)	0.13866(17)	0.066(1)
F(6)	0.47226(16)	0.82162(13)	0.14202(13)	0.047(1)
C(32)	0.7129(2)	0.61980(17)	0.41711(17)	0.023(1)
Cl(1)	0.61426(6)	0.50573(5)	0.43140(5)	0.034(1)
Cl(2)	0.76342(6)	0.57374(5)	0.32148(5)	0.037(1)
Cl(3)	0.84890(5)	0.70492(4)	0.55054(4)	0.028(1)
H(1A)	0.9281	0.7737	1.1810	0.032
H(1B)	0.9496	0.6607	1.1798	0.032
H(2A)	0.7551	0.5658	1.0055	0.035
H(2B)	0.7248	0.6254	1.0965	0.035
H(3A)	1.1627	0.8267	1.1021	0.042
H(3B)	1.1602	0.7967	1.2093	0.042
H(3C)	1.1028	0.8844	1.1664	0.042
H(4A)	0.9156	0.5663	0.9729	0.042
H(4B)	1.0538	0.6068	1.0857	0.042
H(4C)	1.0455	0.6431	0.9783	0.042
H(5A)	0.6533	0.8257	0.9850	0.045
H(5B)	0.7815	0.8439	1.0987	0.045
H(5C)	0.6418	0.7598	1.0697	0.045
H(6A)	0.5429	0.6601	0.8308	0.043
H(6B)	0.5275	0.5889	0.9106	0.043
H(6C)	0.5930	0.5617	0.8363	0.043
H(8)	0.7583	0.9496	0.9082	0.022
H(9)	0.6009	0.9912	0.7719	0.020
H(11)	0.5164	0.7168	0.5309	0.017
H(12)	0.6704	0.6733	0.6684	0.018
H(13A)	0.4389	0.8676	0.4783	0.018
H(13B)	0.4670	0.9691	0.5781	0.018
H(15)	0.3022	0.6768	0.6667	0.024
H(16)	0.3406	0.6984	0.8526	0.032
H(17)	0.3575	0.8603	0.9620	0.035
H(18)	0.3364	1.0032	0.8881	0.035
H(19)	0.2909	0.9821	0.7013	0.025
H(21)	0.0200	0.7966	0.4697	0.021
H(22)	-0.1196	0.8790	0.3747	0.024
H(23)	-0.0442	1.0211	0.3109	0.024
H(24)	0.1688	1.0824	0.3435	0.025
H(25)	0.3092	1.0022	0.4405	0.023
H(27)	0.0654	0.6287	0.4865	0.025
H(28)	-0.0425	0.4492	0.3573	0.034
H(29)	0.0321	0.3920	0.2375	0.035
H(30)	0.2133	0.5149	0.2421	0.030
H(31)	0.3185	0.6965	0.3656	0.023
H(32)	0.6605	0.6634	0.3858	0.027

Table 3. Anisotropic displacement parameters (Å^2) for
$[Pd(TMEDA)(C_6H_4CH_2PPh_3)(I)]^+[PF_6]^-$.
The anisotropic displacement factor exponent takes the form:
$-2\pi^2[h^2a^{*2}U_{11} + ... + 2hka^*b^*U_{12}]$

	U_{11}	U_{22}	U_{33}	U_{23}	U_{13}	U_{12}
I(1)	0.0151(1)	0.0219(1)	0.0175(1)	0.0064(1)	0.0063(1)	0.0053(1)
Pd(1)	0.0137(1)	0.0137(1)	0.0110(1)	0.0039(1)	0.0038(1)	0.0061(1)
P(1)	0.0109(2)	0.0123(2)	0.0132(2)	0.0064(2)	0.0061(2)	0.0043(2)
N(1)	0.0204(8)	0.0197(8)	0.0132(7)	0.0042(6)	0.0040(6)	0.0103(7)
N(2)	0.0209(9)	0.0238(8)	0.0176(8)	0.0085(7)	0.0094(7)	0.0081(7)
C(1)	0.0321(12)	0.0349(11)	0.0154(9)	0.0127(8)	0.0102(8)	0.0172(10)
C(2)	0.0338(12)	0.0345(12)	0.0264(11)	0.0207(9)	0.0172(10)	0.0149(10)
C(3)	0.0229(11)	0.0283(11)	0.0177(9)	0.0042(8)	-0.0004(8)	0.0086(9)
C(4)	0.0355(12)	0.0268(10)	0.0193(10)	0.0065(8)	0.0070(9)	0.0207(10)
C(5)	0.0342(12)	0.0358(12)	0.0277(11)	0.0093(9)	0.0212(10)	0.0167(10)
C(6)	0.0204(11)	0.0308(11)	0.0289(11)	0.0128(9)	0.0102(9)	0.0030(9)
C(7)	0.0116(8)	0.0158(8)	0.0146(8)	0.0067(7)	0.0048(7)	0.0045(7)
C(8)	0.0161(9)	0.0162(9)	0.0146(8)	0.0025(7)	0.0033(7)	0.0045(7)
C(9)	0.0154(9)	0.0134(8)	0.0198(9)	0.0052(7)	0.0068(7)	0.0056(7)
C(10)	0.0092(8)	0.0162(8)	0.0165(8)	0.0089(7)	0.0061(7)	0.0036(7)
C(11)	0.0108(8)	0.0172(8)	0.0134(8)	0.0048(7)	0.0054(7)	0.0037(7)
C(12)	0.0127(9)	0.0149(8)	0.0160(8)	0.0051(7)	0.0070(7)	0.0051(7)
C(13)	0.0123(8)	0.0153(8)	0.0165(8)	0.0086(7)	0.0072(7)	0.0037(7)
C(14)	0.0121(8)	0.0181(8)	0.0148(8)	0.0074(7)	0.0078(7)	0.0051(7)
C(15)	0.0228(10)	0.0221(9)	0.0219(9)	0.0125(8)	0.0135(8)	0.0110(8)
C(16)	0.0275(11)	0.0387(12)	0.0266(11)	0.0221(9)	0.0168(9)	0.0173(10)
C(17)	0.0272(11)	0.0500(14)	0.0181(10)	0.0149(9)	0.0141(9)	0.0175(11)
C(18)	0.0328(12)	0.0348(12)	0.0207(10)	0.0052(9)	0.0144(9)	0.0156(10)
C(19)	0.0235(10)	0.0227(10)	0.0202(9)	0.0088(8)	0.0117(8)	0.0112(8)
C(20)	0.0145(9)	0.0135(8)	0.0138(8)	0.0052(6)	0.0064(7)	0.0066(7)
C(21)	0.0159(9)	0.0184(9)	0.0206(9)	0.0092(7)	0.0101(7)	0.0067(7)
C(22)	0.0138(9)	0.0231(9)	0.0215(9)	0.0066(7)	0.0082(7)	0.0079(8)
C(23)	0.0207(10)	0.0205(9)	0.0179(9)	0.0068(7)	0.0065(8)	0.0126(8)
C(24)	0.0233(10)	0.0189(9)	0.0243(10)	0.0131(8)	0.0118(8)	0.0098(8)
C(25)	0.0151(9)	0.0217(9)	0.0232(9)	0.0125(8)	0.0102(8)	0.0074(8)
C(26)	0.0148(9)	0.0133(8)	0.0152(8)	0.0065(7)	0.0056(7)	0.0052(7)
C(27)	0.0224(10)	0.0169(9)	0.0243(10)	0.0082(8)	0.0121(8)	0.0065(8)
C(28)	0.0272(11)	0.0157(9)	0.0327(11)	0.0081(8)	0.0120(9)	0.0018(8)
C(29)	0.0375(13)	0.0156(9)	0.0237(10)	0.0037(8)	0.0075(9)	0.0085(9)
C(30)	0.0311(12)	0.0272(10)	0.0161(9)	0.0060(8)	0.0088(8)	0.0157(9)
C(31)	0.0175(9)	0.0233(9)	0.0167(9)	0.0076(7)	0.0074(7)	0.0097(8)
P(2)	0.0232(3)	0.0256(3)	0.0269(3)	0.0142(2)	0.0154(2)	0.0132(2)
F(1)	0.0408(8)	0.0599(10)	0.0728(11)	0.0536(9)	0.0395(8)	0.0333(8)
F(2)	0.0693(11)	0.0417(9)	0.0533(10)	0.0139(7)	0.0431(9)	0.0283(8)

F(3)	0.0268(8)	0.0601(11)	0.0542(10)	0.0200(8)	0.0089(7)	0.0084(8)
F(4)	0.0227(7)	0.0604(10)	0.0657(11)	0.0348(9)	0.0154(7)	0.0113(7)
F(5)	0.0971(15)	0.0388(9)	0.0989(15)	0.0157(9)	0.0824(14)	0.0265(10)
F(6)	0.0585(10)	0.0547(10)	0.0425(8)	0.0369(8)	0.0275(8)	0.0255(8)
C(32)	0.0183(10)	0.0241(10)	0.0273(10)	0.0132(8)	0.0116(8)	0.0074(8)
Cl(1)	0.0277(3)	0.0301(3)	0.0343(3)	0.0123(2)	0.0149(2)	-0.0016(2)
Cl(2)	0.0324(3)	0.0447(3)	0.0269(3)	0.0037(2)	0.0175(2)	0.0045(3)
Cl(3)	0.0298(3)	0.0211(2)	0.0288(3)	0.0037(2)	0.0159(2)	0.0025(2)

Table 4. Bond lengths [Å] for uvic1230.

atom-atom	distance	atom-atom	distance
I(1)-Pd(1)	2.5807(2)	Pd(1)-C(7)	1.9842(17)
Pd(1)-N(2)	2.1411(17)	Pd(1)-N(1)	2.2009(15)
P(1)-C(14)	1.7883(18)	P(1)-C(26)	1.7951(18)
P(1)-C(20)	1.7998(17)	P(1)-C(13)	1.8161(18)
N(1)-C(4)	1.471(2)	N(1)-C(3)	1.478(3)
N(1)-C(1)	1.487(3)	N(2)-C(6)	1.480(3)
N(2)-C(5)	1.483(3)	N(2)-C(2)	1.492(2)
C(1)-C(2)	1.508(3)	C(7)-C(8)	1.397(3)
C(7)-C(12)	1.398(2)	C(8)-C(9)	1.396(2)
C(9)-C(10)	1.393(3)	C(10)-C(11)	1.394(2)
C(10)-C(13)	1.520(2)	C(11)-C(12)	1.397(2)
C(14)-C(19)	1.398(3)	C(14)-C(15)	1.399(2)
C(15)-C(16)	1.392(3)	C(16)-C(17)	1.378(3)
C(17)-C(18)	1.387(3)	C(18)-C(19)	1.382(3)
C(20)-C(25)	1.390(2)	C(20)-C(21)	1.391(3)
C(21)-C(22)	1.392(3)	C(22)-C(23)	1.392(3)
C(23)-C(24)	1.380(3)	C(24)-C(25)	1.390(3)
C(26)-C(27)	1.396(3)	C(26)-C(31)	1.397(3)
C(27)-C(28)	1.390(3)	C(28)-C(29)	1.376(3)
C(29)-C(30)	1.387(3)	C(30)-C(31)	1.386(3)
P(2)-F(6)	1.5817(14)	P(2)-F(3)	1.5844(16)
P(2)-F(5)	1.5876(16)	P(2)-F(4)	1.5911(16)
P(2)-F(2)	1.6017(15)	P(2)-F(1)	1.6036(14)
C(32)-Cl(1)	1.759(2)	C(32)-Cl(3)	1.761(2)
C(32)-Cl(2)	1.769(2)	C(1)-H(1A)	0.9900
C(1)-H(1B)	0.9900	C(2)-H(2A)	0.9900
C(2)-H(2B)	0.9900	C(3)-H(3A)	0.9800
C(3)-H(3B)	0.9800	C(3)-H(3C)	0.9800
C(4)-H(4A)	0.9800	C(4)-H(4B)	0.9800
C(4)-H(4C)	0.9800	C(5)-H(5A)	0.9800
C(5)-H(5B)	0.9800	C(5)-H(5C)	0.9800
C(6)-H(6A)	0.9800	C(6)-H(6B)	0.9800
C(6)-H(6C)	0.9800	C(8)-H(8)	0.9500
C(9)-H(9)	0.9500	C(11)-H(11)	0.9500
C(12)-H(12)	0.9500	C(13)-H(13A)	0.9900
C(13)-H(13B)	0.9900	C(15)-H(15)	0.9500
C(16)-H(16)	0.9500	C(17)-H(17)	0.9500
C(18)-H(18)	0.9500	C(19)-H(19)	0.9500
C(21)-H(21)	0.9500	C(22)-H(22)	0.9500
C(23)-H(23)	0.9500	C(24)-H(24)	0.9500
C(25)-H(25)	0.9500	C(27)-H(27)	0.9500
C(28)-H(28)	0.9500	C(29)-H(29)	0.9500

C(30)-H(30)	0.9500	C(31)-H(31)	0.9500
C(32)-H(32)	1.0000		

Symmetry transformations used to generate equivalent atoms:

Table 5. Bond angles [°] for $[Pd(TMEDA)(C_6H_4CH_2PPh_3)(I)]^+[PF_6]^-$

atom-atom-atom	angle	atom-atom-atom	angle
C(7)-Pd(1)-N(2)	92.62(7)	C(7)-Pd(1)-N(1)	176.11(7)
N(2)-Pd(1)-N(1)	83.72(6)	C(7)-Pd(1)-I(1)	87.54(5)
N(2)-Pd(1)-I(1)	179.65(5)	N(1)-Pd(1)-I(1)	96.12(5)
C(14)-P(1)-C(26)	110.38(8)	C(14)-P(1)-C(20)	109.59(8)
C(26)-P(1)-C(20)	108.34(8)	C(14)-P(1)-C(13)	108.20(8)
C(26)-P(1)-C(13)	110.89(9)	C(20)-P(1)-C(13)	109.43(8)
C(4)-N(1)-C(3)	108.55(17)	C(4)-N(1)-C(1)	110.23(17)
C(3)-N(1)-C(1)	109.06(16)	C(4)-N(1)-Pd(1)	110.65(11)
C(3)-N(1)-Pd(1)	113.96(12)	C(1)-N(1)-Pd(1)	104.31(11)
C(6)-N(2)-C(5)	108.45(17)	C(6)-N(2)-C(2)	108.48(16)
C(5)-N(2)-C(2)	110.24(16)	C(6)-N(2)-Pd(1)	114.87(12)
C(5)-N(2)-Pd(1)	108.99(13)	C(2)-N(2)-Pd(1)	105.76(13)
N(1)-C(1)-C(2)	110.65(16)	N(2)-C(2)-C(1)	110.97(17)
C(8)-C(7)-C(12)	117.78(16)	C(8)-C(7)-Pd(1)	119.31(13)
C(12)-C(7)-Pd(1)	122.89(13)	C(9)-C(8)-C(7)	121.29(17)
C(10)-C(9)-C(8)	120.34(17)	C(9)-C(10)-C(11)	118.98(16)
C(9)-C(10)-C(13)	118.70(16)	C(11)-C(10)-C(13)	122.32(16)
C(10)-C(11)-C(12)	120.33(16)	C(11)-C(12)-C(7)	121.21(16)
C(10)-C(13)-P(1)	112.77(12)	C(19)-C(14)-C(15)	120.32(17)
C(19)-C(14)-P(1)	118.39(14)	C(15)-C(14)-P(1)	120.79(14)
C(16)-C(15)-C(14)	119.07(19)	C(17)-C(16)-C(15)	120.45(19)
C(16)-C(17)-C(18)	120.37(19)	C(19)-C(18)-C(17)	120.3(2)
C(18)-C(19)-C(14)	119.48(18)	C(25)-C(20)-C(21)	119.96(16)
C(25)-C(20)-P(1)	121.74(14)	C(21)-C(20)-P(1)	118.22(13)
C(20)-C(21)-C(22)	120.00(17)	C(23)-C(22)-C(21)	119.58(18)
C(24)-C(23)-C(22)	120.46(17)	C(23)-C(24)-C(25)	120.03(17)
C(24)-C(25)-C(20)	119.96(18)	C(27)-C(26)-C(31)	119.96(17)
C(27)-C(26)-P(1)	119.37(14)	C(31)-C(26)-P(1)	120.43(14)
C(28)-C(27)-C(26)	119.26(19)	C(29)-C(28)-C(27)	120.7(2)
C(28)-C(29)-C(30)	120.1(2)	C(31)-C(30)-C(29)	120.2(2)
C(30)-C(31)-C(26)	119.75(19)	F(6)-P(2)-F(3)	91.73(9)
F(6)-P(2)-F(5)	91.20(10)	F(3)-P(2)-F(5)	91.09(11)
F(6)-P(2)-F(4)	89.61(9)	F(3)-P(2)-F(4)	178.64(9)
F(5)-P(2)-F(4)	89.13(11)	F(6)-P(2)-F(2)	90.09(9)
F(3)-P(2)-F(2)	89.38(10)	F(5)-P(2)-F(2)	178.62(10)
F(4)-P(2)-F(2)	90.37(10)	F(6)-P(2)-F(1)	179.42(9)
F(3)-P(2)-F(1)	88.62(9)	F(5)-P(2)-F(1)	89.25(9)
F(4)-P(2)-F(1)	90.04(8)	F(2)-P(2)-F(1)	89.45(9)
Cl(1)-C(32)-Cl(3)	110.20(11)	Cl(1)-C(32)-Cl(2)	109.82(11)
Cl(3)-C(32)-Cl(2)	110.67(11)	N(1)-C(1)-H(1A)	109.5
C(2)-C(1)-H(1A)	109.5	N(1)-C(1)-H(1B)	109.5
C(2)-C(1)-H(1B)	109.5	H(1A)-C(1)-H(1B)	108.1

N(2)-C(2)-H(2A)	109.4	C(1)-C(2)-H(2A)	109.4
N(2)-C(2)-H(2B)	109.4	C(1)-C(2)-H(2B)	109.4
H(2A)-C(2)-H(2B)	108.0	N(1)-C(3)-H(3A)	109.5
N(1)-C(3)-H(3B)	109.5	H(3A)-C(3)-H(3B)	109.5
N(1)-C(3)-H(3C)	109.5	H(3A)-C(3)-H(3C)	109.5
H(3B)-C(3)-H(3C)	109.5	N(1)-C(4)-H(4A)	109.5
N(1)-C(4)-H(4B)	109.5	H(4A)-C(4)-H(4B)	109.5
N(1)-C(4)-H(4C)	109.5	H(4A)-C(4)-H(4C)	109.5
H(4B)-C(4)-H(4C)	109.5	N(2)-C(5)-H(5A)	109.5
N(2)-C(5)-H(5B)	109.5	H(5A)-C(5)-H(5B)	109.5
N(2)-C(5)-H(5C)	109.5	H(5A)-C(5)-H(5C)	109.5
H(5B)-C(5)-H(5C)	109.5	N(2)-C(6)-H(6A)	109.5
N(2)-C(6)-H(6B)	109.5	H(6A)-C(6)-H(6B)	109.5
N(2)-C(6)-H(6C)	109.5	H(6A)-C(6)-H(6C)	109.5
H(6B)-C(6)-H(6C)	109.5	C(9)-C(8)-H(8)	119.4
C(7)-C(8)-H(8)	119.4	C(10)-C(9)-H(9)	119.8
C(8)-C(9)-H(9)	119.8	C(10)-C(11)-H(11)	119.8
C(12)-C(11)-H(11)	119.8	C(11)-C(12)-H(12)	119.4
C(7)-C(12)-H(12)	119.4	C(10)-C(13)-H(13A)	109.0
P(1)-C(13)-H(13A)	109.0	C(10)-C(13)-H(13B)	109.0
P(1)-C(13)-H(13B)	109.0	H(13A)-C(13)-H(13B)	107.8
C(16)-C(15)-H(15)	120.5	C(14)-C(15)-H(15)	120.5
C(17)-C(16)-H(16)	119.8	C(15)-C(16)-H(16)	119.8
C(16)-C(17)-H(17)	119.8	C(18)-C(17)-H(17)	119.8
C(19)-C(18)-H(18)	119.9	C(17)-C(18)-H(18)	119.9
C(18)-C(19)-H(19)	120.3	C(14)-C(19)-H(19)	120.3
C(20)-C(21)-H(21)	120.0	C(22)-C(21)-H(21)	120.0
C(23)-C(22)-H(22)	120.2	C(21)-C(22)-H(22)	120.2
C(24)-C(23)-H(23)	119.8	C(22)-C(23)-H(23)	119.8
C(23)-C(24)-H(24)	120.0	C(25)-C(24)-H(24)	120.0
C(24)-C(25)-H(25)	120.0	C(20)-C(25)-H(25)	120.0
C(28)-C(27)-H(27)	120.4	C(26)-C(27)-H(27)	120.4
C(29)-C(28)-H(28)	119.6	C(27)-C(28)-H(28)	119.6
C(28)-C(29)-H(29)	120.0	C(30)-C(29)-H(29)	120.0
C(31)-C(30)-H(30)	119.9	C(29)-C(30)-H(30)	119.9
C(30)-C(31)-H(31)	120.1	C(26)-C(31)-H(31)	120.1
Cl(1)-C(32)-H(32)	108.7	Cl(3)-C(32)-H(32)	108.7
Cl(2)-C(32)-H(32)	108.7		

Symmetry transformations used to generate equivalent atoms:

Table 6. Torsion angles [°] for $[Pd(TMEDA)(C_6H_4CH_2PPh_3)(I)]^+[PF_6]^-$.

atom-atom-atom-atom	angle	atom-atom-atom-atom	angle
C(7)-Pd(1)-N(1)-C(4)	124.0(10)	N(2)-Pd(1)-N(1)-C(4)	104.29(15)
I(1)-Pd(1)-N(1)-C(4)	-76.02(14)	C(7)-Pd(1)-N(1)-C(3)	-113(10)
N(2)-Pd(1)-N(1)-C(3)	-133.06(14)	I(1)-Pd(1)-N(1)-C(3)	46.63(14)
C(7)-Pd(1)-N(1)-C(1)	5.5(10)	N(2)-Pd(1)-N(1)-C(1)	-14.23(12)
I(1)-Pd(1)-N(1)-C(1)	165.45(11)	C(7)-Pd(1)-N(2)-C(6)	47.76(15)
N(1)-Pd(1)-N(2)-C(6)	-133.56(14)	I(1)-Pd(1)-N(2)-C(6)	164(17)
C(7)-Pd(1)-N(2)-C(5)	-74.14(14)	N(1)-Pd(1)-N(2)-C(5)	04.54(13)
I(1)-Pd(1)-N(2)-C(5)	42(8)	C(7)-Pd(1)-N(2)-C(2)	67.35(14)
N(1)-Pd(1)-N(2)-C(2)	-13.97(13)	I(1)-Pd(1)-N(2)-C(2)	-76(8)
C(4)-N(1)-C(1)-C(2)	-78.1(2)	C(3)-N(1)-C(1)-C(2)	62.83(17)
Pd(1)-N(1)-C(1)-C(2)	40.72(18)	C(6)-N(2)-C(2)-C(1)	64.67(18)
C(5)-N(2)-C(2)-C(1)	-76.7(2)	Pd(1)-N(2)-C(2)-C(1)	41.0(2)
N(1)-C(1)-C(2)-N(2)	-57.8(2)	N(2)-Pd(1)-C(7)-C(8)	81.10(15)
N(1)-Pd(1)-C(7)-C(8)	61.5(10)	I(1)-Pd(1)-C(7)-C(8)	-98.59(15)
N(2)-Pd(1)-C(7)-C(12)	-97.44(16)	N(1)-Pd(1)-C(7)-C(12)	-117.1(9)
I(1)-Pd(1)-C(7)-C(12)	82.87(15)	C(12)-C(7)-C(8)-C(9)	2.9(3)
Pd(1)-C(7)-C(8)-C(9)	-175.73(15)	C(7)-C(8)-C(9)-C(10)	-1.6(3)
C(8)-C(9)-C(10)-C(11)	-0.6(3)	C(8)-C(9)-C(10)-C(13)	79.67(17)
C(9)-C(10)-C(11)-C(12)	1.4(3)	C(13)-C(10)-C(11)-C(12)	-78.85(16)
C(10)-C(11)-C(12)-C(7)	-0.1(3)	C(8)-C(7)-C(12)-C(11)	-2.0(3)
Pd(1)-C(7)-C(12)-C(11)	176.52(13)	C(9)-C(10)-C(13)-P(1)	-94.84(18)
C(11)-C(10)-C(13)-P(1)	85.43(19)	C(14)-P(1)-C(13)-C(10)	43.11(15)
C(26)-P(1)-C(13)-C(10)	-78.08(14)	C(20)-P(1)-C(13)-C(10)	62.47(13)
C(26)-P(1)-C(14)-C(19)	-157.54(15)	C(20)-P(1)-C(14)-C(19)	-38.30(18)
C(13)-P(1)-C(14)-C(19)	80.95(16)	C(26)-P(1)-C(14)-C(15)	30.60(18)
C(20)-P(1)-C(14)-C(15)	149.84(15)	C(13)-P(1)-C(14)-C(15)	-90.90(17)
C(19)-C(14)-C(15)-C(16)	1.4(3)	P(1)-C(14)-C(15)-C(16)	73.12(16)
C(14)-C(15)-C(16)-C(17)	-1.3(3)	C(15)-C(16)-C(17)-C(18)	0.0(3)
C(16)-C(17)-C(18)-C(19)	1.2(3)	C(17)-C(18)-C(19)-C(14)	-1.0(3)
C(15)-C(14)-C(19)-C(18)	-0.3(3)	P(1)-C(14)-C(19)-C(18)	-72.18(16)
C(14)-P(1)-C(20)-C(25)	124.51(16)	C(26)-P(1)-C(20)-C(25)	-15.01(16)
C(13)-P(1)-C(20)-C(25)	6.01(18)	C(14)-P(1)-C(20)-C(21)	-58.70(17)
C(26)-P(1)-C(20)-C(21)	61.78(16)	C(13)-P(1)-C(20)-C(21)	-77.20(14)
C(25)-C(20)-C(21)-C(22)	0.2(3)	P(1)-C(20)-C(21)-C(22)	-76.62(15)
C(20)-C(21)-C(22)-C(23)	0.4(3)	C(21)-C(22)-C(23)-C(24)	-0.5(3)
C(22)-C(23)-C(24)-C(25)	0.0(3)	C(23)-C(24)-C(25)-C(20)	0.6(3)
C(21)-C(20)-C(25)-C(24)	-0.7(3)	P(1)-C(20)-C(25)-C(24)	76.03(15)
C(14)-P(1)-C(26)-C(27)	43.16(17)	C(20)-P(1)-C(26)-C(27)	-76.83(16)
C(13)-P(1)-C(26)-C(27)	163.05(14)	C(14)-P(1)-C(26)-C(31)	-42.43(14)
C(20)-P(1)-C(26)-C(31)	97.57(15)	C(13)-P(1)-C(26)-C(31)	-22.54(17)
C(31)-C(26)-C(27)-C(28)	0.6(3)	P(1)-C(26)-C(27)-C(28)	75.03(15)
C(26)-C(27)-C(28)-C(29)	0.7(3)	C(27)-C(28)-C(29)-C(30)	-0.9(3)
C(28)-C(29)-C(30)-C(31)	-0.4(3)	C(29)-C(30)-C(31)-C(26)	1.7(3)
C(27)-C(26)-C(31)-C(30)	-1.8(3)	P(1)-C(26)-C(31)-C(30)	-76.17(14)

Symmetry transformations used to generate equivalent atoms.